Ion Beam Analysis of Solute Incorporation in GaAsN and GaAsNBi Alloys

by

Timothy Yu Cheng Jen

A dissertation submitted in partial fulfillment
of the requirements for the degree of
Doctor of Philosophy
(Materials Science and Engineering)
in the University of Michigan
2017

Doctoral Committee:

Professor Rachel S. Goldman, Chair
Assistant Professor John Heron
Professor Cagliyan Kurdak
Assistant Professor Liang Qi
Yongqiang Wang, Los Alamos National Laboratory

Timothy Yu Chen Jen

timyjen@umich.edu

ORCID iD: 0000-0002-8425-1784

Acknowledgements

I would like to thank my advisor, Rachel S. Goldman, for her guidance and support throughout my studies at University of Michigan. I would also like to thank my thesis committee members Cagliyan Kurdak, John Heron, Liang Qi, and Yongqiang Wang for their valuable discussions and suggestions.

This dissertation would not have been possible without the help of many collaborators. I would like to thank especially Yongqiang Wang and Joe Tesmer at the Los Alamos National Lab (LANL), who shared valuable ion beam knowledge with me during my time at LANL.

I thank my fellow group members for their help and support as well. I would like to thank, in particular, Jordan Occena, Davide Del Gaudio, Richard Field, Simon Huang, Michael Warren, and Myungkoo Kang for their assistance, discussions, and suggestions.

I gratefully acknowledge support from National Science Foundation (Grant No. DMR 1410282), U.S. Department of Energy Office of Science Graduate Student Research (SCGSR) Program and the Center for Integrated Nanotechnologies (CINT), a DOE nanoscience user facility jointly operated by Los Alamos and Sandia National Laboratories.

Finally, I would like to thank my family and friends for their constant support and encouragement throughout my journey.

Table of Contents

List of Figures

List of Tables

List of Appendices

Abstract

Ion Beam Analysis of Solute Incorporation in GaAsN and GaAsNBi Alloys

By

Timothy Yu Cheng Jen

Chair: Rachel S. Goldman

Highly mismatched alloys (HMAs) consist of highly immiscible solute atoms in a solvent. In dilute nitride semiconductor alloys, due to the resonant interactions between the conduction and/or valence band of the solvent and energy levels of the N solute, the bangdgap energies can be tuned dramatically without a significant change in lattice parameter, making them promising for a wide variety of optolelectronic applications. However, it has been shown that post-growth rapid thermal annealing (RTA) is needed to achieve suitable transport properties and emission efficiencies. Therefore, identification of the local atomic environments of the N solute atoms and the influence of RTA and anion co-incorporation on those environments is needed.

In the case of GaAsN, several groups have suggested that N shares an arsenic site with either arsenic or another N atom, often termed $(N\text{-}As)_{As}$ or $(N\text{-}N)_{As}$ split interstitials. To distinguish $(N\text{-}N)_{As}$ and $(N\text{-}As)_{As}$ interstitials in GaAsN alloys, we compare nuclear reaction analysis (NRA) spectra with simulations utilizing full numerical integration of ion trajectories. In both cases, incident particle paths along the [100], [110], and [111] directions are considered. Both the measured and simulated channeling NRA spectra

exhibit the highest (lowest) yields in the [111] ([100]) directions, suggesting that dominant interstitial complex is $(N\text{-}As)_{As}$. In addition, we use our combined computational-experimental approach to examine the influence of rapid-thermal annealing (RTA) on the local environment of N atoms, identifying a plausible mechanism for dissociation of $(N\text{-}N)_{As}$ into N_{sub} and $(N\text{-}As)_{As}$.

For GaAsN and related alloys, co-alloying with larger group V elements such as Sb or Bi is expected to lead to significant energy bandgap narrowing using a substantially lower N fraction, and a correspondingly lower concentration of N-related defects that degrade carrier mobilities and optical efficiencies. For GaAsNBi, the published experimental work has focused primarily on growth parameters and optical properties, without addressing the mechanisms for N and Bi co-incorporation during epitaxy. The incorporation of Bi is found to be independent of N flux, while the total N incorporation and the fraction of N atoms occupying non-substitutional lattice sites increase with increasing Bi flux. In addition, a comparison of channeling nuclear reaction analysis along the [100], [110], and [111] directions with Monte Carlo-Molecular Dynamics simulations indicates that the non-substitutional N primarily incorporate as $(N\text{-}As)_{As}$ interstitial complexes. Finally, we determine the "magic ratio" for lattice matching of GaAsNBi to GaAs: $[Bi] \approx (1.23 \pm 0.04)[N]$.

Chapter 1

Introduction

1.1 Overview

Alloys of dilute nitride and dilute bismuthide ("bismide") semiconductors are of significant interest as their energy bandgaps can be tuned dramatically without a significant change in lattice parameter. Figure 1.1 shows a plot of energy bandgap versus bond length for Si, Ge, and several compound semiconductors.[1,2,3,4,5,6] Here, the bandgap of GaAs is reduced by approximately 150 meV for each $x_N = 0.01$ incorporated into $GaAs_{1-x}N_x$.[7] In addition, the bandgap of GaAs is reduced by approximately 84 meV for each $y_{Bi} = 0.01$ incorporated into $GaAs_{1-y}Bi_y$.[8] This significant reduction of the band gap energy enables growth of dilute nitride or bismide semiconductors alloys on common substrates such as GaAs and InP, with a variety of bandgap energies in the long wavelength regime, without a substantial change in the lattice parameter. Therefore, dilute nitride, dilute bismuthide, and related alloys and heterostructures are promising for a wide variety of optoelectronic applications including long-wavelength lasers[9,10,11] and detectors,[12,13,14] ultra-high-efficiency solar cells,[15,16] and high performance heterojunction bipolar transistors.[17,18,19,20,21,22]

In this chapter, we discuss the device applications and the motivation of exploring new semiconductor alloys in the context of device applications. In addition, we provide an overview of theoretical and experimental understanding of GaAsN and GaAsNBi alloys. We also discuss N-related interstitial complexes and the challenge of co-incorporating N and Bi in GaAs. Finally, a dissertation outline will be provided.

1.2 Motivation

1.2.1 Electronic Doping and p-n junction formation

The energy band gap of a semiconductor determines the wavelength of light that can be absorbed or emitted. However, continuous electrically-driven operation of a light absorbing or emitting device requires the presence of an energy barrier which allows uni-directional carrier transport (i.e. a diode). Typically, a diode is formed with a rectifying metal-semiconductor, or a p-n junction, with "designer" negative type (n-type) and positive type (p-type) impurities providing free electrons or free holes, respectively. Therefore, for new alloys to make their way into optoelectronic devices, an understanding of both their formation and electronic doping is needed.

1.2.2 Light Emitting Diode and Photovoltaic

One example of a device fabricated using p-n junction as a building block is the light emitting diode. For light emitting devices operating at 1.3 μm (0.95 eV) and 1.55 μm

(0.8 eV) wavelengths, both Rayleigh scattering and infrared absorption are sufficiently low for long distance data transmission. In essence, optical fibers are near transparent at these wavelengths, allowing long-range transmission without significant power losses.[23] However, there are challenges in selecting the proper materials. For example, InP-based devices, such as InAs/InP and InGaAsP/InP, suffer from high threshold currents and a large sensitivity to temperature in the 1.3-1.6 μm telecommunications range due to the presence of non-radiative Auger recombination process and inter-valence band absorption between split-off and light/heavy-hole valence band.[24,25,26] Similarly, 1.3μm InAs/GaAs quantum dot based lasers also have been shown to suffer from Auger recombination.[27] In recent years, GaInNAs (~4% N, ~10% In) and GaAsNBi (~3.5% Bi, ~1.5% N) have emerged as promising materials light emitting devices.[9,28,29]

Figure 1.2 shows the record research cell efficiency vs year for a variety of materials systems. Although the reported solar cell efficiencies have been increasing monotonically for more than 40 years, physical limits to the light-to-energy conversion efficiencies are apparent. In particular, the efficiency of PV devices are constrained by the Schockley-Queisser limit (SQ limit).[30] Photons with energy less than the bandgap will are transmitted through the materials while photons with energy higher than the bandgap will be absorbed with any excess energy higher than the bandgap lost as heat. Thus, a single-junction PV device captures a limited portion of the available solar spectrum. For terrestrial applications, flat-plate silicon PV is the current market leader, but its performance has approached the Shockley-Queisser theoretical limit for a single junction Si PV device at 25%[31], while its manufacturing costs have leveled.

A promising alternative is concentrated PV (CPV) technologies, where incident sunlight is concentrated onto III-V multijunction (MJ) solar cells using refractive or reflective optics.[32] For MJ PV, a series configuration of GaInP, GaAs, and Ge p-n junections with bandgaps of 1.9 eV, 1.42 eV, and 0.67 eV, which have similar lattice parameters, held the efficiency record for many years. [22,32,33] It has long been predicted the insertion of an additional p-n junction, with a 1 eV bandgap, between the GaAs and Ge junctions, would lead to further efficiency increase, ultimately approaching 52%.[34,34] Considerable effort was made by several groups to grow InGaAsN for the 1 eV junction, but the success of the approach was reportedly limited by "N-defect" induced limits to minority carrier transport, with minority carrier diffusion lengths typically less than 0.1 μm.[35, 36,37] In recent years, Solar Junction demonstrated new alloy for the 1.05 eV junction cell, InGaAsN(Sb), which led to a MJ cell efficiency of 43.5%.[38,39,40] However, the electron mobility of InGaAsN alloys are typically $< 100\ cm^2/V-s$.[41,42,43] Therefore, post growth rapid thermal annealing (RTA) is needed to achieve high performance optoelectronic devices. For multi-junction solar cells, tunnel junctions which can withstand the RTA step are needed. For this purpose, an ErAs tunnel junction was developed.[39] However, erbium is an expensive and rare element that prevents cost-lowering of the PV devices.

1.2.3 Incorporation of Bi in GaAsN

Co-alloying GaAsN with larger elements such as indium (In), antimony (Sb), and/or Bi allows lattice-matching to GaAs or Ge substrates, with significant bandgap

narrowing using a substantially lower N fraction and correspondingly lower fraction of N-related defects.[30,44] Specifically, Bi incorporation into GaAs with $x = 0.01$ leads to a bandgap reduction of 84 meV, a much larger than the reduction for similar fractions of Sb (21 meV) or In (16 meV).[45] In addition, Bi induces a lowering of the split-off band away from light/heavy-hole valence band GaAs.[46] The resulting $\Delta E_{HH/LH-SO}$, which is larger than ΔE_g, as illustrated in Fig. 1.3, is expected to lead to reduced nonradiative Auger recombination and inter-valence band absorption that typically occurs in pure GaAs due to the similarities of $\Delta E_{HH/LH-SO}$ and ΔE_g .[47,48,49] Thus, GaAsNBi is promising for optoelectronic applications operating in the near-infrared range. Although GaAsNBi alloys lattice-matched to GaAs, with a bandgap of 1.3μm, have been demonstrated,[50,51] the precise composition was not quantified. Finally, with the incorporation of Bi, it is possible to eliminate the need for post-growth thermal treatments and rare-earth tunnel junctions, thereby lowering costs by enabling a faster production process and by minimizing the need for rare and expensive elements such as indium and erbium.[40,41]

To date, very few groups have reported on successful growth of GaAsNBi, all of whom are outside of the United States.[43,52,53,54] For GaAsNBi growth, two groups, one in Japan and one in Canada, used MBE technique, while one group in Germany used organic vapor phase epitaxy (MOVPE).

1.3 Bandgap Bowing in Highly Mismatched Alloys

Figure 1 shows a plot of energy bandgap versus bond length for Si, Ge, and several compound semiconductors.[1,2,3,4,5,6] The points correspond to binary or elemental

semiconductors. We note that alloys of these binaries or elemental semiconductors are estimated by lines connecting the points, which are generally not linear interpolations of the endpoints but instead are slightly bowed to a lower bandgap. Such behavior is typically well-described by a quadratic deviation from Vegard's law of mixtures, expressed as

$$\left(E_g\right)_{GaAsN}(x) = x\left(E_g\right)_{GaN} + (1-x)\left(E_g\right)_{GaAs} - x(1-x)b_{GaAsN} \qquad 1.1$$

and

$$\left(E_g\right)_{GaAsBi}(y) = y\left(E_g\right)_{GaBi} + (1-x)\left(E_g\right)_{GaAs} - y(1-y)b_{GaAsBi} \qquad 1.2$$

where x and y are the N fraction and Bi fraction substituting for As, respectively. In conventional III-V alloys, the so-called "bowing" parameter, b, is typically fractions of an eV[55]; however, for III-V-N and III-V-Bi alloys, b is composition-dependent, and is typically several eV.[37,44] For GaAsN and GaAsBi alloys, large bowing parameters, $b_{GaAsN} \approx 16 - 26\ eV$[56] and $b_{GaAsBi} \approx 2\ eV$[57,58], allow for a significant decreases in bandgap energy with only a small fraction of incorporated N or Bi.

Due to the large (small) atomic size of Bi (N) in comparison to that of As, GaAsBi (GaAsN) alloys are expected to induce compressive (tensile) strains at the GaAsBi/GaAs (GaAsN/GaAs) interfaces. However, for a ratio of Bi:N of 1:1.7, alloys of GaAsNBi are predicted to be lattice-matched to GaAs, with energy band gaps ranging from ~0.6 to ~1.4 eV.[59,60]

1.4 Band Anti-Crossing Model

To describe the electronic structure of so-called highly mismatched alloys (HMAs) a simple 2-level model termed the "band anti-crossing model" has been proposed.[61,62] As

illustrated in Fig. 1.4 for GaAsN, a N-induced level is assumed to interact with the GaAs conduction band states, splitting them into two sub-bands, E_+ and E_-. As the N fraction in GaAsN is increased, the E_+ and E_- splitting increases, effectively lowering the bandgap as E_- moves to a lower state. In the case of GaAsBi, a similar valence band anti-crossing (VBAC) model has been invoked to predict a Bi-induced splitting of the three valence sub-bands: heavy-hole (HH), light-hole (LH), and split-off (SO), as shown in Fig. 1.4.[46] Each sub-band is split into E_+ and E_- forming $E_+(HH^+, LH^+, SO^+)$ and $E_-(HH^+, LH^+, SO^+)$. Thus, as the Bi fraction in GaAsBi is increased, the net effect is an upward movement of the valence band as E_+moves to a higher energy.

Although these single local environment models (i.e. BAC and VBAC) have been used to accurately predict energy band gaps for III-As(Bi, N P, Sb) and Zn-Te(S, Se, O)[45,63,64,65,66], several extraordinary physical phenomena are not predicted by such models. For example, non-monotonic composition-dependent electron effective mass[67,68,69,70,71] and the persistent photoconductivity (PPC), in which an illumination-induced increase in conductivity persists following the termination of illumination[72,73,74], are not predicted by BAC but have been reported in GaAsN. In addition, a non-monotonic composition dependence of gyromagnetic factor, g_e, which describes the magnetic field induced splitting of electron energy levels, is not predicted by BAC but has been reported in InGaAsN alloys.[75] Finally, a non-monotonic composition dependence of the splitting of the SO from the HH and LH valence bands, which has been reported in GaAsBi, is not predicted by the VBAC models.[58]

To consider multiple atomic environments, the BAC model has been extended to include states associated with pairs and clusters, as shown in Fig. 1.5. For example, the

linear combination of isolated N resonant states (LCINS) model, which includes hybridization between the conduction band edge and the N cluster states, is shown in Fig. 1.5 (b) and (c).[76] The LCINS model has been used to accurately predict the observed N composition dependence of the position of the E_- level and the broadening of the E_+ level. Although this LCINS replicates the non-monotonic composition-dependence of the effective mass and g_e in the ultra-dilute alloy regime, its agreement is limited for the dilute alloy regime.[63,77,78,79,80] Indeed, the local atomic environments of solute atoms are composition-dependent and determine the properties of highly-mismatched semiconductor alloys. Therefore, more detailed understanding of the local atomic environments such of solute atoms are needed.

1.5 Interstitial Complexes in Related Dilute Nitrides

In the case of GaAsN and related dilute nitrides, it has been reported that N solute atoms do not all "see" the same atomic environment, as shown in Fig 1.5. It has been suggested that GaAsN may contain Ga interstitials and/or As_{Ga}-N_{As} complexes, and (Sb-N)$_{In}$ in (InGa)(AsSbN).[81,82,83,84] In addition, it has been shown that up to ~20% of N solute atoms share an arsenic site with either arsenic or another N atom, often termed (N-As)$_{As}$ or (N-N)$_{As}$ split interstitials as shown in Fig 1.6 and 1.7.[85,86,87,88,89] However, the precise N atomic configuration, including the relative fractions of (N-N)$_{As}$, (N-As)$_{As}$, or (As_{Ga}-N_{As}) complexes, remains unknown. Electronic structure computations have suggested that the most energetically favorable configuration of (N-N)$_{As}$ involves alignment of nitrogen dimers (N_2) along the [111] direction, with its center of mass in the center of the Group V

site.[86] For $(N\text{-}As)_{As}$, the predicted lowest energy configuration involves alignment of the N-As pair along the [010] direction.[90] Finally, at low growth temperatures, excess arsenic is often incorporated, introducing As antisites, As_{Ga}, and possibly (As_{Ga}-N_{As}) complexes.[73,91,92,93,94] In earlier studies, $(N\text{-}As)_{As}$ and $(N\text{-}N)_{As}$ split interstitials pairs have been shown to act as both trapping and scattering centers.[95,96] In addition, it has been reported that post-growth thermal annealing can be used to reduce the concentration of these interstitial complexes, as illustrated in Fig 1.6.[97] In addition, is has been suggested N-As and N-N pairs are the primary contributors to extraordinary physical phenomena such as non-monotonic composition-dependent electron effective mass[65, 98 , 99 , 100 , 101] and persistent photoconductivity (PPC)[69,102,103].

One of the goal of this thesis is to identify the dominant interstitial complexes, such as $(N\text{-}N)_{As}$ and $(N\text{-}As)_{As}$ configurations. For this purpose, we use channeling ion beam analyses, in which the crystal films are aligned along a specific crystal direction in order to detect the exposure or shadowing of various atoms. For example, in the [111] channeling condition, $(N\text{-}N)_{As}$ split interstitials, shown in Fig. 1.7, are shadowed by the Ga sublattice and would not be detected by nuclear reaction analysis measurements. However, $(N\text{-}As)_{As}$ split interstitials, aligned along the [010] axis, would be detected in [111] NRA spectra. Therefore, to quantify the relative contributions of N_{As}, $(N\text{-}As)_{As}$, and $(N\text{-}N)_{As}$, both measured and computed [100], [110], [111] channeling data are needed. To simulate NRA channeling experiment, the author adopted a Monte Carlo-Molecular Dynamic simulation code written in C++, from the Ph.D thesis of Dr. Wijesundera (University of Houston).[104] Specifically, the thermal vibrational amplitude,[105] atomic species, and ion velocities were replaced with those corresponding to our experiments, as listed in Appendix G. To simulate

multiple unit cells, the code was modified to use MatLab scripts which automatically generate the multiple unit cells structure. The MatLab script written by the author and undergraduate students working with him (James Horwath and Tim Johnson) are included in Appendix F.

1.6 GaAsNBi Alloys

To date, only three groups in the world have reported on the synthesis of quaternary GaAsNBi alloys, by either molecular-beam epitaxy[41,42] or metal-organic vapor phase epitaxy[40]. For GaAsN, growth temperatures of ~400ºC are needed to achieve >80% substitutional N incorporation.[70] In addition, as shown in Fig 1.8, to achieve smooth GaAsN surfaces by avoiding the so-called "forbidden window" of growth, the As_2/Ga or As_4/Ga beam-equivalent-pressure (BEP) ratio needs to be carefully selected.[106,107,108] On the other hand, for GaAsBi, due to the high vapor pressure[109,110] and low sticking coefficient of Bi[111,112], low growth temperatures, ~280ºC, are needed to achieve smooth, droplet-free films. Furthermore, as shown in Fig 1.9, there is a narrow As_2/Ga BEP window for incorporation of Bi into GaAsBi films.[113] Finally, for GaAsN and related alloys, bismuth is often reported to surface segregate without incorporating.[114,115,116,117,118] Indeed, the growth conditions of GaAsN and GaAsBi will need to be compromised to find a growth window that is suitable for GaAsNBi.

To date, the bandgap[119], emission wavelength[35], and electron mobility[40] of select compositions of GaAsNBi alloys have been reported. However, structural studies linking epitaxial growth processes to the optical and electronic properties of GaAsNBi are limited.

Furthermore, the presence of a Bi flux has been reported to increase or decrease the incorporation of N. For example, metalorganic vapor-phase epitaxy (MOVPE) with a Bi flux has been reported to decrease the N fraction,[96,120] while molecular-beam epitaxy (MBE) with a sufficiently high Bi flux has been reported to increase the N fraction.[88,121,122] Finally, although GaAsNBi alloys lattice-matched to GaAs with a bandgap of 1.3μm has been demonstrated and x-ray diffraction was used to estimate the Bi and N molar fractions,[46,47] the precise "magic" ratio of Bi to N compositions needed for lattice-matching remains unknown.

1.7 Dissertation Objectives

As described in Section 1.4, the BAC model, which is based upon a single local atomic environment, cannot explain extraordinary phenomena such as the non-monotonic N composition dependence of the effective mass and PPC observed in GaAsN and related alloys, which also contain N-related interstitial complexes.[86,87] In addition, the PPC effect is found to be suppressed after rapid thermal annealing (RTA) and InGaAsN-related devices often require RTA to achieve optimum performance.[12,116,123] Thus, the objective of the first part of the work in this dissertation is to identify the dominant N-interstitial complex in GaAsN alloys and examine the influence of RTA on the interstitial complexes.

As described in Section 1.6, prior to this thesis work, three other groups world-wide reported on the synthesis of GaAsNBi alloys,[88,96,97] with several others reporting on related electronic properties.[35,109,110] However, the relationship between growth, structure, optical and electronic properties of GaAsNBi is not well understood. For example, the "magic"

ratio of Bi to N for lattice-matching with GaAs has not been reported. Furthermore, the atomistic mechanisms for the influence of Bi flux on N incorporation also remain unknown. Thus, the goal of the second part of this dissertation is to identify growth conditions for the synthesis of GaAsNBi, to determine the "magic" ratio for lattice matching of GaAsNBi with GaAs, and to examine the influence of Bi flux on N incorporation in GaAsNBi.

1.8 Outline of dissertation

This dissertation is organized as follows. Chapter 2 describes the experimental and computational methods, including molecular-beam epitaxy (MBE), reflection high-energy electron diffraction (RHEED), rapid-thermal annealing (RTA), high-resolution X-ray diffraction (HRXRD), atomic force microscopy (AFM), Raman spectroscopy, atomic probe tomography (APT), Rutherford backscattering spectroscopy (RBS), nuclear reaction analysis (NRA), and Monte Carlo-Molecular Dynamics (MC-MD) simulations.

In Chapter 3, we introduce point defect complexes in GaAsN and related dilute nitride materials. We then describe our approach to determine the dominant interstitial in dilute GaAsN alloys, namely, a comparison between measured and simulated NRA channeling data. In both cases, the highest (lowest) yields in the [111] ([100]) directions were observed for simulations of the $(N\text{-}As)_{As}$ interstitial complex, suggesting that $(N\text{-}As)_{As}$ is the dominant interstitial complex in dilute GaAsN alloys.

In Chapter 4, we describe literature studies on RTA of dilute nitride alloys, which revealed reductions in the fraction of N-related interstitial.[124,125,126,127] We then describe

our combined computational-experimental approach to investigate the influence of RTA on GaAsN alloys. Our data suggests RTA-induced decreases in the fraction of $(N\text{-}N)_{As}$ interstitial complexes and increases in the fraction of $(N\text{-}As)_{As}$ interstitial complexes. These findings are supported by our multiple unit cell simulations that accommodate of multiple interstitial complexes. We propose three possible $(N\text{-}N)_{As}$ dissociation mechanisms, identify one which explains the observed increases in the fractions of N_{sub} and $(N\text{-}As)_{As}$ interstitial complexes.

In Chapter 5, we provide an overview of the current understanding of the growth and properties GaAsNBi. Then, we describe our approaches to meet the challenges associated with maintaining III-V stoichiometry while incorporating both N and Bi into GaAs. We then present a "magic ratio" $[Bi] = (1.25 \pm 0.02)[N]$ for lattice matched GaAsNBi alloy and discuss Bi-enhanced N incorporation that is attributed to preferential N-As pairing at [110]-oriented step-edges.

In Chapter 6, we present a summary and offer suggestions for future work. To determine the precise locations of the N-containing interstitial complexes, i.e. how far each atom is displaced from the lattice site, we propose to use angular channeling scans. To quantify the Ga:As stoichiometry in the quaternary GaAsNBi alloys, we propose LEAP experiments using algorithms that allow precise control of local electric fields to resolve Ga and As fractions. We also suggest time-of-flight elastic recoil detection and RBS with higher energy α particles, especially with a gas ionization chamber detector. To test our hypothesis on the role of reconstruction and step-edges on enhanced N incorporation in the presence of a Bi flux, we suggest using miscut substrates to alter the density of A- and B-type step edges. In particular, we suggest an approach to enhance N

incorporation into $(N\text{-}As)_{As}$ complexes without the need for post-growth RTA. Finally, to achieve structures which are capable of capturing multiple wavelengths of light (for PV), we suggest the design and growth of multiple compositions of lattice-matched GaAsNBi films on GaAs.

1.9 Figures

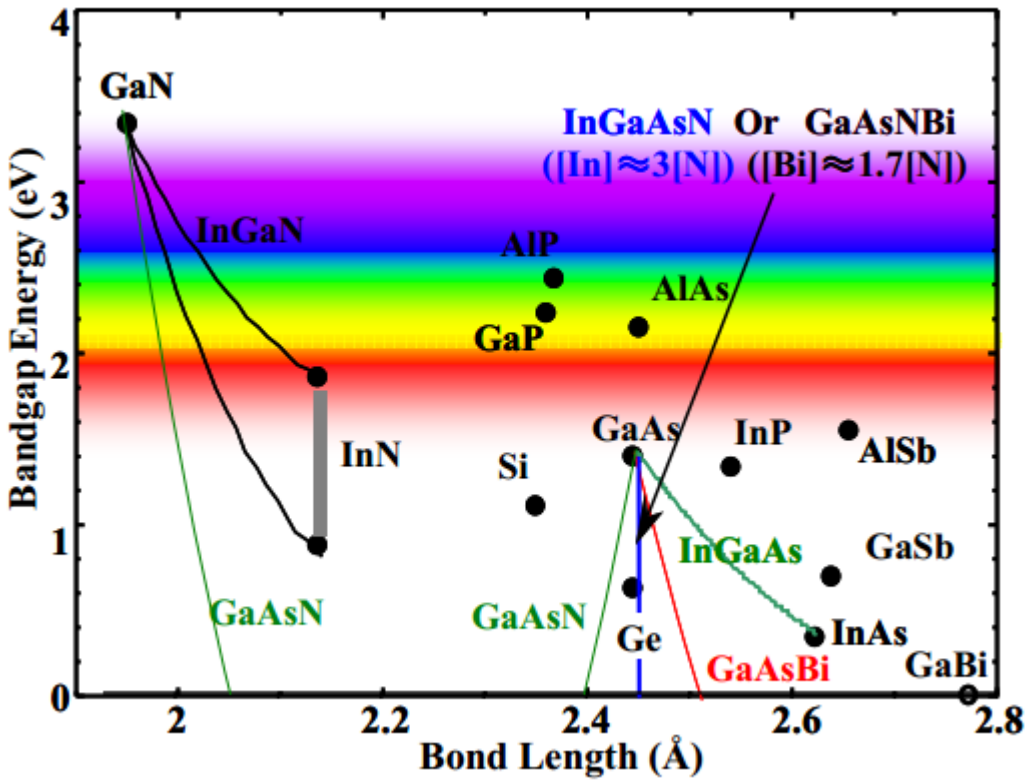

Figure 1.1 Bandgap energy vs bond length for various III-V semiconductor compounds.[5,128,129,130,131,132,133] Each point corresponds to the specific bandgap and the bond length for an element or compound. The lines corresponds to the binary alloys. (Note GaAsN line is shown with higher slope, it should not exhibit such extreme slope in reality). It has been predicted that GaAsNBi can be lattice matched to GaAs when [Bi]~1.7[N] for a variety of bandgap energy.[49] Adapted and printed with permission from Ref. 108 (Copyright 2015, Richard L. Field).[108]

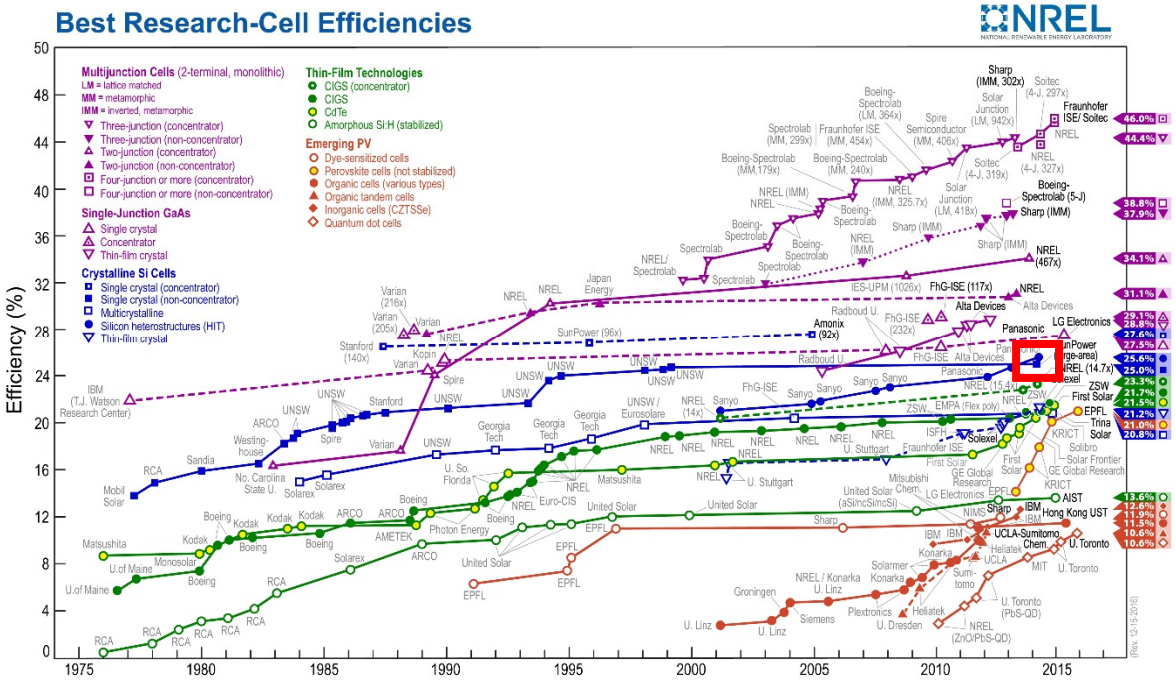

Figure 1.2 A plot of record "research" solar cell efficiency vs years compiled by NREL.[33] Navy blue represents crystalline Si cells. Purple represents single-junction, and Green and orange represents thin-film technologies and emerging PV technologies respectively. The red box emphasize the record efficiency of 25% reported for single crystal Si, which is near the Shockley Quiesser theoretical limit of 32%.[30] Thus, further efficiency increases beyond 25% will require the use of multi-junction cells based upon GaAs and related materials, which has a record of 43.5%.[22,32,33]

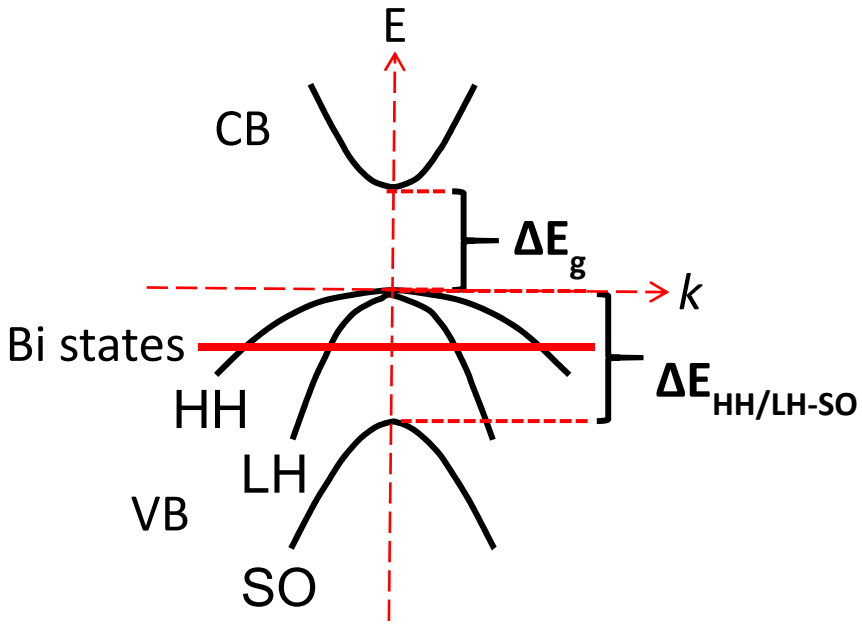

Figure 1.3 An illustration of the band structure of a GaAs alloy with Bi induced states in the vicinity of the Γ point. Since ΔE_g is similar to $\Delta E_{HH/LH-SO}$ in pure GaAs, nonradiative Auger recombination and inter-valence band absorptions often occur. For example, when the electron transition from conduction down to valence band, instead of having a radiative process, the energy can be used to excite another electron up into HH/LH valence band from the SO band, causing a non-radiative inter-valence recombination. It has been is predicted that Bi will induce a lowering of the split-off band away from light/heavy-hole valence band yielding $E_{HH/LH-SO}$ which is larger than ΔE_g, reducing the probability for nonradiative Auger recombination and inter-valence band absorption.

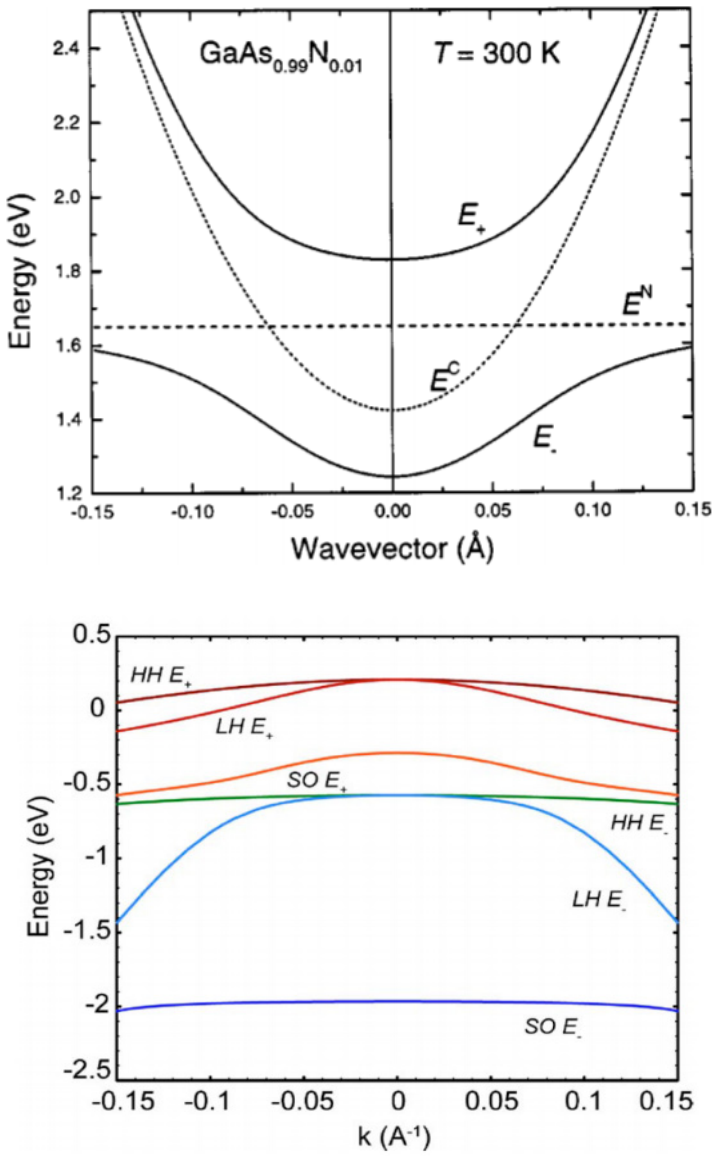

Figure 1.4 Schematic of dispersion relationship for the sub-bands for GaAsN (Top) and GaAsBi (Bottom) using band anti-crossing (BAC) and valance band anti-crossing (VBAC) models respectively. N localized states interact with the GaAs conduction band, splitting it into E_+ and E_- sub-bands, lowering the effective bandgap. Bi related localized states will induce similar effect to the valence band and split the heavy-hole (HH), light-hole (LH), and spin-orbit (SO) into E_+ and E_- forming $E_+(HH^+, LH^+, SO^+)$ and $E_-(HH^+, LH^+, SO^+)$, effectively lowering the bandgap by shifting E_+ to a higher level.[46,52,53] Reprinted with permission from Ref. 44 (Copyright 2003, AIP Publishing LLC) and 60 (Copyright 2007, AIP Publishing LLC).

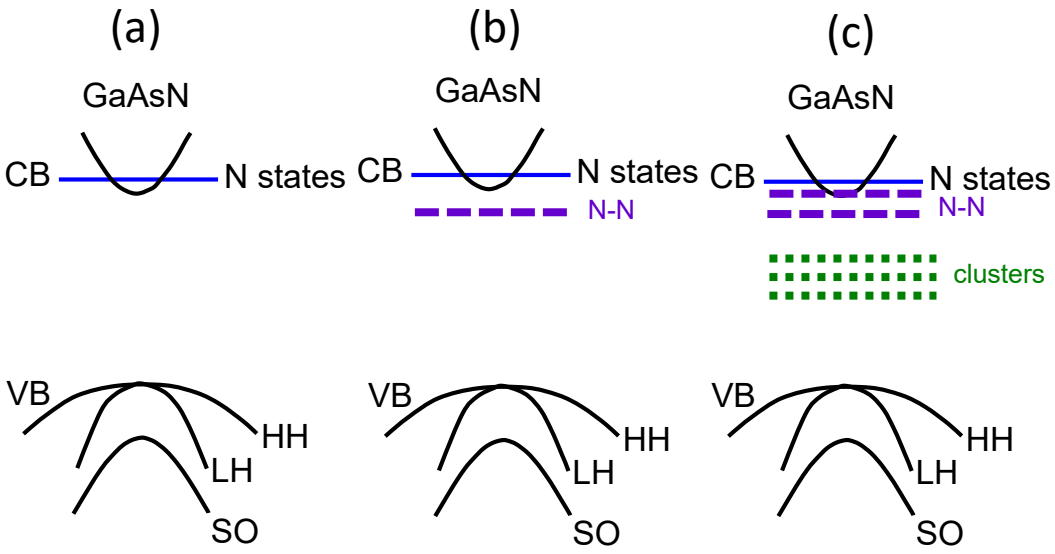

Figure 1.5 Schematics of GaAsN band structure considering (a) a single N atomic environment (i.e. the band anti-crossing model)[44], (b) N atoms and N-N pairs, and (c) N atoms, N-N pairs, and N clusters (the linear combination of isolated resonant states[57])

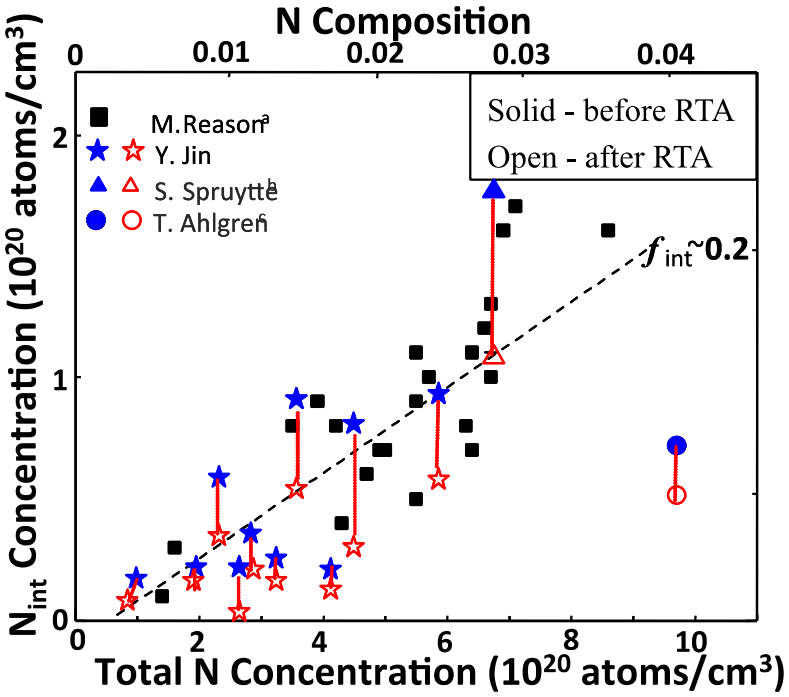

Figure 1.6 Interstitial N concentrations vs. total N concentrations for $GaAs_{1-x}N_x$ with varying x. The concentration of interstitial N increase with total N concentration. Linear extrapolation of the data before RTA suggests ~20% of N incorporated interstitially, as indicated in the plot. In addition, interstitial N concentration decreases after annealing, while the total N concentration remains constant.[69,78,79, 134] (Copyright 2013, APS Publishing LLC)

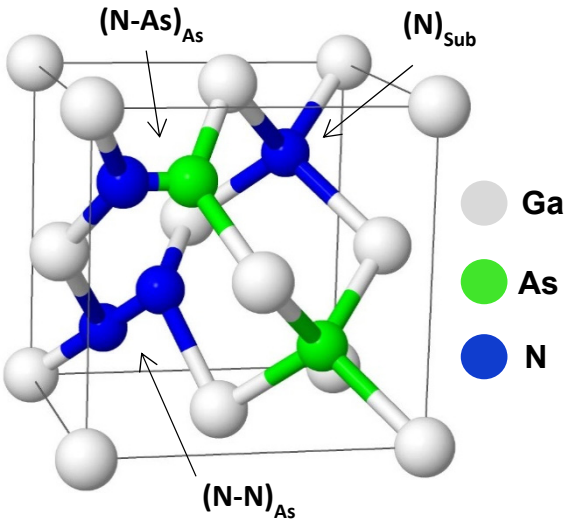

Figure 1.7 Ball-stick model of a GaAsN unit cell with $(N\text{-}As)_{As}$, $(N\text{-}N)_{As}$ and N_{sub} interstitials. The white, green, and blue spheres represent Ga, N, and As. We assume that $(N\text{-}N)_{As}$ is aligned along the [111] direction, while $(N\text{-}As)_{As}$ is aligned along the [010] direction. Each different interstitial complex will lead to different local atomic environment that is not considered in simple BAC models. (Copyright 2015, AIP Publishing LLC).

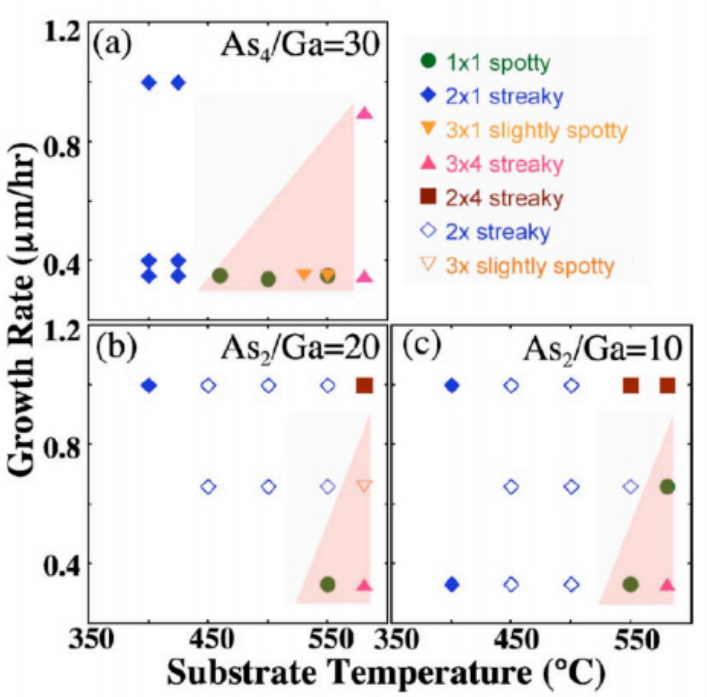

Figure 1.8 Surface reconstructions observed during growth of GaAsN films: growth rate vs substrate temperature for (a) As4/Ga BEP ratio ~30; (b) As2/Ga BEP ratio ~20; and (c) As2 /Ga BEP ratio ~10. Solid (open) symbols denote 500 nm (10–100 nm) thick GaAsN films. The shaded regions indicate the conditions which lead to significant surface roughness, referred to as the "forbidden window." Reprinted with permission from Ref. 113 (Copyright 2007, AIP Publishing LLC).

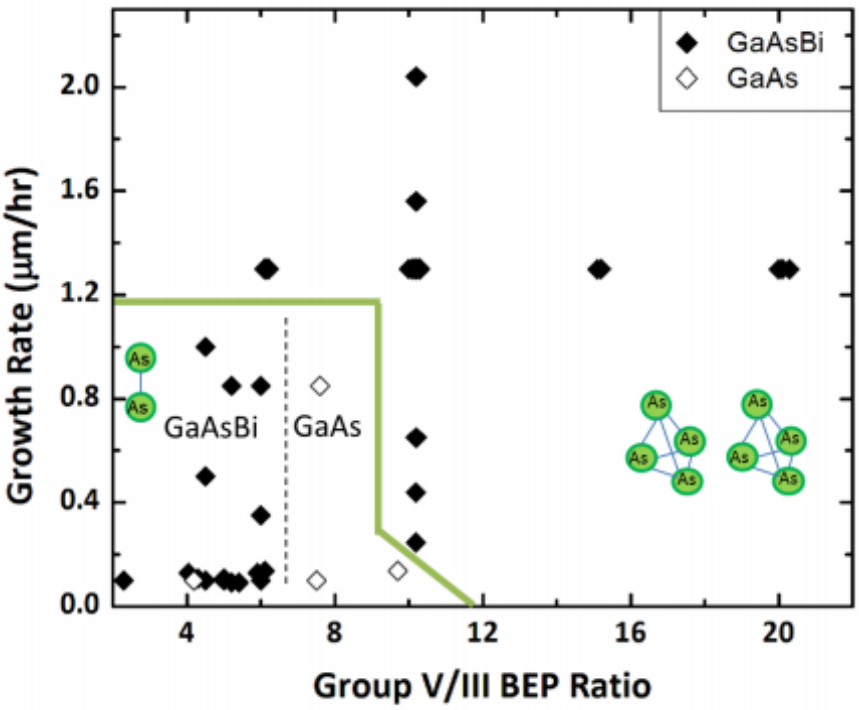

Figure 1.9 Bi incorporation into GaAs, as a function of growth rate and Group V/III BEP ratio, for various GaAs(Bi) films grown using either As_2 or As_4. The solid line separates films grown with As_2 and As_4, with films grown using As_2 in the lower-left-hand corner of the plot. All films were exposed to As, Ga and Bi flux. Films with Bi incorporation (no Bi incorporation) are shown as solid (open) symbols. For films grown using As_2, a dashed line separates films with Bi incorporation from films without Bi incorporation, with Bi incorporation for Group V/III BEP ratios ≤ 6. It is shown here that As_2 has a very limited growth window in comparison to growths using As_4. Adapted and printed with permission from Ref. 136 (Copyright 2015, Richard L. Field).

1.10 References

[1] K. Uesungi, N. Morooka, and I. Suemune, Appl. Phys. Lett. 74, 1254 (1999).

[2] I. Vurgaftman, J.R. Meyer and L.R. Ram-Mohan, J. Appl. Phys. 89, 5815 (2001).

[3] H.J. Hovel and J.J. Cuomo, Appl. Phys. Lett. 20, 71 (1972).

[4] T.L. Tansley and C.P. Foley, J. Appl. Phys. 59, 3241 (1986).

[5] P. Specht, J.C. Ho, X. Xu, R. Armitage, E.R. Weber, R. Erni and C. Kisielowski, Solid State Commun. 135, 340 (2005).

[6] B. Monemar, P.P. Paskov and A. Kasic, Superlattices Microstruct. 38, 38 (2005).

[7] G. Bi and C.W. Tu, Appl. Phys. Lett. 70, 1608 (1997).

[8] S. Francoeur, M.-J. Seong, A. Mascarenhas, S. Tixier, M. Adamcyk, and T. Tiedje, Appl.Phys. Lett. 82, 3874 (2003).

[9] J.S. Harris, Semicond. Sci. Technol. 17, 880 (2002).

[10] L.H. Li, V. Sallet, G. Patriarche, L. Largeau, S. Bouchoule, K. Merghem, L. Travers, and J.C. Harmand, Electron. Lett. 39, 519 (2003).

[11] H. Reichert, A. Ramakrishnan, and G. Steinle, Development of InGaAsN-based 1.3 μm VCSELs, Semicond. Sci. Technol. 17, 892 (2002).

[12] M.R. Gokhale, J. Wei, H. Wang, and S.R. Forrest, Appl. Phys. Lett. 74, 1287 (1999).

[13] B. Sciana, I. Zborowska-Lindert, D. Pucicki, B. Boratynski, D. Radziewicz, M. Tlaczala, J. Serafinczuk, P. Poloczek, G. Sek, and J. Misiewicz, Opto-Electronics Review 16, 1 (2008).

[14] J.-Y. Duboz, M. Hugues, B. Damilano, A. Nedelcu, P. Bois, N. Kheirodin, and F.H. Julien, Appl. Phys. Lett. 94, 022103 (2009).

[15] J.F. Geisz and D.J. Friedman, Semicond. Sci. Technol. 17, 769 (2002).

[16] D.B. Jackrel, S.R. Bank, H.B. Yuen, M.A. Wistey, J.S. Harris, A.J. Ptak, S.W. Johnston, D.J. Friedman, and S.R. Kurtz, J. Appl. Phys. 101, 114916 (2007).

[17] P.C. Chang, N.Y. Li, A.G. Baca, H.Q. Hou, C. Monier, J.R. Laroche, F. Ren, and S.J. Pearton, IEEE Electron Dev. Lett. 22, 113 (2001).

[18] C. Monier, A.G. Baca, P.C. Chang, N.Y. Li, H.Q. Hou, F. Ren, and S.J. Pearton, Electron. Lett. 37, 198 (2001).

[19] P.M. Asbeck, R.J. Welty, C.W. Tu, H.P. Xin, and R.E. Welser, Semicond. Sci. Techno. 17, 898 (2002).

[20] K.L. Lew, S.F. Yoon, H. Wang, W. Wicaksono, J.A. Gupta, S.P. McAlister, J. Vac. Sci. Technol. B 24, 1308 (2006).

[21] I. Hase, US Patent #7,009,225 (2006).

[22] Z.D. Marks, I.W. Haygood, and B. VanZeghbroeck, IEEE Trans. Electron Dev. 60, 200 (2012).

[23] A. Buchwald, and K.W. Martin. Vol. 306. Springer Science & Business Media, 2012.

[24] S. Seki, H. Oohashi, H. Sugiura, T. Hirono, and K. Yokoyama, IEEE J. Quantum Electron. 32, 1478 (1996).

[25] A. R. Adams, M. Asada, Y. Suematsu, and S. Arai, Jpn. J. Appl. Phys. 19, L621 (1980).

[26] N. K. Dutta and R. J. Nelson, Appl. Phys. Lett. 38, 407 (1981).

[27] I. P. Marko, A. R. Adams, S. J. Sweeney, D. J. Mowbray, M. S. Skolnick, H. Y. Liu, and K. M. Groom, IEEE J. Sel. Top. Quantum Electron. 11, 1041 (2005).

[28] L.H. Li, V. Sallet, G. Patriarche, L. Largeau, S. Bouchoule, K. Merghem, L. Travers, and J.C. Harmand, Electron. Lett. 39, 519 (2003).

[29] H. Reichert, A. Ramakrishnan, and G. Steinle, Semicond. Sci. Technol. 17, 892 (2002).

[30] S. Rühle. *Solar Energy* 130, 139 (2016)

[31] NREL Effiency Record, https://www.nrel.gov/pv/assets/images/efficiency-chart.png; Download 3:00pm (August, 7, 2017).

[32] U.S. Department of Energy "Sunshot Vision Study 2012", http://www1.eere.energy.gov/solar/pdfs/47927.pdf

[33] S.R. Kurtz, D. Myers, J.M. Olson, in: 26th IEEE Photovoltaic Specialists Conf., 1997, pp. 875.

[34] D.J. Friedman, J.F. Geisz, S.R. Kurtz and J.M. Olson, J. Crsyt. Growth 195, 409 (1998).

[35] D.J. Friedman and S.R. Kurtz, Prog. Photovolt.: Res. Appl. 10, 331 (2002).

[36] A. Ptak, S. Kurtz, S.W. Johnston, D.J. Friedman, J.F. Geisz, J.M. Olson, W.E. McMahon, A.E. Kibbler, C. Kramer, M. Young, and S.H. Wei, National Center for Photovoltaics and Solar Program Review Meeting, Denver, CO March 24-26, NREL/CP-520-33555 (2003)

[37] F. Dimroth, C. Baur, A.W. Bett, K. Volz, and W. Stolz, J. of Cryst. Growth 272, 726 (2004).

[38] M. Wiemer, V. Sabnis, H. Yuen, Proc. of SPIE 8108, 810804 (2011).

[39] R.E. Jones, H.B. Yuen, T. Liu, and P. Misra, Solar Junction Corporation, 2014. U.S. Patent 8,912,433.

[40] M.W. Wiemer, Yuen, H.B., Sabnis, V.A., Sheldon, M.J. and Fushman, I., Solar Junction Corp., 2010. U.S. Patent Application 20,100,319,764

[41] S.G. Spruytte, C.W. Coldren, J.S. Harris, W. Wampler, P. Krispin, K. Ploog and M.C. Larson, J. Appl. Phys. 89, 4401 (2001).

[42] W. Li, M. Pessa and J. Likonen, J. Appl. Phys. 78, 2864 (2001).

[43] S. Kurtz, Steven R., J. F. Klem, A. A. Allerman, R. M. Sieg, C. H. Seager, and E. D. Jones. Appl. Phys. Lett. 80, 1379 (2002).

[44] A. Mascarenhas, US Patent #6,815,736 (2004).

[45] S. Tixier, M. Adamcyk, T. Tiedje, S. Francoeur, A. Mascarenhas, P. Wei, and F. Schiettekatte, Appl. Phys. Lett. 82, 2245 (2003).

[46] B. Fluegel, S. Francoeur, A. Mascarenhas, S. Tixier, E. C. Young, and T. Tiedje. Phys. Rev. Lett. 97, 067205 (2006).

[47] Z. Batool, K. Hild, T.J.C. Hosea, X. Lu, T. Tiedje, and S.J. Sweeney, J. Appl. Phys. 111, 113108 (2012).

[48] B.A, Ikyo, Barnbas Achakpa. American Journal of Optics and Photonics 5, 80 (2015).

[49] S.J. Sweeney, S. J., I. P. Marko, S. R. Jin, K. Hild, Z. Batool, N. Hossain, and T. J. C. Hosea. Bismuth-Containing Compounds (Springer, New York, USA 2013) pp. 29-33.

[50] M. Yoshimoto, W. Huang, K. Oe, *MRS Proceedings* 829, (2004)

[51] Z.L. Bushell, P. Ludewig, N. Knaub, Z. Batool, K. Hild, W. Stolz, S.J. Sweeney, and K. Volz, J. Cryst. Growth 396, 79 (2014).

[52] M. Yoshimoto, W. Huang, Y. Takehara, J. Saraie, A. Chayahara, Y. Horino, and K. Oe, Jap. J. Appl. Phys. Lett., L845 (2004).

[53] S. Tixier, S.E. Webster, E.C. Young, T. Tiedje, S. Francoeur, A. Mascarenhas, P. Wei, and F. Schiettekatte, Appl. Phys. Lett. 86, 112113 (2005).

[54] C.A. Broderick, S. Jin, I.P Marko, K. Hild, P. Ludewig, Z.L. Bushell, W. Stolz, J.M. Rorison, E.P. O'Reilly, K. Volz, and S.J. Sweeney, Scientific Reports 7, 46371. (2017).

[55] I. Vurgaftman and J. R. Meyer, J. Appl. Phys. 94, 3675 (2003).

[56] U. Tisch, E. Finkman, and J. Salzman, Appl. Phys. Lett. 81, 463 (2002).

[57] A. Abdiche, H. Abid, R. Riane, and A. Bouaza, Physica B 405, 2311 (2010).

[58] A. Janotti, S.-H. Wei, and S.B. Zhang, Phys. Rev. B 65, 115203 (2002).

[59] S.J. Sweeney, K. Hild, and S. Jin, IEEE PVSC, (2013) .

[60] S.J. Sweeney and S.R. Jin, J. Appl. Phys. 113, 043110 (2013).

[61] W. Shan, W. Walukiewicz, J.W. Ager, E.E. Haller, J.F. Geisz, D.J. Friedman, J.M. Olson,
and S.R. Kurtz, Phys. Rev. Lett. 82, 1221 (1991).

[62] K. Alberi, O.D. Dubon, W. Walukiewicz, K.M. Yu, K. Bertulis, and A. Krotkus, Appl. Phys. Lett. 91, 051909 (2007).

[63]J. Wu, W. Shan, and W. Walukiewicz, Semiconductor Science and Technology, 17, 860 (2002).

[64] Y.N. Qui and J.M Rorison, Appl. Phys. Lett. 87, 081111 (2005).

[65] I.A. Buyanova, M. Izadifard, A. Kasic, H. Arwin, W.M. Chen, H.P. Xin, Y.G. Hong, and C.W. Tu, C.W, Phy. Rev. B 70, 085209 (2004).

[66] P.H. Jefferson, T.D. Veal, L.F.J. Piper, B.R. Bennett, C.F. McConville, B.N. Murdin, L. Buckle, G.W. Smith, and T. Ashley, Appl. Phys. Lett. 89, 111921 (2006).

[67] P.N. Hai, W.M. Chen, I.A. Buyanova, H.P. Xin and C.W. Yu, Appl. Phys. Lett. 77, 1843
(2000).

[68] E.P. O'Reilly, A. Lindsay and S. Fahy, J. Phys-Condense Mat. 16, S3257 (2004).

[69] F. Masia, G. Pettinari, A. Polimeni, M. Felici, A. Miriametro, M. Capizzi, A. Lindsay, S.B. Healy, E.P. O'Reilly, A. Cristofoli, G. Bais, M. Piccin, S. Rubini, F. Martelli, A. Franciosi, P.J. Klar, K. Bolz and W. Stolz, Phys. Rev. B 73, 073201 (2006).

[70] S. Kurtz, S. Johnston and H. M. Branz, Appl. Phys. Lett. 86, 113506 (2005).

[71] G.B. von Hogersthal, A. Polimeni, F. Masia, M. Bissiri, M. Capizzi, D. Gollub, M. Fischer and A. Forchel, Phys. Rev. B 67, 233304 (2003).

[72] D.V. Lang, R.A. Logan, and M. Jaros, Phys. Rev. B 19, 1015 (1979).

[73] M.G. Craford, G.E. Stillman, J.A. Rossi, and N. Holonyak, Phys. Rev. B 168, 867 (1968).

[74] R.L. Field III, Y. Jin, H. Cheng, T. Dannecker, R.M. Jock, Y.Q. Wang, C. Kurdak, R.S. Goldman, *Phys. Rev. B* 87, 155303 (2013)

[75] G. Pettinari, F. Masia, A. Polimeni, M. Felici, A. Frova, M. Capizzi, A. Lindsay, E.P. O'Reilly, P.J. Klar, W. Stolz, G. Bais, M. Piccin, S. Rubini, F. Martelli, and A. Fanciosi, Phys. Rev. B 74, 245202 (2006).

[76] E.P. O'Reilly, A. Lindsay and S. Fahy, J. Phys-Condense Mat. 16, S3257 (2004).

[77] T. Dannecker, Y. Jin, H. Cheng, C.F. Gorman, J. Buckeridge, C. Uher, S. Fahy, C. Kurdak, and R.S. Goldman, Phys. Rev. B 82, 125203 (2010).

[78] P. Pichanusakorn, Y. J. Kuang, C. Patel, C. W. Tu, and P. R. Bandaru, Phys. Rev B 86, 085314 (2012).

[79] D.L. Young, J.F. Geisz and T.J. Coutts, Appl. Phys. Lett. 82, 1236 (2003).

[80] J. Ibanez, R. Cusco, E. Alarcon-Llando, L. Artus, A. Patane, D. Fowler, L. Eaves, K. and I.
Suemune, J. Appl. Phys. 103, 103528 (2008).

[81] P. Laukkanen, M. P. J. Punkkinen, J. Puustinen, H. Levämäki, M. Tuominen, K. Schulte, J. Dahl, J. Lång, H. L. Zhang, M. Kuzmin, K. Palotas, B. Johansson, L. Vitos, M. Guina, and K. Kokko, Phys. Rev. B 86, 195205 (2012).

[82] J. Chen, G. Ciatto, M. Le Du, J.C. Harmand and F. Glas, Phys. Rev. B 82, 125303 (2010).

[83] H.T. Pham, S.F. Yoon, K.H. Tan and D. Boning. Appl. Phys. Lett 99, 092115 (2010).

[84] H.P Nair, A.M. Crook, K.M. Yu and S.R. Bank. Appl. Phys. Lett 100, 021103 (2012)

[85] P. Carrier, S.-H. Wei, S. B. Zhang, and S. Kurtz, Phys. Rev. B 71, 165212 (2005).

[86] K. Laaksonen, H.-P. Komsa, T. T. Rantala, and R. M. Nieminen, J. Phys. Condens. Matter 20, 235231 (2008).

[87] M. Reason, H. McKay, W. Ye, S. Hanson, V. Rotberg, and R.S. Goldman, Appl. Phys. Lett. 85, 1692 (2004).

[88] S.B. Zhang and S.H. Wei, Phy. Rev. Lett. 86, 1789 (2001).

[89] Y. Jin, R.M. Jock, H. Cheng, Y. He, A.M. Mintairov, Y. Wang, C. Kurdak, J. L. Merz, R.S. Goldman, Appl. Phys. Lett., 95, 062109 (2009).

[90] E. Arola, J. Ojanen, H.-P. Komsa and T. T. Rantala, Phys. Rev. B 72, 045222 (2005).

[91] K.M. Yu, M. Kaminska, and Z. Liliental-Weber. J. Appl. Phys., 72, 2850 (1992).

[92] P. Wei, M. Chicoine, S. Gujrathi, F. Schiettekatte, J-N. Beaudry, R. A. Masut, and P. Desjardins. J. Vac. Sci. Technol., A, 22, 908 (2004)

[93] T. E. M. Staab, R. M. Nieminen, M. Luysberg, J. Gebauer, and T. Frauenheim, Phys. Rev. B: Condens. Matter, 340, 293 (2003).

[94] G. Zollo, and R. M. Nieminen. J. Phys.: Condens. Matter, 15.6 (2003)

[95] S. Fahy and E. P. O'Reilly, Appl. Phys. Lett. **83**, 3731 (2003)

[96] P. R. C. Kent and A. Zunger, Phys. Rev. B **64**, 115208 (2001)

[97] Y. Jin, R.M. Jock, H. Cheng, Y. He, A.M. Mintairov, Y. Wang, C. Kurdak, J.L. Merz, and R.S. Goldman, Appl. Phys. Lett. 95, 062109 (2009).

[98] P.N. Hai, W.M. Chen, I.A. Buyanova, H.P. Xin and C.W. Yu, Appl. Phys. Lett. 77, 1843 (2000).

[99] G.B. von Hogersthal, A. Polimeni, F. Masia, M. Bissiri, M. Capizzi, D. Gollub, M. Fischer and A. Forchel, Phys. Rev. B 67, 233304 (2003).

[100] S. Kurtz, S. Johnston and H. M. Branz, Appl. Phys. Lett. 86, 113506 (2005).

[101] F. Masia, G. Pettinari, A. Polimeni, M. Felici, A. Miriametro, M. Capizzi, A. Lindsay, S.B. Healy, E.P. O'Reilly, A. Cristofoli, G. Bais, M. Piccin, S. Rubini, F. Martelli, A. Franciosi, P.J. Klar, K. Bolz and W. Stolz, Phys. Rev. B 73 073201 (2006).

[102] T. Ahlgren, E. Vainonen-Ahlgren, J. Likonen, W. Li and M. Pessa, Appl. Phys. Lett. 80, 2314 (2002).

[103] S.H. Hsu, W.R. Chen, Y.K. Su, R.W. Chuang, S.J. Chang, and W.C. Chen, J. of Crys. Grow 290, 97 (2006).

[104] D. Wijesundera, PhD. Thesis, University of Houston, Houston, 2010.

[105] J.L. Whitton, G. Carter, J. H. Freeman, and G. A. Gard. *Journal of Materials Science* 4, 208 (1969)

[106] R.L. Schwoebel and E.J. Shipsey, J. Appl. Phys. 37, 3682 (1966).

[107] G. Ehrlich and F.J. Hudda, J. Chem. Phys. 44, 1069 (1966).

[108] M. Reason, N.G. Rudawki, H.A. McKay, X. Weng, W. Ye, and R.S. Goldman, J. Appl. Phys. 101, 083520 (2007).

[109] T. A. O'Donnell, Aust. J. Chem. 8, 493 (1955).

[110] R. Speiser and H. L. Johnston, J. Am. Chem. Soc. 75, 1469 (1953).

[111] X. Lu, D.A. Beaton, et al., Applied Physics Letters 92 (2008) 192110.

[112] F. Bastiman, A. Mohmad, J. Ng, J. David, S. Sweeney, J. Cryt. Growth 338 (1) (2012) 57–61.

[113] R.L Field, Ph.D. Thesis, Ch. 1, University of Michigan, Ann Arbor, 2015.

[114] G. Vardar, S.W. Paleg, M.V. Warren, M. Kang, S. Jeon, and R.S. Goldman. Appl. Phys. Lett, 102, 042106 (2013).

[115] K. Nakayama, K. Tanabe, and H. A. Atwater, Appl. Phys. Lett. 93, 121904 (2008).

[116] X. Lu, D. A. Beaton, R. B. Lewis, T. Tiedje, and M. B. Whitwick, Appl. Phys. Lett. 92, 192110 (2008).

[117] I. Moussa, H. Fitouri, A. Rebey, and B. El Jani, Thin Solid Films 516, 8372 (2008).

[118] H. Fitouri, I. Moussa, A. Rebey, A. Fouzri, and B. El Jani, J. Cryst. Growth 295, 114 (2006).

[119] D. G. Cooke, F.A. Hegmann, E.C. Young, and T. Tiedje, Appl. Phys. Lett. 89, no. 12 (2006).

[120] F. Dimroth, A. Howard, J.K. Shurtleff, and G.B. Stringfellow, J. Appl. Phys. 91, 3687 (2002).

[121] E.C. Young, S. Tixier, and T. Tiedje, J. Cryst. Growth 279, 316 (2005).

[122] T. Liu, S. Chandril, A.J. Ptak, D. Korakakis, and T.H. Myers, J. Cryst. Growth 304, 402 (2007).

[123] Y.G. Hong, C.W. Tu and R.K. Ahrenkiel, J. Cryst. Growth 227-228, 536 (2001).

[124] M. Ramsteiner, D. S. Jiang, J. S. Harris, and K. H. Ploog, Appl. Phys. Lett. **84**, 1859 2004.

[125] T. Prokofyeva, T. Sauncy, M. Seon, M. Holtz, Y. Qiu, S. Nikishin, and H. Temkin. Appl. Phys. Lett. **73** 1409 (1998)

[126] E.M. Pavelescu, J. Wagner, , H.P. Komsa, T.T. Rantala, M. Dumitrescu, and M. Pessa, J. Appl. Phys 98, 083524 (2005).

[127] Y. Jin, R.M. Jock, H. Cheng, Y. He, A.M. Mintairov, Y. Wang, C. Kurdak, J. L. Merz, R.S. Goldman, APL **95**, 062109 (2009)

[128] W.G. Bi and C. W. Tu, Appl. Phys. Lett. 70, 1608 (1997).

[129] K. Uesugi, N. Morooka and I. Suemune, Appl. Phys. Lett. 74, 1254 (1999).

[130] B. Monemar, P. P. Paskov and A. Kasic, Superlattices Microstruct. 38, 38 (2005).

[131] I. Vurgaftman, J. R. Meyer and L. R. Ram-Mohan, J. Appl. Phys. 89, 5815 (2001).

[132] H. J. Hovel and J. J. Cuomo, Appl. Phys. Lett. 20, 71 (1972).

[133] T. L. Tansley and C. P. Foley, J. Appl. Phys. 59, 3241 (1986).

[134] Y. Jin, Ph.D. Thesis, Ch. 1, University of Michigan, Ann Arbor, 2010.

Chapter 2

Methods

2.1 Overview

In this chapter, the experimental procedures and computational methods used in this dissertation work are described. First, we describe the MBE growth process, including details relevant to the growth of GaAsN, GaAsBi, and GaAsNBi alloys. Then, we describe post-growth thermal annealing and characterization methods including atomic force microscopy (AFM), scanning electron microscopy (SEM), x-ray diffraction (XRD), atomic probe tomography (APT), Raman spectroscopy, Rutherford backscatter spectrometry (RBS), and nuclear reaction analysis (NRA). Finally, we discuss our Monte Carlo-Molecular Dynamics Simulations.

2.2 Molecular-Beam Epitaxy

2.2.1 Overview

Molecular-beam epitaxy (MBE) is an ultra-high vacuum based vapor deposition method, which allows growth of high quality epitaxial films one atomic layer at a time.[1,2] The molecular-beams are formed by either sublimation or evaporation from heated solids or liquids, which then interact chemically with the heated substrate to form epitaxial films by condensation.[3] A radio-frequency plasma nitrogen source is also used to produce reactive nitrogen species. Because the incoming molecules are highly reactive, epitaxial growths typically occur at conditions far from equilibrium. The samples described in Chapters 3 and 4 were grown by Dr. Reason in the Goldman Group Modified Varian Gen II MBE (Gen II) using the Veeco plasma source. The samples described in Chapter 4 are grown by the author and Jordan Occena in the Gen II using the Addon plasma source. Additional GaAsBi growths, not discussed in this dissertation, were performed in the Riber Compact 21 MBE system (C21).

2.2.2 MBE system details

Both the Gen II and C21 MBEs contain interconnected but separately-pumped load-locks, buffer chambers, and growth chambers (GCs). Samples are transferred between the chambers via magnetic transfer rods and trolleys, as shown schematically in Fig. 2.1 and Fig 2.2. The sample blocks are mounted onto the manipulator, referred to as the CAR (for

continuous azimuthal rotation) in the Gen II and ARM (for azimuthal rotation manipulator) in the C21. To achieve optimum film uniformity, the CAR (or ARM) is rotated at 10 rpm.

Both growth chamber source flanges house seven high purity metal sources, including 99.99999% [7N] In, Ga and As; 99.99995% [6N5] Al; 99.9999% [6N] Bi and Si. The high purity metal sources are contained in pyrolytic boron nitride (PBN) crucibles, which are housed in Knudsen effusion cells. In each effusion cell, heating filaments are wrapped around the crucibles and the effusion cell temperature are monitored by a thermocouple in contact with the crucible. The desired temperatures are set using a proportional-integral-derivative (PID) controller paired with a direct current power supply. Each source is heated to a temperature above its sublimation/evaporation point in order to produce molecular beams. Both MBE chambers contained so-called As "cracking" cells, which include a "bulk" and "cracking" zones. The "bulk" zone (BZ) which contains the As solid source material, is heated to a low (450ºC) temperature, leading to the sublimation of As_4 into the "cracking" zone (CZ), which is then heated to a high temperature (900ºC for Gen II) to dissociate (or "crack") As_4 into As_2. Details of the calibration of the As cracking cell for the C21 are available in Appendix A. The fluxes of the molecular beams are exponentially dependent on the temperature; the fluxes are monitored and calibrated by a beam flux ion gauge at the sample position prior to the commencement of each growth sequence.

The Gen II source flange also houses a radio frequency (RF) plasma source, outfitted with ultrahigh purity (6N) N_2 gas that is filtered with an Entegris 0.003 μm filter, to produce active N. The RF plasma nitrogen source requires a process of "striking" or "igniting" the plasma. For the Addon plasma source, the plasma is ignited into a "low-

brightness" mode followed by a "medium-brightness" mode, and finally, into a "high-brightness" mode. Details of the N_2 plasma ignition processes for both the Veeco and the Addon plasma sources are included in Appendix B. To control the N flux, we use a Stanford Research Systems RGA300 residual gas analyzer (RGA) in leak test mode; we adjust the mass-flow controller accordingly to monitor N_{14}.

2.2.3 Substrate Preparation

All films were grown on "epi-ready" GaAs substrates. For each growth, approximately one-eighth of a 3-inch GaAs substrate is cleaved and indium-mounted onto a molybdenum block. Once the samples are mounted and loaded onto the sample trolley, the sample load-lock is pumped down to <1E-5 Torr and baked at 150ºC for 8 hours. Prior to transferring each block from the buffer to the growth chamber, each block is individually outgassed at 180ºC in the buffer chamber heating station for 30 minutes. (We note that the heated station in C21 is currently non-functional.) Within the GC, each sample is heated to 300ºC, at which point the As shutter and needle valve are opened, thereby providing an As overpressure. Next, the substrate temperature is ramped to 580ºC for oxide desorption. Following observation of the signature RHEED transition to a streaky (2x4) pattern, the substrate temperature is raised an additional 20ºC and held for 10 minutes to ensure complete oxide desorption.

2.2.4 Temperature calibration

In both MBE systems, the sample surface temperature is often inferred by a thermocouple (TC) in contact with the back of each molybdenum block. However, the TC temperature (T_{CAR}) is typically higher than the temperature at the sample surface. Therefore, a substrate temperature (T_{sub}) calibration was determined for each surface. For the GaAsN films discussed in Chapter 3 and 5, the T_{sub} calibration was based upon the oxide desorption temperature. Specifically, in the presence of a sufficient As flux, the RHEED pattern transforms from a hazy (2x4) to a spotty-hazy (2x4), and then finally to a streaky (2x4) pattern upon desorption of the surface oxide. Although the precise oxide desorption temperature depends on the initial thickness of the oxide, we consider the T_{sub} to be 580ºC and linearly extrapolate the T_{CAR} between 400 and 900ºC.[4,5]

For the Bi-containing films discussed in Chapter 4, the T_{sub} calibration was refined using the Ircon Modline 3-3V pyrometer, which is accurate down to 400°C with appropriately adjusted emissivity.[6] To calibrate the pyrometer, a GaAs substrate is heated to ~200°C and left in the growth chamber overnight with liquid N_2 flowing. On the next day, while the shutters remain closed (i.e. without arsenic overpressure), T_{CAR} is raised until the RHEED pattern transforms from (3x1) to (4x1). The pyrometer emissivity is then adjusted to set the pyrometer temperature to 595°C.[7] After the pyrometer emissivity is calibrated, the relationship between T_{sub} and T_{CAR} was determined using an indium-mounted GaAs substrate. For each block, following oxide desorption, with As overpressure maintained, T_{CAR} is lowered from ~600°C in 50°C steps, and the corresponding T_{sub} from the pyrometer is recorded. The T_{sub} is then plotted as a function of T_{CAR}, and a linear least-

square fit is used to extrapolate the relationship between T_{sub} and T_{CAR} for temperatures below 400°C.

2.2.5 Reflection High-Energy Electron Diffraction (RHEED)

During MBE growth, RHEED is used to monitor the surface crystallinity and reconstructions, as well as for determining the growth rate (GR) and the incorporation rate ratio (IRR),[8,9,10] a quantification of how long it takes a surface to recover its surface stoichiometry after being deprived of an As flux. The Gen II and C21 MBE systems include STAIB RHEED sources, operating at 18 keV and 12 keV, respectively. As shown in Fig 2.3[11], during RHEED, an electron beam is accelerated toward the sample surface at a incidence angle of ~1º; subsequently, the diffracted electrons impinge upon a phosphor screen, producing a diffraction pattern. A charge coupled device (CCD) camera is then used to collect the luminescence from the phosphor screen. During growth, the intensity of the central spot oscillates, with one period corresponding to a bilayer of growth, i.e. one "layer" of GaAs, for example.[12, 13, 14] Thus, the GR is estimated by considering the thickness of one bilayer divided by the time interval for one period of intensity oscillation. For GaAs, the GR is typically adjusted by varying the Ga flux. Since the GaAs(Bi)(N) alloys contains dilute concentrations of N and Bi, we assume negligible differences between the GaAs and GaAs(Bi)(N) GRs. For the GaAsNBi films in Chapter 4, a targeted GaAs growth rate of 1 μm/hr, with V/III (As_4/Ga) flux ratio of 20, was used. In all cases, the IRR values range from 1.5 to 1.8, consistent with literature reports for GaAs growths.[15]

Detailed procedures for determining GR and IRR are available in Section 2.2.5 of R.L. Field's PhD thesis.[16]

2.3 Rapid Thermal Annealing

For select GaAsN films presented in this thesis, post-growth rapid thermal annealing (RTA) was performed by the author using a JetFirst-150 Rapid Thermal Processor at Los Alamos National Laboratory. For each RTA experiment, the samples were capped with a new GaAs substrate, polished side facing the film of interest. For RTA, the samples were inserted into the stainless steel chamber (with quartz window), with 1 atm N_2 atmosphere, and ramped at 20ºC/s from room temperature to 780ºC and held for 60s. For the GaAsNBi samples, RTA was performed *prior* to the removal of the backside indium, leading to indium droplet formation on the surfaces of both the sample and the RTA chamber. Interestingly, the HRXRD of these samples suggested *possible* diffusion of In into the epilayer film forming InGaAsNBi – see Chapter 6 for more details. As will be discussed in Chapter 6, the author recommends that additional RTA be performed *following* the removal of the backside indium.

2.4 Atomic Force Microscopy and Scanning Electron Microscopy

To examine the surface morphology, we used both atomic force microscopy (AFM) and scanning electron microscopy (SEM). While the AFM piezo tubes have <1Å sensitivities in both the vertical and lateral direction, the lateral resolution is typically

limited by tip convolution effects, which typically lead to lateral resolution in excess of >1 nm. SEM is also used to collect images over larger areas (on the order of square millimeters) with lateral resolution of ~1 nm, but without quantitative height sensitivity.

AFM images were collected in the Veeco Dimension Icon AFM using ScanAsyst mode, which consists of a modified tapping mode with a proprietary scan-tuning algorithm. We used Nanoscience AFM probes, consisting of etched silicon, with tip radius < 10 nm, tip length ≈ 125 μm, resonance frequency = 300 kHz, and spring constant = 40 N/m. In all cases, image "flattening", root-mean-square (RMS) analysis and feature height analysis were performed using the Nanoscope Analysis software. Typically, 3μm x 3μm or 1μm x 1μm sized images were collected with 512x512 pixel resolution.

SEM images were collected in the FEI Nova 200 using secondary electron (SE) detection, as shown in Fig. 2.4. In Chapter 4, normal incidence e^- irradiation (i.e. 0º sample tilt) mostly used for areal images. To avoid large excitation volume and to maintain surface features contrasts, 5kV accelerating voltage and 0.4 nA beam current were typically used. For imaging of the conical-shaped tips for APT, normal-incidence ion irradiation (i.e. 52º sample tilt) was used. The FEI Nova 200 has an additional SEM imaging mode called "immersion mode". During this imaging mode using the 5kV/0.4nA settings, an additional electric field is applied at the tip of the electron column to further focus the electron beam, allowing resolution down to ~1nm. Author primary used 5keV accelerating voltage and 0.4nA beam current to avoid large excitation volume and to maintain surface feature contrasts.

2.5 Raman Spectroscopy

To detect the local vibrational modes associated with N-related defect states, we used resonant Raman spectroscopy (in which lasers with frequencies near the target vibrational modes are used to enhance the vibrational mode intensity). The resonant Raman spectra were obtained using a Renishaw Raman microscope spectrometer, equipped with a 785 nm diode laser, a Nikon LU plan 20x objective lens, an edge filter to reject the 785 nm excitation line, and a CCD detector in a 180º backscatter geometry. The laser is focused to a <1x1mm spot and the signal is integrated over 10 scans with 20 seconds signal integration time for each scan. Each spectrum was then individually normalized to its "highest" peak. All the Raman data shown in Chapter 4 was collected in Professor Maldonado's laboratory in the Chemistry Department at University of Michigan.

2.6 High-Resolution X-Ray Diffraction

We performed double-axis high-resolution X-ray diffraction (HRXRD) measurements using Cu $K\alpha_1$ radiation in the BEDE D^1 system located at the MSE department in University of Michigan. For the HRXRD measurements, each sample was "rocked" about the substrate Bragg angle, while the detector remained fixed at $2\theta_B$. Ideally, two sets of reflections, the symmetric (004) and the asymmetric glancing-incidence (224), were collected. For some samples, epilayer tilt was accounted for via measurements at $\varphi = 0^\circ$ and $\varphi = 180^\circ$. We used the so-called "small angle" approximation algorithm described in Appendix A.2 of M. Reason's Ph.D thesis[17] to calculate the in-plane and out-of-plane

strain. In turn, the epilayer lattice parameter and composition are determined assuming a linear interpolation of binary lattice parameters. For these calculations, we used the "Peak Split" function within the Bede Software, assuming a linear interpolation of the GaAs and GaN (GaBi) lattice parameter, along with a Poisson's ratio of 0.33. It should be noted that since GaBi has not yet been synthesized, the GaBi lattice parameter is a computed value,[18] and therefore the GaAsBi and GaAsNBi lattice parameters are also an approximation. For quaternary alloys such as GaAsNBi, one of the compositions, N or Bi, is needed before the full composition analysis can be performed. For this purpose, we used HRXRD data in conjunction with NRA/RBS data to quantify the compositions.

We also used HRXRD to estimate the upper bound of excess arsenic incorporated in our low-temperature-grown GaAs (LT-GaAs) layers. Detailed discussions of the measurements and analysis are included in Chapter 5.

2.7 Atom Probe Tomography (APT)

For these studies, both the stoichiometry of the host and the composition of the incorporated solutes are needed. For this purpose, we use local-electrode atom probe (LEAP) tomography as shown schematically in Fig 2.5. For this dissertation work, most of the LEAP experiments were performed in the LEAP 4000X with last-minute work on the LEAP 5000XR. To prepare for the LEAP experiment, a conical-shaped sample (the "tip") is fabricated and welded onto a silicon post, which is then mounted on the cryo-cooled stage in the LEAP system. During the LEAP experiment, atoms from the sample are evaporated by voltage or laser pulses; the ion are subsequently accelerated toward the

detector by an applied DC high voltage. With the electrode and detector independently grounded, the applied voltages needed for the initiation of ion evaporation are ~2500V and ~6000V for laser and voltage mode, respectively. As the LEAP experiment progresses, the voltages are automatically adjusted by computer algorithm to maintain a constant detection rate; thus, the voltage is typically increased gradually. In addition, for the voltage mode, each pulse is +20% of the applied DC high voltage. For example, for an applied DC high voltage of 6000V, each "pulse" is 7200V. A position-sensitive detector is then used to detect the evaporated atoms, separating them by their mass-to-charge ratio.

For these experiments, we used LEAP in laser mode, using a 355 nm laser with a laser pulse energy of 0.25 pJ, a 100 kHz laser pulse rate, and a 0.5% detection rate. To minimize mass overlaps due to delayed thermal evaporation and multiple charge state production, the laser energy is tuned, as described in Appendix C. In addition, to account for the time-of-flight needed for heavy elements such as Bi, often termed "mass wrap around", the pulse frequency must be sufficiently slowed, as also described in Appendix C.

To maximize the probability for useful data acquisition without tip fraction, a six-step tip shaping procedure was performed in the FEI NOVA 200 dual-beam SEM-FIB. The computer-assisted annular mill-pattern design is shown in top of Fig. 2.6, with the FIB parameters for each step listed in the table below. During the FIB tip shaping process, the tip shape is monitored using immersion-mode SEM where an extra external field is applied to focus the electron beam for high resolution (~1 nm). To avoid electron transparency of the tip as it is shaped, a low electron accelerating voltage (5 kV) is utilized. Example immersion SEM images for a GaAsNBi samples are shown in Fig. 2.7, where contrast

differences between the sample and deposited platinum are apparent. Additional lift-out and tip-shaping procedure are provided in Section 2.5.1 of A. Chang's Ph.D thesis.[19] The LEAP reconstructions were all performed using Visualization and Analysis Software (IVAS) provided by Cameca, as described in Appendix K of J. Walrath's Ph.D thesis, with careful attention to the consideration of molecular species and fragments with identical mass-to-charge ratios, as described in Appendix C.

2.8 Ion Beam Analysis

For this dissertation work, both random and channeling Rutherford backscattering spectroscopy (RBS/C) and nuclear reaction analysis (NRA/C) were performed in tandem ion accelerators in which each charged ion is accelerated twice under a static electric potential. The details of the 3MeV NEC tandem at Los Alamos National Laboratory (LANL) and the 1.7MeV General Ionics tandem at the Michigan Ion Beam Laboratory (MIBL) are provided in Appendix D.

For RBS, α particles are elastically scattered by a target (i.e. the sample) and collected by a silicon surface barrier detector located at 167º with respect to the incident ion beam direction. In this work, we used RBS to determine the Bi concentration in ternary (GaAsBi) and quaternary (GaAsNBi) alloys. The RBS technique is often limited by its limited mass resolution (for similar masses) and/or small backscatter cross-section (for light masses). For example, signals associated with Ga and As cannot be resolved due to the similarity in atomic mass between Ga and As.[20] For lighter elements, such as nitrogen, the RBS cross-section is too low to be detected with reliable accuracy.[21,22] Instead, we

select a nuclear reaction whose reaction products are easily detected and can be maximized by careful selection of the ion beam energy. Nuclear reactions are often described in a short-hand form, $T(P,x)R$, where P is the incident projectile, T is the target, x is the emitted particle, and R is the residual nucleus. For NRA, emitted particles are collected by a silicon surface barrier detector located at 135º with respect to the incident ion beam direction.

In earlier studies of GaAsN by Dr. Reason[23], Jin[24], and Vardar, the $^{14}N(d,\alpha_{1,0})^{12}C$ reaction was used. For example, a set of channeling data collected using $^{14}N(d,\alpha_{1,0})^{12}C$ reaction from a GaAsN sample, obtained by G. Vardar during a visit to LANL, is shown in Fig. 2.8(a). Although the signal-to-noise ratio (SNR) for these data is low, it was not feasible to increase the incident ion beam current because another an additional nuclear reaction, $^{14}N(d,n)^{15}N$, which involves the emission of neutrons, can also occur during the $^{14}N(d,\alpha_{1,0})^{12}C$ reaction. Instead, the author utilized an alternative nuclear reaction, $^{14}N(\alpha,p)^{17}O$,[25] using a higher incident ion beam current, which led to a substantial improvement in SNR, as shown in Fig. 2.8(b). For the $^{14}N(\alpha,p)^{17}O$ measurements, we used the nuclear reaction cross section data for $^{14}N(\alpha,p)^{17}O$, as shown in Fig. 2.9(a)[26], to determine the beam energies used for various film thicknesses. Various beam energies are needed for different film thicknesses due to the atomic stopping energy – as the α particle travels through the film, it will gradually lose its kinetic enegy, as shown in Fig. 2.9(b). Therefore, it is important to avoid the beam energy that corresponds to maximum reaction cross-section availiable because most of the reactions would then occur at the surface, since as soon as the α particle penetrates the film of interest, the effective reaction cross-section decreases dramatically. Prior to the experiments, SIMNRA with various ion beam energies

was used to determine the ion beam energy expected to lead to the highest yield. Typically, for 100 to 400nm film, a beam energy of 4.46 to 4.64 MeV is used, as illustrated in Fig. 2.9(b).

With both RBS and NRA detectors mounted in the "RBS" analysis chamber of the LANL tandem, shown in Fig. D.1 of Appendix D, both channeling RBS and RBS and random NRA and RBS were each collected simultaneously. As shown in Fig 2.10, when the ion beam is directly aligned along a crystallographic direction, the energetic ions are streered by small-angle scattering collisions between rows and planes of atoms. To achieve axial channeling, careful tuning procedures are utilized, as described in Appendix D.3. For both RBS and NRA, when the channeling conditions are achieved, the yields decrease dramatically. To collect random spectra, the samples are rocked φ_x ±4º about the channeling conditions. Examples of random and channeling RBS (NRA) spectra from GaAs(N)(Bi) are shown in Fig 2.11. In the RBS spectra shown in Fig 2.11(a), the signals at ~3.5 MeV (~4.1 MeV) are due to backscattering from Ga and As (Bi). For the channeling RBS spectrum, the distinct peaks near ~3.6 MeV are due to preferential scattering from exposed surface atoms. For the NRA spectra shown in Fig. 2.11(b), the signal at ~1.05 MeV is associated with protons emitted by the $^{14}N(\alpha,p)^{17}O$ nuclear reaction.

To evaluate the quality of axial channeling, we consider the fraction of ions that are channeled, $\frac{\pi r_o^2 - \pi r_{min}^2}{\pi r_o^2}$, as shown in Fig. 2.10, where r_{min} is the radius of the atom and r_0 is the radius of ion channel surrounding the atom. To estimate the ratio of the channeling yield to the random yield, χ_{min}, we consider the fraction of ions that are not channeled

$$\chi_{min} = \frac{\pi r_{min}^2}{\pi r_o^2}$$

For pure GaAs, axial channeling is considered adequate when the minimum yield is ~4-5%.[27,28] The detailed procedures for alignment, spectral fitting and analysis are described in Appendix D.3 and D.4.

2.9 Monte Carlo-Molecular Dynamics (MC-MD) Ion Beam Simulation

To simulate the channeling RBS and NRA spectra, we use a combined Monte Carlo-Molecular Dynamics (MC-MD) approach, building upon the code developed in Ref. 27.[29] In our simulation, the Monte Carlo algorithm is used to give each of the $2\text{x}10^4$ alpha particles a randomly-assigned starting point within the primitive cell of the zincblende lattice, as shown in Fig. 2.12. Each ion is then injected into the lattice, and Molecular Dynamics is used to determine its subsequent trajectory via numerical integration of the Molière potential function,[30] with a resolution of 2Å for each step. As an ion passes through the film, its proximity to the atoms of interest is recorded and converted to a close-encounter probability given by the equation $P_{ce} \propto \sum_{i=i}^{N} \exp\left(\frac{-|r-r_i|^2}{2u_1^2}\right)$ where u_1 is the root mean square of thermal vibrational amplitude, r is the position of the ion, and r_i is the position of the i^{th} atom of interest in the lattice. In practice, the summation is carried out for the neighbors falling within a given radius of the position of the ion; in this case, the cutoff radius is 4Å. By rotating the constructed crystal, various ion channeling directions are simulated. To predict the channeling yields for GaAsN with various interstitial complexes, we assume that one particle is produced for each ion-N close-encounter. Using the energy-dependent cross-sections, modified to take into account energy loss due to nuclear and electron stopping in GaAsN, we determine the sum of NRA yields for

$^{14}N(\alpha,p)^{17}O$. Finally, the simulated result is plotted in a yield-vs channel form, as shown in Fig. 2.12, in order to be compared with the experimental data. Additional details and verification of the simulation can be found in Appendix E.

For simulations with a single primitive cell of the zincblende lattice, it is possible to include one defect type and location, as shown in Fig. 2.13. Single cell simulations were used for the studies presented in Chapter 3. To enable the inclusion of multiple defect types and locations, as needed for ternary and quaternary alloys, multiple primitive cells are needed. Therefore, we set up cells with up to 5x5x5 cells of the zincblende lattice. An example 2x2x2 cell is shown in Fig. 2.14. Multiple cell simulations were used for the studies presented in Chapter 4 and 5.

2.10 Figures

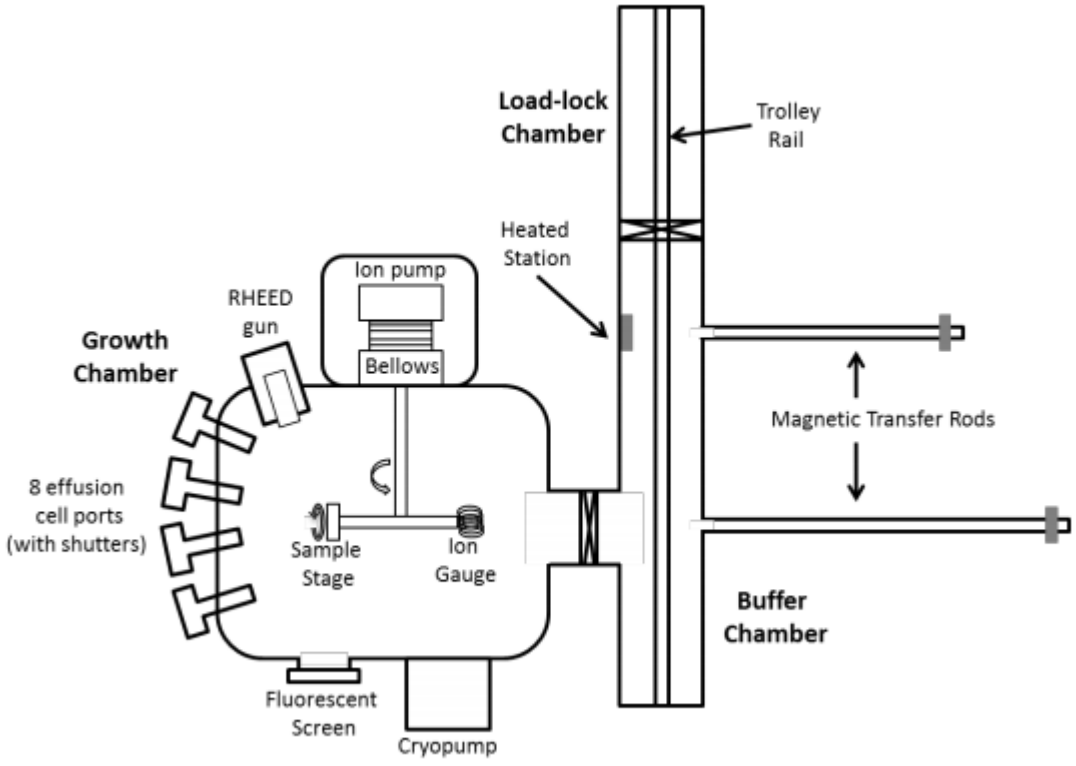

Figure 2.1 Schematic of the Modified Varian Gen II molecular-beam epitaxy system, which contains a horizontal facing source flange. Seven high purity metal sources (Ga, In, Al, Si, Be, Bi, and As) and the radio frequency N_2 plasma source (separated from the main chamber by a gate valve) are each located at one of the effusion cell ports. (adapted from Ref. 31.)[31]

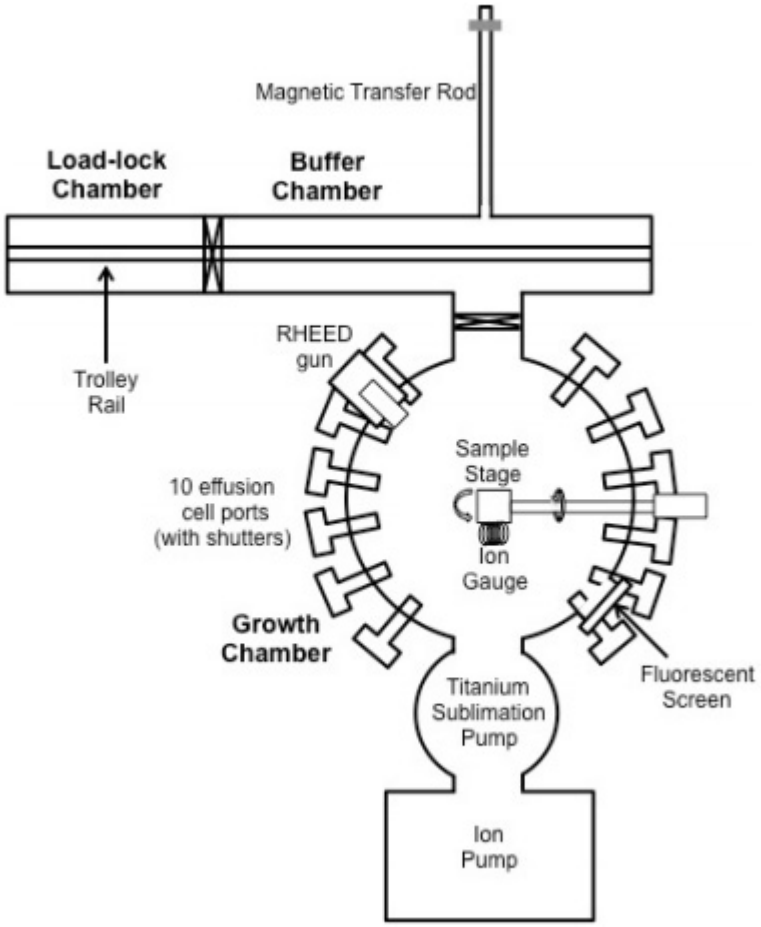

Figure 2.2 Schematic of the Riber Compact 21 molecular-beam epitaxy system, with an upward facing source flange. The seven high purity sources (Ga, In, Al, Si, Be [not yet loaded], Bi, and As) are each located in one of the effusion cell ports. Adapted from Ref 24.[24]

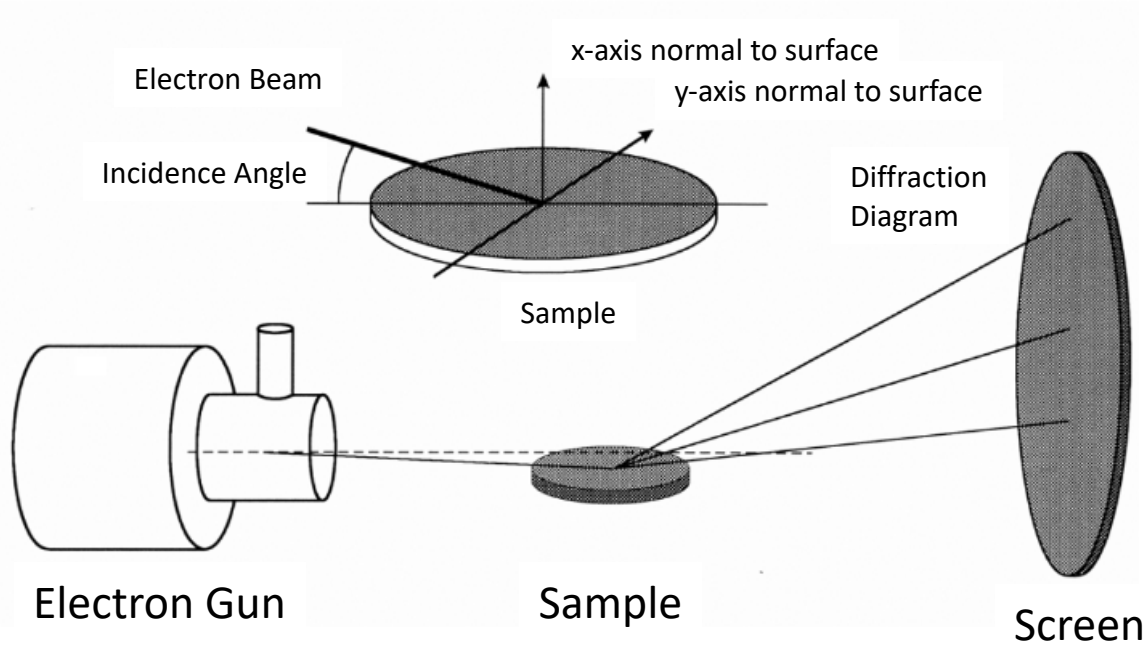

Figure 2.3 Schematic of the RHEED experiment, adapted from Ref. 7. The beam of electrons is directed at the sample at a grazing incidence angle of ~1º, and is diffracted onto a phosphor screen.

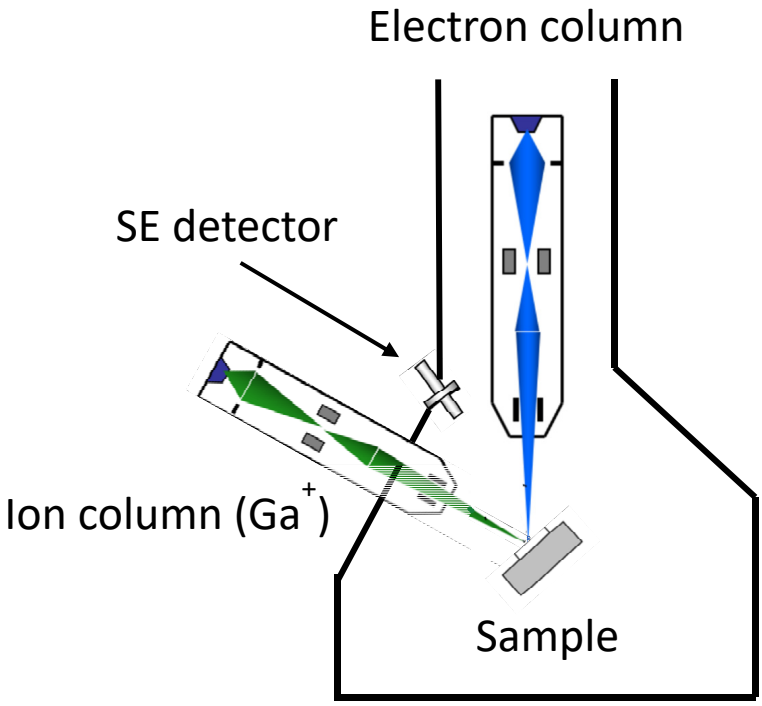

Figure 2.4 Schematic of NOVA 200 dual beam workstation. The ion (electron) beam angle of incidence is defined as the angle between the incident ion (electron) beam and the sample surface normal. The secondary electron detector in Nova 20 is located at 20° away from the electron beam. The angle between the ion and electron beam columns is fixed at 52°. Therefore, to achieve normal-incidence ion irradiation, the sample is tilted to 52° with respect to the electron beam. Adapted from Ref. 32.[32]

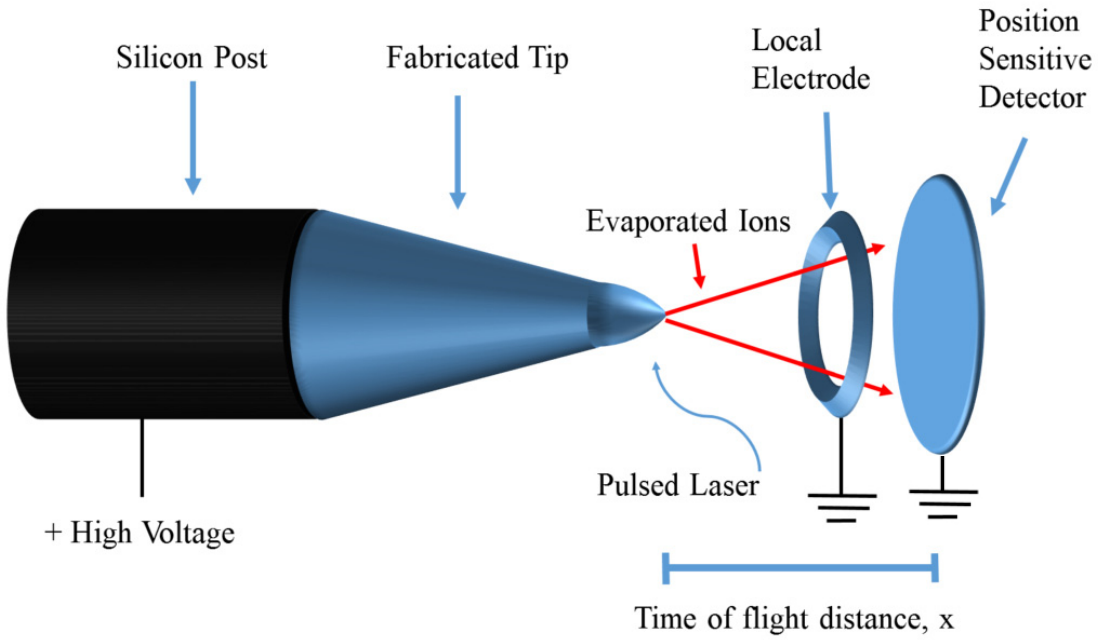

Figure 2.5 Schematic of the atom-probe tomography experiment. A conical-shaped sample (the so-called "tip") is welded to a silicon post, is mounted on a cyro-cooled stage. For laser mode, 355 nm laser pulses assist the evaporation of atoms from the sample; the atoms are subsequently accelerated toward the position sensitive detector using a DC applied high voltage. The distance, x, used to calculate the time of flight is distance between the tip and the detector, as marked in the schematic. For voltage pulse mode, the DC applied high voltage is pulsed (at +20%) in order to evaporate the ions. For example, voltage pulses of 7200V are used to evaporate atoms and subsequent acceleration toward the position sensitive detector is achieved using a DC applied high voltage of 6000V.

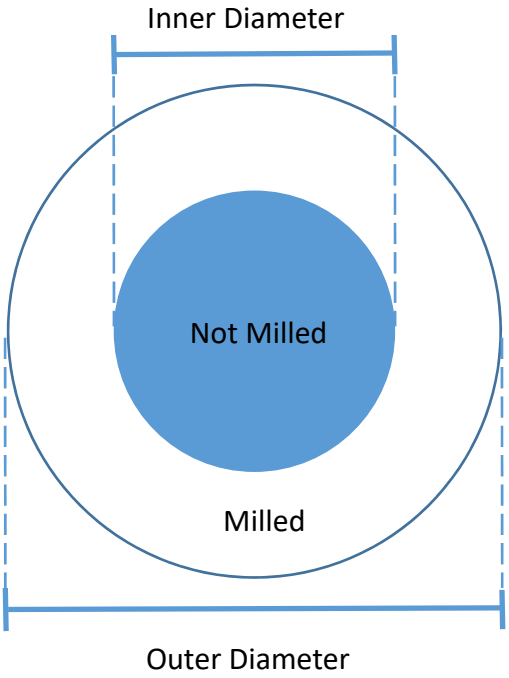

Steps	Outer Diameter	Inner Diameter	Beam Voltage	Beam Current	Milling Depth
1	10 µm	4 µm	30 kV	3 nA	1 µm
2	6 µm	2 µm	30 kV	1 nA	1 µm
3	3 µm	1 µm	30 kV	0.5 nA	1 µm
4	2 µm	0.5 µm	30 kV	100 pA	400 nm
5	1.5 µm	0.15 µm	30 kV	30 pA	200 nm
6	1.5 µm	0 µm	5 kV	70 pA	100-400nm

Figure 2.6 (Top): a schematic of annular region to be milled, defined by its inner and outer diameters. (Bottom) the sequence of steps used for milling, including the inner and outer diameters, the milling depth, and the ion beam currents and voltages.

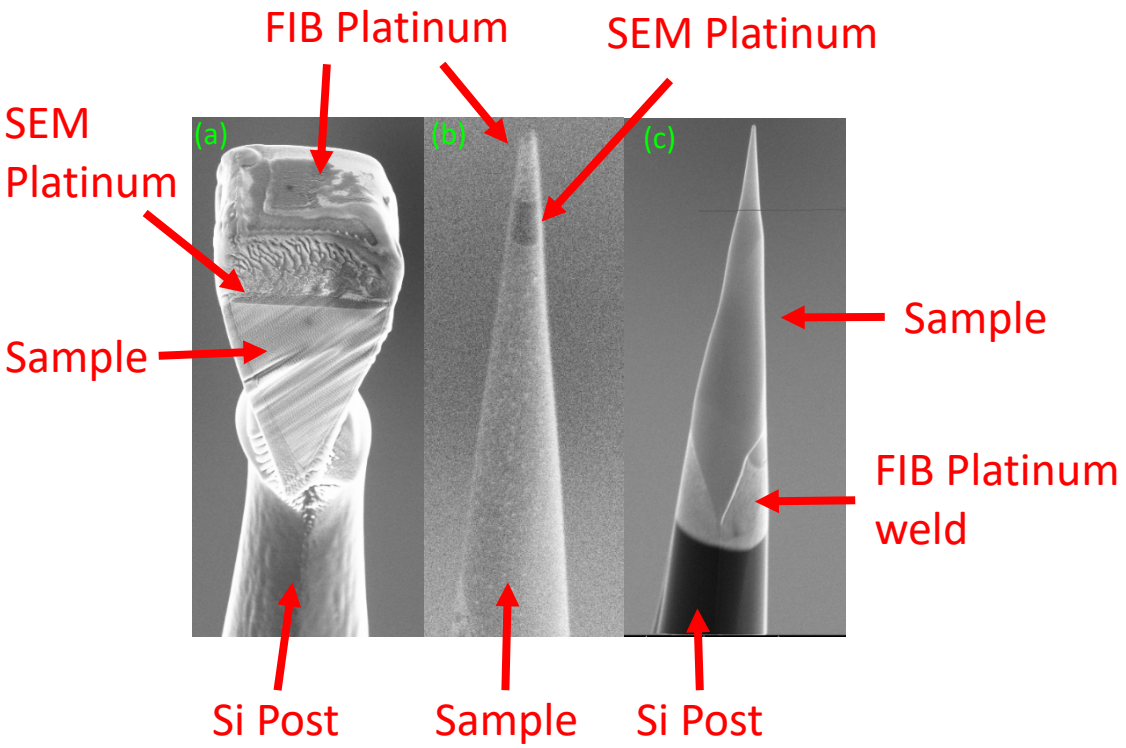

Figure 2.7 Immersion-mode SEM images of the tip shaping process for LEAP: (a) GaAsNBi sample mounted on a silicon post, with a thin layer of SEM-deposited Pt and a thick layer of FIB-deposited Pt clearly on top of the sample. (b) partially-shaped (step 3-5) sample which resembles a cone with the layers of SEM- and FIB-deposited Pt apparent. (c) After step 6, a cone-shaped sample, with the FIB-deposited Pt weld apparent, is ready for the LEAP experiment.

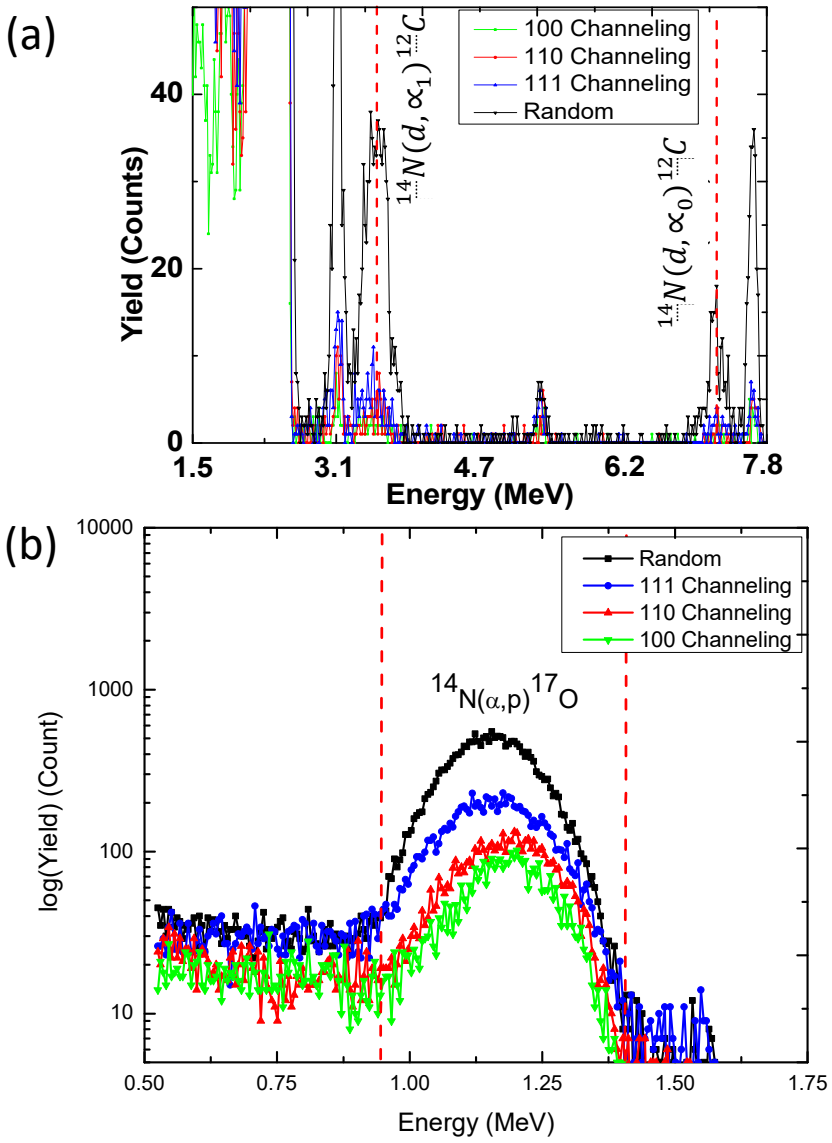

Figure 2.8 Measured NRA yield versus emitted particle energy for GaAsN, along the [100] (green), [110] (red), [111] (blue), and random (black) channeling directions for the (a) $^{14}N(d,\alpha_{1,0})^{12}C$ and (b) $^{14}N(\alpha,p)^{17}O$ nuclear reactions. Due to the neutron production from $^{14}N(d,n)^{15}N$ reaction that occurs along with the $^{14}N(d,\alpha_{1,0})^{12}C$ reaction, it is not feasible to increase the ion beam current as needed to achieve a suitable signal-to-noise ratio in (a). In (b), using $^{14}N(\alpha,p)^{17}O$, we increase the signal-to-noise ratio by ~50x.[33] (Copyright 2015, AIP Publishing LLC for Fig. 2.7(b)).

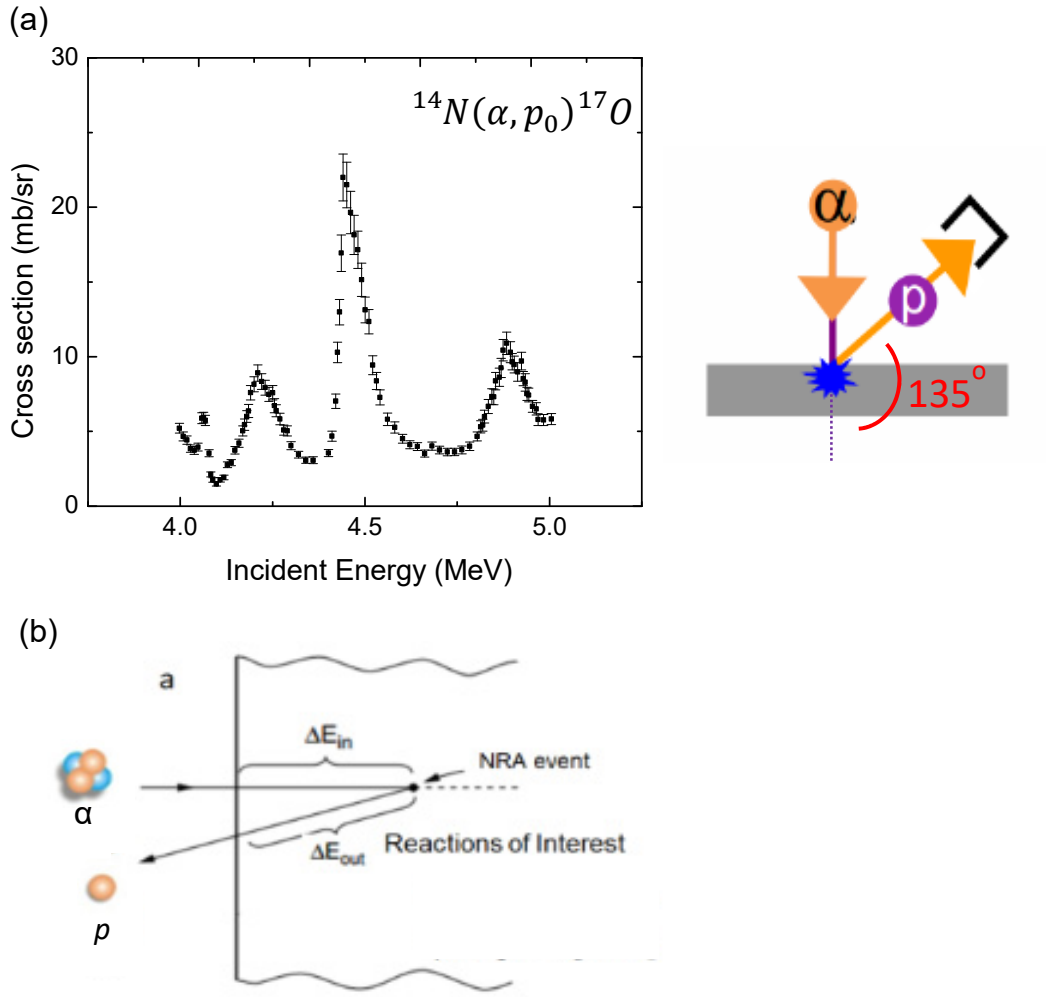

Figure 2.9 (a) Measured cross-section vs. incident ion beam energy for the $^{14}N(\alpha, p)^{17}O$ reaction obtained from the Ion Beam Analysis Nuclear Data Library[18] The plot reveals three distinct resonances peaks in the range of ~4 MeV to 5 MeV. Since the cross-section at ~4.5 MeV is the largest among the three, we targeted energies in the vicinity of the ~4.5 MeV. However, since ion loses energy as it traverse through the film (~241 keV/μm for ~4.5MeV alpha ion in GaAs), as illustrated in (b) the ion energy must be selected to maximize the cross-section while the ion is traversing through the film of interest – if the ion energy is too low, we do not utilize the benefit of the resonance peak; if the ion energy is too high, it can travel through the film without losing enough energy to utilize the benefit of the resonance peak as well. Prior to experiments, we use SIMNRA with various ion beam energies to determine the ion beam energy expected to provide the highest yields.

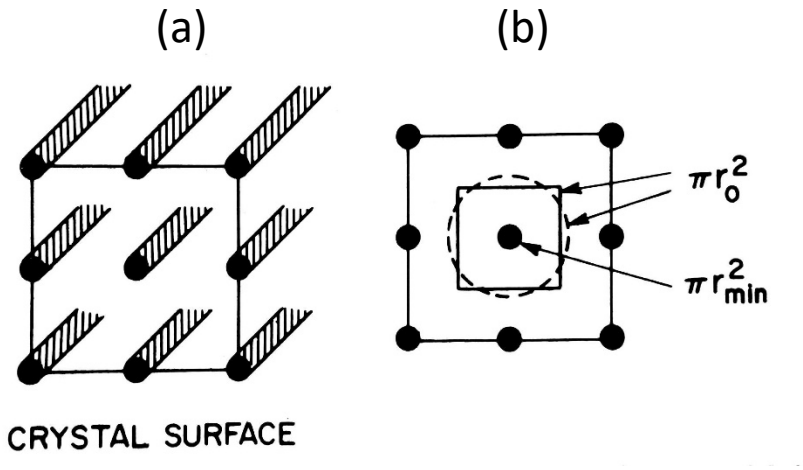

Figure 2.10 (a) Schematic illustration of a face-centered cubic crystal, with black circles representing atoms, hashed regions representing a column of atoms with radius r_{min}, and the remaining white spaces representing the ion channels with radius r_0. (b) within πr_o^2 of each column of atoms, particles channel only for $r > r_{min}$. Thus, the fraction channeled is $\frac{\pi r_0^2 - \pi r_{min}^2}{\pi r_o^2}$.[34] (Copyright 1986, Elsevier Books).

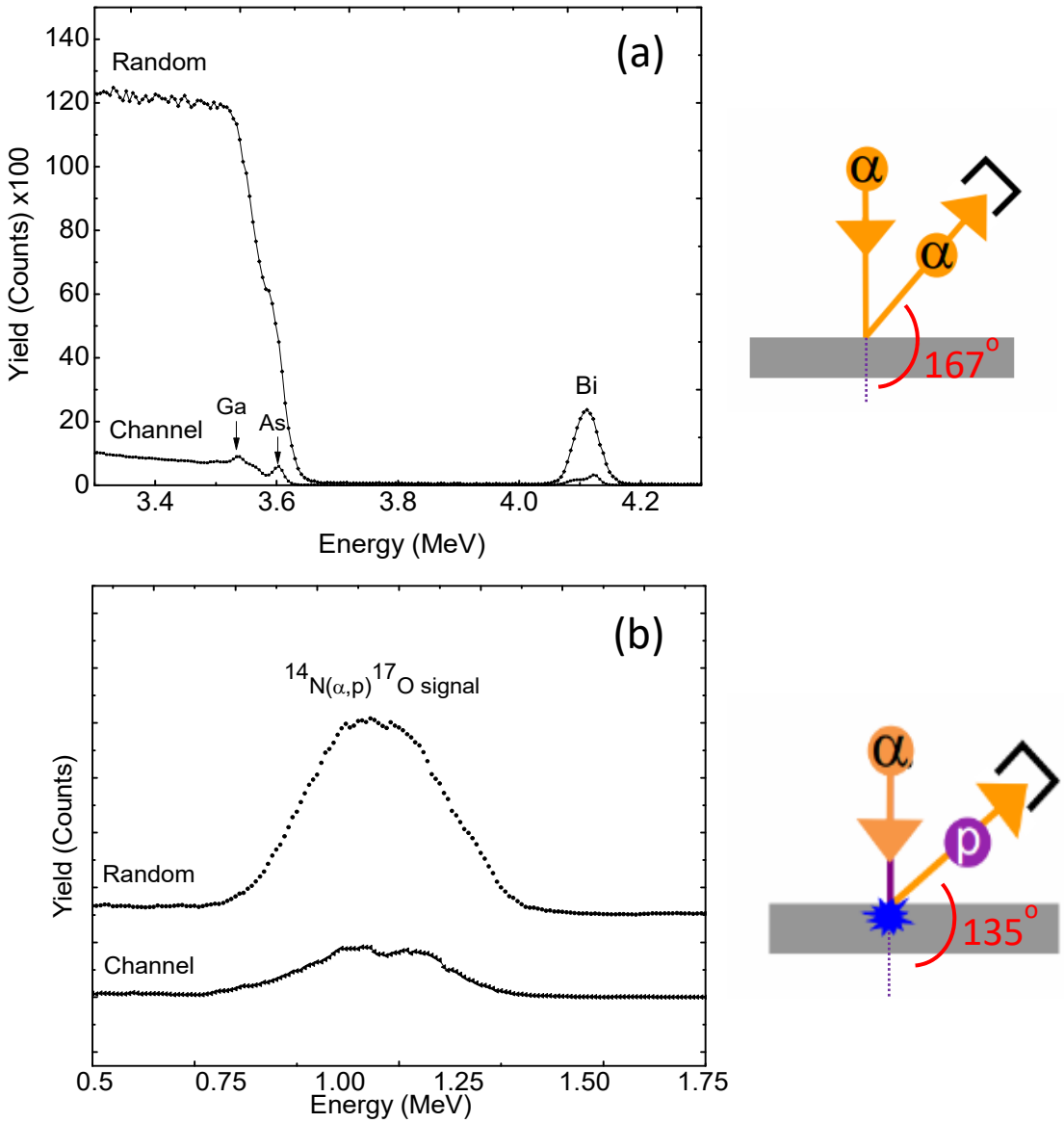

Figure 2.11 (a) Example random and channeling RBS spectra for GaAs(N)Bi. When the precise channeling condition is achieved, the backscattered yields are significantly reduced. The channeling quality is determined by the ratio of the channeled to random yields, χ_{min}. In the channeling spectrum in (a), the distinct peaks for Ga and As and the asymmetry of the Bi peak are due to the preferential surface scattering as the ions enter the channels. (b) Example random and channeling NRA spectra for GaAsN(Bi). As with RBS, the nuclear reaction events are also dramatically reduced as the channeling condition is achieved. In this particular experiment, we have configured the ion beam condition to observe ^{14}N(α,p)^{17}O nuclear reaction, with emitted protons collected by the detector.

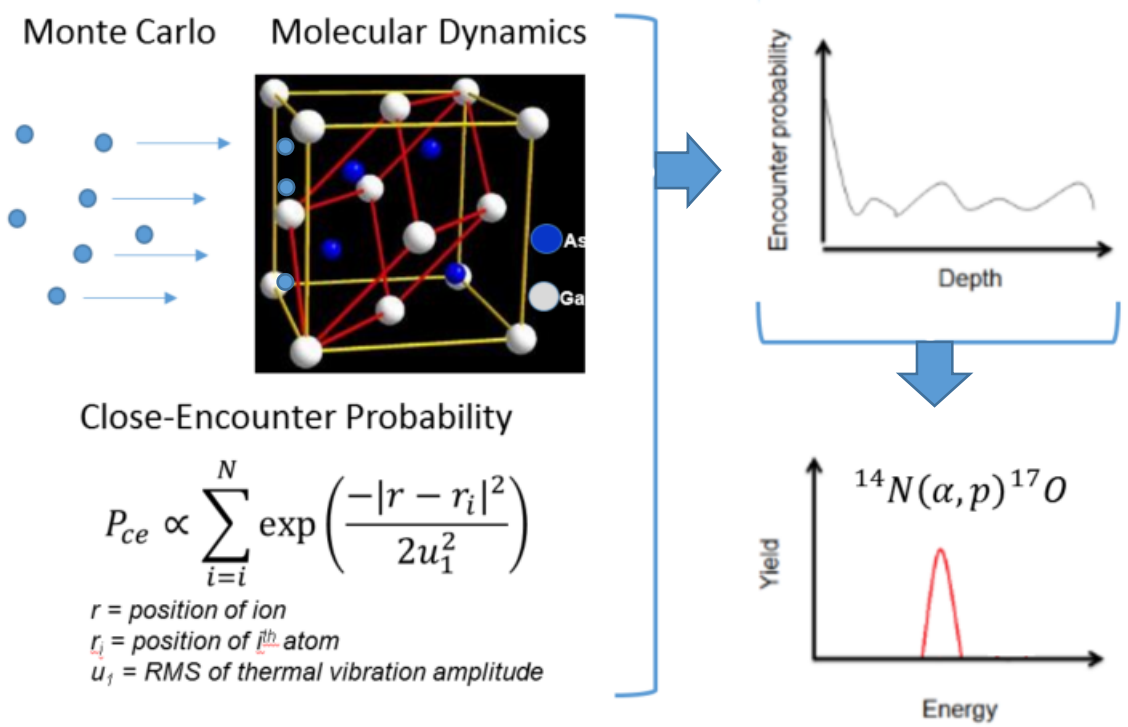

Figure 2.12 Schematics of the Monte Carlo Molecular Dynamics simulations used in this dissertation. For each of the $2x10^4$ incident ions, the Monte Carlo algorithm randomly generates the starting point (within the unit cell). As each ion moves through the crystal lattice, molecular dynamics is used to calculate its trajectories. At each new ion position in the crystal lattice, the close-encounter probability of the ion and atom of interest is calculated and recorded. Finally, the depth-dependent close-encounter probability is convoluted with the energy-dependent cross section to determine the predicted yield vs. energy.

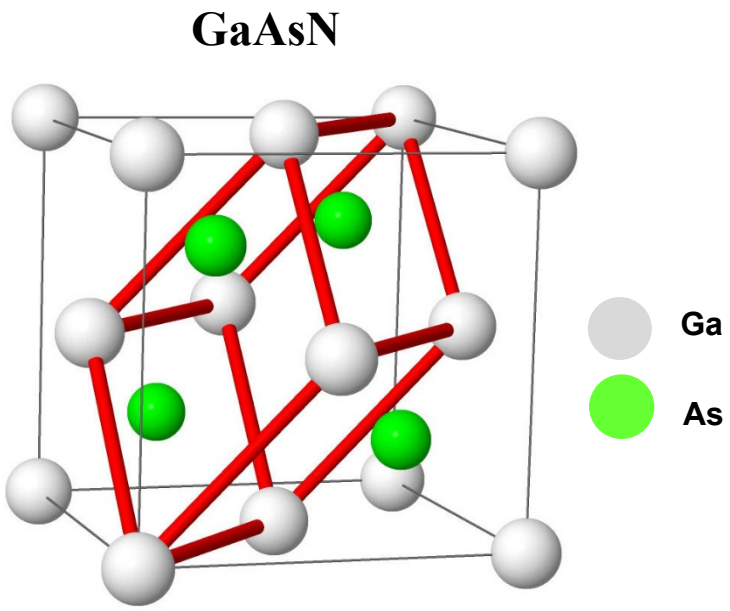

Figure 2.13 A zincblende GaAs structure, with Ga (As) shown as white (green). The primitive cell is outlined in red and the unit cell is outlined by the grey box. For the simulation, we use the red primitive cell, modified to include N_{sub}, $(N\text{-}N)_{As}$, or $(N\text{-}As)_{As}$ replacing an As atom within the cell.

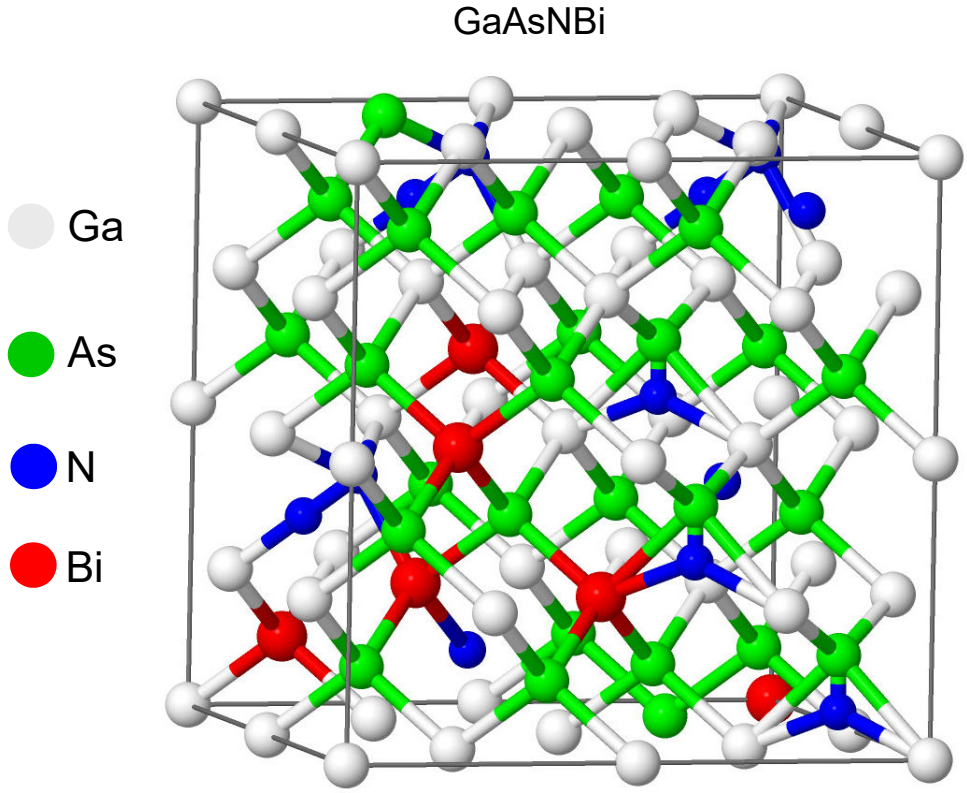

Figure 2.14 Example ball-stick model for a 2x2x2 cell of GaAs (white/blue) for simulation of complex compositions and defect combinations with various Bi (red) and N blue) interstitials. For example, the $(N\text{-}N)_{As}$, $(N\text{-}As)_{As}$, N_{As}, Bi_{Ga}, and Bi_{As} defects is shown in the diagram. Since each unit cell includes 4 defect sites, the 2x2x2 cell has 32 sites and 5x5x5 cell has 500 sites.

2.11 References

[1] A. Y. Cho and J. R. Arthur, Progr. Solid State Ch. 10, 157 (1975).

[2] A. Y. Cho, J. Crys. Growth 202, 1 (1999).

[3] C. T. Foxon and B. A. Joyce, Growth and Characterisation of Semiconductors (Adam Hilger, 1991) pp. 35.

[4] T. Vanbuuren, M.K. Weilmeier, I. Athwal, K.M Colbow, J.A. Mackenzie, T. Tiedje, P.C. Wong and K.A.R. Mitchell, Appl. Phys. Lett. 59, 464 (1991).

[5] A.J. Springthorpe, S.J. Ingrey, B. Emmerstorfer, P. Madeville and W.T. Moore, Appl. Phys.Lett. 50, 77 (1987).

[6] Ircon Modline 3-3V Manual, http://www.belmet.si/Custom/Modules/Products/uploadedFiles/Products/Datoteke/Modline%203-GY936.pdf; Download 5:00pm (September 4, 2017).

[7] M. Reason, Ph.D Thesis, Chapter 2, University of Michigan, 2006.

[8] R. Farrow, *Molecular Beam Epitaxy*, (Noyes, Park Ridge, NJ, 1995), pp. 84-87.

[9] J.H. Neave, B.A. Joyce, P.J. Dobson and N. Norton, Appl. Phys. A *1*, 1 (1981).

[10] J.M. Van Hove, C.S. Lent, P.R. Pukite and P.I. Cohen, J. Vac. Sci. Technol. B *1*, 741 (1983).

[11] Staib Instrumente, *Instruction Manual, RHEED System RH 30* (2000).

[12] J. H. Neave, B. A. Joyce and P. J. Dobson, Appl. Phys. a-Mater 34, 179-184 (1984).

[13] J. M. Van Hove, C. S. Lent, P. R. Pukite and P. I. Cohen, J. Vac. Sci. Technol. B 1, 741(1983).

[14] R. Farrow, Molecular Beam Epitaxy (Noyes, Park Ridge, NJ, 1995), pp. 84-87.

[15] S. Banks, An Introduction to MBE, http://lase.ece.utexas.edu/mbe.php; Download 5:00pm (July 18, 2017).

[16] RL. Field, Ph.D. thesis, Ch. 2. University of Michigan, 2015.

[17] M. Reason, Ph.D Thesis, Appendix A, University of Michigan, 2006.

[18] A. Janotti, S.-H. Wei, and S.B. Zhang, Phys. Rev. B 65, 115203 (2002).

[19] A.Chang, Ph.D. thesis, Ch. 2. University of Michigan, 2016

[20] W.Chu, J. Mayer, M. Nicolet, Backscattering Spectrometry, (Academic Press, New Work, 1978) pp. 23-26.

[21] L.C. Feldman and J.W. Mayer, *Fundamentals of Surface and Thin Film Analysis*, (Elsevier Science Publishing, The Netherlands, 1986)

[22] J. R. Tesmer and M. A. Nastasi, *Handbook of Modern Ion Beam Materials Analysis* (Materials Research Society, Pittsburgh, 1995)

[23] M. Reason, H. McKay, W. Ye, S. Hanson, V. Rotberg, and R.S. Goldman, Appl. Phys. Lett. **85**, 1692 (2004).

[24] Y. Jin, R.M. Jock, H. Cheng, Y. He, A.M. Mintairov, Y. Wang, C. Kurdak, J. L. Merz, R.S. Goldman, Appl. Phys. Lett., **95**, 062109 (2009).

[25] P. Wei, M. Chicoine, S. Gujrathi, F. Schiettekatte, J-N. Beaudry, R. A. Masut, and P. Desjardins. *Journal of Vacuum Science & Technology A* 22, no. 3 (2004)

[26] https://www-nds.iaea.org/exfor/ibandl.htm; Download 4:45pm (December 19, 2016.

[27] Theoretical calculated minimum is ~3.6%, however, instrument alignment limitation puts the actual minimum closer to ~4-5%

[28] J. R. Tesmer and M. A. Nastasi, *Handbook of Modern Ion Beam Materials Analysis* (Materials Research Society, Pittsburgh, 1995

[29] D. Wijesundera, Ph.D. thesis, Ch 6. University of Houston, 2006.

[30] M.T. Robinson and I.M. Torrens, Physical Review B, 9(12), (1974) p.5008.

[31] RL. Field, Ph.D. thesis, Ch. 2. University of Michigan, 2015.

[32] M. Kang, Ph.D. thesis, Ch. 2. University of Michigan, 2014.

[33] Dr. Vardar collected the data shown (a) in 2012 at Los Alamos National Laboratory.

[34] L.C. Feldman and J.W. Mayer, *Fundamentals of Surface and Thin Film Analysis*, (Elsevier Science Publishing, The Netherlands, 1986) pp. 102-103

Chapter 3

GaAsN: Identifying the Dominant Interstitial Complex in Dilute GaAsN Alloys

3.1 Overview

This chapter describes experimental and computational investigations of interstitial complexes in dilute GaAsN alloys. The objective of this work is to identify the dominant interstitial complex in GaAsN alloys, which is needed for predictive modeling of extraordinary phenomenon in GaAsN and related highly mismatched alloys.

This chapter begins with a review of earlier investigations of ultra-dilute and dilute GaAsN alloys. Next, we describe the experimental and computational approaches we used to investigate the dominant N-interstitial in GaAsN. The bulk of the chapter is then devoted to describing our experimental and computational ion beam analyses of GaAsN films. In particular, we present a comparison of channeling RBS and NRA spectra with Monte Carlo-Molecular Dynamics (MC-MC) simulations along the [100], [110], and [111] directions. The measured channeling NRA spectra exhibit the highest (lowest) yield in the [111] ([100]) directions. Similar trends are also observed for simulations of the $(N\text{-}As)_{As}$ interstitial complex, suggesting that $(N\text{-}As)_{As}$ is the dominant interstitial complex in dilute GaAsN.

3.2 Background

For N solute atom fractions less than 0.0001, i.e. "ultra-dilute" GaAsN alloys, the formation of localized single impurity levels has been reported.[1] As the N solute atom fraction is increased beyond 0.005, i.e. "dilute" GaAsN alloys, extraordinary physical properties have been reported and attributed to the formation of N-induced cluster states, whose configurations remain elusive.[2] In the case of dilute $GaAs_{1-x}N_x$, large composition-dependent bowing parameters are typically explained in the context of the band anti-crossing (BAC) model, which considers interactions between the conduction band edge states of the host and a localized state associated with the solute atom.[3] In the modified BAC model of *Lindsay et. al*, "clusters" consisting of two or more N atoms as 2nd nearest-neighbors were considered.[4,5] Although this model replicates the non-monotonic composition-dependence of the effective mass in the ultra-dilute alloy regime, its agreement is limited for the dilute alloy regime.[6,7] Therefore, new insight into the precise configurations of the N-induced clusters are needed to develop predictive models for these extraordinary physical phenomena.

It has been suggested that GaAsN may contain Ga interstitials and/or (As_{Ga}-N_{As}) complexes.[8] In addition, it has been shown that ~20% of N solute atoms share an arsenic site with either arsenic or another N atom, often termed $(N\text{-}As)_{As}$ or $(N\text{-}N)_{As}$ split interstitials.[9,10,11,12,13] However, the precise N atomic configuration, including the relative concentrations of $(N\text{-}N)_{As}$, $(N\text{-}As)_{As}$, or (As_{Ga}-N_{As}) complexes, remains unknown. Electronic structure computations have shown that the most energetically favorable configuration of $(N\text{-}N)_{As}$ involves alignment of nitrogen dimers (N_2) along the [111]

direction, with its center of mass in the center of the Group V site. For $(N\text{-}As)_{As}$, the predicted lowest energy configuration involves alignment of the N-As pair along the [010] direction.[14] Finally, at low growth temperatures, excess arsenic is often incorporated, introducing As antisites, As_{Ga}, and possibly (As_{Ga}-N_{As}) complexes.[11,15,16,17,18] The presence of $(N\text{-}As)_{As}$ may be determined by [111] channeling NRA. However, in the [100] and [110] channels, interstitial complexes are not shadowed by a sublattice; therefore, the interstitial complexes are indistinguishable.

3.3 Methods

3.3.1 Experimental Details

The $GaAs_{1-x}N_x$ alloy films were grown by Dr. Matt Reason on semi-insulating (001) GaAs substrates by MBE using Ga, As_4 and a N_2 rf plasma source in the Gen II MBE system. After an initial 500-nm thick GaAs buffer layer grown at 580ºC, the substrate temperature was lowered to 500ºC for the growth of an additional 20-nm GaAs. 500-nm GaAsN films were then grown at relatively low *T* (~400ºC) with As/Ga beam equivalent pressure ratio >30 to avoid growth in the so-called "forbidden window," a specific *T* range where multilayer growth has been reported.[19] Using a growth rate of 0.4 μm/hr for the dilute GaAsN layer, we targeted a N fraction, x, of 0.016, which is sufficiently high to involve the presence of N "cluster" states, while limiting the presence of other misfit-strain related linear and planar defects.[20] More details about the growth procedures are provided elsewhere.[11]

NRA/C measurements were performed at Los Alamos National Laboratory using the methods described in Section 2.8 and Appendix E. Briefly, we used 4.64 MeV He ions incident on GaAsN films induce the $^{14}N(\alpha,p)^{17}O$ reactions for NRA.[20,21] The yields of the reaction-emitted protons were detected by a silicon surface-barrier detector located at 135° with respect to the incident beam direction. To filter out scattered He particles, a 18-μm-thick aluminum foil was placed in front of the NRA detector. For RBS measurements, 4.64 MeV He ions incident on GaAsN films are backscattered by Ga, As, and N atoms and recorded by a silicon surface-barrier detector located at 167° with respect to the incident beam direction.

To estimate x_N in each $GaAs_{1-x}N_x$ film, high-resolution X-ray rocking curves (HRXRC) were performed using Cu $K\alpha_1$ radiation. A series of $\Delta\omega$ scans were collected near the GaAs (004) and GaAs (224) reflections, as shown in Fig. 3.1. Assuming a tetragonal distortion of the GaAsN film, and a linear interpolation of the binary elastic constants and lattice parameters for GaN and GaAs,[22,23] the GaAsN film lattice parameter is estimated as 5.62Å, corresponding to a nitrogen fraction of $x = 0.016$.

3.3.2 Monte Carlo-Molecular Dynamics Simulation

To simulate the channeling RBS and NRA spectra, we use a combined Monte Carlo-Molecular Dynamics (MC-MD) approach, based upon Ref. 24.[24] In our simulation, $2x10^4$ alpha particles are each given a randomly assigned starting point within the primitive cell of the zincblende lattice, as shown in Fig. 3.2. Each ion is then injected into the lattice and its subsequent trajectory is determined by numerical integration of the Molière

potential function, with a resolution of 2Å for each step. As the ion passes through the film, its proximity to the atoms of interest is recorded and converted to a close-encounter probability given by the equation

$$P_{ce} \propto \sum_{i=i}^{N} \exp\left(\frac{-|r-r_i|^2}{2u_1^2}\right) \quad 3.1$$

where u_1 is the root mean square of thermal vibrational amplitude, r is the position of the ion, and r_i is the position of the i^{th} atom of interest in the lattice. In practice, the summation is carried out with the neighbors falling within a given radius of the position of the ion; in this case, the cutoff radius is 4Å.

To predict the channeling RBS and NRA yields for GaAsN with various interstitial complexes, we assume that alpha particles are scattered during close encounters between alpha particles and gallium/arsenic atoms (RBS), while proton production results from close encounters between alpha particles and nitrogen atoms (NRA). Using the energy-dependent cross sections, considering energy loss due to nuclear and electronic stopping in GaAsN, we determine the sum of RBS yields from Ga and As backscattering, and NRA yield for $^{14}N(\alpha,p)^{17}O$ reaction. We assume that $(N\text{-}N)_{As}$ is aligned along the [111] direction, while $(N\text{-}As)_{As}$ is aligned along the [010].[15,25] Thus, the Ga sublattice shadows $(N\text{-}N)_{As}$ and N_{As} along the [111] direction, as shown in Fig 3.3. To compare the total RBS yields in [100], [110], and [111] channeling direction, we integrate areas under the spectra close to the Ga/As edge. To compare the total NRA yields in [100], [110] and [111] channeling direction, we integrate the areas under the maxima in yield associated with protons. For each of the interstitial complexes (a) N_{Sub}, (b) $(N\text{-}N)_{As}$, and (c) $(N\text{-}As)_{As}$, the projections of the crystal structure as well as the total RBS (NRA) yields in the [100], [110], and [111] directions are presented in bar graph format in Fig. 3.4 (Fig. 3.5).

3.4 Channeling RBS

We now compare the measured and the MC-MD simulated RBS spectra, as shown in Fig. 3.4. For all the N interstital complexes, the RBS simulations predict the highest (lowest) yields in the [111] ([110]) directions, as shown in Fig. 3.4(a)-(c). On the other hand, the measured RBS spectra reveal the highest (lowest) yields in the [111] ([100]) directions, as shown in Fig. 3.4(d). For an ideal GaAs lattice, the highest (lowest) RBS yield is expected in the [100] ([110]) directions. For GaAs films growth at "low" substrate temperature (i.e. $T \leq 400^{o}C$), As antisites in the form of As monomers or dimer sitting on a Ga or As site, i.e. As_{Ga} or $(As\text{-}As)_{As}$, are often observed.[18,19,20,21] For both As antisite configurations, As atoms are displaced into the [110] and [111] channels. Channeling RBS may be sensitive to such displacements.[26] Similarly, tetrahedral Ga interstitials would be detected in the [110] channel. Thus, the increase in measured [110] and [111] RBS yield (in comparison to the ideal GaAs structure) may be due to the presense of As antisites and/or Ga interstitials in the GaAsN films.

3.5 Channeling NRA

We now compare the measured and the MC-MD simulated NRA spectra, as shown in Fig. 3.5. For both the N_{Sub} and $(N\text{-}N)_{As}$ interstitial complexes, the NRA simulations predict the highest (lowest) yields in the [100] ([111]) directions, as shown in Figs. 3.5(a)-(b), leading to a yield trend of $Y_{[100]} > Y_{[110]} > Y_{[111]}$. In contrast, for the interstitial pair $(N\text{-}As)_{As}$, the simulation predicts the highest (lowest) yield in the [111] ([100]) directions as

shown in Fig. 3.5(c), giving a yield trend of $Y_{[111]} > Y_{[110]} > Y_{[100]}$. For comparison, we consider the measured NRA yields versus energy, shown in Fig. 3.6, for channeling directions [100] (green), [110] (red), [111] (blue), and random (black). The vertical dashed lines indicate the energy window of the protons emitted from the $^{14}N(\alpha,p)^{17}O$ reaction. For the measured spectra, the highest yield is in the [111] channeling direction, while the lowest yield is in the [100] channeling direction. Thus, as shown in Fig. 6(d), the measured yield trend is $Y_{[111]} > Y_{[110]} > Y_{[100]}$. As shown in Figs. 3.5(a)-(c), a yield trend of, $Y_{[111]} > Y_{[110]} > Y_{[100]}$ is predicted for only for the case where $(N\text{-}As)_{As}$ is the dominant interstitial complex. Therefore, our combined computational-experimental approach suggests that $(N\text{-}As)_{As}$ is the dominant interstitial complex in GaAsN alloys.

3.6 Conclusion

In summary, we have developed a combined computational-experimental approach consisting of MC-MD simulations, along with RBS and NRA experiments, to examine the dominant interstitial configurations in GaAsN films. We compared channeling NRA and RBS spectra with MC-MD simulations along the [100], [110], and [111] directions. During the MC simulation, we assume that $(N\text{-}N)_{As}$ is aligned along the [111] direction and is shadowed by Ga sublattice, while $(N\text{-}As)_{As}$ is aligned along the [010] direction and is not shadowed by Ga sublattice. The measured channeling RBS spectra reveal the lowest yield in the [100] direction, in contrast to those predicted for an ideal GaAs lattice, i.e. the lowest yield in the [110] direction, suggesting the possible presence of Ga interstitials and/or As antisites in the GaAsN alloys. The measured channeling NRA spectra have the highest

(lowest) yields in the [111] ([100]) directions, while similar trends are also observed for simulations of the $(N\text{-}As)_{As}$ interstitial complex. Thus, we conclude that $(N\text{-}As)_{As}$ is the dominant interstitial complex in dilute GaAsN alloys. This combined computational-experimental approach is applicable to determining the atomic structure of many HMAs, such as (In)GaAsBi and GaAsN(Bi).

3.7 Figures

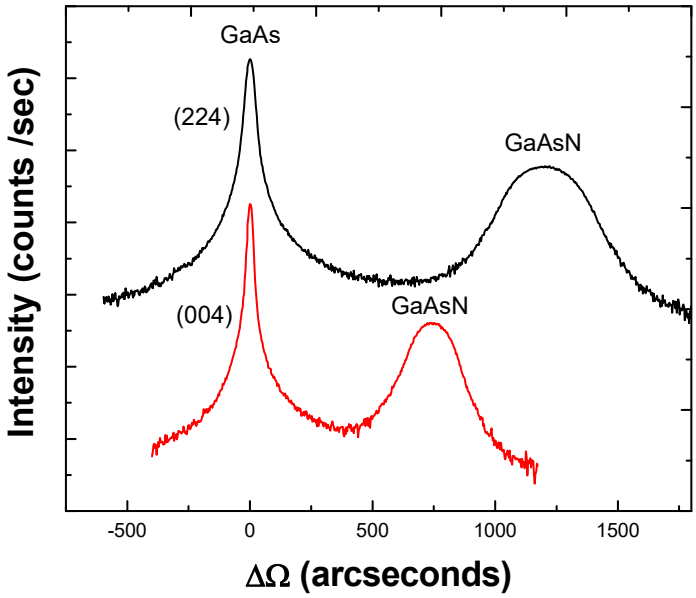

Figure 3.1 Plots of high resolution x-ray rocking curves (Intensity vs Δω) for GaAsN layers on GaAs. For both plots, the GaAs substrate peak position is set to Δω=0 arcsecond, thereby facilitating comparison of Δω between the GaAs substrate and GaAsN epilayers. Using a linear interpolation of the binary elastic constants described by Vegard's Law and lattice parameter for GaN and GaAs leads to a nitrogen fraction of x = 0.016. (Copyright 2015, AIP Publishing LLC).

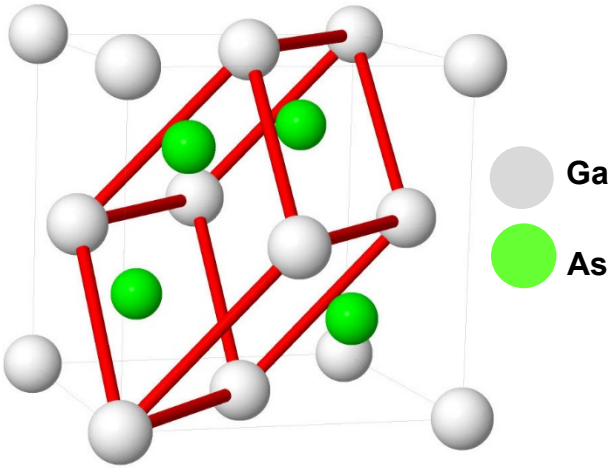

Figure 3.2 A zincblende GaAs structure with Ga (As) shown as white (green), and the primitive cell outlined in red. For the simulaton, we use the red primitive cell, modified to include N_{sub}, $(N\text{-}N)_{As}$, or $(N\text{-}As)_{As}$ replacing an As atom within the cell. (Copyright 2015, AIP Publishing LLC).

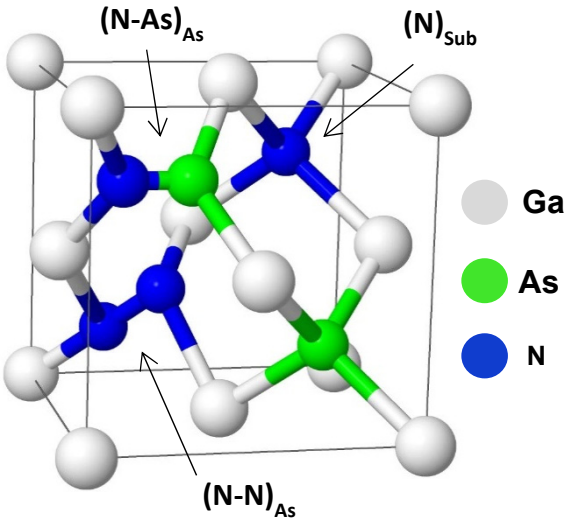

Figure 3.3 Ball-stick model of a GaAsN unit cell with $(N\text{-}As)_{As}$, $(N\text{-}N)_{As}$ and N_{sub} interstitials. The white, green, and blue spheres represent Ga, As, and N, respectively. We use the lowest energy configurations of $(N\text{-}N)_{As}$ and $(N\text{-}As)_{As}$., as predicted by density functional theory[27], namely $(N\text{-}N)_{As}$ aligned along the [111] direction, and $(N\text{-}As)_{As}$ aligned along the [010] direction. (Copyright 2015, AIP Publishing LLC).

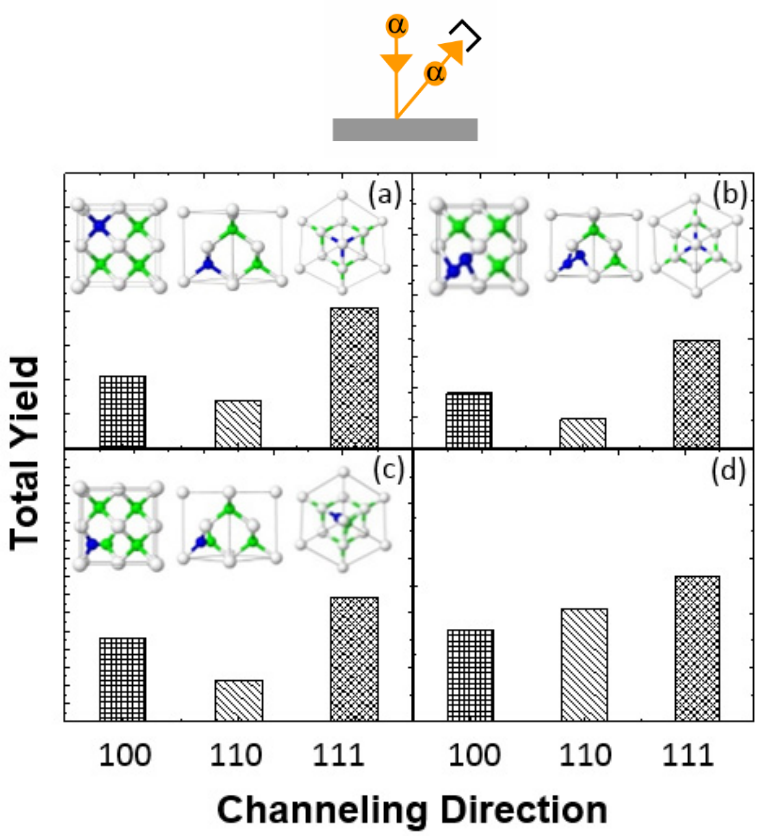

Figure 3.4 Projections of the crystal structure as well as the total simulated RBS yields in the [100], [110], and [111] directions for (a) N_{Sub}, (b) $(N\text{-}N)_{As}$, and (c) $(N\text{-}As)_{As}$. (d) Measured total RBS yield in each channeling direction. For (a)-(c), the highest (lowest) yields are in the [111] ([100]) directions, while the highest (lowest) yields are in the [111]([100]) in (d). For an ideal GaAs lattice, the highest (lowest) RBS yield is expected in the [100] ([110]) directions. The increase in the measured [110] and [111] RBS yield (in comparison to calculated values) may be due to As antisites and/or Ga interstitials in the GaAsN films. (Copyright 2015, AIP Publishing LLC).

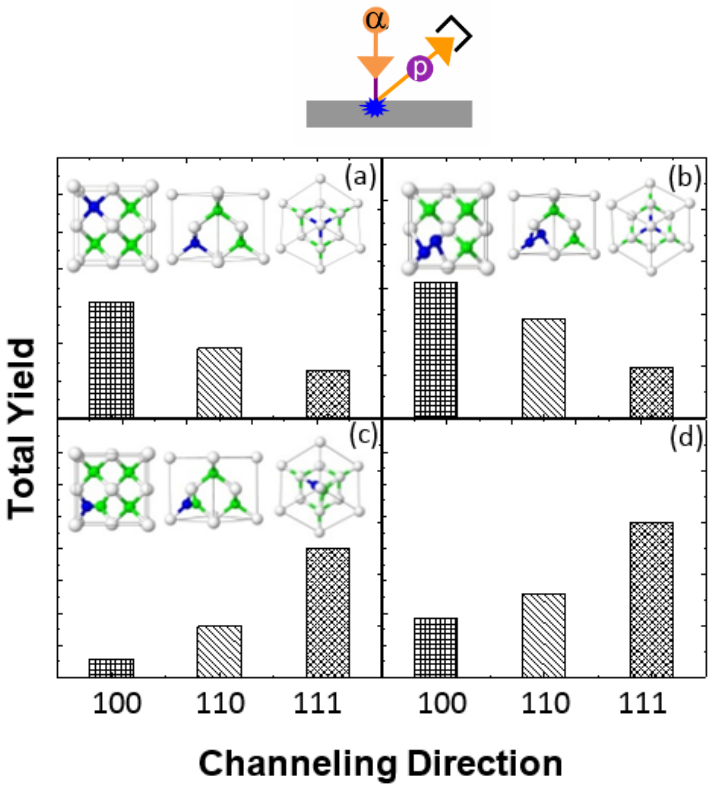

Figure 3.5 Projections of the crystal structure, as well as the total simulated NRA yields in the [100], [110], and [111] directions for (a) N_{Sub}, (b) $(N\text{-}N)_{As}$, and (c) $(N\text{-}As)_{As}$ are presented. (d) Measured total NRA in each channeling direction. Similar yield trends of $Y_{[111]} > Y_{[110]} > Y_{[100]}$ are observed for (c) and (d), suggesting that $(N\text{-}As)_{As}$ is the dominant interstitial complex in GaAsN alloys. (Copyright 2015, AIP Publishing LLC).

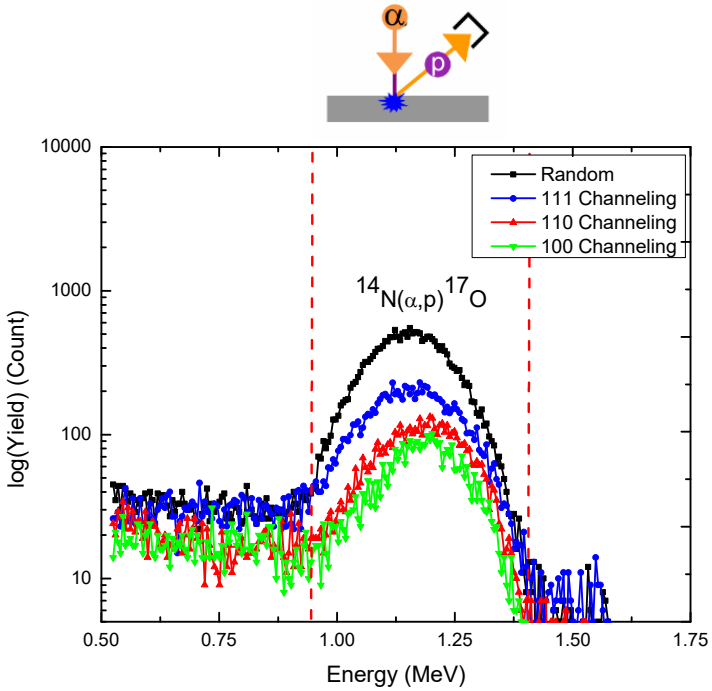

Figure 3.6 Measured NRA yield versus emitted particle energy for GaAsN, along the [100] (green), [110] (red), [111] (blue), and random (black) channeling directions. The vertical dashed lines indicate the energy window of the protons emitted during the $^{14}N(\alpha,p)^{17}O$ reaction. To compare the yields in [100], [110] and [111] channeling directions, we integrate the yields associated with protons. The highest (lowest) yield is in the [111] ([100]) channeling direction. (Copyright 2015, AIP Publishing LLC).

3.8 References

[1] P. R. C. Kent, L. Bellaiche, and A. Zunger, Semicond. Sci. Technol. **17**, 851 (2002)

[2] M. Henini. "Dilute Nitride Semiconductors", *Elsevier* (2004).

[3] W. Shan, W. Walukiewicz, J. W. Ager III, E. E. Haller, J. F. Geisz, D. J. Friedman, J. M. Olson, and Sarah R. Kurtz. Phys. Rev. Lett, **82**, 1221 (1999).

[4] A. Lindsay and E.P. O'Reilly, Phys. Rev. Lett. **93**, 196402 (2004)

[5] F. Masia, G. Pettinari, A. Polimeni, M. Felici, A. Miriametro, M. Capizzi, A. Lindsay, S. B. Healy, E. P. O'Reilly, A. Cristofoli, G. Bais, M. Piccin, S. Rubini, F. Martelli, A. Franciosi, P. J. Klar, K. Volz, and W. Stolz, Phys. Rev. B **73**, 073201 (2006)

[6] T. Dannecker, Y. Jin, H. Cheng, C.F. Gorman, J. Buckeridge, C. Uher, S. Fahy, C. Kurdak, and R.S. Goldman, Phys. Rev. B **82**, 125203 (2010).

[7] P. Pichanusakorn, Y. J. Kuang, C. Patel, C. W. Tu, and P. R. Bandaru, Phys. Rev B **86**, 085314 (2012)

[8] P. Laukkanen, M. P. J. Punkkinen, J. Puustinen, H. Levämäki, M. Tuominen, K. Schulte, J. Dahl, J. Lång, H. L. Zhang, M. Kuzmin, K. Palotas, B. Johansson, L. Vitos, M. Guina, and K. Kokko, Phys. Rev. B **86**, 195205 (2012).

[9] P. Carrier, S.-H. Wei, S. B. Zhang, and S. Kurtz, Phys. Rev. B **71**, 165212 (2005).

[10] K. Laaksonen, H.-P. Komsa, T. T. Rantala, and R. M. Nieminen, J. Phys. Condens. Matter **20**, 235231 (2008).

[11] M. Reason, H. McKay, W. Ye, S. Hanson, V. Rotberg, and R.S. Goldman, Appl. Phys. Lett. **85**, 1692 (2004).

[12] S.B. Zhang and S.H. Wei, Phy. Rev. Lett. **86**, 1789 (2001).

[13] Y. Jin, R.M. Jock, H. Cheng, Y. He, A.M. Mintairov, Y. Wang, C. Kurdak, J. L. Merz, R.S. Goldman, Appl. Phys. Lett., **95**, 062109 (2009).

[14] E. Arola, J. Ojanen, H.-P. Komsa and T. T. Rantala, Phys. Rev. B **72**, 045222 (2005).

[15] K.M. Yu, M. Kaminska, and Z. Liliental-Weber. J. Appl. Phys., **72**, 2850 (1992).

[16] P. Wei, M. Chicoine, S. Gujrathi, F. Schiettekatte, J-N. Beaudry, R. A. Masut, and P. Desjardins. J. Vac. Sci. Technol., A, **22.3** 908 (2004)

[17] T. E. M. Staab, R. M. Nieminen, M. Luysberg, J. Gebauer, and T. Frauenheim, Phys. Rev. B: Condens. Matter, **340**, 293 (2003).

[18] G. Zollo, and R. M. Nieminen. J. Phys.: Condens. Matter, **15.6** (2003)

[19] M. Reason, N. G. Rudawski, H. A. McKay, X. Weng, W. Ye, and R. S. Goldman, J. Appl. Phys. **101**, 083520 (2007).

[20] In the reaction $^{14}N(\alpha,p)^{17}O$, α reacts with ^{14}N, forming a compound nucleus ^{18}O, which subsequently decays, leaving residual ^{17}O in its ground state, with emission of a proton particle. The reaction is endothermic.

[21] P. Wei, M. Chicoine, S. Gujrathi, F. Schiettekatte, J-N. Beaudry, R. A. Masut, and P. Desjardins. *Journal of Vacuum Science & Technology A* 22, no. 3 (2004)

[22] J. E. Ayers, *Heteroepitaxy of Semiconductors: Theory, Growth, and Characterization* (CRC Press, 2007).

[23] L. Vegard, Z. Phys. **5**, 17 (1921).

[24] D. Wijesundera. (2010) *Ion-beaming channeling in non-centrosymmetric crystals* (Doctoral dissertation).

[25] We note that this figure is similar to the schematic in Ref 11, but the orientation of $(N\text{-}N)_{As}$ is modified to be aligned along the [111] direction.

[26] W.K. Chu, J.W. Mayer, and M.A. Nicolet. "Backscattering Spectrometry" *Academic Press* (1978).

[27] E. Arola, J. Ojanen, H.-P. Komsa and T. T. Rantala, Phys. Rev. B **72**, 045222 (2005).

Chapter 4

Influence of Thermal Annealing on Interstitial Complexes in GaAsN

4.1 Overview

This chapter describes experimental and computational investigations of interstitial complexes in GaAsN following rapid thermal annealing (RTA). The objective of this work is to determine the influence of RTA on the stability and/or transformation of the dominant interstitial complexes in GaAsN alloys.

The chapter begins with a review of earlier studies of the influence of RTA on the atomic structure and optoelectronic properties of GaAsN and related dilute nitride alloys. Next, we describe the experimental and computational approaches used to examine the influence of RTA on the structure of GaAsN alloys. The bulk of this chapter describes our investigations of the influence of RTA on the surface morphology, III-V stoichiometry, and related interstitial complex formation/dissociation.

4.2 Background

In dilute nitride materials, N-related defects, which often limit device performance, can be manipulated to some extent by RTA, as discussed in Chapter 1.[1,2,3,4,5,6] For example, RTA has been shown to suppress the photopersistent current effect (PPC)[7], to increase the photoluminescence (PL) intensity[8], and to improve the electron mobilities of Ga(In)NAs and related alloys.[9] In addition, RTA-induced improvements in the performance of lasers[10] and high efficiency solar-cells[11,12,13] based on InGaAsN and related alloys have been reported. Deep-level transient fourier spectroscopy (DLTFS) and photoluminescence (PL) studies have suggested an annealing-induced decrease in the concentration of $(N\text{-}N)_{As}$ or V_{Ga}.[14,15,16] In addition, using density functional theory (DFT), Raman signatures for $(N\text{-}N)_{As}$ and $(N\text{-}N)_{Sb}$ have been calculated.[17,18] Finally, RTA-induced decreases in the $(N\text{-}N)_{As}$ interstitial concentrations have been reported.[8,19,20,21] Although the reports to date suggest a link between $(N\text{-}N)_{As}$ and device performance, direct experimental observation of RTA-induced removal of the $(N\text{-}N)_{As}$ interstitials were not available prior to this thesis research. In addition, a mechanism for the RTA-induced dissociation of the $(N\text{-}N)_{As}$ interstitial complex has not been proposed. Here, we will examine and discuss the influence of RTA on the dominant interstitial incorporation and dissociation mechanisms.

4.3 Methods

4.3.1 Experimental Details

For these investigations, five $GaAs_{1-x}N_x$ films with $x_N \sim 0.0063,\ 0.019,\ 0.021,\ 0.025$ and 0.032 were utilized.[22] These films were grown by Dr. Matt Reason using the MBE process discussed in Section 3.3. Further details of the samples are also available in Appendix C of M. Reason's thesis. The samples were cleaved into 1 x 1 x 1 cm pieces for the RTA experiment described in Section 2.3. For all cases, random and channeling NRA data in [100], [110], and [111] directions were collected from both the as-grown and post-RTA GaAsN films. Additional pieces of the $x_N \sim 0.019,\ 0.021$ and 0.025 films were cleaved for further investigations, both before and after RTA. The surface morphology was examined using AFM, as described in Section 2.4. The III:V stoichiometry was examined using HRXRC. In addition, the N-related vibrational modes were monitored using Raman spectroscopy as described in Section 2.5.

4.4 GaAsN Surface Morphology

AFM images for the $x_N \sim 0.019,\ 0.021$ and 0.025 are shown in Fig. 4.1(a)-(c) and Fig. 4.1(d)-(f) for the as-grown and post-RTA $GaAs_{1-x}N_x$ films, respectively. For the as-grown films, the RMS roughness is $1.1 \pm 0.1nm$, with surface "mound" features elongated along the $[1\bar{1}0]$ direction, consistent with earlier reports by Dr. Matt Reason, shown in Fig. 3.5 of his PhD thesis.[23] These mound-like features are likely related to a "forbidden

window" of growth for GaAs, similar to the temperature-dependent mound formation observed for AlGaAs, attributed to a growth instability associated with Ehrlich-Schwoebel barrier.[23] These "mound" features are not expected to affect the overall channeling measurements, as confirmed by the low values of $\chi_{min}(GaAs)$, $0.45 - 0.55$, which are similar to earlier reports for high-quality GaAs.[24]

4.5 GaAsN Stoichiometry

To examine the GaAsN film stoichiometry, we examined (004) XRCs before and after RTA, as shown in Fig. 4.2. Due to their tensile misfit with respect to GaAs, the GaAsN diffraction peaks appear on the high-angle side of the GaAs substrate peak. For both as-grown and post-RTA the GaAsN layer peak position is fixed, suggesting the absence of N out-diffusion during RTA. Since there is no evidence for additional peaks on the low-angle side of the GaAs substrate peak, the presence of a non-stoichiometric GaAsN layer is unlikely.

However, to estimate an upper bound for [As_{Ga}], we use the full width half maximum (FWHM) of the GaAs peak. The concentration of excess arsenic in the LT-GaAs layer is estimated by its increase in lattice parameter with respect to the GaAs substrate, according to

$$\frac{\Delta a}{a} = 1.24 \times 10^{-23} \times [As_{Gs}] \tag{4.1}$$

where a is the lattice parameter of the GaAs substrate, Δa is the difference between a and the LT-GaAs lattice parameter, and $[As_{Gs}]$ is in cm^{-3}.[24] However, due to the absence of a distinct diffraction peak associated with LT-GaAs, we estimate an upperbound for $[As_{Gs}]$,

using the FWHM of the GaAs peak. For all the GaAsN films (both as-grown and post-RTA) shown in Fig. 4.2, the FWHM is $35 \pm 5\ arcseconds$, corresponding to an upper bound of $[As_{Ga}] \sim (2.1 \pm 0.3) \times 10^{19} cm^{-3}$ at least one order of magnitude lower than standard LT-GaAs ($10^{20} cm^{-3}$).[24,25,26,27]

4.6 N-Interstitial Formation and Dissociation

To examine the formation and dissociation of N-interstitial complexes following RTA, we consider both the Raman spectroscopy signatures for $(N\text{-}N)_{As}$ interstitials, as well as the channeling ion beam analyses described in Section 2.5, 2,8 and 3.5. We then compare with computations of N interstitial complexes, and propose two possible mechanisms for N interstitial complex dissociation.

4.6.1 Vibrational Signature for the $(N\text{-}N)_{As}$

Raman spectra for $GaAs_{1-x}N_x$ alloys with $x_N \sim 0.019,\ 0.021$ and 0.025 are shown in Fig. 4.3. For all values of x_N, several features are apparent, including the GaAs-like transverse-optical (TO) and longitudinal-optical (LO) phonons at 565 and 580 cm^{-1} respectively. The GaN-like LO phonon mode at 470cm^{-1}, as well as an additional feature at 425cm^{-1}, which has been identified as a signature for $(N\text{-}N)_{As}$, are also apparent.[8,15,19,20,21] Following RTA, spectral features associated with GaAs-like LO and TO, the GaN-like LO, with intensities similar to the as-grown films, were observed for all samples. Although the spectral feature associated with $(N\text{-}N)_{As}$ is also observed following RTA, its intensity has

decreased, suggesting an RTA induced a reduction in the concentration of $(N\text{-}N)_{As}$ interstitial complexes, consistent with earlier reports on GaAsN and InGaAsN .[8,19,20,21]

4.6.2 Channeling NRA Data

We now describe channeling NRA data for $GaAs_{1-x}N_x$ alloys, considering the influence of both x_N and RTA on the predominant interstitial formation and transformation. In all cases, data similar to those shown in Fig. 3.4, were obtained. To facilitate comparison across x_N, in Fig. 4.4, we plot the total yield as a function of x_N, along with the projections of the crystal structure to the right for (a) [100], (b) [110], and (c) [111] channeling conditions. In the plots, the data for as-grown (annealed) GaAsN films is shown in black (blue), with lines connecting the dots serving as guides to the eye. For all channeling directions, there is a monotonic decrease in the total yield with increasing x_N, suggesting the N interstitial fraction is influenced by x_N. For all values of x_N, RTA induces an increase in the [111] total yield, a decrease in the [100] total yield, and negligible changes in the [110] total yield. As discussed in Section 3.5, $(N\text{-}As)_{As}$ interstitial complexes are predicted to be aligned along the [010] direction.[28] Therefore, an increase in the [111] total yield suggest an increase in the fraction of $(N\text{-}As)_{As}$ interstitial complexes. Since the interstitial complexes are not shadowed in the [100] and [110] directions, an RTA-induced decrease in the [100] total yield suggests an increase in N_{sub}.

4.7 Mechanisms for N-related Interstitial Dissociation

We now discuss possible mechanisms for the RTA-induced dissociation of N-related interstitial complexes. As discussed above, our Raman spectroscopy data suggests that RTA has reduced the fraction of $(N\text{-}N)_{As}$ interstitial complexes. Furthermore, our channeling NRA data suggests that RTA has increased the fraction of N_{sub} and $(N\text{-}As)_{As}$ interstitial complexes. Therefore, we compute channeling spectra GaAsN with 80% N_{sub}, 6% $(N\text{-}N)_{As}$, and 14% $(N\text{-}As)_{As}$, plus three possible dissociations of the 6% $(N\text{-}N)_{As}$ into both $2N_{sub}$, and $(N\text{-}As)_{As} + N_{sub}$, as illustrated in Fig. 4.5. For these studies, we performed channeling simulations as described in Section 3.3.2, using an input structure consisting of 3x3x3 unit cells, as described in Section 2.9. With 27 unit cells, up to 108 defect sites may be included in the simulation. Therefore, we consider multiple defect types and locations for both the as-grown and post-RTA GaAsN Films.

In Fig. 4.6(a)-(d), a comparison of the [100], [110], and [111] total channeling NRA yields for GaAsN are shown. The slanted filled bars represent the simulated or measured as-grown GaAsN, and the diamond-filled bars correspond to simulated or measured post-RTA GaAsN. In Fig. 4.6(a), all $(N\text{-}N)_{As}$ dissociates into $2N_{sub}$, leading to a lower [100] yield while the [111] remains fixed. In Fig. 4.6(b), all $(N\text{-}As)_{As}$ dissociates into $(N\text{-}As)_{As} + N_{sub}$, leading to an decreased (increase) [100] ([111]) yield. In Fig. 4.6(c), we assume that ½ of the $(N\text{-}N)_{As}$ dissociates into $(N\text{-}As)_{As} + N_{sub}$, while the other ½ $(N\text{-}N)_{As}$ dissociates into $2N_{sub}$, leading to an increase in the [111] yield and a decrease in the [100] yield. The small dissociation induced increase of the simulated [110] yield might be due to differences in the effective cross-section of the $(N\text{-}As)_{As}$ and the $(N\text{-}N)_{As}$ interstitial complexes in the

[110] channel.[28] For the measured values shown in Fig. 4.6(d), RTA induces an decrease in the [100] and an increase in the [111] total yields, along minor increases or decreases in the [110] total yield. Therefore, our combined computational-experimental approach suggests an RTA-induced dissociation of $(N\text{-}N)_{As}$ into a combination of $2N_{sub}$ and N_{sub} + $(N\text{-}As)_{As}$.

4.8 Summary and Conclusions

In summary, we have examined the influence of RTA on the structure of GaAsN films, with a focus on the stability and/or transformation of the dominant interstitial complexes. X-ray rocking curve data suggest that the GaAsN films are coherently strained and compositionally stoichiometric, with minimal RTA-induced out-diffusion. Raman spectroscopy data reveals vibrational modes associated with $GaN(LO_2)$, $GaAs(TO_1)$, $GaAs(LO_1)$, and $(N\text{-}N)_{As}$. Following RTA, the intensities of most features remained fixed, but those attributed to the $(N\text{-}N)_{As}$ are reduced. Finally, NRA reveals an RTA-induced decrease (increase) in the total [100] ([111]) yields, suggesting an increase in the fractions of N_{sub} and $(N\text{-}As)_{As}$ interstitial complexes. Based upon a comparison with MC-MD simulations of channeling yields, we hypothesize that half of $(N\text{-}N)_{As}$ interstitial dissociate into $2N_{sub}$, while half dissociate into N_{sub} + $(N\text{-}As)_{As}$. These results are likely to be applicable to other dilute nitride alloys which contain significant fractions of $(N\text{-}N)_{As}$ interstitial complexes.

4.9 Figures

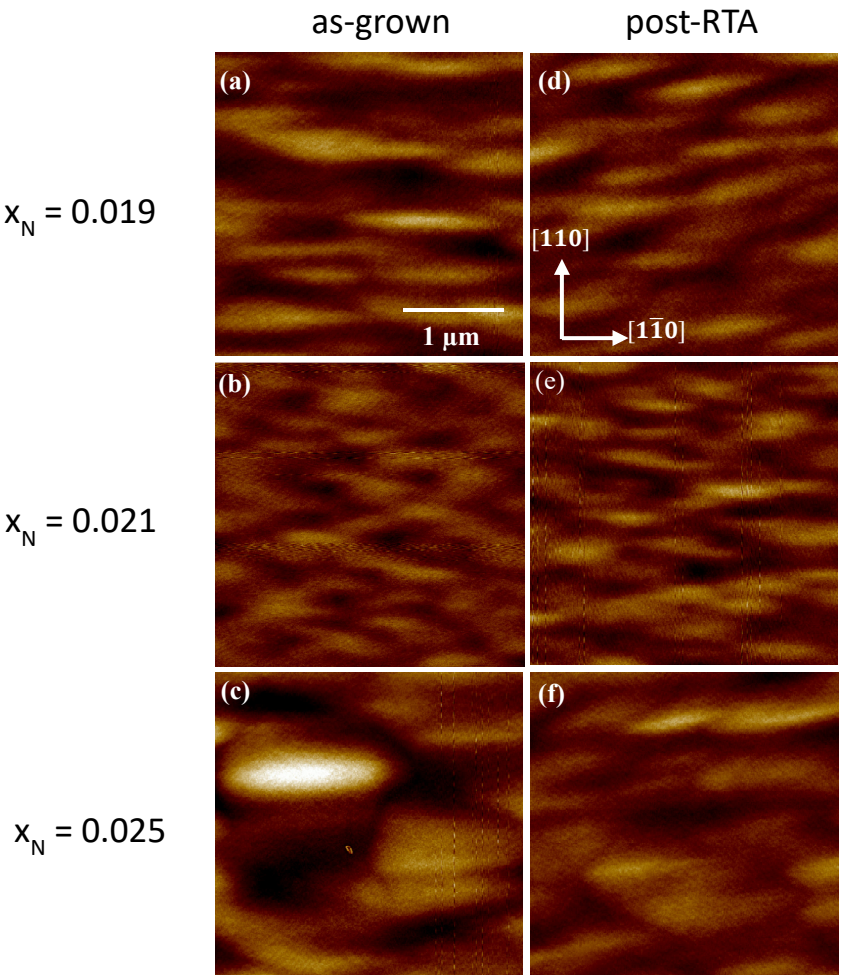

Figure 4.1 AFM images of the GaAsN films: (a)-(c) as-grown and (d)-(f) post RTA. For all images, the gray-scale range displayed is 12nm; and the rms roughness is 1.1nm ± 0.1nm, and $[1\bar{1}0]$-oriented surface features are observed, consistent with earlier reports by Dr. Matt Reason, shown in Fig. 3.5 of his PhD thesis.[23] These mound-like features are likely related to a "forbidden window" of growth for GaAsN, similar to the temperature-dependent mound formation observed for AlGaAs, attributed to a growth instability associated with Ehrlich-Schwoebel barrier.[23] These "mound" features are not expected to affect the overall channeling measurements, as confirmed by the values $\chi_{min}(GaAs)$, $0.45 - 0.55$, similar to earlier reports for high quality GaAs.[29]

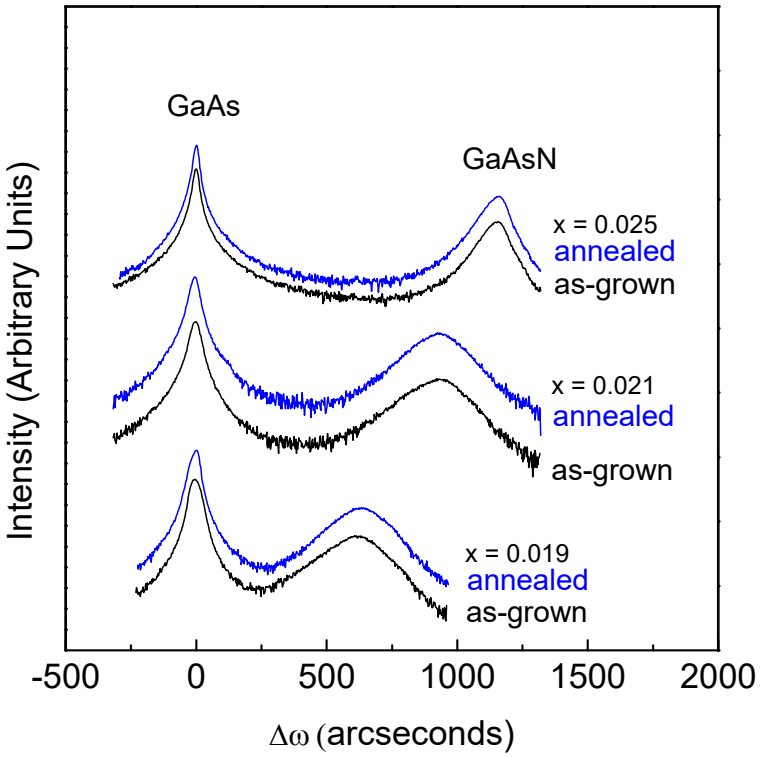

Figure 4.2 (004) high-resolution x-ray rocking curves for $GaAs_{1-x}N_x$ layers on GaAs, before ("as-grown", black) and after RTA ("annealed",blue). For all plots, the GaAs substrate peak position is set to $\Delta\omega = 0$ arcseconds, thereby facilitating comparison of $\Delta\omega$ between the GaAs substrate and the GaAsN films. For all films, the GaAsN peak position is unchanged with annealing, suggesting the absence of N out-diffusion. Using the full width half maximum of the GaAs peak,[24] we estimate an upper bound of $[As_{Ga}]\sim(2.1 \pm 0.3) \times 10^{19} cm^{-3}$ for all the as-grown and post-RTA GaAsN films.

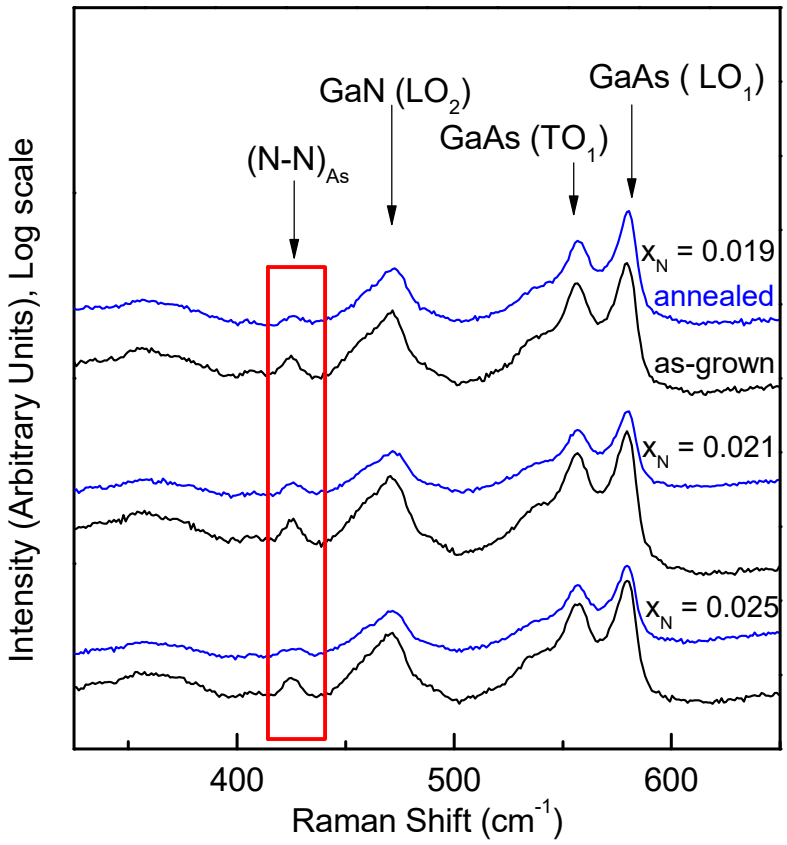

Figure 4.3 Raman spectra for $GaAs_{1-x}N_x$ alloys with $x_N = 0.019, 0.021$ and 0.025 both before and after RTA, shown in black and blue, respectively. Several spectral features are apparent, including the $565cm^{-1}$ GaAs-like transverse-optical (TO) phonons, $580cm^{-1}$ GaAs-like longitudinal-optical (LO) phonons, and the $470cm^{-1}$, which is associated with GaN-like LO phonons. In addition, spectral features are observed at $425cm^{-1}$, which has been identified as a signature for $(N\text{-}N)_{As}$.[8,19,20,21] The annealed Raman spectra has a lower intensity for the feature at $425cm^{-1}$, suggesting an RTA-induced reduction in the concentration of $(N\text{-}N)_{As}$ interstitial complexes.

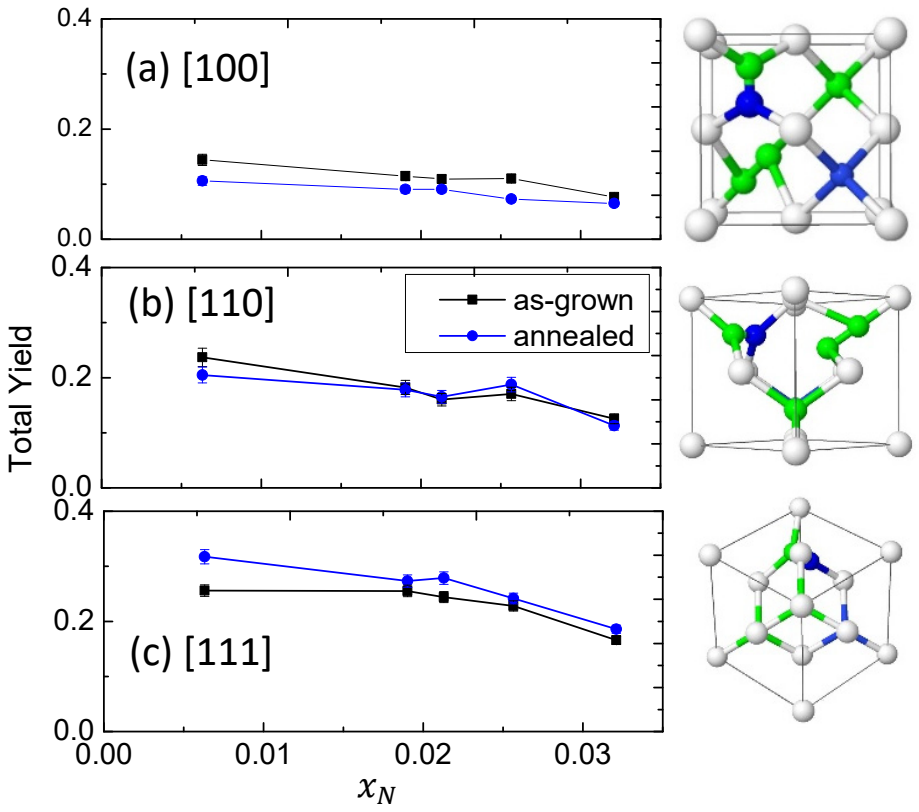

Figure 4.4 Total NRA yield as a function of x_N, along with the projections of the crystal structure to the right for (a)[100], (b)[110], and (c)[111] channeling conditions. The data for the as-grown (annealed) GaAsN films is shown in black (blue), with lines connecting the dots serving as guides to the eye. For the as-grown GaAsN films, as x_N increases, the total yields decreases monotonically, independent of channeling direction, suggesting that the N interstitial fraction is influenced by x_N. Following RTA, the [100] total yield decreases; thus, the fraction of N-related interstitial complexes has decreased and the fraction of N_{sub} has increased. On the other hand, the [111] total yield increases following RTA. Since the [111] yield is influenced primarily by the $(N\text{-}As)_{As}$ interstitial complexes, we hypothesize that RTA has increased the fraction of $(N\text{-}As)_{As}$ interstitial complexes.

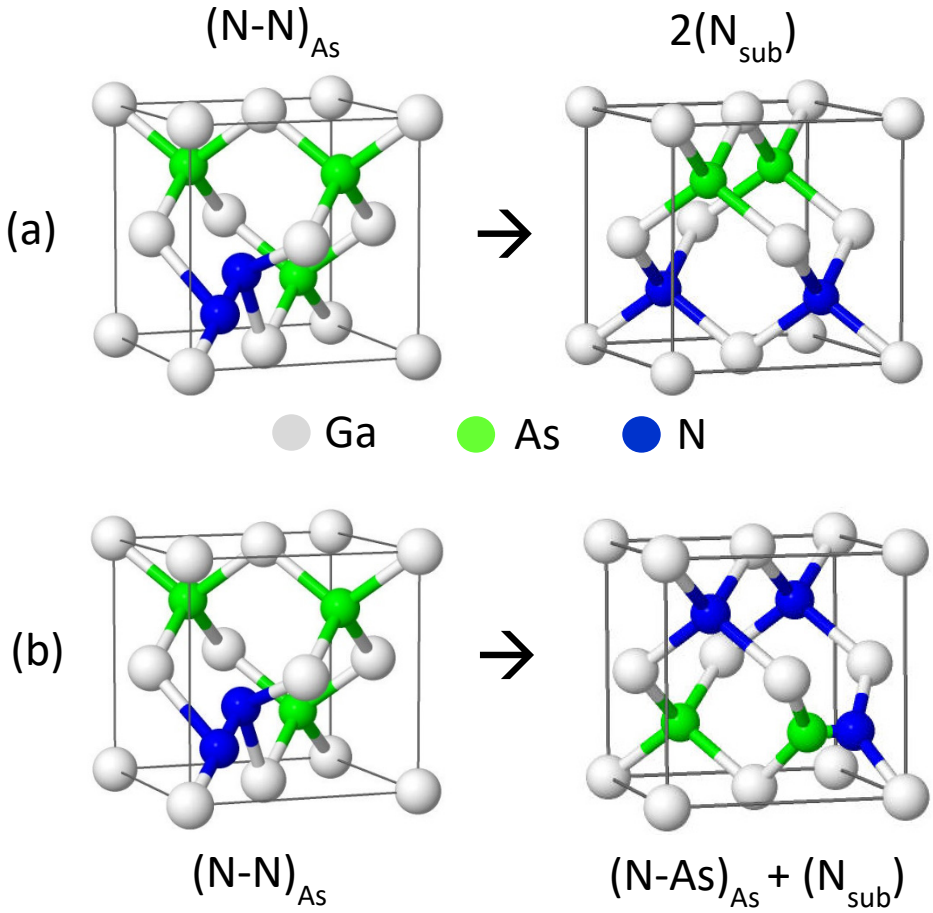

Figure 4.5 Ball-stick models of GaAsN unit cell with $(N\text{-}N)_{As)}$ interstitial complexes and possible dissociations into (a) $2(N_{sub})$ and (b) $N_{sub} + (N\text{-}As)_{As}$ interstitials. The white, green, and blue spheres represent Ga, As, and N, respectively. We use the lowest energy configurations, as predicted by density functional theory, with $(N\text{-}N)_{As}$ aligned along the [111] direction, and $(N\text{-}As)_{As}$ aligned along the [010] direction.[25]

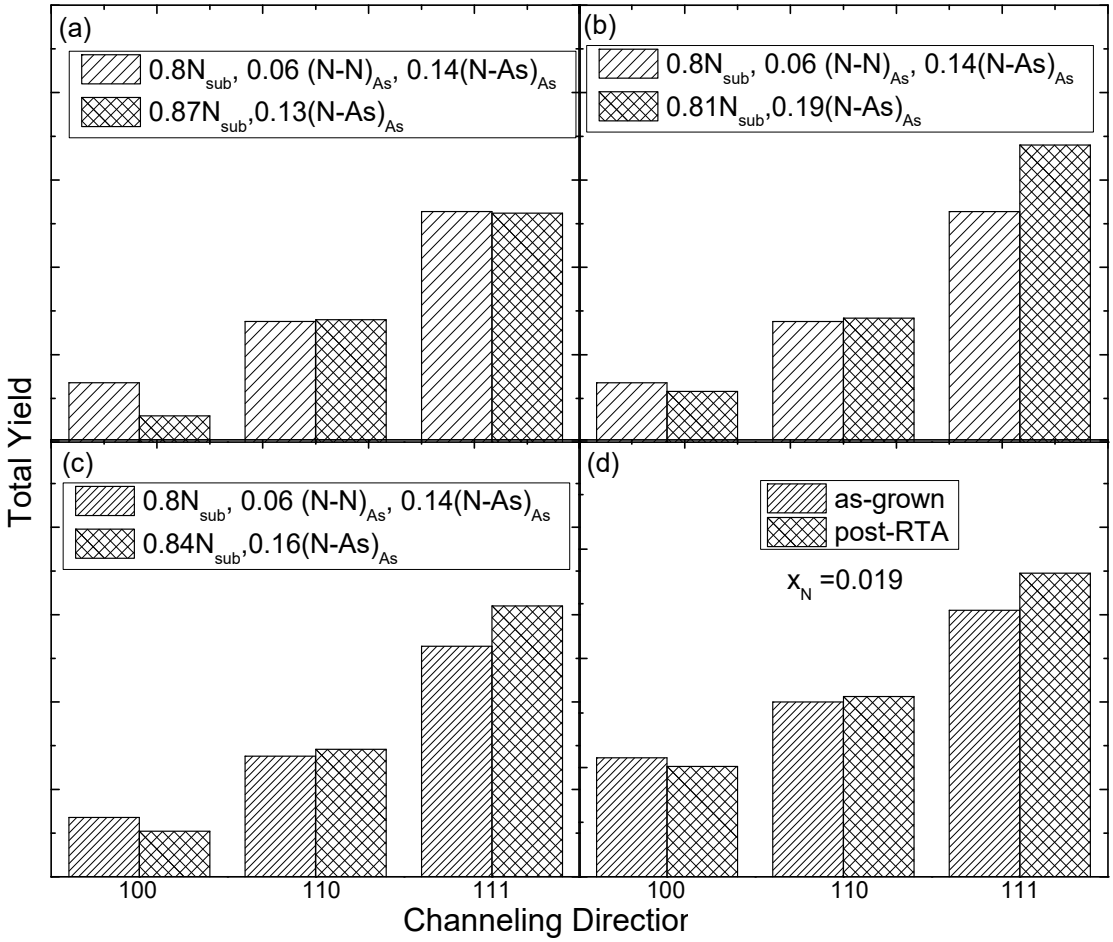

Figure 4.6 Comparison of [100], [110], and [111] nuclear reaction analysis (NRA) channeling total yields for GaAsN. The slanted filled bars represent the simulated or measured as-grown GaAsN, and the diamond-filled bars correspond to simulated or measured post-RTA GaAsN. In (b), all $(N\text{-}N)_{As}$ dissociates into $2N_{sub}$, leading to a lower [100] yield while the [111] remains fixed. In (b), all $(N\text{-}As)_{As}$ dissociates into $(N\text{-}As)_{As}$ + N_{sub}, leading to an decreased (increase) [100] ([111]) yield. In (c), we assume that ½ of the $(N\text{-}N)_{As}$ dissociate into $(N\text{-}As)_{As}$ + N_{sub}, while another ½ dissociates into $2N_{sub}$, leading in to an increase in the [111] yield and a decrease in the [100] yield, which is consistent with the experiment trends in (d). The slight RTA-induced increases in the [110] yields for both the simulation and data may be due to differences in the effective cross-section for the $(N\text{-}As)_{As}$ and the $(N\text{-}N)_{As}$ interstitial complexes in the [110] channel.[28]

4.10 References

[1] P. Laukkanen, M. P. J. Punkkinen, J. Puustinen, H. Levämäki, M. Tuominen, K. Schulte, J. Dahl, J. Lång, H. L. Zhang, M. Kuzmin, K. Palotas, B. Johansson, L. Vitos, M. Guina, and K. Kokko, Phys. Rev. B **86**, 195205 (2012).

[2] J. Chen, G. Ciatto, M. Le Du, J.C. Harmand and F. Glas, Phys. Rev. B **82**, 125303 (2010).

[3] H.T. Pham, S.F. Yoon, K.H. Tan and D. Boning. Appl. Phys. Lett **99**, 092115 (2010).

[4] Y.G. Hong, C.W. Tu and R.K. Ahrenkiel, J. Cryst. Growth **227-228**, 536 (2001)

[5] M.R. Gokhale, J. Wei, H. Wang and S.R. Forrest, Appl. Phys. Lett. **74**, 1287 (1999).

[6] R.A. Stradling, Semicond. Sci. Technol. **6**, C52 (1991).

[7] R.L. Field III, Y. Jin, H. Cheng, T. Dannecker, R.M. Jock, Y.Q. Wang, C. Kurdak, R.S. Goldman, Phys. Rev. B **87**, 155303 (2013).

[8] M. Ramsteiner, D. S. Jiang, J. S. Harris, and K. H. Ploog, Appl. Phys. Lett. **84**, 1859 2004.

[9] Y.G. Hong, C.W. Tu and R.K. Ahrenkiel, J. Cryst. Growth **227-228**, 536 (2001).

[10] S.R. Bank, M.A. Wister, L.L. Goddard, H.B. Yuen, H.P. Bae, and J.S. Harris, Electron. Lett. 40, 1186 (2004).

[11] T.W. Kim, T.J. Garrod, K. Kim, J.J. Lee, S.D. LaLumondiere, Y. Sin, W.T. Lotshaw, S.C. Moss, T.F. Kuech, R. Tatavarti, and L.J. Mawst, Appl. Phys. Lett. 100, 121120 (2012).

[12] D.B. Jackrel, S.R. Bank, H.B. Yuen, M.A. Wistey, J.S. Harris, A.J. Ptak, S.W. Johnston, D.J. Friedman, and S.R. Kurtz, J. Appl. Phys. 101, 114916 (2007).

[13] M.W. Wiemer, H.B Yuen, V.A Sabnis, M.J Sheldon, and I. Fushman, U.S. Patent Application 20100319764, 2010.

[14] P. Krispin, V. Gambin, J. S. Harris, and K. H. Ploog, J. Appl. Phys. **93**, 6095 (2003).

[15] G. Mussler, J-M. Chauveau, A. Trampert, M. Ramsteiner, L. Däweritz, and K. H. Ploog. J. Crys. Grow. 267, 60 (2004).

[16] D. Sentosa, T. Xiaohong, Y. Zongyou, and S.J. Chua. J. of Crys. Grow. 307, 229 (2007).

[17] A.M. Teweldeberhan, and Stephen Fahy. Phy. Rev. B. 77, 235216 (2008).

[18] J. Buckeridge, D.O. Scanlon, T.D. Veal, M. J. Ashwin, A. Walsh, and C. R. A. Catlow. Phy. Rev. B. 89, 014107 (2014).

[19] T. Prokofyeva, T. Sauncy, M. Seon, M. Holtz, Y. Qiu, S. Nikishin, and H. Temkin. Appl. Phys. Lett. **73** 1409 (1998)

[20] E.M. Pavelescu, J. Wagner, , H.P. Komsa, T.T. Rantala, M. Dumitrescu, and M. Pessa, J. Appl. Phys 98, 083524 (2005).

[21] Y. Jin, R.M. Jock, H. Cheng, Y. He, A.M. Mintairov, Y. Wang, C. Kurdak, J. L. Merz, R.S. Goldman, Appl. Phys. Lett. **95**, 062109 (2009)

[22] RMBE96, RMBE97, RMBE112, RMBE122 and RMBE158

[23] M. Reason, Ph.D. thesis, Ch. 3. University of Michigan, 2006.

[24] T. Ahlgren, E. Vainonen-Ahlgren, J. Likonen, W. Li, and M. Pessa, Appl. Phys. Lett. **80**, 2314 2002.

[25] R. L. Field, J. Occena, T. Jen, D. Del Gaudio, B. Yarlagadda, C. Kurdak, and R. S. Goldman, Appl. Phys. Lett. 109, 252105 (2016).

[26] J. Betko, P. Kordos, S. Kuklovsky, A. F€orster, D. Gregusova, and H. L€uth, Mater. Sci. Eng. B 28, 147 (1994).

[27] S. O'Hagan and M. Missous, J. Appl. Phys. 75, 7835 (1994).

[28] E. Arola, J. Ojanen, H.-P. Komsa and T. T. Rantala, Phys. Rev. B **72**, 045222 (2005).

[29] T. Ahlgren, E. Vainonen-Ahlgren, J. Likonen, W. Li, and M. Pessa, Appl. Phys. Lett. **80**, 2314 2002.

Chapter 5

Epitaxial Growth and Solute Incorporation in GaAsNBi Alloys

5.1 Overview

In this chapter, we examine molecular-beam epitaxial growth, stoichiometry, and solute incorporation in GaAsNBi alloys. The objective of this chapter is to understand the atomistic mechanisms for N and Bi co-incorporation and their influence on alloy stoichiometry and electronic properties. In addition, we seek to identify the "magic" Bi:N ratio for lattice-matching with GaAs.

This chapter begins with background information, including the motivation for studying GaAsNBi, and the challenges associated with N and Bi co-incorporation while maintaining III-V stoichiometry during low temperature growth. Next, we describe the experimental and computational approaches used for our investigations of GaAsNBi. The bulk of the chapter describes our investigation of III-V stoichiometry in GaAsNBi, N and Bi incorporation in GaAsNBi, and lattice matching of GaAsNBi with GaAs.

5.2 GaAsNBi Background

Due to the significant bandgap narrowing induced by dilute fractions of N in GaAs, dilute nitride alloys are attractive for a variety of applications, including long-wavelength lasers and detectors, ultra-high-efficiency solar cells, and high performance heterojunction bipolar transistors.[1] However, N-related point defects often lead to degraded minority carrier transport properties and optical efficiencies.[2,3] In principle, co-alloying GaAsN with larger elements such as indium (In), antimony (Sb), and/or Bi allows lattice-matching to GaAs or Ge substrates as shown in Fig. 5.1; however, the "magic" Bi:N ratio for lattice-matching of GaAsNBi is currently unknown. Furthermore, In, Sb, or Bi co-alloying with GaAsN is expected to lead to significant bandgap narrowing using a substantially lower N fraction, with a correspondingly lower fraction of N-related defects.[4,5] Bi incorporation into GaAs at a mole fraction of 0.01 leads to a bandgap reduction of ~84 meV, much larger than the reduction for similar fractions of Sb (21 meV) or In (16 meV).[6] In addition, the significant spin-orbit splitting induced by Bi is expected to lead to reduced nonradiative Auger recombination for Bi fractions in excess of 0.105.[7] Thus, GaAsNBi is promising for optoelectronic applications operating in the near-infrared range.

For GaAsN and related alloys, bismuth is often reported to surface segregate without incorporating. However, the presence of a Bi flux has been reported to increase or decrease the incorporation of N. For example, metalorganic vapor-phase epitaxy (MOVPE) with a Bi flux has been reported to decrease the N fraction,[8,9] while molecular-beam epitaxy (MBE) with a sufficiently high Bi flux has been reported to increase the N

fraction.[10,11,12] To date, the atomistic mechanisms for the influence of Bi flux on N incorporation remain unknown.

In GaAs, isovalent co-alloying of Bi and N is expected to involve replacement of As such that III-V stoichiometry is maintained in $GaAs_{1-x-y}N_xBi_y$ alloys.[4] However, direct studies of III-V stoichiometry in GaAsNBi have not yet been reported. In chapter 1 and 3, we discussed the challenges of films growth at lower substrate temperatures, including the possible formation of As antisites, As_{Ga}, or Ga vacancies, V_{Ga}.[13,14,15] Thus, $GaAs_{1-x-y}N_xBi_y$ alloys may have V/III ratio in excess of 1.

5.3 Experimental Details

The $GaAs_{1-x-y}N_xBi_y$ alloy films were grown on semi-insulating (001) GaAs substrates by molecular-beam epitaxy (MBE) using solid Ga, As, and Bi sources and a radio frequency nitrogen plasma source, on the Gen II MBE. The cracking zone of the As source was maintained at a relatively low temperature such that predominantly As_4 was supplied. [16,17] After an initial 500-nm thick GaAs buffer layer grown at 580ºC, the substrate temperature was held at 580ºC for a 5 minute anneal, lowered to the GaAsNBi growth temperature, and held at the growth temperature for 5 minutes prior to growth.[18] 100 nm thick $GaAs_{1-x-y}N_xBi_y$ films were grown at 345 ± 15 ºC with As_4/Ga beam equivalent pressure (BEP) ratios of ~ 20 and growth rate of 1 μm/h. To monitor the influence of Bi and N fluxes on surface reconstruction, reflection high-energy electron diffraction (RHEED) patterns were collected along the [110] and $[1\bar{1}0]$ directions.

To examine the GaAsNBi surface morphologies, we use a combination of atomic-force microscopy (AFM) and scanning electron microscopy (SEM), as described in Chapter 2.4. The AFM images were collected using a Bruker Dimension Icon in tapping, contact, and ScanAsyst modes.

The stoichiometry of the GaAsNBi films was determined using a combination of atomic-probe tomography (APT) and high-resolution x-ray rocking curves (HRXRC). APT measurements were performed in the LEAP 4000X and/or the LEAP 5000HS, using laser mode, and HRXRC measurements were performed using Cu $K\alpha_1$ radiation. A series of $\Delta\omega$ scans were collected near the GaAs (004) and GaAs (224) reflections. More details of the experimental methods were presented in sections 2.6 and 2.7.

RBS and NRA were performed using a NEC tandem accelerator with a 4.46 MeV He^+ beam. The RBS (NRA) detector was placed at 167° (135°) with respect to the incident beam to detect the backscattered He^+ ions. [19] We used nuclear reaction $^{14}N(\alpha,p)^{17}O$ to detect the nitrogen atoms.[20] RBS and NRA measurements were performed in [100], [110], and [111] channeling and non-channeling conditions achieved by oscillating the specimen $\varphi_x = \pm 4^{\circ}$ about the channeling condition during spectra collection, as described in Section 2.8. We note that both RBS and NRA data are analyzed using the simulation of nuclear reaction analysis (SIMNRA) code, an analytical simulation program in which multiple small-angle scattering events are treated as energy broadening. [21] To simulate the channeling NRA spectra, we use a combined Monte Carlo-Molecular Dynamics (MC-MD) approach. More details about the simulation and analysis are provided in Chapter 3 and Appendix E.

5.4 Minimizing Excess Arsenic Incorporation

In preliminary studies of GaAsBi alloys in both the C21 and Gen II MBE systems, we found that the concentration of excess arsenic, As_{Ga}, is highly sensitive to the low substrate temperature during epitaxy.[22,23] Therefore, to find a suitable temperature for minimal As_{Ga} incorporation into GaAsNBi, we grew a series of samples with an extra layer of low temperature grown GaAs, so called "LT-GaAs", as shown in Fig. 5.2. In Fig. 5.3, XRC data for a series of GaAsNBi films grown with fixed Bi beam-equivalent pressures and N_2 flow rates, at substrate temperatures varied from 235℃ to 346℃ $\pm$ 5℃ is presented. For all plots, the GaAs substrates position is set to $\Delta\omega = 0\ arcsec$, and a GaAsNBi epilayer peak is evident at $\Delta\omega \approx -575\ to - 325\ arcsec$. In addition, for the lowest growth temperature, a somewhat broad peak centered at $\Delta\omega \approx -100\ arcsec$, associated with the LT-GaAs layer, is observed.[24] As the substrate temperature is increased, the LT-GaAs peak shifts to higher angles, eventually disappearing for growth temperature exceeding 300℃. We note that the GaAsNBi peak also shifts to higher angles due to a decrease in Bi fraction with increasing growth temperature.

The concentration of excess arsenic in the LT-GaAs layer is estimated by its increase in lattice parameter with respect to the GaAs substrate, according to

$$\frac{\Delta a}{a} = 1.24 \times 10^{-23} \times [As_{Gs}] \tag{5.1}$$

where a is the lattice parameter of the GaAs substrate, Δa is the difference between a and the LT-GaAs lattice parameter, and $[As_{Gs}]$ is in cm^{-3}.[24] For the lowest growth temperature, $[As_{Gs}] \approx 6.85 \times 10^{19} cm^{-3}$. However, due to the absence of a distinct diffraction peak associated with LT-GaAs at temperature > 337℃, we estimate an

upperbound for $[As_{Gs}]$, using the full-width-half-maximum of the GaAs peak, to be $[As_{Gs}] < 9.3 \times 10^{18} cm^{-3}$, at least two orders of magnitude lower than standard LT-GaAs where up to $10^{20} cm^{-3}$ has been reported.[24,25,26,27]

Although we identified the range of substrate temperatures needed to minimize $[As_{Gs}]$ incorporation in the GaAs layers, additional studies are needed to confirm the stoichiometry of the GaAsNBi alloys grown at $T > 300$℃. Therefore, we utilized local electrode atom probe (LEAP) microscopy or atom-probe tomography (APT) to examine whether isovalent co-alloying of GaAs with two anions (Bi, N) is limited to the replacement of As by the anions as predicted.[4] Details of the LEAP technique are described in Section 2.7 with the steps for sample preparation and data analysis described in Appendix C.

We first examine the influence of laser energy on molecular evaporation and the apparent stoichiometry of GaAs. Figure 5.4 shows (a) APT reconstructions, (b) plots of counts vs mass-to-charge ratio, and (c) Ga:As fractions for LEAP experiments on GaAs. For all laser energies, 200,000 ions were collected and reconstructed, yielding contact-lens shaped reconstructions, shown in Fig. 5.4(a), with significant signals at mass-to-charge ratios of 69 (Ga^+), 71 (Ga^+), and 75 (As^+ or As_2^{++}), shown in Fig. 5.4(b). As the laser energy is lowered to below 5 pJ, the uniformity of ion evaporation is increased, as shown by the similarities in ion distribution from the center to the edge of the reconstructions in Fig. 5.4(a). It is interesting to note that the intensity of the signal associated with the mass-to-charge ratio of 75 also increases as the laser energy is lowered, as shown in Fig. 5.4(b). To determine the Ga:As ratio, we assign the mass-to-charge ratio of 75 to As^+ or As_2^{++}, as listed in Fig. 5.4(c). For laser energies greater than 5 pJ, the Ga:As ratio is far from stoichiometric, consistent with the non-uniform ion distributions apparent in the contact

lens-shaped reconstructions in Fig. 4.4(a). In earlier GaAs LEAP studies, non-stoichiometry has been attributed to delayed evaporation of As.[28,29] Instead we attribute this apparent non-stoichiometry to the overlap of the signals associated with As^+ or As_2^{++}. Indeed, for the lowest laser energy, 0.25 pJ, near-stoichiometry Ga:As ratio of 50.6:49.2 is apparent when we assign the mass-to-charge ratio of 75 to As_2^{++}, as shown in Fig. 5.4(c).

Using the laser energy identified for the nearly stoichiometric reconstruction of GaAs, 0.25 pJ, we performed a LEAP experiment on a fabricated tip consisting of ~250 nm GaAsNBi on 500 nm GaAs on a GaAs substrate. In this case, ~5 million ions were collected and reconstructed; the resulting reconstructions of the tip, separated into the Bi, N, As, and Ga atoms, are shown in Fig. 5.5, with the labeled regions corresponding to the GaAsNBi epilayer and the GaAs layer. Ga and As ions are observed throughout the tip while N and Bi ions, for the most part, are confined to the epilayer regions. We note that the apparently uniform distribution of N and Bi atoms in the epilayer suggests the absence of solute clustering.

As shown in the table in Fig. 5.5, we consider the compositional analysis for the cases where the mass-to-charge ratio of 75 is assigned to As^+ and As_2^{++}. For the As^+ assignment, both the GaAs layer and GaAsNBi epilayer are non-stoichiometric, containing excess Ga of 0.055 and 0.015 mole fractions respectively. Since the GaAs layer was grown at 580ºC, it is expected to be stoichiometric; thus, the As^+ assignment is considered unlikely in this case. However, with the As^+ assignment, the Bi mole fraction in the GaAsNBi layer is 0.022, similar to the 0.023 value determined by RBS. For the As_2^{++} assignment, both substrate and epilayer are non-stoichiometric, in this case containing excess As. Since the GaAs layer is nearly stoichiometric, the As_2^{++} assignment for the 75

mass-to-charge ratio is best for GaAs. For the GaAsNBi layer, grown at 345 ± 15ºC, the LEAP analysis using As_2^{++} for mass-to-charge ratio of 75 suggests that epilayer has up to 0.062 mole fraction of excess arsenic; assuming Bi and N replaces group V site, $y_{Bi} = 0.019$ and $x_N = 0.0082$, then the As mole fraction must be 0.4728 to maintain stoichiometry, with $z_{Ga} = 0.5$. However, the measured As mole fraction is 0.535, which is $0.535 - 0.4728 = 0.062$ in excess. Given the GaAs density is $4.42 \times 10^{22} cm^{-3}$,[30] 6.2% of that is $2.74\times 10^{21} cm^{-3}$, or $[As_{Gs}] \approx 2.74 \times 10^{21} cm^{-3}$. This value is roughly three orders of magnitude higher than the XRC estimated value, $[As_{Gs}] < 9.3 \times 10^{18} cm^{-3}$, for LT-GaAs also grown 345 ± 15ºC, as described in Section 5.4, and one order of magnitude higher than the $10^{20} cm^{-3}$ reported for GaAs grown at 200 ℃ growth temperature.[24] Therefore, it appears that the As^+ and As_2^{++}assignments for the mass-to-charge ratio of 75 works best for the GaAsNBi and GaAs layers, respectively. This difference in effective arsenic assignment is likely due to the local electric field variations induced by variations in the effective permittivities of GaAsNBi vs GaAs. Further discussion is included in Ch. 6.3.1.

5.5 Solute Incorporation Mechanisms

A series of films with a range of N and Bi fractions were achieved by independently varying the Bi BEP from 0 to 1 × 10^{-7} Torr (with N_2 flow rate fixed at 0.25 sccm), and the N_2 flow rate from 0.17 to 0.35 sccm (with Bi BEP fixed at 5.7 × 10^{-7} Torr), which we will refer to as the "Bi flux series" and the "N flux series", respectively.

5.5.1 Surface Reconstructions and Morphologies

For all films, a (2 x 4) RHEED pattern [Fig. 5.6 (a) and (b)] was observed for growth of the GaAs buffer layer at 580°C; it transitioned to a (2 x 3) pattern [Fig. 5.6 (c) and (d)] as the temperature was ramped under As overpressure to 345 ± 15°C. During GaAsNBi growth with low Bi fluxes, a (1 x 3) pattern [Fig. 5.6 (e) and (f)] was observed, consistent with the Bi-induced (1 x 3) reconstruction reported by others for GaAsN growth in the presence of a Bi flux.[10,12] At higher Bi flux, above BEP ~ 5.7×10^{-8} Torr, a (2 x 1) reconstruction was observed instead [Fig. 5.6 (g) and (h)]. In the N flux series, with the Bi flux maintained at 5.7×10^{-8} Torr, all films showed either a (1 x 3) or a (2 x 1) pattern, suggesting that this Bi flux is near the threshold between the (1 x 3) induced by lower Bi fluxes and the (2 x 1) induced by higher Bi fluxes. Growth of GaAsN without a Bi flux resulted in a (2 x 1) pattern similar to Fig. 5.6 (g) and (h).

AFM images for the Bi flux series and N flux series are presented in Fig. 5.7(a)-(d) and Fig. 5.7(e)-(h) respectively. For both the Bi and N flux series, the surfaces appear featureless, with rms roughness <0.5nm, consistent with observations of layer-by-layer growth of GaAsN.[31,32] To confirm the absence of μm-sized surface droplets, 400 μm x 500 μm SEM images were also collected, as shown in Fig. 5.7(i)-(j). The images include features associated with dust, in order to demonstrate the suitable focus condition. Indeed, in the well-focused condition, the surface is featureless, without the presence of surface droplets.

5.5.2 N Flux Series

HRXRC of the N flux series and Bi flux series are presented in Fig. 5.8(a) and 5.8(b). Due to their compressive and tensile misfit with respect to GaAs, the GaAsBi and GaAsN diffraction peaks appear on the low-angle and high-angle side of the GaAs substrate peak, respectively. For the N flux series, the GaAs(N)Bi peak is shifted toward the high-angle side as the N incorporation is increased. In addition, as shown in Fig. 5.8(a), the N mole fraction, *x*, and Bi mole fraction, *y*, determined from analyses of NRA and RBS data respectively, are indicated on the HRXRC plots. As the N_2 flow rate increases, *x* increases monotonically. Meanwhile *y* is unchanged with increasing N_2 flow rate, indicating that Bi incorporation is unaffected by co-incorporation with N.

For the N flux series, the NRA yield vs. reaction-emitted proton energy is plotted in Fig. 5.9. Both random and channeling NRA yields associated with N increase with increasing N flux. SIMNRA fits to the random NRA spectra, using a GaAsN standard, reveal *x* ranging from 0 to 0.017; assuming a uniform N depth profile, the SIMNRA fits suggests a uniform incorporation of N throughout the GaAsNBi film. The fraction of substitutionally incorporated N atoms, $f_{N\text{-}sub}$, was calculated according to

$$f_{N-sub} = \frac{1-\chi(N)}{1-\chi_{min}(GaAs)} \tag{5.2}$$

where $\chi(N)$ is the ratio of the channeling to the non-channeling NRA yield and $\chi_{min}(GaAs)$ is the ratio of the channeling to the non-channeling RBS yield for the GaAs reference film. Additional details of the calculations of interstitial and substitutional fraction using channeling and random spectra are available in Appendix A.3.2 of M. Reason's Ph.D thesis.[33]

5.5.3 Bi Flux Series

For the Bi flux series, the GaAsN(Bi) peak is shifted from the high-angle side, with negligible Bi incorporation, to the low-angle side as the Bi incorporation is increased. In addition, as shown in Fig. 5.8(b), the *x* and *y* fractions determined from analyses of NRA and RBS are also indicated on the HRXRC plots. As the Bi flux increases, *y* increases monotonically. Furthermore, although the N flux is fixed, *x* also increases with Bi flux, up to a saturation value at ~0.018.

For the Bi flux series, the RBS yield vs. backscattered ion energies is plotted in Fig. 5.10(a); an enlarged portion is plotted in Fig. 5.10(b) with random spectra data overlaid with SIMNRA fitted spectra. Due to the similar atomic masses of Ga and As, the energies of the He ions backscattered from Ga and As are similar, ~3.6MeV, in Fig. 5.10(a), and similar RBS yields associated with both atoms are also observed due to their similar atomic numbers. Due to the high atomic mass of Bi, the energies of the He ions backscattered from Bi are at higher energy, ~4.1MeV. Both the random and channeling RBS yields associated with Bi increase with increasing Bi flux. SIMNRA fits to the random RBS spectra reveal *y* ranging from 0 to 0.059. In addition, SIMNRA fits, assuming uniform Bi depth profile produces Gaussian-shaped RBS yields that matches with the experimental spectra, suggesting a uniform incorporation of Bi throughout the GaAsNBi film. For the channeling spectra, the distinct peaks (corresponding to He scattering from Ga and As) near ~3.6MeV and the asymmetric peak (associated with He scattering from Bi) at ~4.1MeV are due to preferential scattering from exposed surface atoms.[34]

To determine the fraction of Bi atoms incorporating substitutionally in GaAs(N)Bi films, $f_{Bi\text{-}sub}$, we used an analogous equation with $\chi(N)$ replaced by $\chi(Bi)$, defined as the ratio of the channeling to the non-channeling Bi-related RBS yield.

$$f_{Bi-sub} = \frac{1-\chi(Bi)}{1-\chi_{min}(GaAs)} \quad (5.3)$$

In Fig. 5.11(a), the total, x, substitutional, x_{sub}, and interstitial, x_{int}, mole fractions of N are plotted for the Bi flux series. As pointed out earlier, x increases with increasing Bi BEP. In the GaAsN film (Bi BEP = 0 Torr), the fraction of N occupying substitutional sites, $f_{N\text{-}sub} = x_{sub}/x$, is 0.81, consistent with other literature reports for GaAsN.[17,18,,35] As the Bi BEP is increased, $f_{N\text{-}sub}$ decreases, indicating that the fraction of N atoms occupying non-substitutional sites increases with increasing Bi flux. For all Bi-containing films, $f_{Bi\text{-}sub}$ is ≥ 0.90, independent of Bi BEP or N_2 flow rate. Indeed, in recent studies of GaAsNBi alloys, high precision angular RBS scans revealed substitutional Bi incorporation, consistent with our interpretation.[36] It is likely that the small fraction of non-substitutional Bi detected in the channeling RBS measurements is not associated with Bi interstitials but rather is due to the large atomic size of Bi, which may prevent substitutional Bi atoms from being completely shadowed by the GaAs matrix.

5.5.4 NRA vs XRD N Interstitial Fraction

The N fraction was also determined using the small-angle approximation analysis of XRC described in Section 2.6 (in an attempt to determine if the RBS-determined Bi fraction is sufficient to determine the N fraction without using NRA). For both Bi and N flux series, x_N and y_{Bi} are plotted as a function of Bi BEP and N MFC values shown in

Figs. 5.12(a) and (b). In all cases, the RBS and XRC-determined values of y_{Bi} agree to within <0.1%. For low N fractions, the NRA and XRD determined x_N are similar. However, for x_N values exceeding 0.01, the NRA and XRC-determined values of x_N deviate by in excess of 0.5%. Since only substitutional N (or Bi) is considered in the XRC data analysis, a higher value of NRA-determined x_N (in comparison with the XRD determined x_N value) suggests the presence of N interstitial complexes in those cases. For the two sets of data points enclosed in the red boxes, in Fig 5.12(a) and (b), the fraction of interstitial N complexes is expected to be negligible. Therefore, in the estimation of the "magic" $\frac{y_{Bi}}{x_N}$ ratio for lattice-matching with GaAs to be discussed in Section 5.6, these data points will be discussed separately.

5.5.5 Comparison of Channeling and Simulation Data

To determine the dominant N interstital complex configuration, the measured NRA channeling data are compared with MC-MD simulations of a 3x3 unit cell of GaAsNBi, as shown in Fig. 5.12, with N-to-Bi incorporation ratio of 1-to-2. Within each cell, each N is positioned at the center of the group V site as either substitutional N, N_{As}; $(N\text{-}N)_{As}$, with N_2 aligned along the [111] direction; or $(N\text{-}As)_{As}$, with the N-As pair aligned along the [010] direction.[37,38,39,40] Within each cell, each Bi is positioned at the center of the group V site as substitutional Bi, Bi_{As}. Due to the large size of Bi atoms, we also include atomic displacement of nearest-neighbor Ga.[41]

In Fig. 5.13, we present a comparison of the simulated and measured NRA yields for GaAsNBi. For both the N_{Sub} and $(N\text{-}N)_{As}$ interstitial complexes, the NRA simulations

predict the highest (lowest) yields in the [100] ([111]) directions, as shown in Figs. 5.13(a)-(b), leading to a yield trend of $Y_{[100]} > Y_{[110]} > Y_{[111]}$. In contrast, for the interstitial pair $(N\text{-}As)_{As}$, NRA simulations predict the highest (lowest) yield in the [111] ([100]) directions, as shown in Fig. 5.13(c), with a yield trend of $Y_{[111]} > Y_{[110]} > Y_{[100]}$. As shown in Fig. 5.13(d), the measured yield trend is $Y_{[111]} > Y_{[110]} > Y_{[100]}$; this particular yield trend is predicted only for the case where $(N\text{-}As)_{As}$ is the dominant interstitial complex. Therefore, our combined computational-experimental approach suggests that $(N\text{-}As)_{As}$ is the dominant interstitial complex in GaAsNBi alloys, consistent with other reports for GaAsN and related dilute nitride alloys.[42,43,44,45,46,47]

5.5.6 Mechanism for Bi-enhanced N Incorporation

We next discuss a mechanism for Bi-induced enhancement of N incorporation based upon Bi adatom induced disordering of $[\bar{1}10]$-oriented step edges during growth. Standard MBE growth of GaAs, with a (2x4) reconstruction, typically results in long terraces with step edges oriented along the $[\bar{1}10]$ direction.[48] Dimroth *et al.* showed that N incorporation is suppressed on (111)A offcut surfaces on which the density of $[\bar{1}10]$-oriented step edges is increased.[8] On a (2x4) reconstructed GaAs surface, it has been shown that $[\bar{1}10]$ step edges may be disrupted by exposure to Bi, resulting in (1x3) or (4x3) reconstruction consisting of smaller islands with a higher density of [110]-oriented step edges.[49] Thus, for GaAsN, the surface Bi adatoms, which induce the (1x3) reconstruction shown in Figs. 5.6(e) and 5.6(f), may increase the density of [110] step edges, allowing increased incorporation of N atoms. Furthermore, the [110] step edge consists of As

dangling bonds, such that a N atom incorporating on a [110] step edge would have an increased likelihood of forming a $(N\text{-}As)_{As}$ interstitial complex, as shown in Fig. 5.14.[28,29,30,31,32,33] Consequently, the Bi adatom induced enhancement in N incorporation would be accompanied by an increased fraction of interstitial N, consistent with our observations.

5.6 "Magic Ratio" for Lattice Matching GaAsNBi Films

One major motivation for developing GaAsNBi alloys is the possibility for lattice matching with GaAs substrates for a variety of compositions. In Fig. 5.1, a plot of band gap energy vs lattice parameter is shown for GaAs, GaAsN, and GaAsBi alloys. In the plot, the vertical dashed line indicates the predicted alloy with $[Bi] \approx 1.7[N]$.[50] *Yoshimoto et al*, reported a similar ratio $[Bi] \approx 1.7[N]$, based upon an analysis of XRC measurements. However, the analysis was based upon the computed value of a_{GaBi} from *Janotti et al*,[50,51] without consideration of the expected ~20% interstitial N incorporation.

To identify the "magic" B:N ratio for lattice matching of GaAsNBi with GaAs, we consider our ion beam analysis of Bi and N fraction along with XRD measurements of strain. For this purpose, we selected all the GaAsNBi films presented in Fig. 5.8, including both compressively and tensile strained films, with their (004) GaAsNBi peaks on the low and high angle side of the GaAs substrate peak. For each film, we utilize the values of y_{Bi} and x_N determined from analyses of RBS and NRA data, and we obtain $\varepsilon_\perp$ from XRC data, using the small angle approximation $\varepsilon_\perp = \frac{\Delta\theta}{\theta_{004}}$, described in Section 2.6. In Fig. 5.15(a)-(b), we plot $\frac{y_{Bi}}{x_N}$ vs $\varepsilon_\perp$ and use a linear least-squares fit to extract the $\frac{y_{Bi}}{x_N}$ at which $\varepsilon_\perp = 0$.

In Fig. 5.15(a), we included only those data points for films with significant interstitial fraction (i.e. all but those in the red boxes in Fig. 5.12), leading to $[Bi] \approx 1.23 \pm 0.04[N]$ for the "magic" ratio for lattice-matching to GaAs. In Fig. 5.15(b), we used the two data points for films with negligible interstitial fraction (i.e. those in the red boxes in Fig. 5.12), leading to $[Bi] \approx 1.67[N]$ for the "magic" ratio. It is interesting to note that the magic ratio for the negligible interstitial case (determined with two data points) is in good agreement with theoretical predictions i.e. $[Bi] \approx 1.7[N]$, whereas much lower x_N value is actually needed for lattice-matching based upon the revised "magic" ratio of $[Bi] \approx 1.23 \pm 0.04[N]$ reported here.

5.7 Summary and Conclusions

In summary, we have examined the molecular-beam epitaxial growth, stoichiometry, and solute incorporation in GaAsNBi alloys. Our combined XRD, RBS, NRA, and APT studies suggest a lack of excess arsenic in our GaAsNBi films. In addition, although Bi incorporation into GaAsNBi is independent of N flux, N incorporation, including the fraction of N occupying non-substitutional sites, increases with increasing Bi flux. Since the Bi flux increase leads to a transition in surface reconstruction from (2x4) to (1x3), the enhancement in both the total N content and the fraction of N interstitials is attributed to the Bi-adatom-induced increase in the fraction of [110]-oriented step edges with As dangling bonds, increasing the likelihood for formation of $(N\text{-}As)_{As}$. Finally, our XRD and NRA data suggest a "magic ratio" of $[Bi] = 1.23 \pm 0.04\,[N]$, lower than the predicted value of $[Bi] \approx 1.7[N]$, which considered only the presence of substitutional N

atoms. This insight provides a pathway to tailored N incorporation in GaAsNBi and related alloys.

5.8 Figures

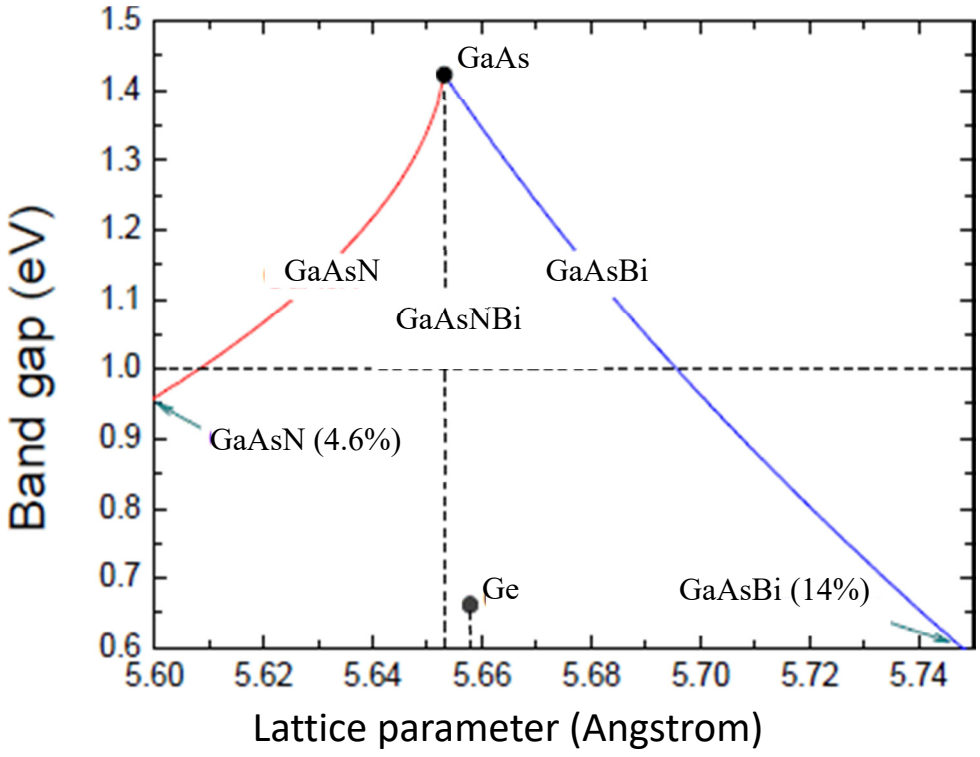

Figure 5.1 Energy band gap vs. lattice parameter for GaAs, GaAsN, and GaAsBi alloys, with the 1.0 eV value of interest for PV shown as a horizontal dashed line. The dashed vertical line indicates the predicted lattice-matched GaAsNBi alloy, with $[Bi] = 1.7[N]$. Adapted from Ref. 49.[49] (Copyright 2013, IEEE).

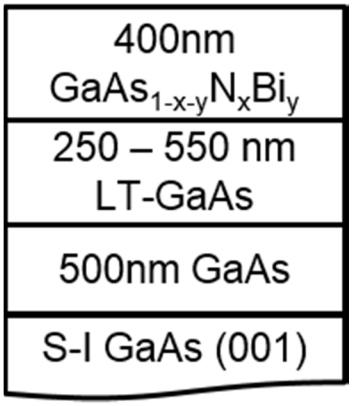

Figure 5.2 Sample structure used for examining the excess As concentration, [As_{Ga}], as a function of growth temperature ranging from 234ºC to 337ºC. The GaAsNBi and LT-GaAs layers are grown at the same temperature. The corresponding XRC data are shown in Fig. 5.3.

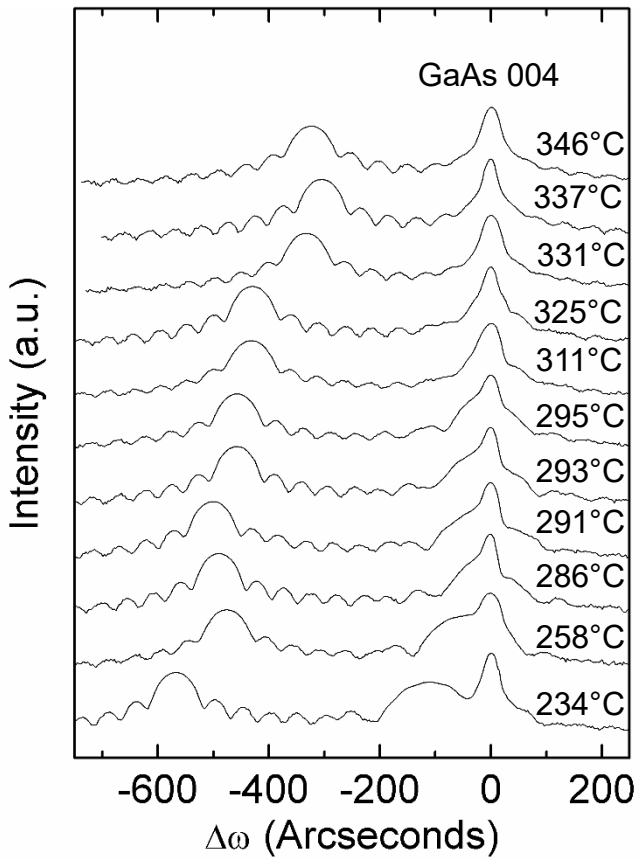

Figure 5.3 Plots of (004) XRC data for the series of GaAsNBi films/LT-GaAs samples, shown schematically in Fig. 5.2, grown with fixed Bi beam-equivalent pressures and N_2 flow rates, and with growth temperature ranging from 234 to 346 (±5)ºC. For all plots, the GaAs substrate position is set to $\Delta\omega = 0$ arcsec, thereby facilitating comparison of $\Delta\omega$ between the GaAs substrate, any As-rich non-stoichiometric (or "low T") GaAs layers, and the GaAsNBi layers. For the lowest substrate temperature, a somewhat broad peak centered at $\Delta\omega \approx -100$ arcsec, associated with As-rich GaAs, is observed. As the substrate temperature is increased, the As-rich GaAs peak shifts to higher angles, eventually disappearing for substrate temperatures exceeding 300ºC. We note that the GaAsNBi peak also shifts to higher angles with increasing substrate temperature, possibly due to a decrease in Bi incorporation.

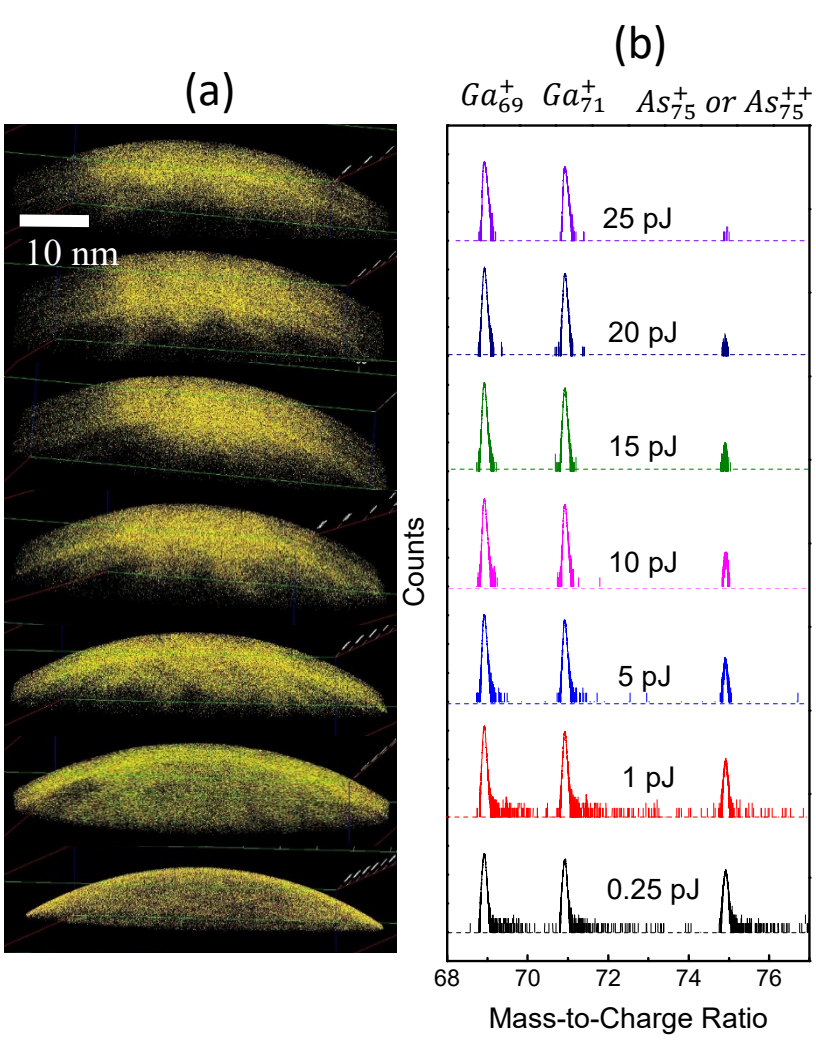

(c)

As species	z_{Ga}	z_{As}
As	0.61	0.39
As	0.60	0.40
As	0.58	0.42
As	0.57	0.43
As	0.54	0.46
As	0.54	0.45
As_2	0.53	0.47
As	0.56	0.44
As_2	0.51	0.49

Figure 5.4 (a) A series of lens-shaped LEAP reconstructions, (b) LEAP spectra, and (c) Ga:As fractions for GaAs LEAP experiments using laser energies ranging from 0.25 pJ (bottom) to 25 pJ (top). As the laser energy is lowered, the ion evaporation becomes more uniform, as shown in (a). At 25 pJ and 20 pJ, the ions (yellow) are not laterally uniform. However, as the energy is lowered to 1 pJ and 0.25 pJ, the lateral uniformity is improved. (b) semi-log plot of counts vs mass-to-charge ratio showing Ga (69 and 71) and As (75) for various laser energies. As the laser energy is lowered from top to bottom, the counts for the mass-to-charge ratio of 75 decrease. In addition, the Ga:As ratio approaches 55/45, suggesting that the ion evaporation is heavily influenced by the laser energy. If the mass-to-charge of 75 is assigned to As_2, a near 50/50 Ga:As is obtained.

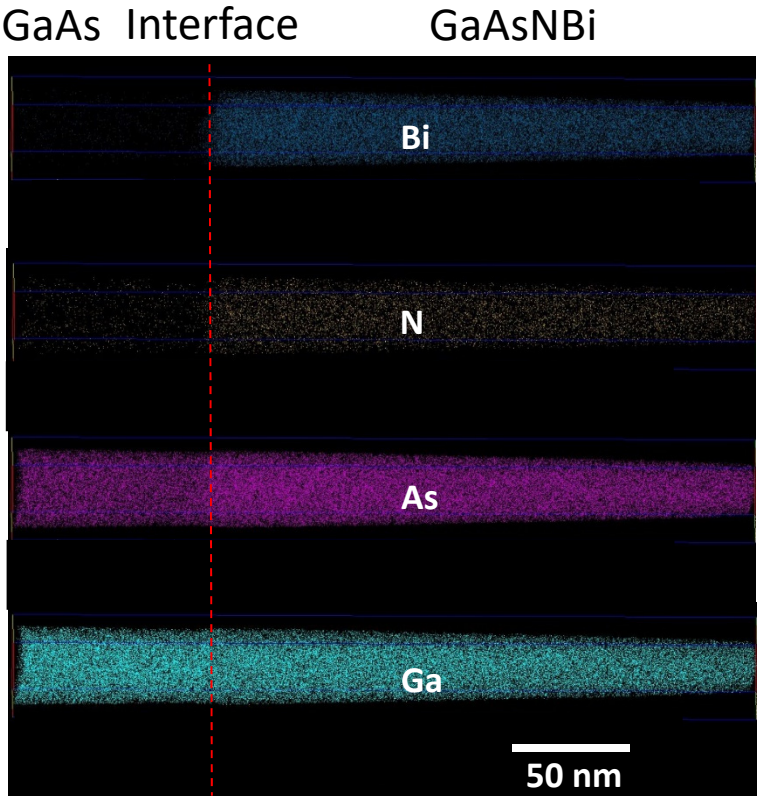

As Species	GaAs Composition		GaAsNBi Composition			
	z_{Ga}	z_{As}	z_{Ga}	z_{As}	y_{Bi}	x_N
As (0.25pJ)	0.555	0.441	0.515	0.453	0.022	0.0096
As2 (0.25 pJ)	0.485	0.515	0.437	0.535	0.019	0.0082

Figure 5.5 Using the laser energy identified for the nearly stoichiometric reconstruction of GaAs, 0.25 pJ, we performed a LEAP experiment on a fabricated tip consisting of ~250 nm GaAsNBi on 500 nm GaAs on a GaAs substrate. In this case, ~5 million ions were collected and reconstructed; the resulting reconstructions of the tip, separated into the Bi, N, As, and Ga atoms, with the labeled regions corresponding to the GaAsNBi epilayer and the GaAs layer. Ga and As ions are observed throughout the tip while N and Bi ions, for the most part, are confined to the epilayer regions. We note that the apparently uniform distribution of N and Bi atoms in the epilayer suggests the absence of solute clustering. We consider the compositional analysis for the cases where the mass-to-charge ratio of 75 is assigned to As^+ and As_2^{++}. For the As^+ assignment, both the GaAs layer and GaAsNBi epilayer are non-stoichiometric, containing excess Ga. On the other hand, for the As_2^{++} assignment, both substrate and epilayer are non-stoichiometric as well, containing excess As.

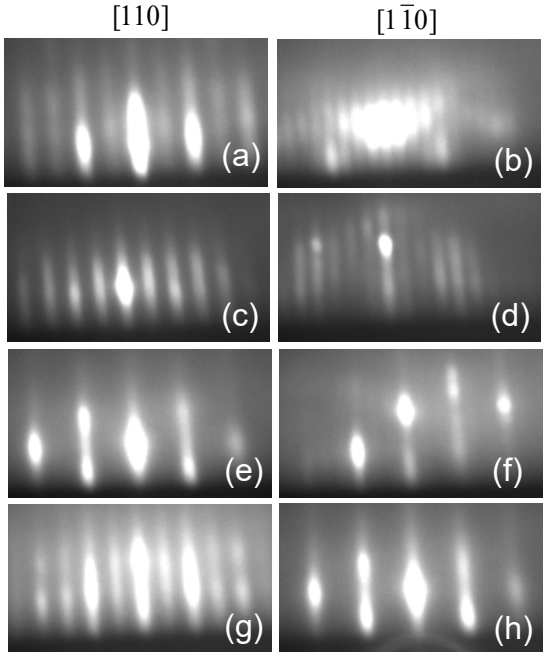

Figure 5.6 Reflection high-energy electron diffraction patterns along the [110] and [1 $\bar{1}$ 0] axes during GaAs(N)(Bi) film growth. [(a), (b)] (2 x 4) pattern following GaAs growth at 580°C; [(c), (d)] (2 x 3) pattern at 345 ± 15°C immediately prior to the beginning of the GaAs(N)(Bi) layer; [(e), (f)] (1 x 3) pattern during GaAsNBi growth at 345 ± 15°C with Bi flux ≤ 5.7×10^{-8} Torr; [(g), (h)] (2 x 1) pattern during GaAsNBi growth with Bi flux ≥ 5.7×10^{-8} Torr. (Copyright 2017, AIP Publishing LLC).

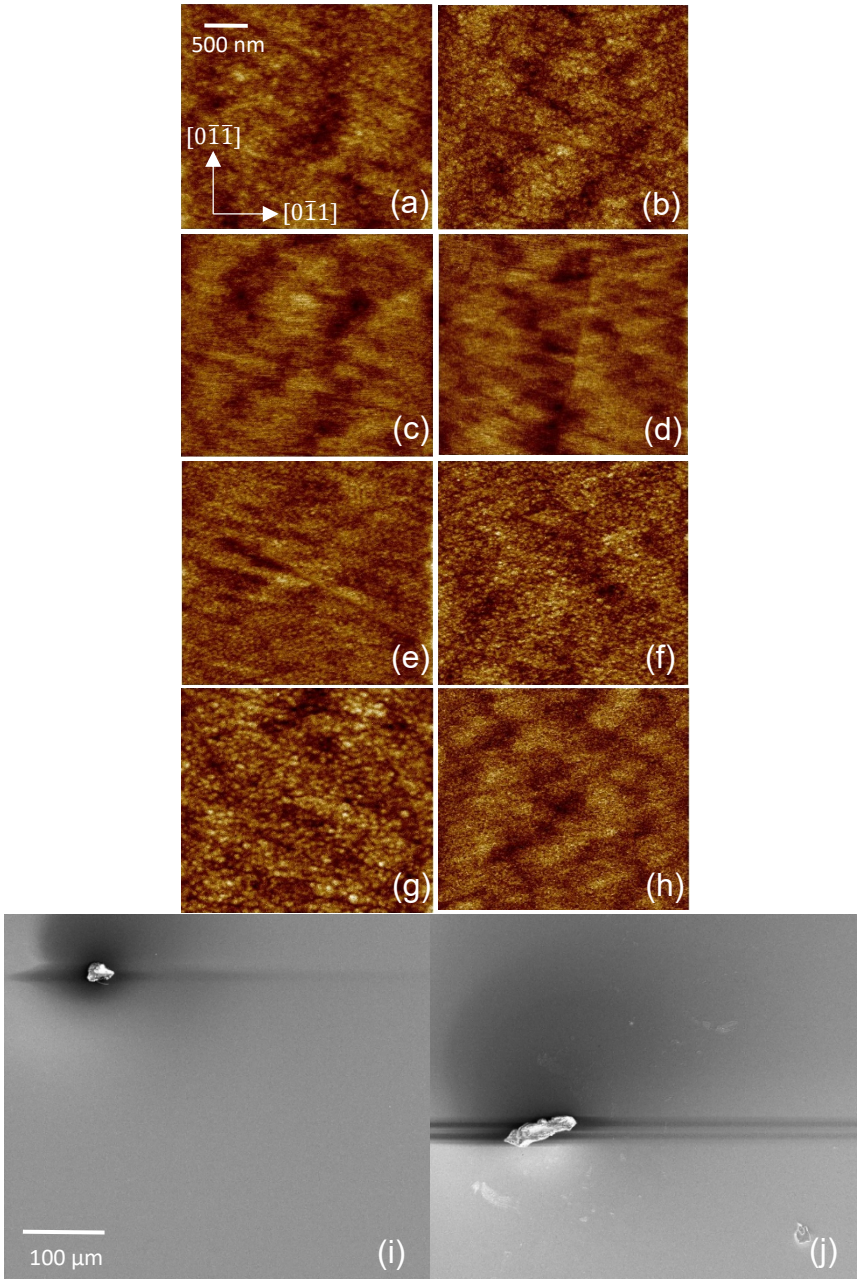

Figure 5.7 AFM images for the Bi flux series and N flux series are presented in (a)-(d) and (e)-(h) respectively. For both the Bi and N flux series, the surfaces appear featureless, with rms roughness <0.5nm, consistent with observations of layer-by-layer growth of GaAsN. To confirm the absence of µm-sized surface droplets, 400 µm x 500 µm SEM images were also collected, as shown in (i)-(j). The images include features associated with dust, in order to demonstrate the suitable focus condition. Indeed, in the well-focused condition, the surface is featureless, without the presence of surface droplets.

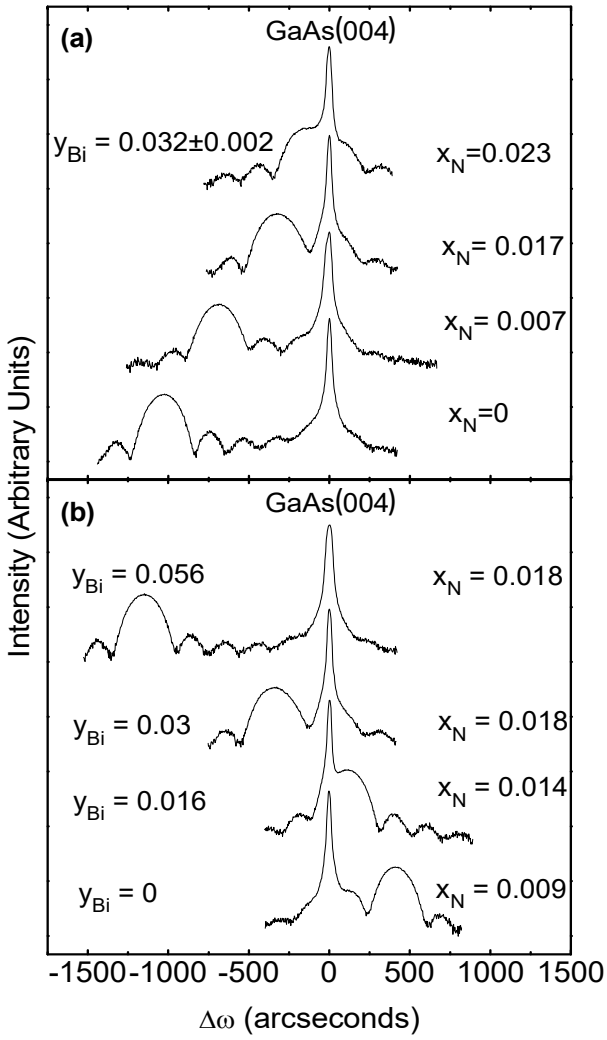

Figure 5.8 (004) High-resolution x-ray rocking curves for the (a) N flux series with *x* ranging from 0 to 0.023 and (b) Bi flux series with *y* ranging from 0 to 0.056. For all plots, the GaAs substrate peak is set to $\Delta\omega = 0$ arcseconds, thereby facilitating comparison of $\Delta\omega$ between the GaAs substrate and the GaAsNBi epilayers. Within the N flux series, *y* remains fixed as *x* is increased. However, within the Bi flux series, x increases as *y* increases, suggesting a Bi-induced enhancement of N incorporation. The two highlighted rocking curves in (b) are an example pair of XRC data used to determine the "magic" N:Bi ratio for lattice-matching of GaAsNBi with GaAs. (Copyright 2017, AIP Publishing LLC).

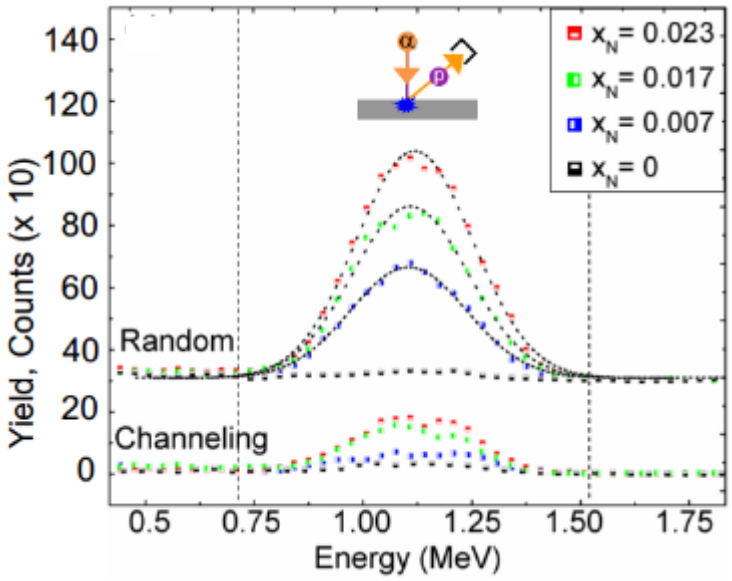

Figure 5.9 Measured NRA yield versus emitted particle energy for the N flux series. The vertical dashed lines indicate the energy window of the protons emitted during the $^{14}N(\alpha,p)^{17}O$ reaction. As the N flux increases, the resulting N signal increases. Non-channeling data are overlaid with SIMNRA fitted spectra assuming a uniform N depth profile. Fitted Gaussian-shape spectra suggest uniform N incorporation throughout the GaAsNBi film. (Copyright 2017, AIP Publishing LLC).

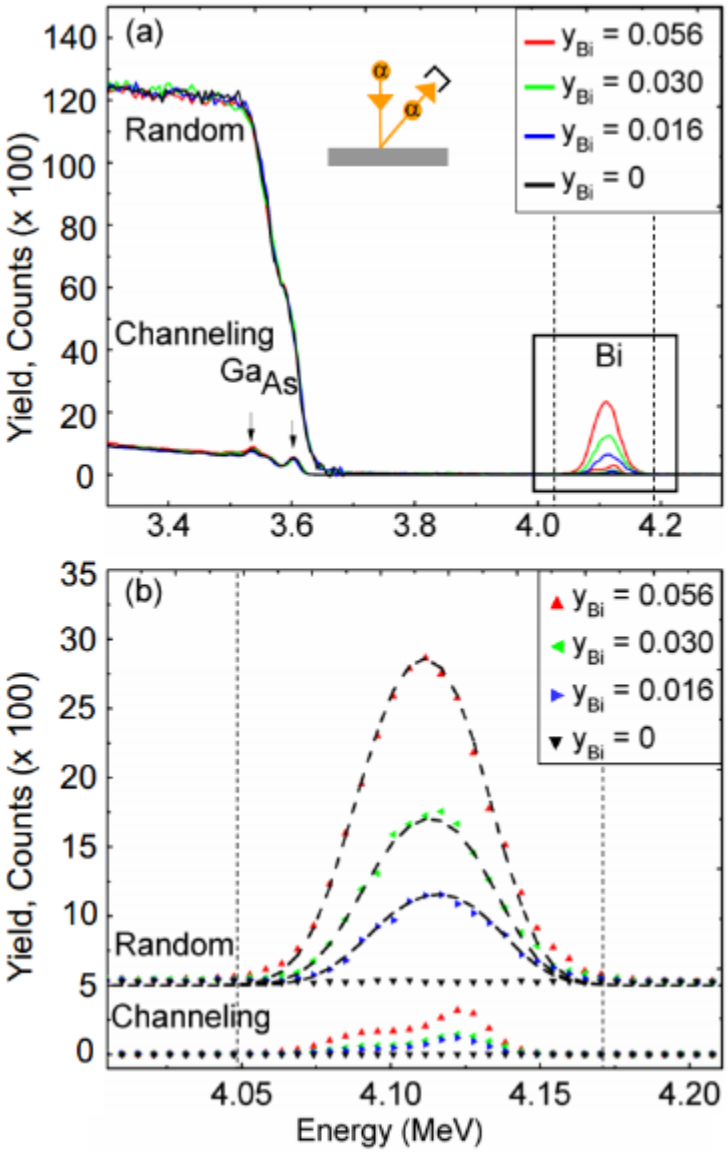

Figure 5.10 (a) Measured RBS yield versus backscattered particle energy for Bi flux series samples plotted in yield versus energy. The vertical dashed lines indicate the energy window of backscattered ions from Bi atoms. As the Bi flux increases, the resulting Bi signal increases. The portions of the RBS spectra enclosed in the box in (a) are shown in (b). Non-channeling data are overlaid with SIMNRA fitted spectrum assuming uniform Bi depth profile. Fitted Gaussian-shape spectra suggest uniform Bi incorporation throughout the GaAsNBi film. (Copyright 2017, AIP Publishing LLC).

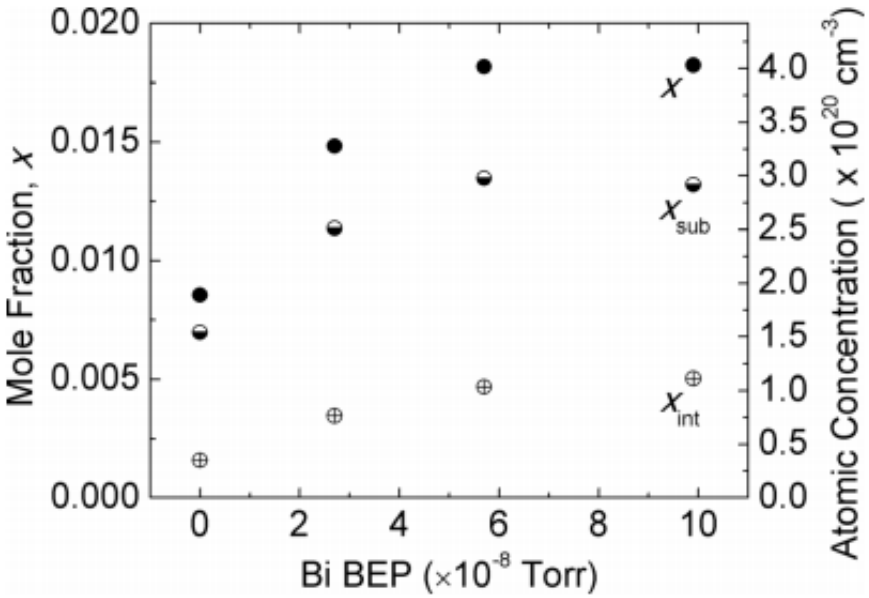

Figure 5.11 Mole fractions of total x, substitutional x_{sub}, and interstitial x_{int} for the Bi flux series of GaAsN(Bi) films, determined by channeling and non-channeling nuclear reaction analysis. The atomic concentrations corresponding to the mole fractions are shown on the right y-axis. Both x and x_{int} increase with Bi flux, suggesting a Bi-induced enhancement of N incorporation, with preferential incorporation in interstitial sites. (Copyright 2017, AIP Publishing LLC).

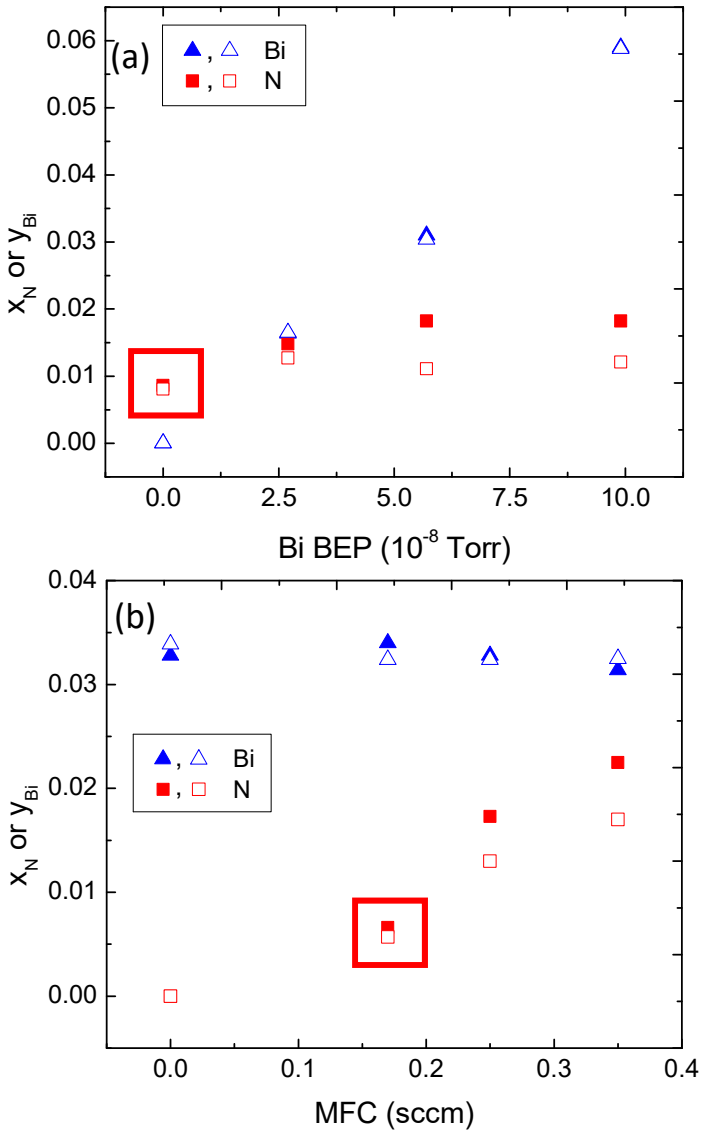

Figure 5.12 x_N or y_{Bi} values determined from RBS (solid symbol), NRA (solid symbol), and XRC (open symbol) are plotted. (a) Bi BEP for the Bi flux series and (b) N MFC for the N flux series. In both cases, the RBS and XRC-determined values of y_{Bi} agree to within <0.1%. Furthermore, for $x_N < 0.01$ the NRA and XRC-determined values of x_N also agree to within <0.1%. However, as the values of x_N exceed 0.01, including those in the N and Bi flux series, the NRA and XRC-determined values of x_N begin to deviate by in excess of 0.5%. Since the XRC data analysis considers only substitutional N incorporation, the higher x_N values for $x_N > 0.01$ obtained from the NRA data analysis are attributed to the presence of N interstitial complexes. The two data points for $x_N < 0.01$, enclosed in a red box for both the (a) Bi and (b) N flux series are expected to contain a negligible fraction of N interstitial complexes, as will be further discussed in Section 5.6.

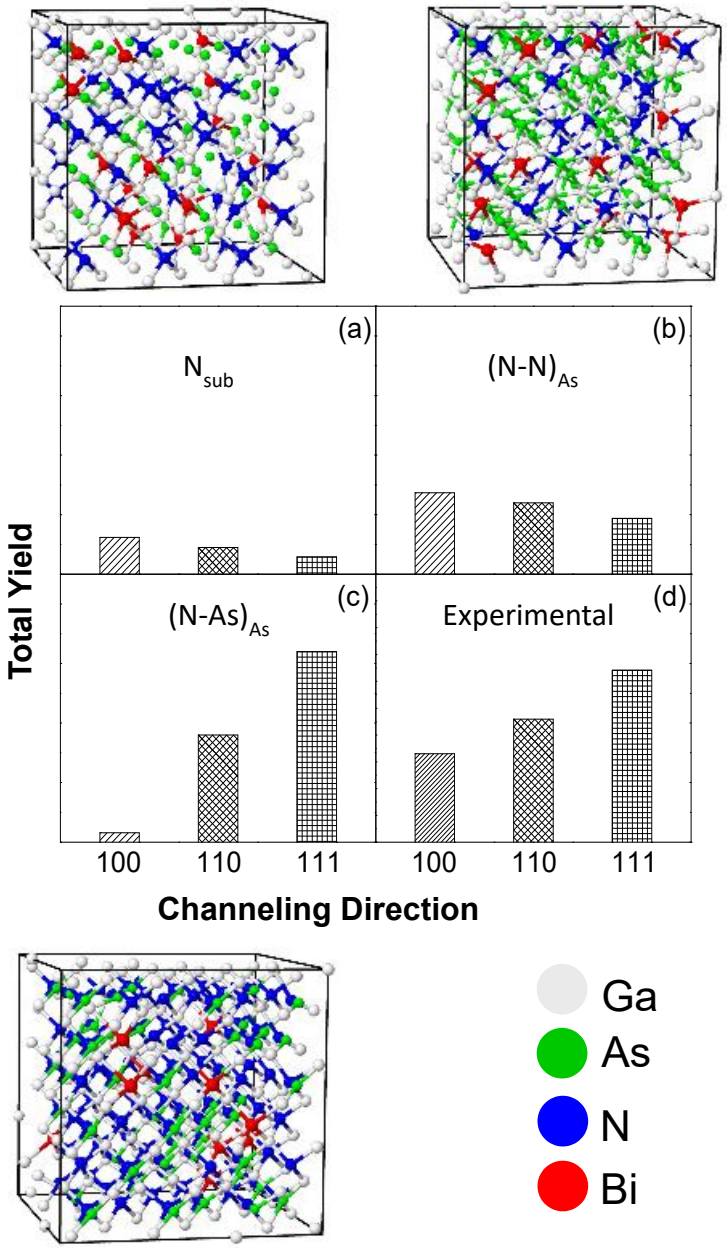

Figure 5.13 Total simulated NRA yields in the [100], [110], and [111] directions for (a) N_{Sub}, (b) $(N\text{-}N)_{As}$, and (c) $(N\text{-}As)_{As}$. (d) Measured total NRA yield in each channeling direction. Similar yield trends of $Y_{[111]} > Y_{[110]} > Y_{[100]}$ are observed for (c) and (d), suggesting that $(N\text{-}As)_{As}$ is the dominant interstitial complex in GaAsN alloys. 3x3x3 unit cell of GaAsNBi with N-to-Bi incorporation ratio of 1-to-2 are used for these simulations. White is gallium, green is arsenic, blue is nitrogen, and red is bismuth. Within each cell, each N is positioned at the center of the group V site as either substitutional N, N_{As}; $(N\text{-}N)_{As}$, with N_2 aligned along the [111] direction; or $(N\text{-}As)_{As}$, with the N-As pair aligned along the [010] direction. (Copyright 2017, AIP Publishing LLC).

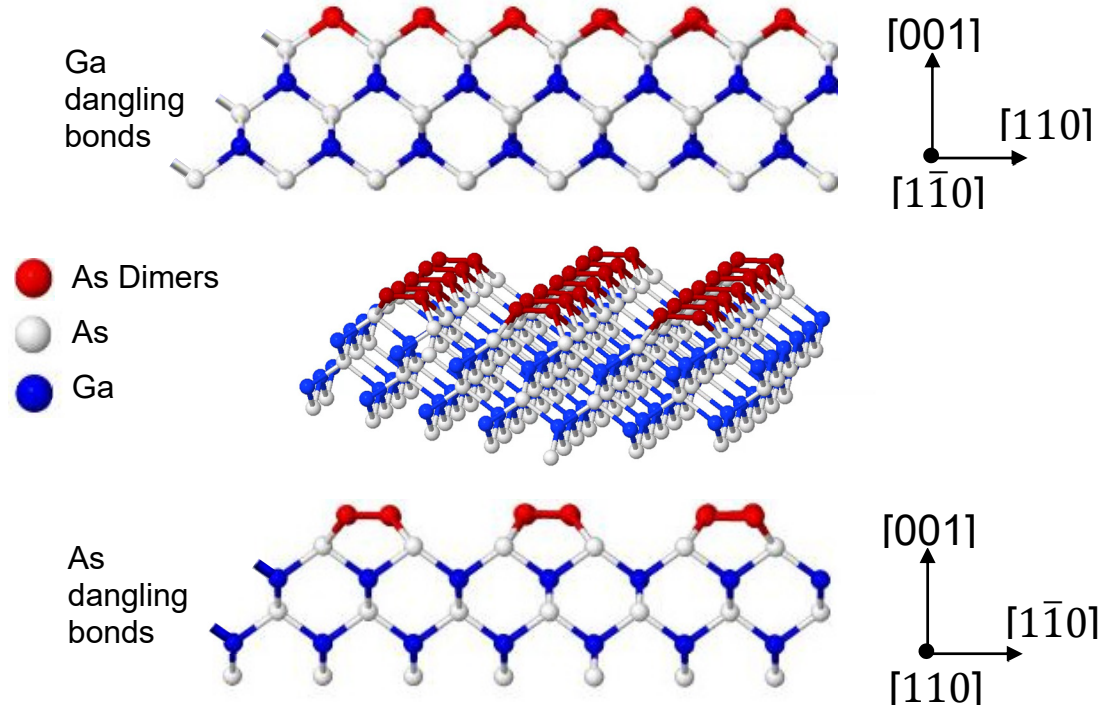

Figure 5.14 Schematic of a reconstructed surface with As dimers and Ga/As dangling bonds along different directions. The [110] step edge consists of As dangling bonds, such that a N atom incorporating on a [110] step edge would have an increased likelihood of forming a $(N\text{-}As)_{As}$ interstitial complex. As the step edge density changes with the introduction of Bi, the RHEED reconstruction pattern changes from (2x4) to (1x3) or (4x3).

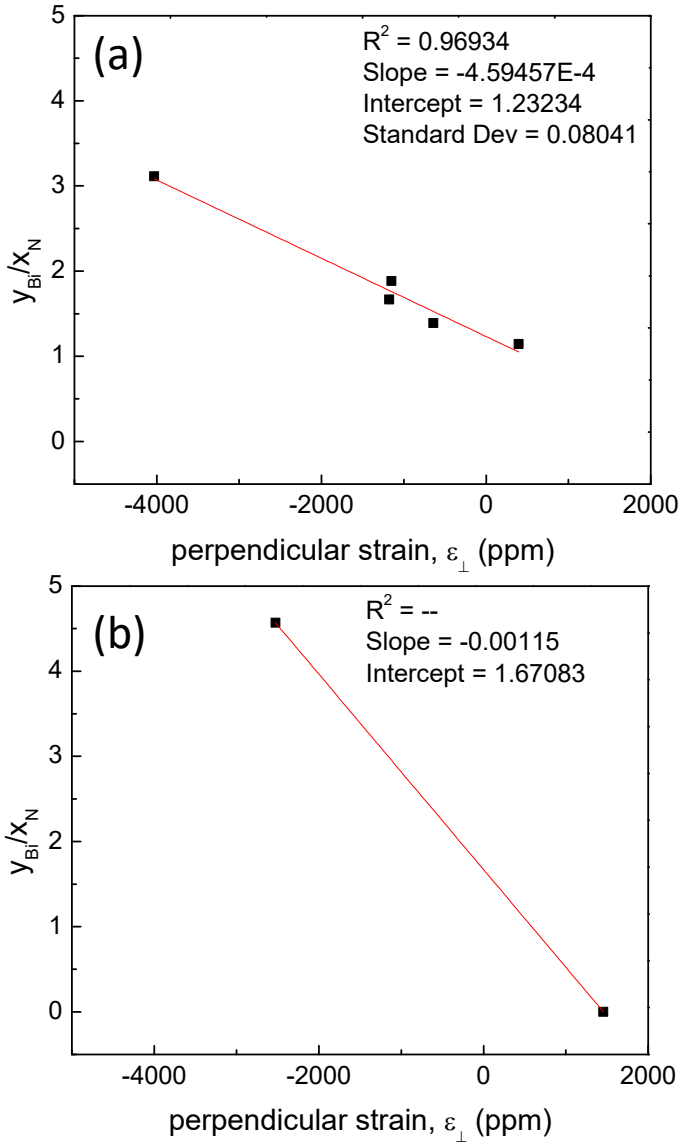

Figure 5.15 Plots of $\frac{y_{Bi}}{x_N}$ obtained from RBS and NRA data verses the perpendicular strain, $\varepsilon_\perp$, obtained from XRC data analyzed using the small angle approximation, as described in Section 2.6. We use a linear least-square fit to extract the $\frac{y_{Bi}}{x_N}$ value at which $\varepsilon_\perp = 0$. In (a), we include data from all films which contain a non-negligible fraction of interstitial N complexes; the "magic" ratio for lattice matching with GaAs is $[Bi] = 1.23 \pm 0.04[N]$. In (b), we include only those data from films with a negligible fraction of interstitial complexes; the "magic" ratio for lattice-matching with GaAs is $[Bi] = 1.67[N]$, consistent with theoretical predictions assuming solely substitutional N incorporation $[Bi] = 1.7[N]$.[50,51]

5.9 References

[1] A. Erol, editor , *Dilute III-V Nitride Semiconductors and Material Systems* (Springer Berlin Heidelberg, Berlin, Heidelberg, 2008).

[2] S.R. Kurtz, A.A. Allerman, C.H. Seager, R.M. Sieg, and E.D. Jones, Appl. Phys. Lett. **77**, 400 (2000).

[3] E.V.K. Rao, A. Ougazzaden, Y. Le Bellego, and M. Juhel, Appl. Phys. Lett. **72**, 1409 (1998).

[4] A. Janotti, S.H. Wei, and S.B. Zhang, Phys. Rev. B **65**, 115203 (2002).

[5] A. Mascarenhas, U.S. Patent No. 6,815,736 (9 November 2004).

[6] S. Tixier, M. Adamcyk, T. Tiedje, S. Francoeur, A. Mascarenhas, P. Wei, and F. Schiettekatte, Appl. Phys. Lett. **82**, 2245 (2003).

[7] Z. Batool, K. Hild, T.J.C. Hosea, X. Lu, T. Tiedje, and S.J. Sweeney, J. Appl. Phys. **111**, 113108 (2012).

[8] F. Dimroth, A. Howard, J.K. Shurtleff, and G.B. Stringfellow, J. Appl. Phys. **91**, 3687 (2002).

[9] Z.L. Bushell, P. Ludewig, N. Knaub, Z. Batool, K. Hild, W. Stolz, S.J. Sweeney, and K. Volz, J. Cryst. Growth **396**, 79 (2014).

[10] S. Tixier, M. Adamcyk, E.C. Young, J.H. Schmid, and T. Tiedje, J. Cryst. Growth **251**, 449 (2003).

[11] E.C. Young, S. Tixier, and T. Tiedje, J. Cryst. Growth **279**, 316 (2005).

[12] T. Liu, S. Chandril, A.J. Ptak, D. Korakakis, and T.H. Myers, J. Cryst. Growth **304**, 402 (2007).

[13] P. Wei, M. Chicoine, S. Gujrathi, F. Schiettekatte, J-N. Beaudry, R. A. Masut, and P. Desjardins. J. Vac. Sci. Technol., A, **22.3** 908 (2004)

[14] K.M. Yu, M. Kaminska, and Z. Liliental-Weber. J. Appl. Phys., **72**, 2850 (1992).

[15] S.B. Zhang and S.-H. Wei, Phys. Rev. Lett. **86**, 1789 (2001).

[16] W. Bennarndt, G. Boehm, and M.-C. Amann, J. Cryst. Growth **436**, 56 (2016).

[17] R.L. Field, J. Occena, T. Jen, D. Del Gaudio, B. Yarlagadda, C. Kurdak, and R.S. Goldman, Appl. Phys. Lett. **109**, 252105 (2016).

[18] M. Reason, H.A. McKay, W. Ye, S. Hanson, R.S. Goldman, and V. Rotberg, Appl. Phys. Lett. **85**, 1692 (2004).

[19] T. Jen., G. Vardar, Y. Q. Wang, and R. S. Goldman. Appl. Phys. Lett. **107**, 22 (2015)

[20] P. Wei, M. Chicoine, S. Gujrathi, F. Schiettekatte, J-N. Beaudry, R. A. Masut, and P. Desjardins. J. Vac. Sci. Technol., A, **22.3** 908 (2004)

[21]M. Mayer., W. Eckstein, H. Langhuth, F. Schiettekatte, and U. von Toussaint. Nucl. Instrum. Meth. B **269**, 24 (2011)

[22] R. L. Field, J. Occena, T. Jen, D. Del Gaudio, B. Yarlagadda, C. Kurdak, and R. S. Goldman, Appl. Phys. Lett. 109, 252105 (2016).

[23] R.L. Field, Ph.D. thesis, Ch. 4. University of Michigan, 2015.

[24] X. Liu, A. Prasad, J. Nishio, E. R. Weber, Z. Liliental-Weber, and W. Walukiewicz, Appl. Phys. Lett. 67, 279 (1995)

[25] R. L. Field, J. Occena, T. Jen, D. Del Gaudio, B. Yarlagadda, C. Kurdak, and R. S. Goldman, Appl. Phys. Lett. 109, 252105 (2016).

[26] J. Betko, P. Kordos, S. Kuklovsky, A. F€orster, D. Gregusova, and H. L€uth, Mater. Sci. Eng. B 28, 147 (1994).

[27] S. O'Hagan and M. Missous, J. Appl. Phys. 75, 7835 (1994).

[28] N. Jeon, B. Loitsch, S. Morkoetter, G. Abstreite, J. Finley, H.J. Krenner, G. Koblmueller and L.J. Lauhon ACS nano, 9(8), 8335-8343 (2015).

[29] N. Dawahre, G. Shen, S.N. Renfrow, S.M. Kim P. Kung, J. Vac. Sci. 31, 041802 (2003).

[30] J.S. Blakemore, J. Appl. Phys. *53*, 121 (1982).

[31] M. Reason, N.G. Rudawski, H.A. McKay, X. Weng, W. Ye, and R.S. Goldman, J. Appl. Phys. Lett. **101**, 083520 (2007)

[32] W.K. Cheah, W.J. Fan, S.F. Yoon, S.Z. Wang and W.K. Loke, J. Appl. Phys. **94**, 3828 (2003).

[33] M. Reason, Ph.D. thesis, Ch. 2. University of Michigan, 2006.

[34] J.R. Tesmer and M.A. Nastasi, *Handbook of Modern Ion Beam Materials Analysis* (Materials Research Society, 1995).

[35] S. Spruytte, M. Larson, W. Wampler, C. Coldren, H. Petersen, and J. Harris, J. Cryst. Growth **227**–**228**, 506 (2001).

[36] P. Wei, S. Tixier, M. Chicoine, S. Francoeur, A. Mascarenhas, T. Tiedje, and F. Schiettekatte. Nucl. Instr. Methods B 219, 671 (2004).

[37] P. Carrier, S.-H. Wei, S. B. Zhang, and S. Kurtz, Phys. Rev. B **71**, 165212 (2005).

[38] K. Laaksonen, H.-P. Komsa, T. T. Rantala, and R. M. Nieminen, J. Phys. Condens. Matter **20**, 235231 (2008).

[39] S.B. Zhang and S.H. Wei, Phy. Rev. Lett. **86**, 1789 (2001).

[40] E. Arola, J. Ojanen, H.-P. Komsa and T. T. Rantala, Phys. Rev. B **72**, 045222 (2005).

[41] G. Ciatto, P. Alippi, A. Amore Bonapasta, and T. Tiedje. Appl. Phys. Lett **99**, 14 (2011).

[42] F. Ishikawa, S. Fuyuno, K. Higashi, M. Kondow, M. Machida, H. Oji, J.-Y. Son, A. Trampert, K. Umeno, Y. Furukawa, and A. Wakahara, Appl. Phys. Lett **98**, 121915 (2011).

[43] K.M. Kim, W.-B. Kim, D. Krishnamurthy, J.H. Ryu, S. Hasegawa, and H. Asahi, J. Cryst. Growth **368**, 35-38 (2013).

[44] J. Chen, G. Ciatto, M. Le Du, J.C. Harmand and F. Glas, Phys. Rev. B **82**, 125303 (2010).

[45] H.T. Pham, S.F. Yoon, K.H. Tan and D. Boning. Appl. Phys. Lett **99**, 092115 (2010).

[46] H.P Nair, A.M. Crook, K.M. Yu and S.R. Bank. Appl. Phys. Lett **100**, 021103 (2012).

[47] J. Buckeridge, D.O. Scanlon, T.D. Veal, M.J. Ashwin, A. Walsh and C.R.A. Catlow. Phys. Rev. B **89**, 014107 (2014).

[48] M. Pashley, K. Haberern, and J. Gaines, J. Vac. Sci. Technol., B **9**, 938 (1991).

[49] A. Duzik, J.C. Thomas, J.M. Millunchick, J. Lång, M.P.J. Punkkinen, and P. Laukkanen, Surf. Sci. **606**, 1203 (2012).

[50] A. Janotti, S.-H. Wei, and S. Zhang, Phys. Rev. B 65, 115203 (2002).

[51] M. Yoshimoto, W. Huang, and K. Oe, MRS Proceedings 829, 845 (2004).

Chapter 6

Summary and Suggestions for Future Work

6.1 Summary

In this dissertation work, we examined solute incorporation into GaAsN and GaAsNBi alloys, using a combined computational-experimental approach. We considered the influence of both growth parameters and post-growth RTA on the alloy stoichiometry and interstitial complex formation and dissociation. We also examined the influence of co-incorporation of Bi and N and identified the "magic ratio" for lattice matching to GaAs. Finally, we identified the possible mechanisms for the dissociation of $(N\text{-}N)_{As}$ interstitial complexes during RTA.

In Chapter 3, our combined computational-experimental approach to identify the dominant interstitial complex in GaAsN is presented. For this purpose, we compared channeling NRA and RBS data with MC-MD simulations along the [100], [110], and [111] directions. For the simulations, we assume that $(N\text{-}N)_{As}$ is aligned along the [111] direction, while $(N\text{-}As)_{As}$ is aligned along the [010] direction. Since the channeling NRA data have the highest (lowest) yields in the [111] ([100]) directions, similar to the computed trends

for the $(N\text{-}As)_{As}$ interstitial complex, we conclude that $(N\text{-}As)_{As}$ is the dominant interstitial complex in GaAsN.

In Chapter 4, our studies of the influence of RTA on the structure of GaAsN films were presented. Using the combined computational-experimental approach from Ch. 3, we examined the film stoichiometry and stability of the dominant interstitial complexes. In as-grown GaAsN films, the presence of N interstitial complexes is observed with NRA, with the presence of $(N\text{-}N)_{As}$ confirmed by Raman spectroscopy. Following RTA, although the film stoichiometry is maintained, with minimal N out-diffusion, the fraction of $(N\text{-}N)_{As}$ interstitial complexes is reduced, presumably due to dissociation of $(N\text{-}N)_{As}$ into N_{sub} and $(N\text{-}As)_{As}$ interstitials. It has been suggested that the improved electronic performance of GaAsN following RTA is due to the disappearance of $(N\text{-}N)_{As}$ interstitial complex. Here, we have identified the possible $(N\text{-}N)_{As}$ dissociation mechanisms in GaAsN which may enable the elimination of the RTA steps typically needed to improve the properties of GaAsN and related alloys. These finding are likely to be applicable to other dilute nitride alloys which contain significant fractions of $(N\text{-}N)_{As}$ interstitial complexes.

In Chapter 5, our investigations of the molecular-beam epitaxial growth, stoichiometry, and solute incorporation into GaAsNBi alloys was presented. Our combined XRD, RBS, and APT studies suggest that the GaAsNBi alloys are stoichiometric, with minimal excess arsenic incorporation. We demonstrate that Bi incorporation into GaAsNBi is independent of N flux. However, N incorporation into GaAsNBi, including the fraction of N occupying non-substitutional sites, increases with Bi flux. The Bi flux increase leads to a transition in surface reconstruction from (2x4) to (1x3). Since the GaAsBi (1x3) surface has been reported to contain a high density of [110]-oriented step edges, with As-

dangling bonds, we consider their role in the enhancement of both the total N content and the fraction of N interstitials, especially through enhancing the formation of $(N\text{-}As)_{As}$. Finally, our NRA, RBS, and XRD data suggest a "magic ratio" for lattice matching with GaAs, of $[Bi] = (1.23 \pm 0.04)\,[N]$, much lower than the predicted value of $[Bi] \approx 1.7[N]$, for which substitutional incorporation of all N was assumed. This insight provides a pathway to tailoring the N incorporation and lattice-matching of GaAsNBi and related alloys.

6.2 Interstitial Complexes Positions: Angular Yield Profile

To determine the precise interstitial complex positions, for comparison with DFT calculations in the literature, angular-channeling scans are suggested. Following the channeling alignments described in Appendix D, an angular yield profile may be obtained, as illustrated in Fig. 6.1. Using this technique, it is possible to detect the narrowing of the channel due to lattice distortion. In addition, if there are interstitial atoms that reside in the channel itself, these atoms will obstruct channeling and induce "flux peaking", a sudden increase in the detected backscattered signals, as illustrated in Fig. 6.2.[1]

6.3 Determining GaAsNBi Stoichiometry

To determine if isovalent co-alloying of GaAs with two anions (Bi, N) is limited to the replacement of As by the anions, we initially considered using RBS data. However with RBS, the Ga and As signals from the epilayer and substrate overlap, as shown for the

GaAsNBi/GaAs RBS data in the random spectra in Fig. 5.10(a) and simulated spectrum in Fig. 6.4. We then attempted to use LEAP, as discussed in Section 5.4, but multiple charge states associated with elemental vs. molecular evaporation of arsenic and the composition-dependent local E-field experienced by the tip prevented quantification of the GaAsNBi III/V stoichiometry. Here, we propose additional LEAP experiments using special algorithms available in the LEAP 5000HS, as well as additional ion beam techniques that may be possible at LANL, and additional LEAP experiments using special algorithms available in the LEAP 5000HS.

6.3.1 Time-Of Flight Elastic Recoil Detection Analysis

To determine the fractions of Ga and As in GaAsNBi and related alloys, we propose to use time-of-flight elastic recoil detection analysis (ToF-ERDA).[2,3] This ToF-ERDA is similar to LEAP, except it uses heavy ions such as carbon or chlorine to "knock off" atoms from the sample of interest, which are then collected by silicon surface barrier detector. Since ToF-ERDA does not involves applied voltages (in contrast to LEAP, which involves 2000-6000V), multi-charged ions are not present. Therefore, ToF-ERDA is expected to enable the identification of Ga and As signals with depth resolution ~2-5nm, allowing for quantification of the Ga and As fractions in both the films and substrate.

6.3.2 RBS at higher Energies

As shown in Fig 6.3, using a heavier ion species (e.g. C rather than α) and ion energies ranging from 3 MeV to 5 Mev, SIMNRA simulations predict that the Ga and As signals would be resolved with RBS. However, due to the backscattered high-energy high-mass ion, the detection resolution of a silicon-based detector is expected to decline, leading eventually to detector failure. Instead, the author suggests an alternative approach for signal detection, namely, a gas ionization chamber (GIC) detector, which relies upon the ionization of noble gases.[4,5]

If a GIC detector is not available, another approach would be to use a higher α beam energies to probe samples following the removal (via etching) of the GaAs substrate. As shown in the SIMNRA simulations in Fig. 6.4, if the substrate is removed and the incident α particle energy is increased to in excess of 4 MeV, the Ga and As signals are expected to be individually resolved. Prior to removal of the GaAs substrate, the author suggests lithographically patterning the backside (following growth) to form a 5 mm x 5 mm square that enables the transmission of the ion beam. For this purpose, the samples would need to be grown with a buried AlAs etch stop layer, as described in Ref. 6 and 7.[6,7]

6.3.3 Controlling Local Electric Field

During a LEAP experiment, each atom experiences $\vec{E} = \frac{V}{kr}$, where V is the applied voltage, r is the radius of the tip, and k is a unit-less factor relating the geometries of the tip and the detector.[8] Typically, the variations in field experienced by the tip are accounted

for in the data analysis process, specifically during tip reconstruction. However, the E-field experienced by the tip varies with local atomic compositions as each layer is evaporated. Therefore, following the LEAP experiment, it is not possible to distinguish As_2^{++}vs As^+. We attempted to use the constant peak ratio function to fix the Ga^+ to Ga^{++} charge state ratio during a LEAP experiment on a GaAs layer with a known 1:1 Ga:As ratio. However, as the LEAP experiment progressed across the GaAsNBi/GaAs interface, significant composition-dependent Ga^+ to Ga^{++} ratios were apparent. Thus, further LEAP studies are needed to identify the LEAP conditions that enable fixed local electric fields across the GaAsNBi/GaAs interfaces.

6.4 Tailoring the Structure and Properties of GaAsNBi

In this thesis, we have made substantial progress in understanding N interstitial complex formation in GaAsN; these findings open up new opportunities for tailoring the structure and properties of GaAsN alloys. In Chapter 3, we showed that $(N\text{-}As)_{As}$ is the dominant interstitial complex in GaAsN. In Chapter 4, we suggested $(N\text{-}As)_{As}$ pairs are formed preferentially at [110]-oriented step edges, which contain As dangling bonds. In Chapter 5, we showed that $(N\text{-}N)_{As}$ interstitial complexes are dissociated into $(N\text{-}As)_{As}$ and N_{sub} during RTA. Together, these findings provide a path way to tailor the structure and properties of GaAsN and related alloys. In literature reports, it has been shown that RTA induces improvement in PL efficiency and electron mobilities of GaAsN and related alloys. Based upon our combined computational-experimental investigations in Ch. 3-5, we hypothesize that $(N\text{-}N)_{As}$ interstitial complexes are the chief "culprits" while $(N\text{-}As)_{As}$

complexes are not. Since the [110] step-edges, with As dangling bonds, appear to enhance the incorporation of $(N\text{-}As)_{As}$ interstitial complexes, we suggest the growth of GaAsN(Bi) alloys with a high density of [110] step-edges, namely (111)B offcut substrates, along with studies of their optoelectronic properties. Indeed, it may be possible to grow GaAsNBi alloys with high PL intensities and high electron mobilities without post-growth thermal annealing.

6.5 Influence of RTA on GaAsNBi

To examine the effects of RTA on the structure of GaAsNBi, several of the samples discussed in Ch. 4 were also annealed at LANL. However, due to the indium on the backside of the GaAsNBi samples, indium droplets was formed on the surfaces of the GaAsNBi epilayers, as shown in Fig. 6.5. The subsequent NRA/RBS measurements showed low quality channeling measurements with $\chi_{min} > 10\%$, whereas good channeling measurements would yield $\chi_{min} < 6\%$.[9] In addition, as shown in the XRC in Fig. 6.6, an additional phase is observed following RTA, likely due to In diffusion into the GaAsNBi layer. Furthermore, as shown in the Raman spectroscopy data in Fig. 6.7, in addition to the vibrational signatures observed in as-grown GaAsNBi, an additional signature associated with InAs is observed post-RTA, further suggesting the In diffusion into the layers.[10] RTA is commonly used for Bi-free dilute nitride alloys to improve the optical properties.[11,12,13,14,15,16] However, RTA has been reported to lead to alloy phase separation in GaAsBi.[17,18,19] Therefore, further studies on the effects of RTA on GaAsNBi

alloys are suggested. For this purpose, removal of indium from the substrate backside, prior to RTA, is suggested.

6.6 Channeling Simulations for Wurtzite Crystals

To examine the incorporation of p-type dopants such as Mg, in GaN, we suggest adapting the MC-MD simulation code for wurtzite crystals.[20,21] As shown in Fig. 6.8, MG can be incorporated both substitutionally, as Mg_{Ga} or interstitially, as Mg_I. There have also been reports of additional Ga and/or N vacancy formation, depending on growth technique and post-growth annealing sequence.[22,23,24] For these studies, the author suggests the development of a script to construct a hexagonal crystal system using the cubic lattice vectors.

6.7 Figures

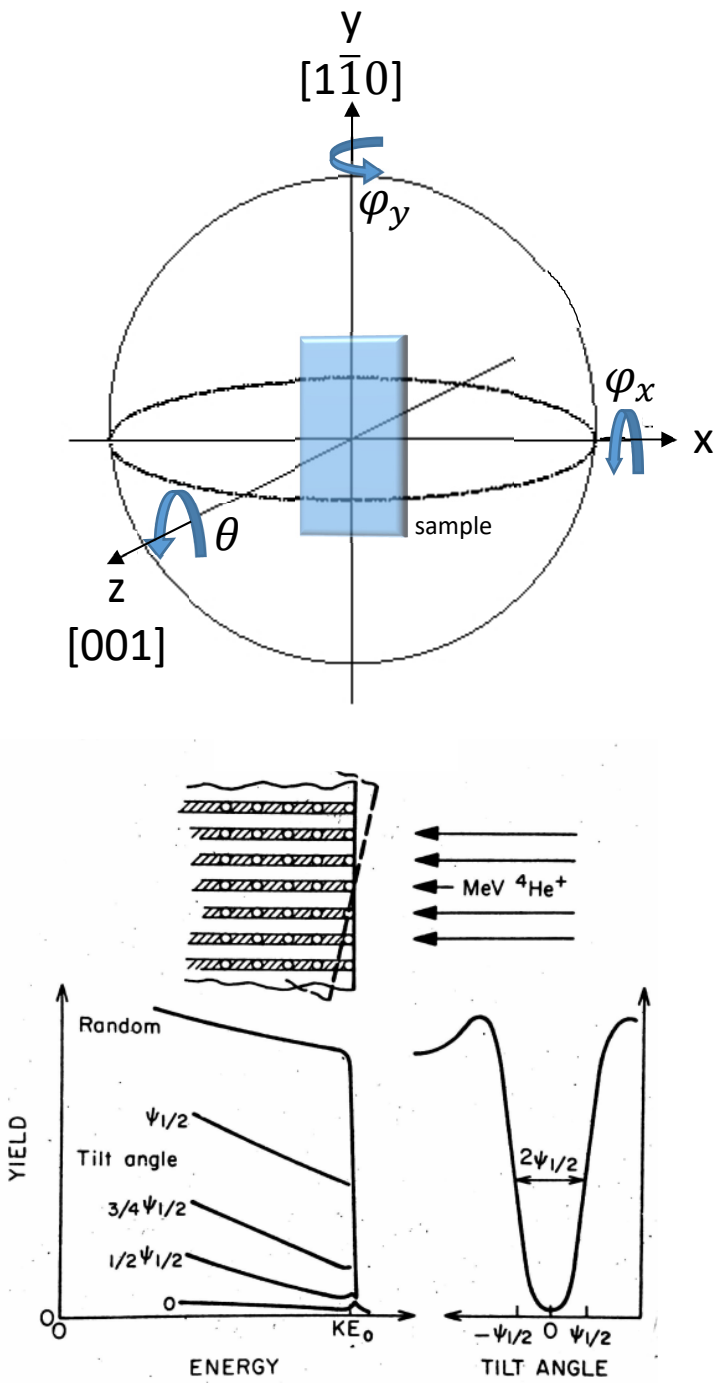

Figure 6.1 Random spectrum and aligned spectra at different tilt angles on the left. For a specific energy channel on the left, the yield is plotted as yield vs tilt angle as shown on the right, forming an angular yield profile. Adapted from Ref. 1. (Copyright 1978, Elsevier Books). The sample can be tilted in both φ_x or φ_y direction as shown above.

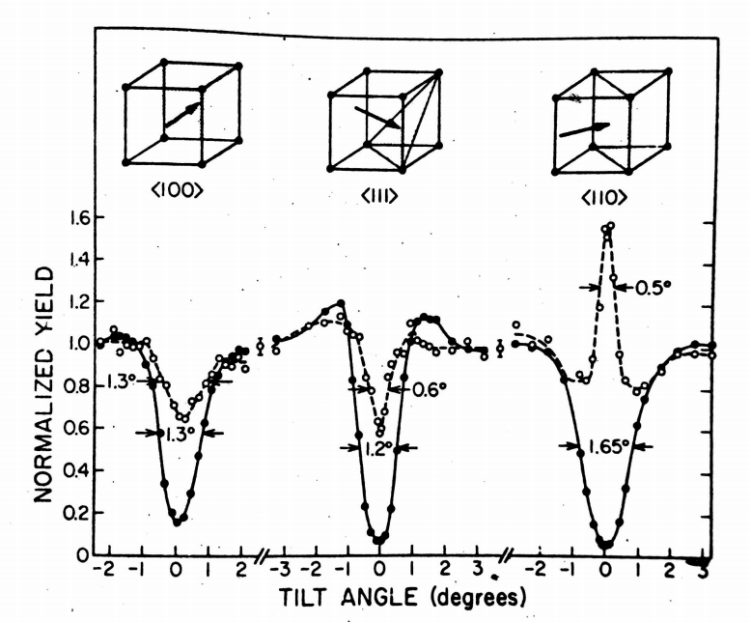

Figure 6.2 Angular yield profiles around the three principal axes of Yb-implanted silicon crystal. The solid lines are the Si signal and the dashed lines are the Yb signal yield profiles. As the Yb is detected, the yield increases, as shown for [110] direction. Adapted from Ref. 11. (Copyright 1978, Elsevier Books).

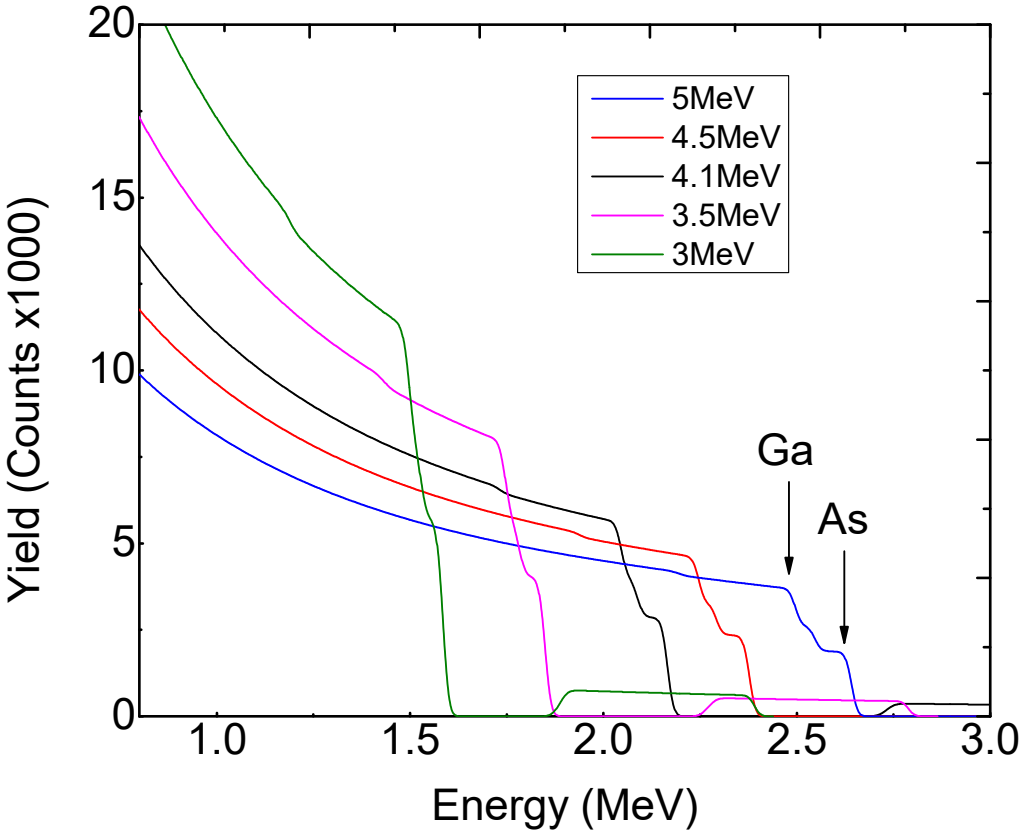

Figure 6.3 SIMNRA simulations of RBS for 100nm GaAsNBi films on GaAs using C ions, with beam energy ranging from 3 to 5 MeV. As the C ion beam energy is increased, the separation between Ga and As signal is predicted to be sufficient for quantification of Ga and As compositions.

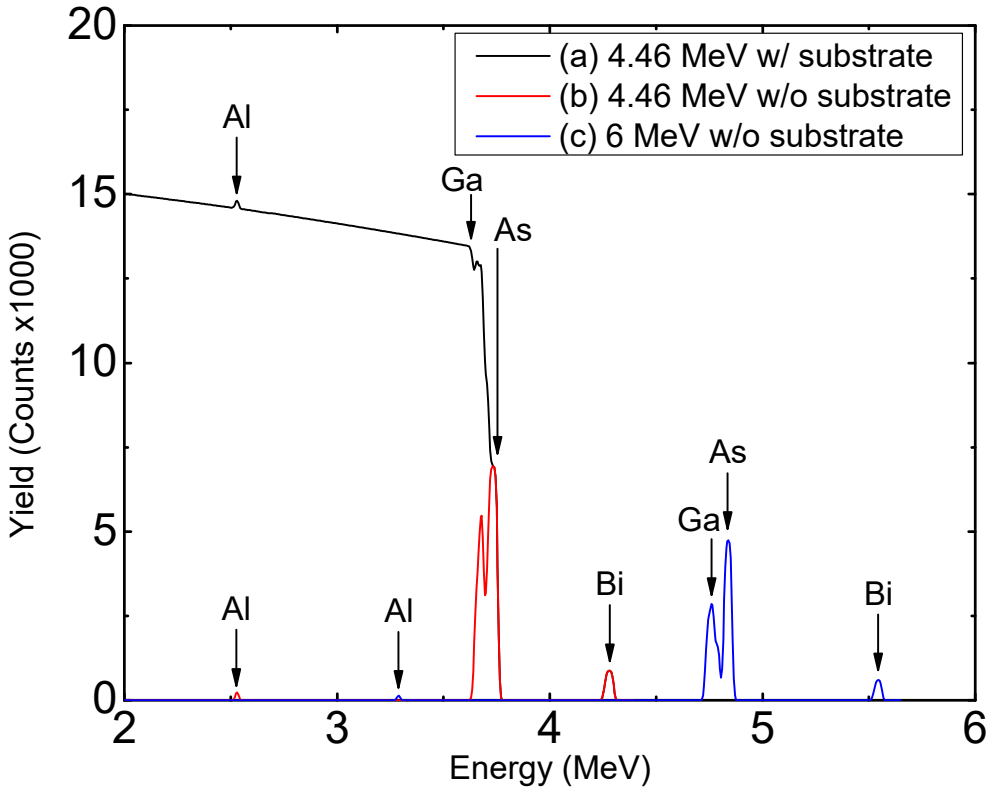

Figure 6.4 Comparison of three SIMNRA simulations of 100nm GaAsNBi films. (a) 4.46 MeV SIMNRA simulation of GaAsNBi/Alas/GaAs, (b) 4.46 MeV SIMNRA simulation of GaAsNBi/AlAs, and (c) 6 MeV SIMNRA simulation of GaAsNBi/AlAs. In (a), the Ga and As signals are not resolvable due to overlap with the substrate signals. In (b), the Ga and As signals are predicted to be partially resolved due to the absence of the substrate. In (c), the Ga and As signals are predicted to be fully resolved due to the higher energy incident α particles and the absence of the substrate.

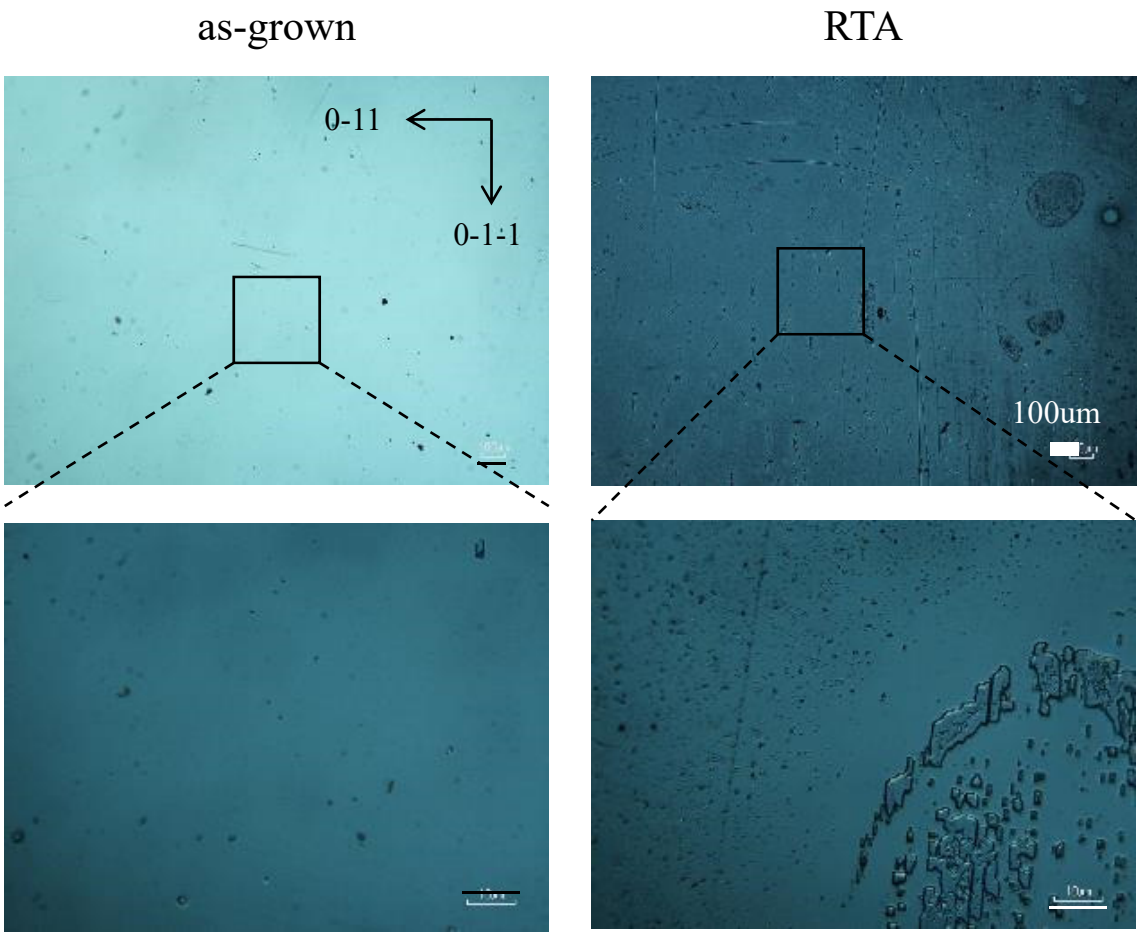

Figure 6.5 Nomarski images of the as-grown and post-RTA GaAsNBi surfaces. Post-RTA, the surface contains In droplets. It is likely that In also diffused into the film leading to higher RBS channeling yield, namely $\chi_{min} < 6\%$ vs. $\chi_{min} > 10\%$ for as-grown vs. post-RTA films, respectively.

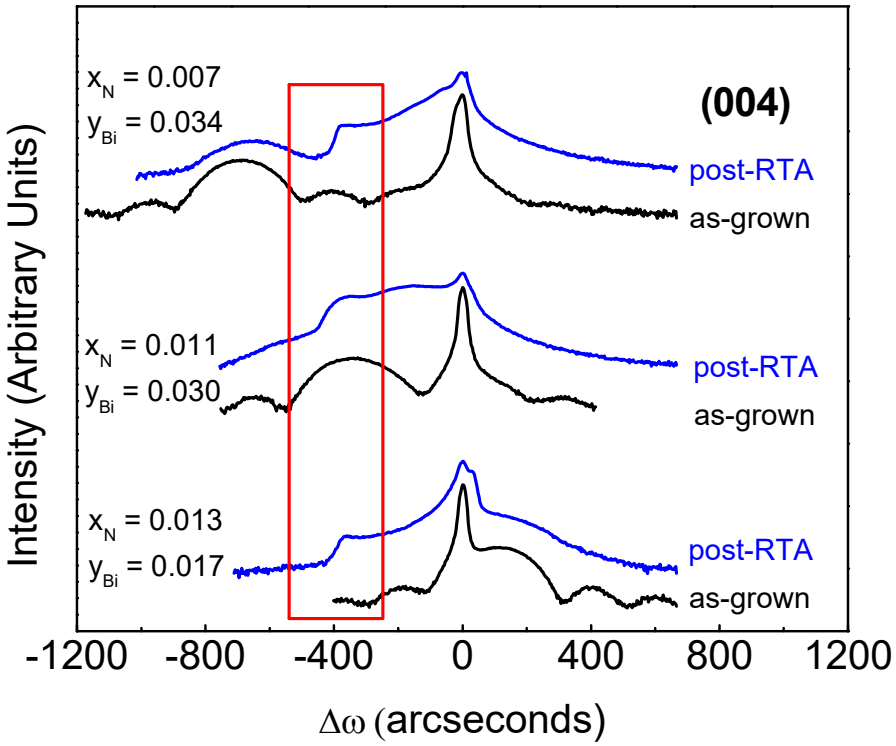

Figure 6.6 Plots of (004) XRC data for a series of as-grown and post-RTA GaAsNBi films with various y_{Bi} and x_N values. For all plots, the GaAs substrate peak position is set to $\Delta\omega = 0$ arcseconds. For all post-RTA films, an extra "shoulder" on the low angle side of the GaAs substrate peak is apparent. This artifact is likely due to In surface diffusion into the GaAsNBi film during the RTA process.

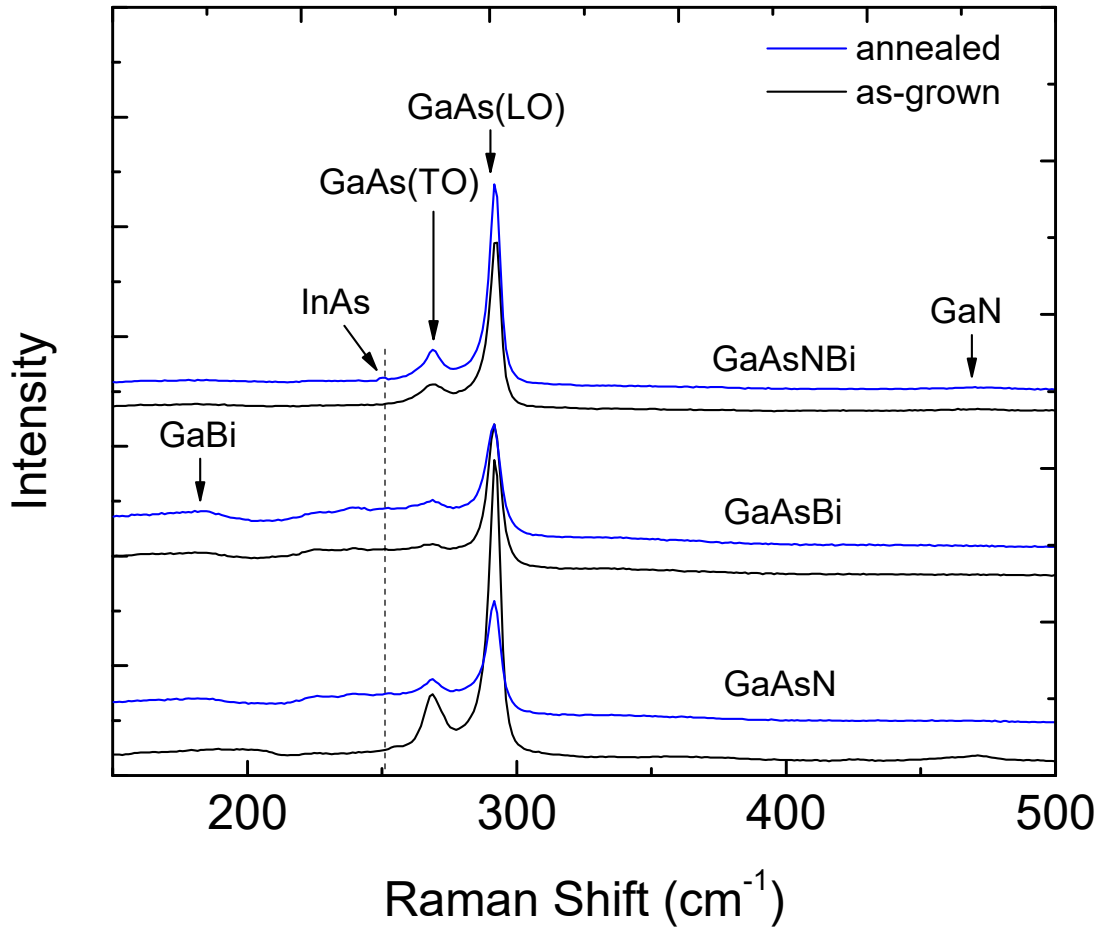

Figure 6.7 Plots of Raman spectroscopy of the post-RTA (blue) and as-grown (black) for GaAsN, GaAsBi, and GaAsNBi. For all as-grown and post-RTA films, several spectral features are apparent, including the ~$275cm^{-1}$ GaAs-like transverse-optical (TO) phonons and the ~ $290cm^{-1}$ GaAs-like longitudinal-optical (LO) phonons. In GaAsN and GaAsNBi, spectral features are also observed at ~$475cm^{-1}$, due to GaN-like LO phonons. In GaAsBi and GaAsNBi, spectral features are also observed at ~$180cm^{-1}$ due to GaBi. Finally, following FTA, an additional feature is observed at ~$250cm^{-1}$, which has been attributed to InAs.[10]

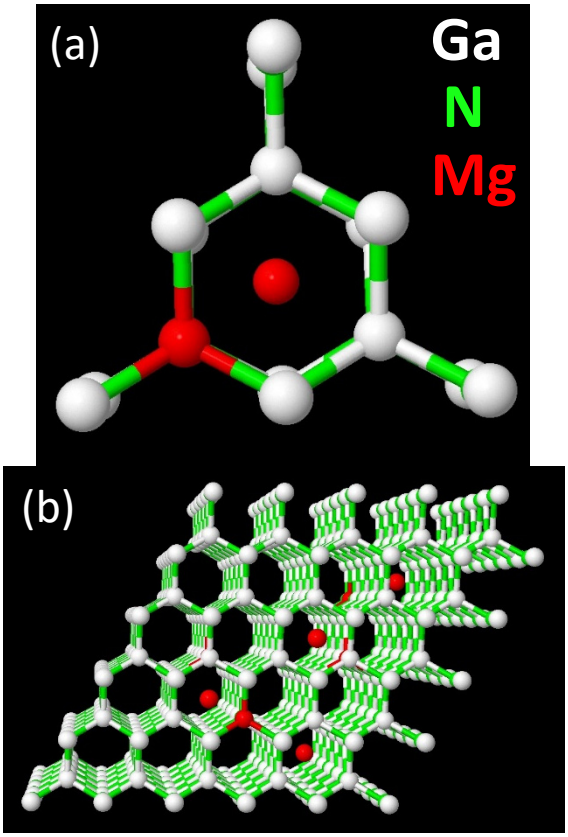

Figure 6.8 Ball stick model of GaN (white and green) with Mg (red) impurities sitting in the substitutional (i.e. Mg_{Ga}) and interstitial sites (Mg_I). (a) Simple one-cell structure, (b) multiple unit cell structure.

6.8 References

[1] W.Chu, J. Mayer, M. Nicolet, Backscattering Spectrometry, (Academic Press, New Work, 1978) pp. 264-270

[2] S. Giangrandi, T. Sajavaar, B. Brijs, K. Arstila, A. Vantomme, and W. Vandervorst, Nucl. Instr. Methods B 266, 5144 (2008).

[3] J. Jokinen, J. Keinonen, P. Tikkanen, A. Kuronen, T. Ahlgren and K. Nordlund, Nucl. Instr. Methods B 119, 533(1996).

[4] W. Assmann, Nucl. Instr. Methods B 64, 267 (1992).

[5] M. Döbeli, C. Kottler, M. Stocker, S. Weinmann, H.A. Synal, M. Grajcar and M. Suter, Nucl. Instr. Methods B 219, 415 (2014).

[6] M. Reason, Ph.D Thesis, Chapter 2, University of Michigan, 2006.

[7] E. Yablonovitch, D. M. Hwang, T. J. Gmitter, L. T. Florez, and J. P. Harbison. Appl. Phys. Lett 56, 2419 (1990).

[8] Cameca, *Instruction Manual, LEAP 5000HS* (2016).

[9] T. Ahlgren, E. Vainonen-Ahlgren, J. Likonen, W. Li, and M. Pessa, Appl. Phys. Lett. **80**, 2314 2002.

[10] W.J. Choi, H. Rho, J.D. Song, J.I. Lee, and Y.H. Cho, Phys. E. 26, 115 (2005).

[11] P. Laukkanen, M. P. J. Punkkinen, J. Puustinen, H. Levämäki, M. Tuominen, K. Schulte, J. Dahl, J. Lång, H. L. Zhang, M. Kuzmin, K. Palotas, B. Johansson, L. Vitos, M. Guina, and K. Kokko, Phys. Rev. B 86, 195205 (2012).

[12] J. Chen, G. Ciatto, M. Le Du, J.C. Harmand and F. Glas, Phys. Rev. B 82, 125303 (2010).

[13] H.T. Pham, S.F. Yoon, K.H. Tan and D. Boning. Appl. Phys. Lett 99, 092115 (2010).

[14] Y.G. Hong, C.W. Tu and R.K. Ahrenkiel, J. Cryst. Growth 227-228, 536 (2001)

[15] M.R. Gokhale, J. Wei, H. Wang and S.R. Forrest, Appl. Phys. Lett. 74, 1287 (1999).

[16] R.A. Stradling, Semicond. Sci. Technol. 6, C52 (1991).

[17] M. Wu, E. Luna, J. Puustinen, M. Guina, and A. Tramper, Nanotechnology, 25(20), 205605 (2014).

[18] M. Yoshimoto, W. Huang, Y. Takehara, J. Saraie, A. Chayahara, Y. Horino, and K. Oe, Jap. J. Appl. Phys. Lett., L845 (2004).

[19] A.R. Mohmad, F. Bastiman, C.J. Hunter, F. Harun, D.F. Reyes, D.L. Sales, D. Gonzalez, R.D. Richards, J.P.R. David and B.Y. Majlis, Semi. Sci. Tech. 30, 094018 (2015).

[20] I.P Smorchkova, E. Haus, B. Heying, P. Kozodoy, P. Fini, J.P. Ibbetson, S. Keller, S.P DenBaars, J.S. Speck and U.K. Mishra, Appl. Phys. Lett. 76, 718 (2000).

[21] H.P. Maruska, D.A. Stevenson, and J.I. Pankove, Appl. Phys. Lett. 22(6), 303 (1973).

[22] W.R. Wampler, S.M. Myers, A.F. Wright, J.C. Barbour, C.H. Seager and J. Han, J. of Appl. Phys. 90,108 (2001).

[23] G. Miceli and A. Pasquarello, Phys. Rev. B 93, 165207 (2016).

[24] T. Schmidt, M. Siebert, J.I. Flege, S. Figge, S. Gangopadhyay, A. Pretorius, T.L. Lee, J. Zegenhagen, L. Gregoratti, A. Barinov and A. Rosenauer, Phys. Stat. Sol. 248, 1810 (2011).

Appendix A

C21 MBE: Control of As_2 vs As_4

To control the sublimation of As_2 vs. As_4 using a cracking cell, one typically tunes the cracking zone (CZ) temperature, which is monitored by a CZ thermocouple, as shown in the photograph in Fig. A.1(a) and the corresponding schematic in Fig. A.1 (b). However, in the C21 MBE, the CZ TC fails to register temperatures exceeding 200°C. Attempts to remove the protective cover shown in Fig A.1(a) were unsuccessful, presumably due to As coating of its inner surface. It is hypothesized that this problem has its origins in the bulk zone (BZ), shown in Fig. A.2. In 2009, when the BZ was loaded with As, the screws shown by a red box in Fig. A.2 were not tightened with a torque wrench. Over time, the screws loosened, resulting in As leaking from the inner to the outer source containment unit of the BZ. It is further hypothesized that As also leaked into the CZ, coating the TC, causing the TC to fail for temperatures exceeding 200°C. We attempted to remove the As coating from the TC by manual scraping and evaporation (by heating the CZ to ~500°C for >12 hours). In both cases, the observed symptom persisted.

Instead, to control the sublimation of As_2 vs As_4, we use the information provided by Riber, shown in Table A.1. Therefore, to achieve As_4 sublimation, we used 36% power, with 3.2 Amp current and 12 volts. To achieve As_2 sublimation, we used 56% power, with 5.3 Amp current and 26 volts.

A.3 Figures

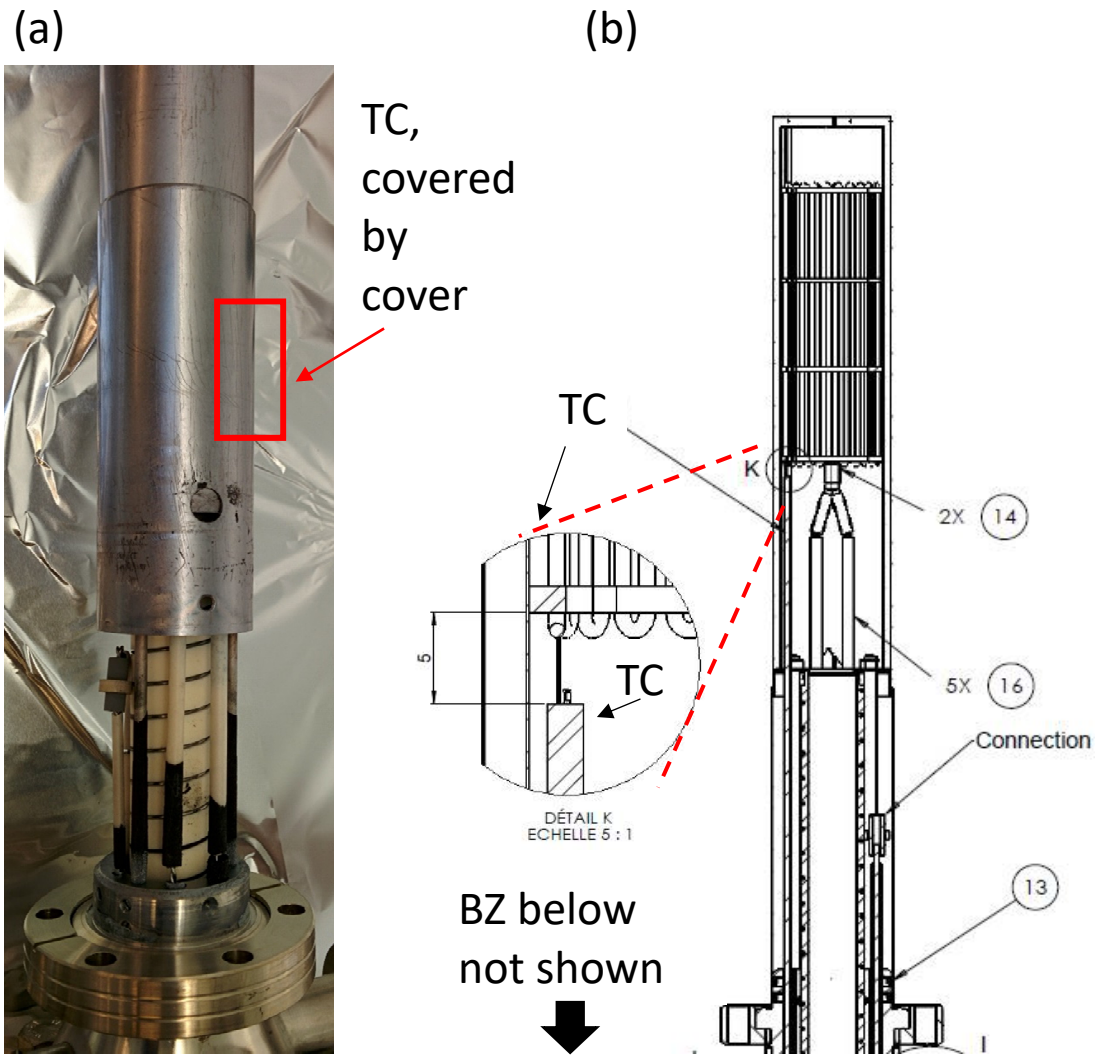

Figure A.1 (a) Photograph of As cracking zone (CZ) module, with corresponding schematic shown in (b). Attempts to remove the protective cover shown in (a) were unsuccessful, presumably due to excess arsenic coating on its inside.

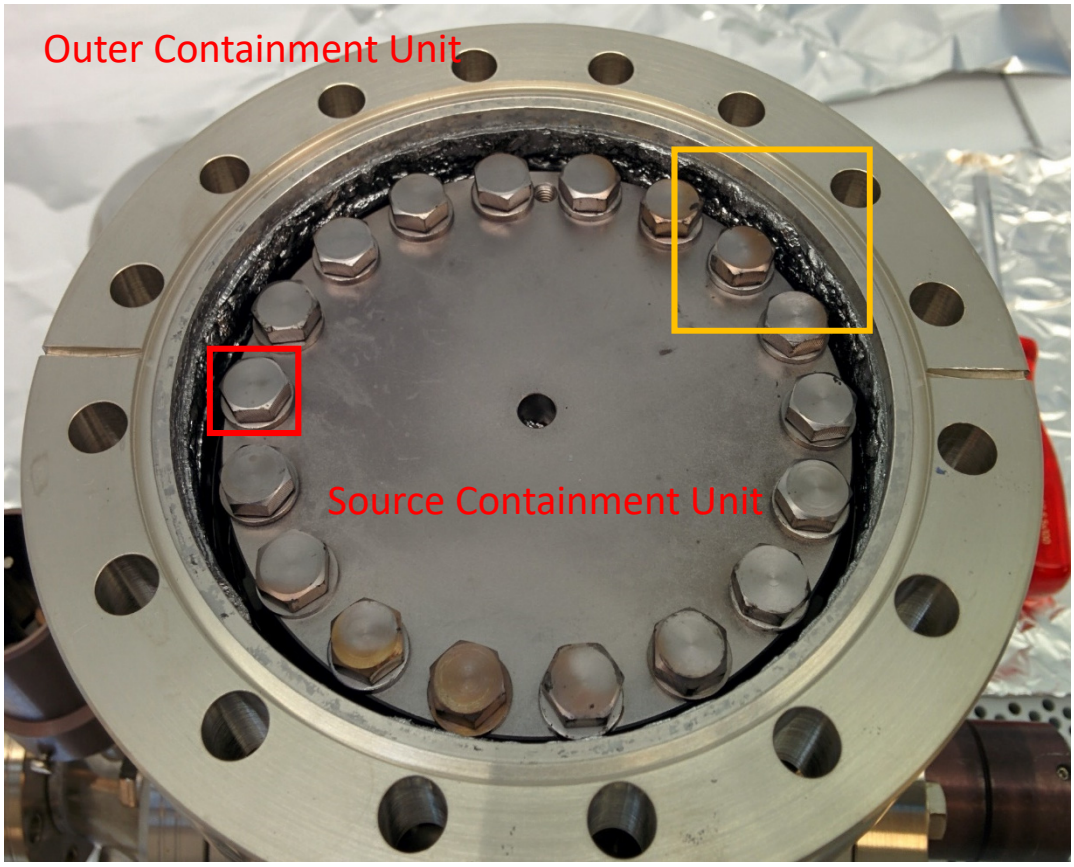

A.2 An image of the bulkzone (BZ) containment units, with the cover from the outer containment unit removed. The source containment unit houses the arsenic material. The screws emphasized by the red box were apparently not tightened to the specified torque, eventually loosening such that arsenic leaked from the inner to outer containment unit, as indicated by the yellow box.

A.4 Table

Condition	Current/Voltage	Power Setting (%)	Ramp Rate (%/m)
Standby (600°C)	I = 3.2A V = 12V	36	-
As4 (600°C)	I = 3.2A V = 12V	36	-
As2 (950°C)	I = 5.3A V = 26V	56	10
Always open NV to 50% before ramping BZ and CZ			

Table A.1 Power settings for the As cracking cell, provided by Riber engineers. The table lists the target CZ temperatures for standby, sublimation of As_4, and cracking of As_4, followed by As_2 sublimation. Computer control allows % power control only, current and voltage is automatically controlled by the power supply unit.

Appendix B

Gen II Nitrogen Plasma Source(s)

B.1 RF N plasma source history

At the start of the work in this dissertation, the Gen II MBE was fitted with a RF N plasma source from Veeco; however, the Veeco source was accidentally powered without water cooling, rendering it non-functional. Subsequently, the water flow safety interlock was re-installed, and a "spare" Addon RF plasma source, originally intended to be installed on the Riber 32 MBE, was installed on the Gen II. Since the Addon source was designed for dilute nitride materials, lower N flow rates are used and the ignition process is quite a bit different than that of the Veeco plasma source. In both cases, it is best to perform the ignition process in pairs, with one person adjusting the plasma power and MFC flow rate, and one person monitoring the plasma color and minimizing the reflected power.

B.2 RF N plasma ignition process

Here, we discuss the plasma ignition process for the Veeco and Addon sources. For both sources, the forward power is raised in a 50W-steps while the reflected power is reduced to as close to zero as possible.

For the Veeco source, a one-step ignition process is utilized. The MFC is set to 0.5 sccm, the RF forward power is raised to 450-500W, while the reflected power is minimized, and the plasma is ignited with a bright purple glow.

For the Addon plasma source, a three-step ignition process is used, as illustrated in Fig. B.1. In the first step, the "low brightness" ignition, the MFC is set to 1.5 sccm and the forward power is raised to 350W while the reflected power is minimized. The resulting "low brightness" plasma exhibits a dim orange-color, as shown in Fig B.1(a). If the low brightness (orange) plasma is not ignited at 350W, the flow rate is increased to 1.5 to 2.0 sccm. If the "low brightness" is still not ignited, the forward power is increased to 400 to 450W, while the reflected power is again minimized. Typically, the "low brightness" (orange) plasma is ignited at 350 to 400W, with a flow rate of 1.5 sccm. In the next step, the "medium brightness" ignition, the MFC flow rate is increased to 3 sccm and the forward power is increased toward 500W, while the reflected power is reduced, until the plasma color transforms from dim-orange to dim-purple, as shown in Fig. B.1(b). Typically, this transition happens for forward power <500W. To obtain the "high brightness" plasma, the forward power is increased to 500W, and the MFC flow rate is lowered to 1 sccm at 0.1 sccm/sec, and then to <1 sccm at 0.02 sccm/sec until the plasma turns purple at ~0.35 sccm, as shown in Fig. B.1(c). We note that in the Addon source, the plasma is often unstable for

MFC > 0.35 sccm. If the plasma is extinguished during the flow rate lowering process, one must re-start the process form the “low brightness” ignition.

B.3 Figures

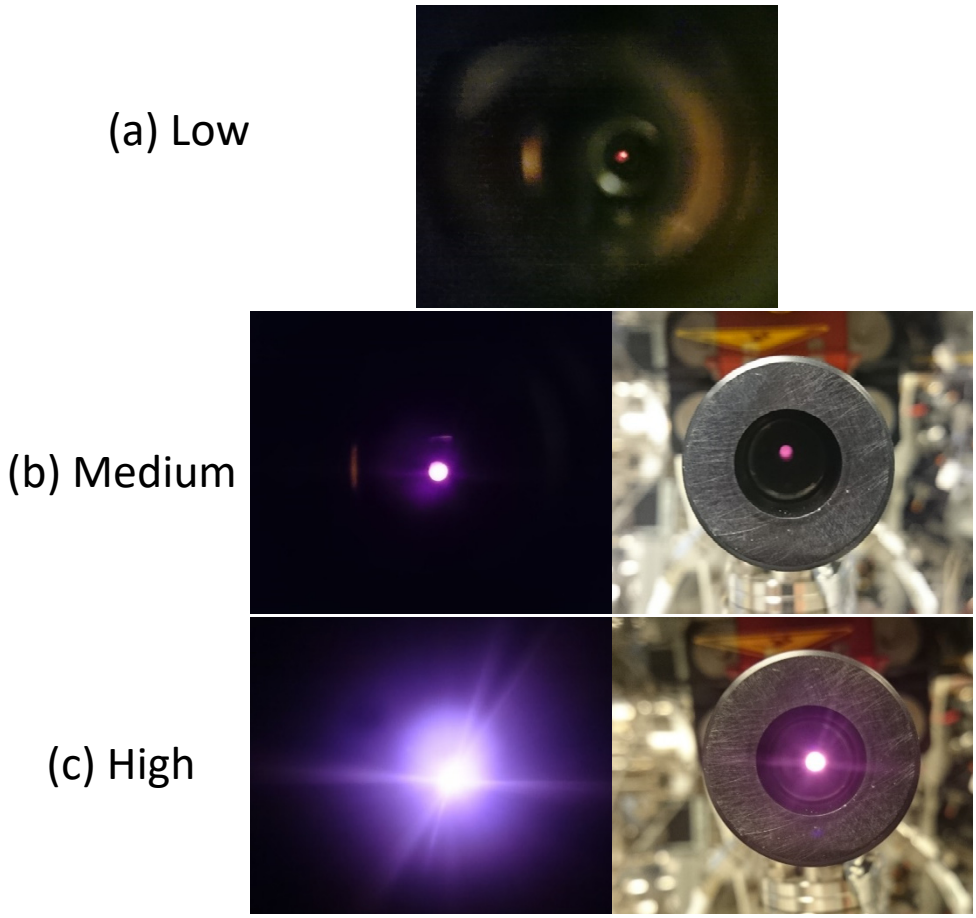

Figure B.1 Images of plasma from Addon plasma source: (a) low, (b) medium, and (c) high brightness mode. Typically, low brightness is achieved with 1.5 sccm and 350W, medium brightness with 3 sccm and ~500W, and high brightness with 0.35 sccm and ~500W.

Appendix C

LEAP Experimental Artifacts

C.1 Overview

In this section, the basic physics associated with the LEAP process is described. We then discuss several issues that must be considered during the analysis of LEAP data, including the complications associated with multiple charge state molecules, delayed thermal evaporation, and pulse "wrap around". In all cases, the strategies used to minimize these effects are discussed.

C.2 Physics of LEAP

When a high voltage is applied to the fabricated tip, the resulting electric field is approximated as follows:

$$E = \frac{-Q_{electrode}}{4\pi\varepsilon_0 r^2} \quad \text{C.1}$$

where ε_0 is the permittivity of free space, $Q_{electrode}$ is the resulting charge on the ground electrode, and *r* is the separation between the tip and $Q_{electrode}$. As an ion is evaporated from the tip, it experiences a force and acceleration, as follows:

$$F = \frac{-kq_{ion}Q_{source}}{r^2} = m_{ion}a \quad \text{C.2}$$

The acceleration of the ion in terms of its charge state is generalized as follows:

$$a = \frac{nkq_{ion}Q_{source}}{m_{ion}x^2} \quad \text{C.3}$$

where *n* is the charge state of the ions. We use the rudimentary equation of motion, as follows:

$$x = x_o + v_0 t + \frac{1}{2}at^2 \quad \text{C.4}$$

where *x* is the distance from the tip to the detector. Assuming negligible initial ion velocity ($v_0 = 0$) and setting the initial ion position at the tip ($x_0 = 0$), we solve for the time-of-flight as follows:

$$t = \sqrt{\frac{2xm_{ion}x^2}{nkq_{ion}Q_{source}}} \quad \text{C.5}$$

Evidently, *t* is dependent on both the mass and charge state of each ion.

C.3 Identifying Multiple Charge States

For many ions, possible charge states associated with molecules must be considered. For example, since $t_{As}^{+} = t_{As_2}^{++}$, the mass-to-charge ratio of 75 could be identified as As_{75}^{+} or $2As_{75}^{++}$ as shown in Fig. C.1.Since the two cases are not easily distinguished, both cases must be considered during the analysis of LEAP data. As discussed in Chapter 1 and Chapter 5, this is particularly important for understanding and controlling the III-V stoichiometry in GaAsNBi alloys.

C.4 Accounting for Delayed Thermal Evaporation and Pulse "wrap around"

As discussed in Chapter 2, the timer for "time-of-flight" starts at the beginning of each laser pulse. During laser-mode LEAP, thermal evaporation is not instantaneous, such that some of the ions experience delayed evaporation. In some cases, this leads to thermal tails in the measured distribution of mass-to-charge ratios.

For example, if Ga^{+} is evaporated with a Δt delay, total travel time in Equation 4 becomes

$$t_{Ga}^{+} + \Delta t = \sqrt{\frac{2xm_{delayed-ion}r^2}{nkq_{ion}Q_{source}}} \qquad \text{C.6}$$

Solving for $m_{delayed-ion}$,

$$m_{delayed-ion} = \frac{nkq_{ion}Q_{source}(t_{Ga}^{+} + \Delta t)^2}{2xr^2} \qquad \text{C.7}$$

Equation C.7 shows that for a longer Δt, the delayed ion would behave as if it is a "heavier ion". Figure C.2 shows an example LEAP spectrum, consisting of counts vs mass-to-charge ratio, for a GaAs buffer layer. In Fig. C.2(a), three peaks with mass-to-charge ratios

corresponding to Ga_{69}^{+}, Ga_{71}^{+}, and $As_{75}^{+}/2As_{75}^{++}$ are labelled. In the zoomed-in view of the LEAP spectrum shown in Fig. C.2(b), thermal tails due to delayed evaporation, which lead to apparently "heavier" ions are apparent.

For heavy elements, such as Bi, the laser pulse frequency must be carefully chosen to ensure ion arrival at the detector prior to the initiation of the subsequent laser pulse. When the heavy ions do not reach the detector prior to the subsequent laser pulse, pulse "wrap-around" counts appear at the light element mass-to-charge ratio location, as shown in Fig. C.3(a). Both thermal tails and the pulse "wrap around" can be remedied by using a lower pulse rate, such as 100kHz, as shown in Fig. C.3(b).

C.5 Figures

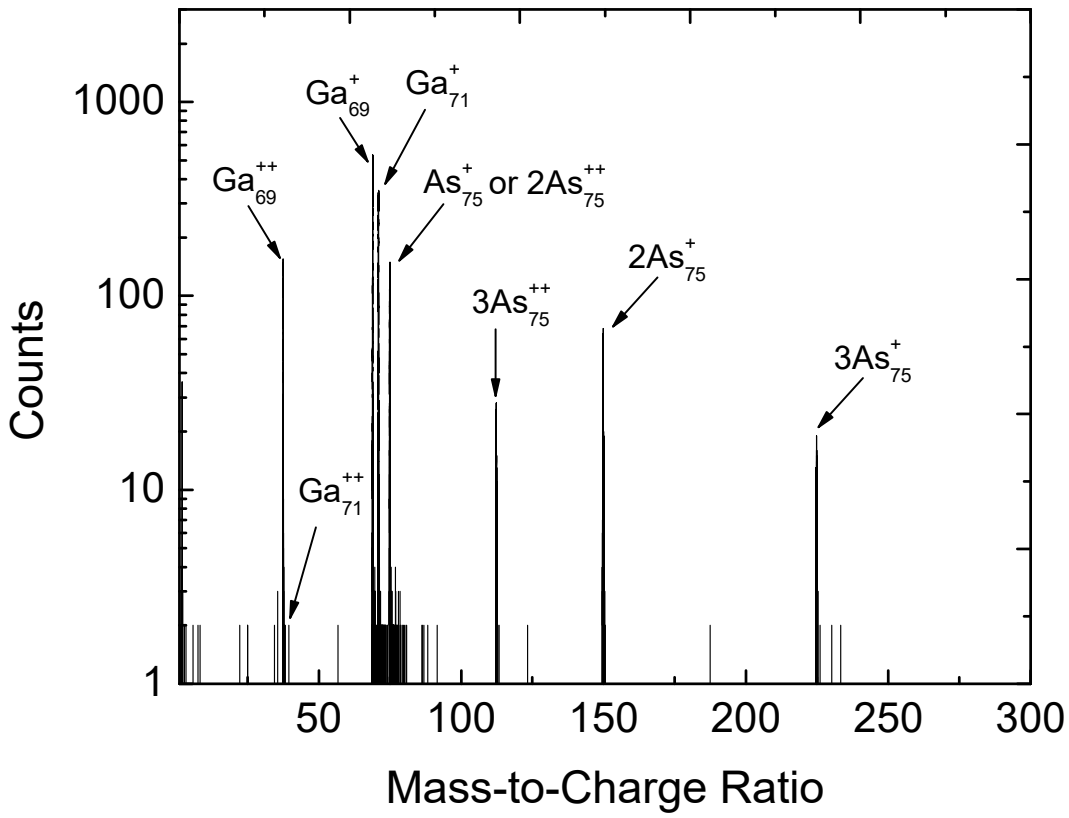

Figure C.1 Example LEAP spectrum for an MBE-grown GaAs buffer layer consisting of counts vs. mass-to-charge ratio. In the plot, several peaks in mass-to-charge ratio and their possible identifies (including element and charge state) are labeled.

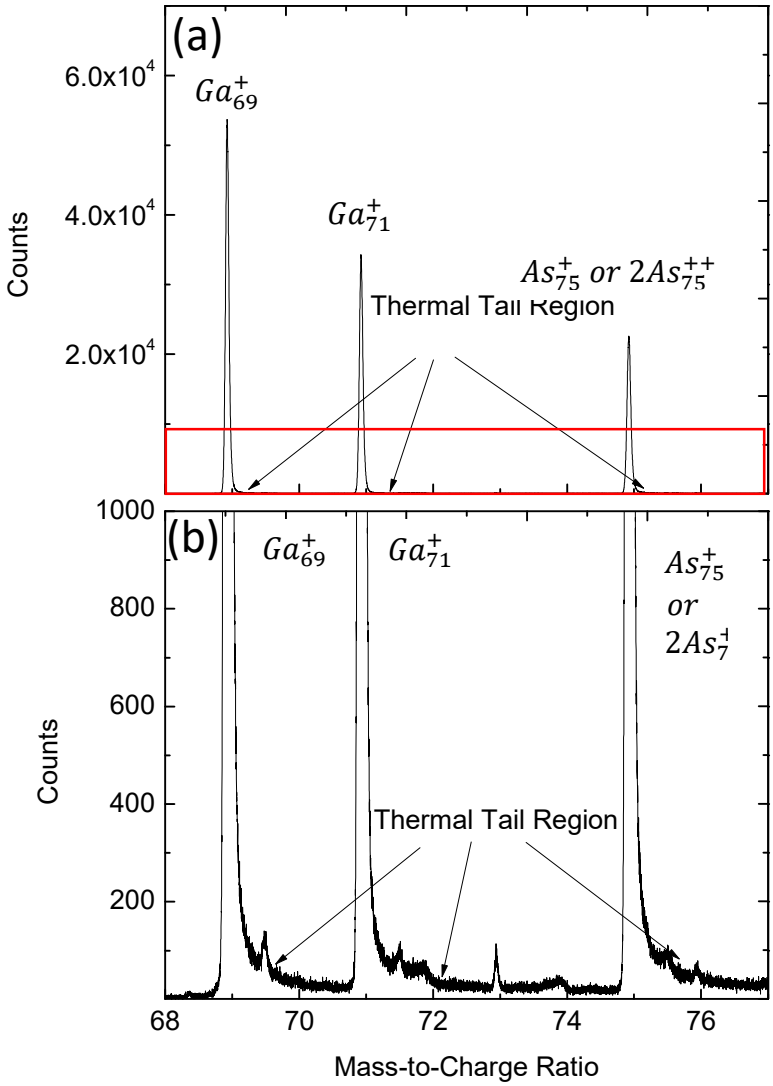

Figure C.2 (a) LEAP spectrum, consisting of counts vs. mass-to-charge ratio, collected from a GaAs buffer layer using laser-assisted LEAP. In the plot, peaks in mass-to-charge ratio, corresponding to Ga_{69}^{+}, Ga_{71}^{+}, and As_{75}^{+}or $2As_{75}^{++}$, are apparent. The portions of LEAP spectrum enclosed in the box in (a) are shown in (b). During the LEAP experiment, some of the atoms experience delayed thermal evaporation and take a longer time to reach the detector, thus appearing at a higher mass-to-charge ratio. In this case, the thermal tails have <0.2% of the main peak intensity; however, up to ~5% was observed by the author.

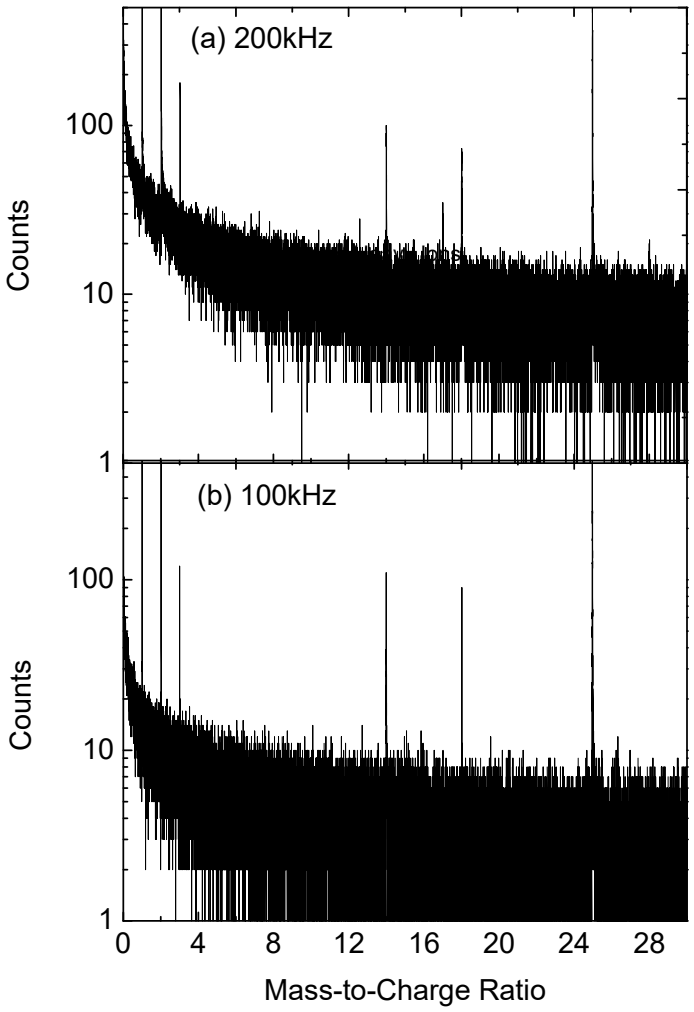

Figure C.3 LEAP spectrum, consisting of counts vs mass-to-charge ratio, collected from a GaAsNBi layer using laser-assisted LEAP with 200kHz. In plot (a), baseline noise level is significantly higher and extends further up into heavier elements, suggesting the presence of pulse wrap-around. In subsequent experiments, the pulse wrap around was eliminated by using a lower pulse rate (~100 kHz), shown in (b).

Appendix D

Tandem Accelerator and Data Analysis

D.1 Overview

In this section, tandem accelerators are described generally, along with specific details regarding the tools at the Michigan Ion Beam Laboratory (MIBL) and Los Alamos National Laboratory (LANL). Next, detailed alignment procedures to achieve [100], [110], and [111] channeling conditions are illustrated. Finally, analysis of RBS and NRA data is discussed.

D.2 Tandem Accelerator

In a tandem ion accelerator, each charged ion is accelerated twice under the same static electric potential. As shown in Fig D.1, the ion source provides negatively charged ions which are injected into the accelerator and accelerated toward the positively charged high voltage (HV) terminal at the center of the accelerator. As the ions reach the HV terminal, the ions pass through a stripper foil or stripper gas. Thus, the electrons will be stripped off, converting the ion polarity from negative to positive. Subsequently, positively charged ions, under the same applied positive voltage, accelerate away from the positively charged terminal; effectively being accelerated by the same high voltage *twice*. Following ion acceleration, bending magnets are used to both select ion energies and to direct the ion beam into various analysis chambers.

The accelerator at MIBL consists of a General Ionics Tandem with 1.7 MV terminal voltage and argon stripper gas. In this case, the ions are converted to doubly charged states in order to achieve >3.4 MeV acceleration. In the MIBL General Ionics Tandem Accelerator, it is not possible to directly measure the total number of incident ions and instead each spectra is normalized to the lowest substrate signal within a set of data collected. Finally, at MIBL, the goniometer is limited to quantitative [100] channeling alignment.

The accelerator at LANL consists of a 3 MV terminal voltage and N_2 stripper gas. In the LANL NEC Tandem, the total number of incident ions is measured by a charge integrator which is electrically connected to the sample. In addition, the NEC Tandem is

equipped with a fully automated five-axis goniometer that enables channeling alignment in [100], [110] and [111] directions.

D.3 Channeling Alignment

Since our films are grown on [001] substrates, the incident beam is typically in the proximity of the <100>-type channeling direction. To optimize the [100] channeling condition, we use a computer automated-goniometer to rotate the sample azimuthally in φ_x, and φ_y, as shown in Fig. D.2. At each step, RBS yields are collected from the first 10-20 channels of the GaAs substrate edge signal for a preset ion dose (typically ~0.2 μC). Starting at $\varphi_x = +4°$ and $\varphi_y = +4°$, we rotate in steps of 0.2°: φ_y to $-4°$, φ_x to $-4°$, φ_y to $+4°$, φ_x to $+4°$, forming a so-called "polar plot" of the backscattered yield, as shown in Fig. D.3. Since minima in the backscattered yield occur at the channeling directions, this data is inputted into MATLAB script, presented in Section D.5, to calculate the $\Delta\theta$, $\Delta\varphi_x$, and $\Delta\varphi_y$ to achieve channeling. An example of the calculated rotation correction for [100] alignment is shown in Fig. D.4. In addition, if subsequent [111] or [110] channeling conditions are needed, the sample will also need rotation of $\Delta\theta = -7.13°$ before any further rotations.

To achieve [110] channeling from the starting point of [100] channeling with $\Delta\theta = 0°$, θ is rotated $45°$, followed by φ_y rotation of $45°$. Subsequently, to optimize the [110] channeling conditions, we repeat optimization the process described above, forming the polar plot of the backscattered yield shown in Fig. D.5. To achieve [111] channeling condition from the starting point of [100] channeling, one φ_y rotation of $54.74°$ is needed.

Similarly, to optimize the [111] channeling condition, we repeat the optimization process described above, forming the polar plot of the backscattered yield shown in Fig. D.6.

D.4 Spectra Fitting

To determine the composition of thin alloy films, we use a combination of approximative and quantitative analyses. First, we estimate the mole fractions from the ratios of the NRA or RBS yields, as described in Appendix B of R.L. Field's Ph.D thesis. Quantitative analyses are achieved using software packages such as Rutherford Backscattering Data Analysis, Plotting and Simulation Package (RUMP), or Simulation of Nuclear Reaction Analysis (SIMNRA). For this dissertation, all the spectra are analyzed using SIMNRA.

To fit the data using SIMNRA, several fixed input parameters are needed, including the incident ion species (alpha, deuterium, carbon, and etc), the ion energy (usually in ~MeV range), the incident ion angle (0° in RBS and NRA), the ion scattering angle (usually ~135 ° for NRA and ~167 ° for RBS) and the target material including its layer configuration. Several variable parameters are also utilized during the fitting process, including the energy per channel (usually ~5 keV/ch), the number of particles (~10E11), and the detector resolution (~15 keV for RBS, ~100 keV for NRA). The general approach is an iterative process that often requires repetition of various steps to achieve the "best fit" spectrum. An example of iterative process for RBS data from a GaAsBi alloy film is listed below and is shown in Fig. D.7. Similar approaches were used for the analysis of both NRA and RBS spectra.

1) The number of particles is varied until the SIMNRA and measured substrate data match (Fig. D.8(a)) – too low in the example shown,

2) The keV/ch and calibration offset are varied until the SIMNRA and measured substrate and solute atom high energy edges match (Fig. D.8(b)) – too lower in the example shown,

3) The detector energy resolution is varied until the shape of the SIMNRA and measured substrate and solute atom high energy edges matches (Fig. D.8(c)) – too low in the example shown,

4) The target thickness is varied until the SIMNRA and measured width of the solute element signals match (Fig. D.8(d)) – too low in the example shown,

5) The target composition is varied until the SIMNRA and measured solute element signal match (accounting for background noise) (Fig. D.8(e)) – too high in the example shown.

D.5 MATLAB script to identify channeling conditions

The script used to identify $\Delta\theta$, $\Delta\varphi_x$, and $\Delta\varphi_y$ positions of the channels, based upon the <100>, <110>, and/or <111> polar plots shown in Figs. D.3, D.5, and D.6.

```
clear
prompt2 = 'how many pairs of reading?'; %how many pairs of dips we are
getting?
a = input(prompt2);
prompt = 'What is the Degree Readout?'; %what is the degree readout on
the polyplot?
if (a<3)
s = input(prompt); %input order is in the increasing fashion
t = input(prompt);
u = input(prompt);
v = input(prompt);
if (s<40) %if/else statement on how to form the coordinate for the
inputted value
```

```
    p0 = [40 (40-s)];
elseif (40<=s) && (s<80)
    p0=[(80-s) 0];
elseif (80<=s) && (s<=120)
    p0=[0 (s-80)];
else
    p0=[(s-120) 40];

end
if (t<40)
    p1 = [40 (40-t)];
elseif (40<=t) && (t<80)
    p1=[(80-t) 0];
elseif (80<=t) && (t<=120)
    p1=[0 (t-80)];
else
    p1=[(t-120) 40];
end
if (u<40)
    p2 = [40 (40-u)];
elseif (40<=u) && (u<80)
    p2=[(80-u) 0];
elseif (80<=u) && (u<=120)
    p2=[0 (u-80)];
else
    p2=[(u-120) 40];
end
if (v<40)
    p3 = [40 (40-v)];
elseif (40<=v) && (v<80)
    p3=[(80-v) 0];
elseif (80<=v) && (v<=120)
    p3=[0 (v-80)];
else
    p3=[(v-120) 40];
end
if (p0==p2)%this statement prevents undefined slope (vertical line)
    plot x = p0
else
vectarrow(p0,p2); %plots a vector arrow from one coordinate to another
end
hold
if (p1==p3)
    plot x = p1
else
vectarrow(p1,p3);
end
m1=(p0(2)-p2(2))/(p0(1)-p2(1)); %solving where the plotted vectors
cross
m2=(p1(2)-p3(2))/(p1(1)-p3(1));
b1=p0(2)-m1*p0(1);
b2=p1(2)-m2*p1(1);
x1= (b2-b1)/(m1-m2);
y1= m1*x1+b1;
moveX = (x1-20)*.2; %how many degrees to move in (x,y) fashion
moveY = (y1-20)*.2;
```

```
rotate=atan((p0(2)-y1)/(p0(1)-x1))*180/pi; %how many degrees to rotate
the sample?
text(x1+1,y1,['(', num2str(moveX), ', ', num2str(moveY),
')'],'fontsize', 14) %display text of the coordinate of movement
text(15,35,['rotate   ', num2str(rotate), ',', 'd',
'egree'],'fontsize', 14) %display how much to rotate the sample by
elseif (a<4) && (a>2)
s = input(prompt);
t = input(prompt);
u = input(prompt);
v = input(prompt);
w = input(prompt);
x = input(prompt);
if (s<40)
    p0 = [40 (40-s)];
elseif (40<=s) && (s<80)
    p0=[(80-s) 0];
elseif (80<=s) && (s<=120)
    p0=[0 (s-80)];
else
    p0=[(s-120) 40];
end
if (t<40)
    p1 = [40 (40-t)];
elseif (40<=t) && (t<80)
    p1=[(80-t) 0];
elseif (80<=t) && (t<=120)
    p1=[0 (t-80)];
else
    p1=[(t-120) 40];
end
if (u<40)
    p2 = [40 (40-u)];
elseif (40<=u) && (u<80)
    p2=[(80-u) 0];
elseif (80<=u) && (u<=120)
    p2=[0 (u-80)];
else
    p2=[(u-120) 40];
end
if (v<40)
    p3 = [40 (40-v)];
elseif (40<=v) && (v<80)
    p3=[(80-v) 0];
elseif (80<=v) && (v<=120)
    p3=[0 (v-80)];
else
    p3=[(v-120) 40];
end
if (w<40)
    p4 = [40 (40-w)];
elseif (40<=w) && (w<80)
    p4=[(80-w) 0];
elseif (80<=w) && (w<=120)
    p4=[0 (w-80)];
else
    p4=[(w-120) 40];
```

```
end
if (x<40)
    p5 = [40 (40-x)];
elseif (40<=x) && (x<80)
    p5=[(80-x) 0];
elseif (80<=x) && (x<=120)
    p5=[0 (x-80)];
else
    p5=[(x-120) 40];
end
vectarrow(p0,p3);
hold
vectarrow(p1,p4);
hold
vectarrow(p2,p5);
m1=(p0(2)-p3(2))/(p0(1)-p3(1));
m2=(p1(2)-p4(2))/(p1(1)-p4(1));
m3=(p2(2)-p5(2))/(p2(1)-p5(1));
b1=p0(2)-m1*p0(1);
b2=p1(2)-m2*p1(1);
b3=p2(2)-m3*p2(1);
x1= (b2-b1)/(m1-m2);
y1= m1*x1+b1;
x2= (b3-b2)/(m2-m3);
y2= m2*x2+b2;
x3= (b1-b3)/(m3-m1);
y3= m3*x3+b3;
moveX1 = (x1-20)*.2;
moveY1= (y1-20)*.2;
moveX2 = (x2-20)*.2;
moveY2= (y2-20)*.2;
moveX3 = (x3-20)*.2;
moveY3= (y3-20)*.2;
rotate=atan((p0(2)-y1)/(p0(1)-x1))*180/pi;
text(x1+1,y1,['(', num2str(moveX1), ', ', num2str(moveY1),
')'],'fontsize', 14)
text(x2+2,y2-2,['(', num2str(moveX2), ', ', num2str(moveY2),
')'],'fontsize', 14)
text(x3+3,y3-4,['(', num2str(moveX3), ', ', num2str(moveY3),
')'],'fontsize', 14)
text(15,35,['rotate   ', num2str(rotate), ',', 'd',
'egree'],'fontsize', 14)
end
set(gca, 'XTickLabel',{'-4','3','-2','-
1','0','1','2','3','4'},'fontsize', 14)
set(gca, 'YTickLabel',{'-4','3','-2','-
1','0','1','2','3','4'},'fontsize', 14)
xlabel('\phi _{x}', 'FontSize',14)
ylabel('\phi _{y}', 'FontSize',14)
grid off
```

D.6 Figures

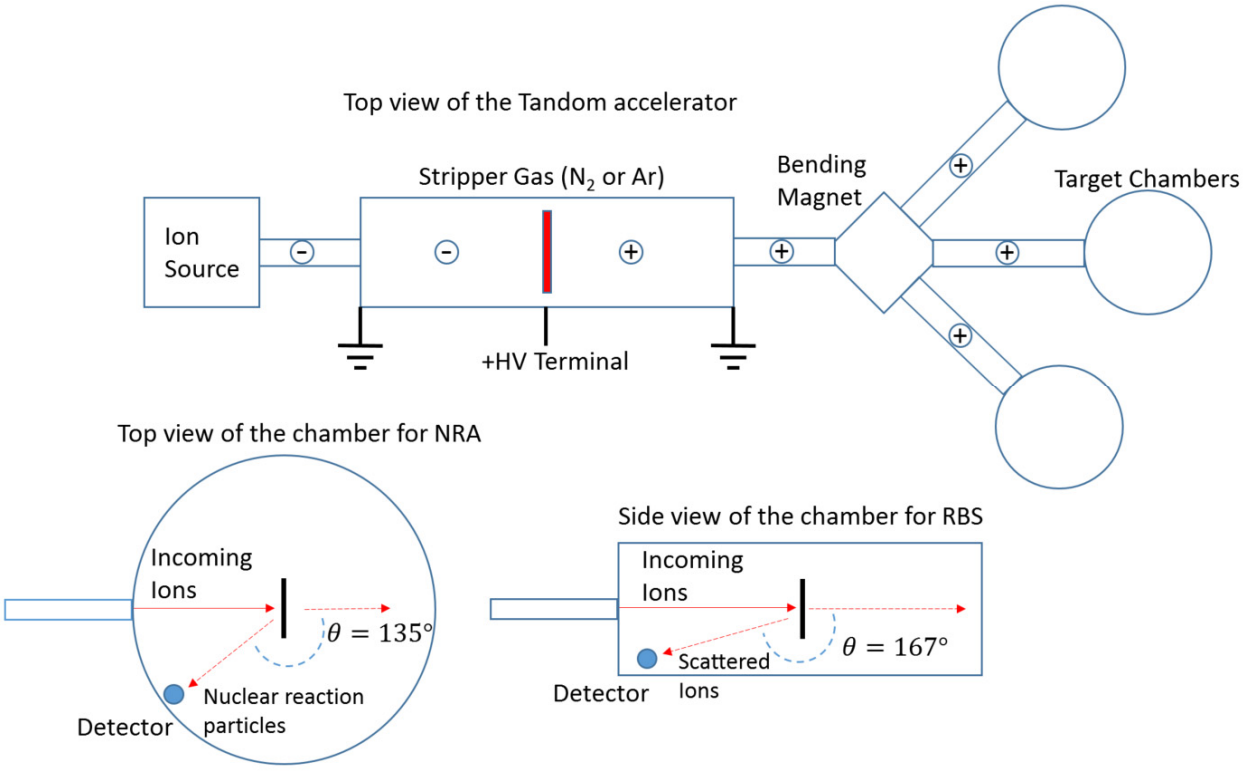

Figure D.1 Top view of a general tandem accelerator, along with enlarged top and side views of a target chamber. As the ions are injected into the accelerator from the ion source, they are accelerated toward the high voltage terminal at the center. The stripper gas then converts the ions from negatively to positively charged ions, such that they subsequently to accelerate away from the high voltage terminal – hence the "tandem" name. The bending magnets are used to select ion energies and/or to direct the ion beam into various analysis chambers. The top (side) view of the chamber shows the detector geometry for NRA (RBS). The tandem used at LANL is a NEC Tandem with terminal voltage of 3 MV. The tandem used at MIBL is a General Ionex Tandem with terminal voltage of 1.7 MV.

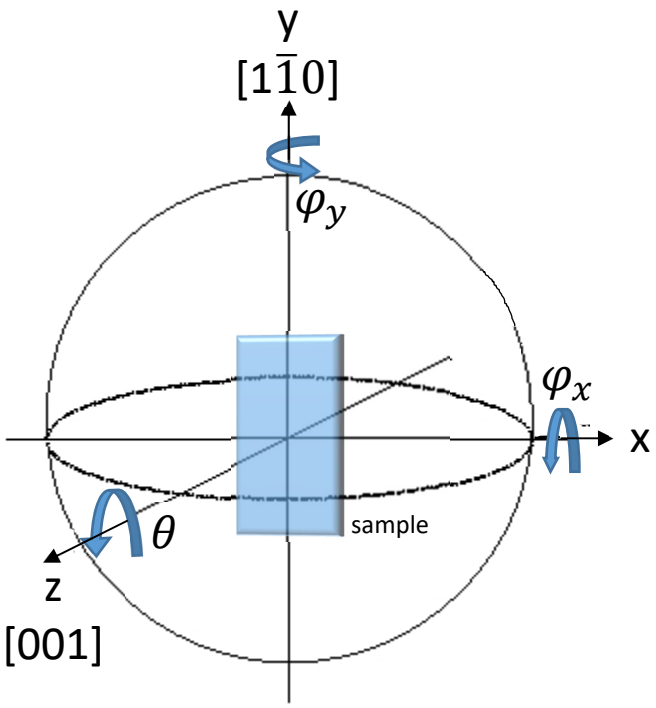

Figure D.2 A diagram showing the sample orientation and the related rotational axes used to aligning the sample for channeling conditions. The incident ion beam is parallel to the rotational θ-axis.

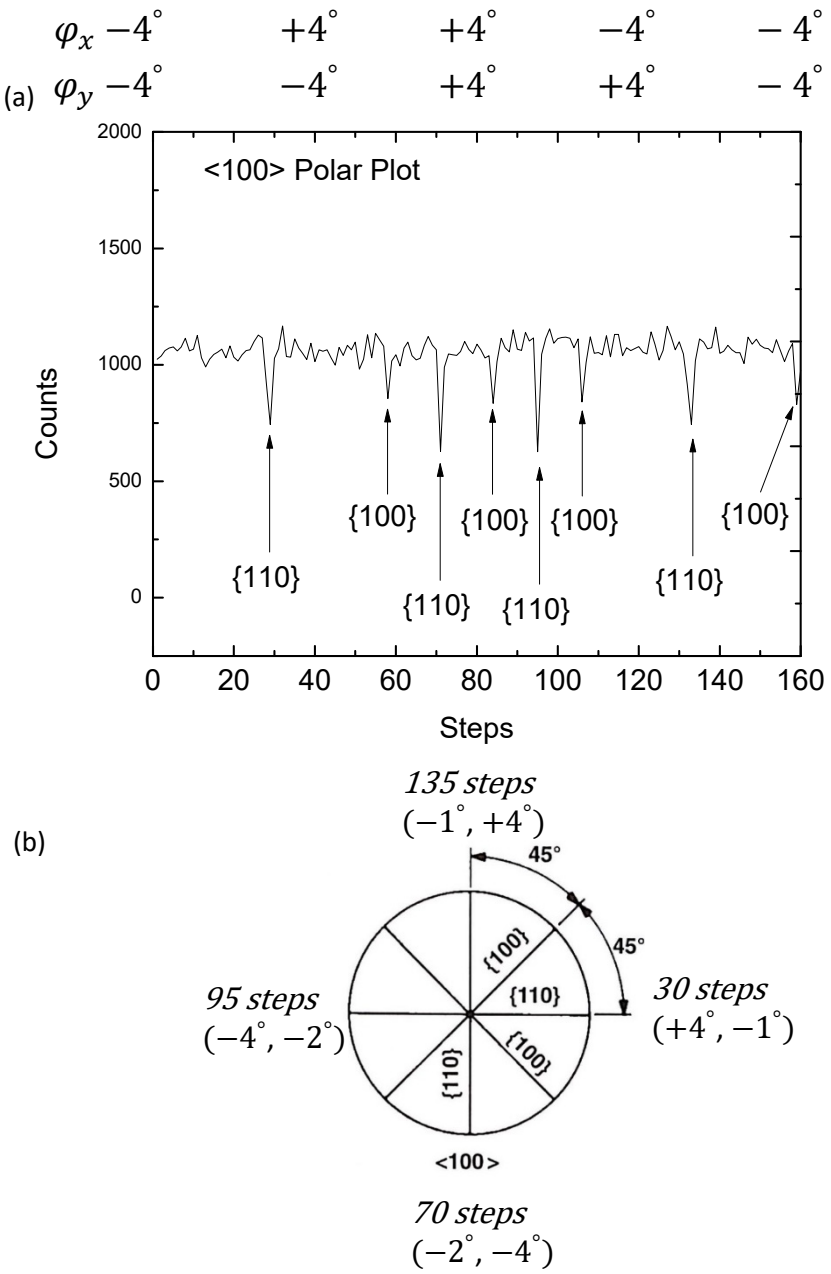

Figure D.3 (a) <100> channel "polar plot" of a RBS counts vs steps of rotation (0.2° in and φ_x or φ_y (b) corresponding <100> stereographic projection. The {110} and {100} minima in counts, indicated by upward arrows in (a), correspond to alternating {110} and {100} channels. The values of φ_x and φ_y needed to achieve each channeling condition are extracted by the MatLab script in Section D.5.

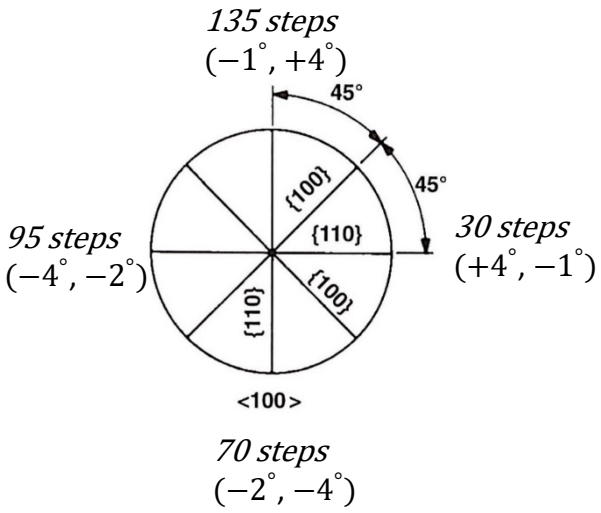

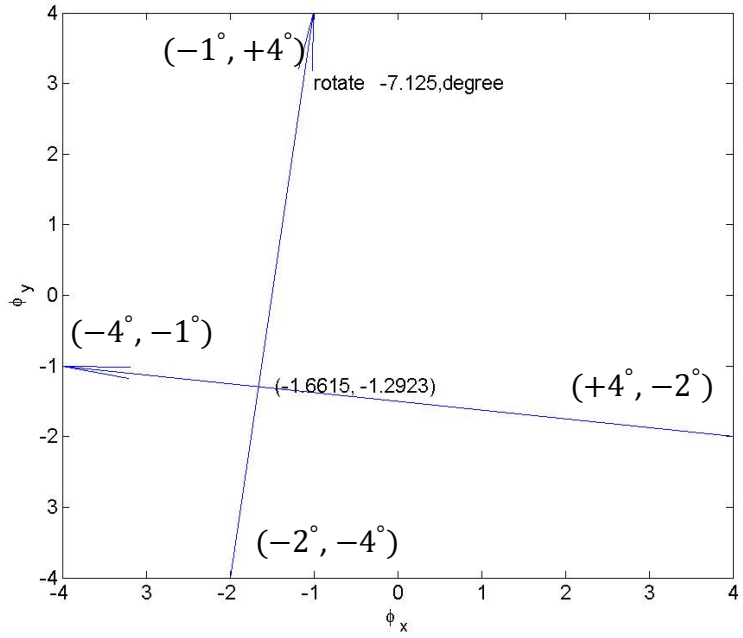

Figure D.4 Using pairs of {110} minima at ~30/95 steps and ~70/130 steps from Fig. D.3, the rotation needed for [100] channel are identified as $\Delta\varphi_x = -1.66°$ and $\Delta\varphi_y = -1.29°$.

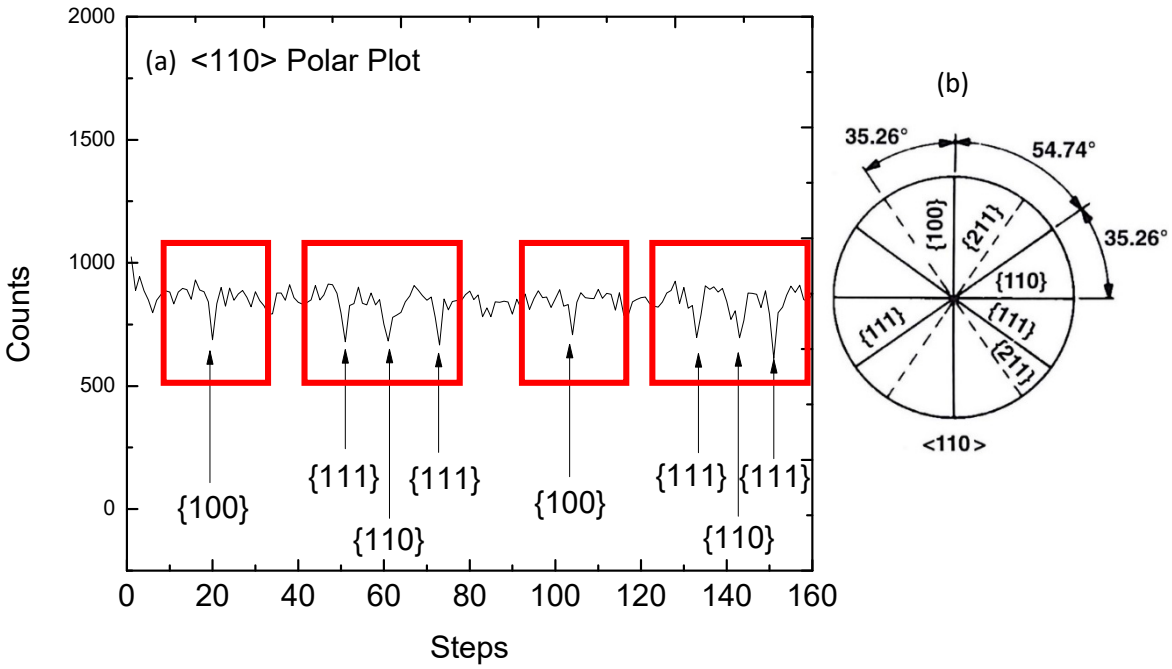

Figure D.5 (a) <110> channel "polar plot" of a RBS counts vs steps of rotation (0.2° in and φ_x or φ_y) and (b) corresponding <110> stereographic projection. The minima in counts, indicated by upward arrows in (a), correspond to {100}, {111}, and {110} channels. The 1-3-1-3 pattern of minima typical of <110> polar plot are indicated by red boxes. The values of $\Delta\varphi_x = 0.33°$ and $\Delta\varphi_y = 0.46°$ needed to achieve the <110> channeling condition are extracted by the MatLaB script in section D.5.

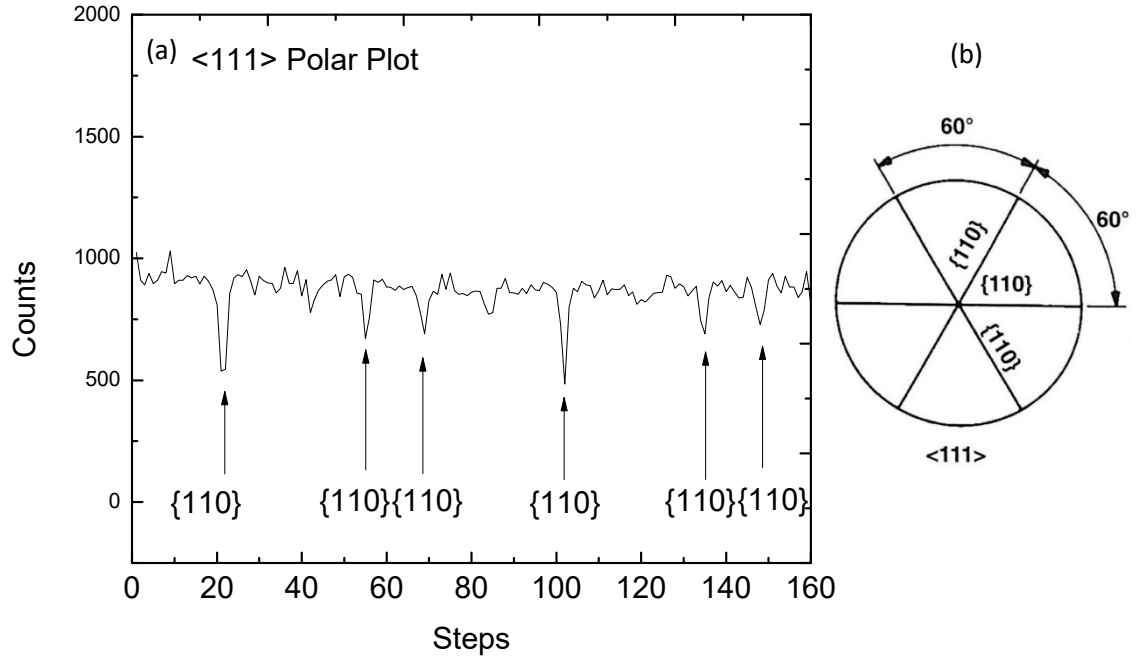

Figure D.6 (a) <111> channel "polar plot" of a RBS counts vs steps of rotation (0.2° in and φ_x or φ_y) and (b) corresponding <110> stereographic projection. The minima in counts, indicated by upward arrows in (a), correspond to {110} channels. The values of $\Delta\varphi_x = 0.19°$ and $\Delta\varphi_y = 0.38°$ needed to achieve the <111> channeling condition are extracted by the MatLaB script in section D.5.

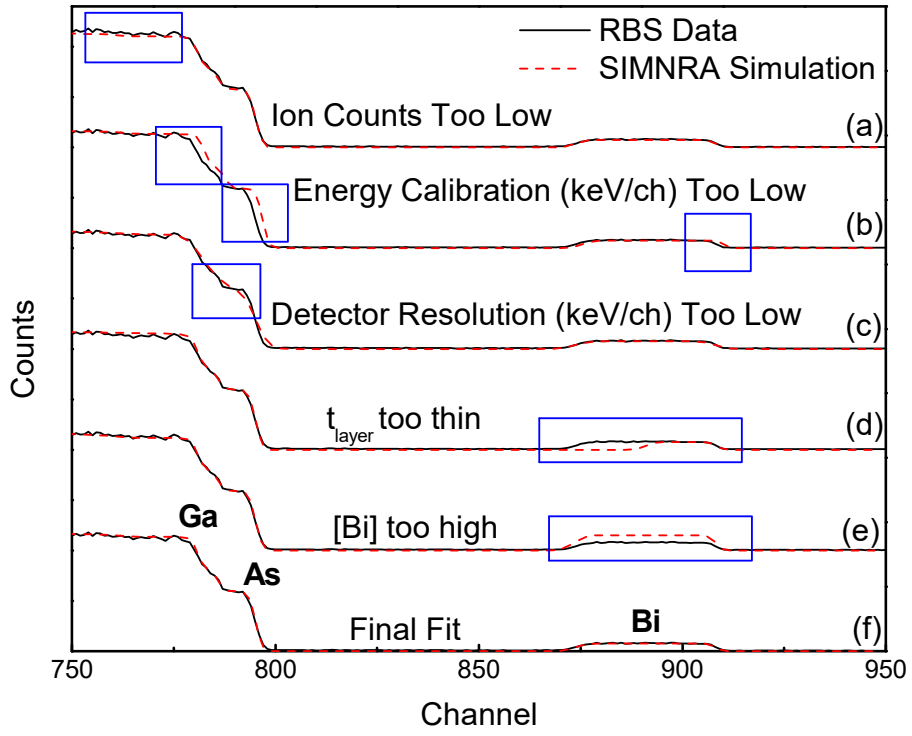

Figure D.7 Comparison of SIMNRA simulation (red dashed line) with RBS data (black solid line) for 400 nm thick GaAsBi films, using the parameters in Table D.1. (a) simulated ion counts lower than the RBS data. (b) simulated spectrum shifted to higher channel numbers than RBS data due to low energy calibration value. (c) simulated spectrum contains smeared-out version of step-like feature in the RBS data due to low detector resolution. (d) simulated spectrum with narrowing of the GaAsBi layer feature apparent in the RBS data due to low t_{layer}. (e) simulated spectrum with enhanced counts for the feature associated with epilayer in the RBS data, due to high [Bi]. (f) Well fitted spectrum.

D.7 Tables

Spectrum	Simulated Ions Count	Energy Calibration (keV/Ch)	Energy Calibration Offset (keV)	Detector Resolution (keV)	Epilayer Thickness (nm)	Bi Fraction
a	4.30E+11	15	-9	15	400	0.0102
b	4.50E+11	30	-6	15	400	0.0102
c	4.50E+11	15	-9	30	400	0.0102
d	4.50E+11	15	-9	15	200	0.0102
e	4.50E+11	15	-9	15	400	0.204
f	4.50E+11	15	-9	15	400	0.0102

Table D.1 Tabulated values used for SIMNRA simulations spectra in Fig. D.7. The fitting parameters needing correction for each spectra (a)-(e) are highlighted in yellow. The final parameters used for the well-fitted SIMNRA spectrum are shown in (f).

Appendix E

MC-MD Ion Beam Simulations: Validation and Input File

E.1 Overview

In this section, we describe the validation of our MC-MD ion beam simulations, including both the primitive cell and multi-unit cells simulations. Through the validation, we confirm that our input crystal structures lead to the same yield trends as those measured for silicon. In addition, an example simulation input file with comments is presented.

E.2 Validation

When a crystal is aligned along different axes and/or planes, the spacing between atomic rows and planes change, and as a result, the effects of channeling are affected as well. When the atoms are spaced closer together, the coulomb potential are stronger and is able to more effectively steer the ions. However, when the atoms are spaced further apart, the weaker coulomb potential allow higher probability of close encounter events (scattering). For example for both zincblende and diamond cubic structures, [110] has the smallest atomic row spacing while [100] has the largest atomic row spacing. Thus, the [110] channeling effect is the strongest for [110] and weakest for [100].

Therefore, to validate our simulation, we calculate and compare channeling yields for 2 MeV He particles in silicon to experimental data. To determine the total yield in the [100], [110], and [111] channeling directions, we consider the integrated area under the yield versus energy spectra for both the simulated and measured data. In Fig. E.1 and Fig. E.2, the simulated total yields for both primitive cell and multi-unit cell (3x3x3 is used for validation) are represented by slant-filled bars, and the measured total yields are represented by diamond-filled bars. For both cases, the trend of $Y_{[100]} > Y_{[111]} > Y_{[110]}$ is apparent, consistent with the yield trend for an ideal diamond structure[1], thus validating the simulation approach.[2]

E.3 Simulation Input File

In this section, a sample simulation input file is present and commented. Comments starts after "#" symbol

// Random generator

RndSeed:5310 #A random number generating seed to start off the ions at different locations. This number would need to be changed between jobs, otherwise output will be exactly the same.

// File description

FileHeader:A

// Scan settings #This section can be modified so there is a tile to simulate a random spectrum. In addition, it can also be setup to simulate angular channeling map to pin-point defect locations.

ScnTiltSt:0.0

ScnTiltEnd:0.0

ScnTiltStep:0.2

ScnAzSt:0

ScnAzEnd:0

ScnAzStep:1.0

//

// Simulation settings

SimNParticles:100 #Number of ions to simulate in this job submission

SimTime:20.0 #Simulation time. If a segfault error is received, try a shorter simulation time

SimzVelo:146.66 #This is the ion velocity in the unit of angstrom/femtoseconds. This is calculated using the beam energy and the ion's mass

SimPotProx2:16.0 #This defines the radius in which the program will consider when calculating forces acting on the ion by the host material. This term is radius squared and has a unit of angstrom. So here we are considering a sphere with radius of 4 angstrom

// end simulation settings

// Unit cell definition #This section can be divided into two sections. 1) defining the unit vector, a, b, c for the crystal lattice, and 2) specific atom locations in the structure of interest using a linear combination of unit vectors a, b, c. Note that the x, y, z coordinate of the atoms are not inputted here, it will need to be expressed by a linear combination of a, b, and c.

Unit_nAtoms:2 #how many atoms are in the structure described below

Unit_aX:2.826598 #using unit vector x, y, and z, user will be able to rotate the structures in any directions.

Unit_aY:-2.826598

Unit_aZ:0

Unit_bX:2.826598

Unit_bY:0

Unit_bZ:2.826598

Unit_cX:0

Unit_cY:-2.826598

Unit_cZ:2.826598

Atom1_ANo:31

Atom1_MNo:39

Atom1_Mass:69.723

Atom1_a:0.0

Atom1_b:0.0

Atom1_c:0.0

Atom2_ANo:7

Atom2_MNo:14

Atom2_Mass:14.0067

Atom2_a:0.25

Atom2_b:0.25

Atom2_c:0.25

// end unit cell

// Ion definition

Ion_ANo:2

Ion_MNo:4

Ion_Mass:4.0015

// end ion

// Probability distribution collection

PColl_Atom:2 #Which atom number from above we will be collecting the close encounter probability for. If there are more than one number for a specific atom, any number will work – program consider all the atoms from the atom specie specified.

//

// Crystal def

Crys_Trans:2 #How many times we will translate the input structure in x, y, z direction to make a bigger structure. This is not used when we are simulation XxXxX unit cells.

// end crystal def

E.5 Figures

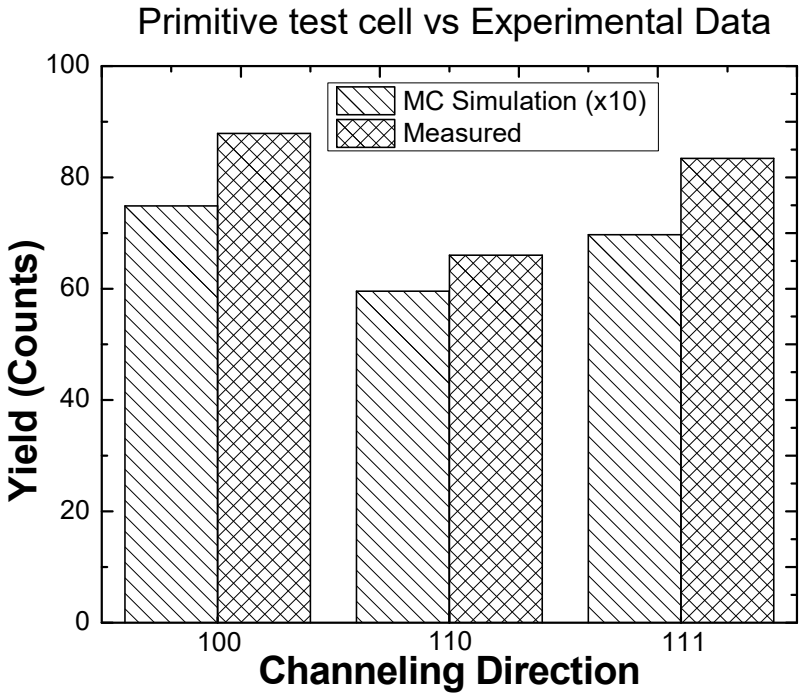

Figure E.1 Comparison of [100], [110], and [111] Rutherford Backscattering Spectrometry (RBS) channeling yields for He in silicon. The slant-filled bars represent the simulated RBS yield of a primitive cell structure (amplified 10 times), and the diamond-filled bars correspond to measured RBS yields. Similar trends of $Y_{[100]} > Y_{[111]} > Y_{[110]}$ are observed for both measurements and Monte Carlo simulations, thereby validating the simulation.

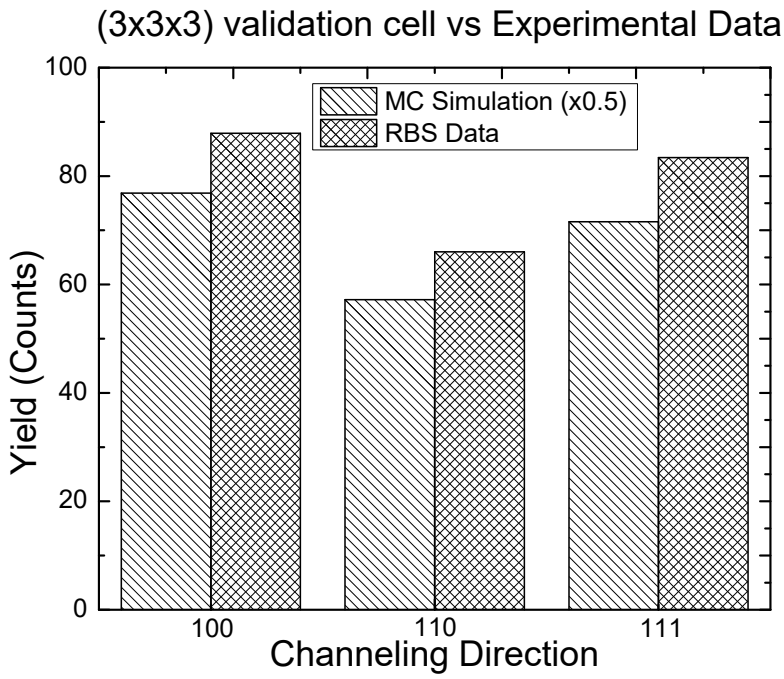

Figure E.2 Comparison of [100], [110], and [111] Rutherford Backscattering Spectrometry (RBS) channeling yields for He in silicon. The slant-filled bars represent the simulated RBS yield of a 3x3x3 cell structure (amplified 0.5 times), and the diamond-filled bars correspond to measured RBS yields. Similar trends of $Y_{[100]} > Y_{[111]} > Y_{[110]}$ are observed for both measurements and Monte Carlo simulations, thereby validating the simulation.

E.6 References

[1] J.R. Tesmer, and M. Nastasi. "Handbook of modern ion beam materials analysis." *Materials Research Society 700* (1995).

[2] T. Jen., G. Vardar, Y. Q. Wang, and R. S. Goldman. Appl. Phys. Lett. **107**, 22 (2015).

Appendix F

Automated MatLab Script for Structures Generation

F.1 Overview

To generate the multiple unit cell structures used for the MC-MD simulations described in Appendix C, Chapter 4, and Chapter 5, the following MatLab scripts were used. The scripts were written by James Horwarth and Timothy Johnson, under the supervision of the author. For primitive cell simulations (i.e. Chapter 3), atomic positions are easily determined from the coordinates provided in crystal visualizing programs such as Diamond. However, for multiple-unit cell simulations (>100 atoms), automated scripts are preferred. The automated scripts involved several steps, including rotation of crystal structure to the channeling direction [100], [110], and [111] via "Structure Rotation" and generation of X by X by X cell structure via "Cell Structure Generation". We note that a 3 x 3 x 3 cell was utilized in Chapter 4 and 5. Once all the atomic positions are generated for the desired structure size, and atomic positions, we use the MatLab script "input File

Generation" to automatically generate the input file needed for the simulation program in Appendix E.

F.2 Structure Rotation

```
clear all

%root 2
rt = 1/sqrt(2);
theta = -35.26*pi/180;

R_x = [1 0 0; 0 cos(theta) -sin(theta); 0 sin(theta) cos(theta)];
R_y = [rt 0 rt; 0 1 0; -rt 0 rt];
R_z = [rt -rt 0; rt rt 0; 0 0 1];

R_110 = R_y;
R_111 = R_y*R_x;
R_100_new = [0 -1 0; 1 0 0; 0 0 1];
R_100_N_As_along_y_axis = [0 0 -1; 0 1 0; 1 0 0];

Values = [
%             0 0 0;
%              3.89 0 0 ;
%              0 3.89 0;
%              0 0 3.89;
%              0 0 0;
%              3.89 0 0;
%              1.945 0 1.945;
%              0 0   3.89;
%              3.89 0 3.89;
%              1.945 1.945   0;
%              0 1.945   1.945;
%              3.89 1.945 1.945;
%              1.945 1.945   3.89;
%              0 3.89 0;
%              3.89 3.89 0;
%              1.945 3.89    1.945;
%              0 3.89    3.89;
%              3.89 3.89 3.89;
%              0.9725 0.9725 0.9725;
%              2.9175 2.9175 0.9725;
%              2.9175 0.9725 2.9175;
%              0.9725 2.9175 2.9175;
%              0.9725 0.9725 2.9175;
%              2.9175 2.9175 2.9175;
%              0.9725 2.9175 0.9725;
%              2.9175 0.9725 0.9725;
```

```
                0,0,0
                0,-3.89000000000000,0
                3.89000000000000,0,0
                0,0,3.89000000000000
                0,0,0
                0,-3.89000000000000,0
                0,-1.94500000000000,1.94500000000000
                0,0,3.89000000000000
                0,-3.89000000000000,3.89000000000000
                1.94500000000000,-1.94500000000000,0
                1.94500000000000,0,1.94500000000000
                1.94500000000000,-3.89000000000000,1.94500000000000
                1.94500000000000,-1.94500000000000,3.89000000000000
                3.89000000000000,0,0
                3.89000000000000,-3.89000000000000,0
                3.89000000000000,-1.94500000000000,1.94500000000000
                3.89000000000000,0,3.89000000000000
                3.89000000000000,-3.89000000000000,3.89000000000000
                0.972500000000000,-0.972500000000000,0.972500000000000
                2.91750000000000,-2.91750000000000,0.972500000000000
                0.972500000000000,-2.91750000000000,2.91750000000000
                2.91750000000000,-0.972500000000000,2.91750000000000
                0.972500000000000,-0.972500000000000,2.91750000000000
                2.91750000000000,-2.91750000000000,2.9175000000000
                2.91750000000000,-0.972500000000000,0.972500000000000
                0.972500000000000,-2.91750000000000,0.972500000000000
 ];

rotated_values = zeros(26,3);
for i = 1:26
   vector = Values(i,:);
   rotated_values(i,:) = vector*R_111;
end
```

F.3 Cell Structure Generation

```
function [ Atom_positions, a_vect, b_vect, c_vect, y ] =
MCMD_Input_func(sim_num, cell_size, direction, defects )
%UNTITLED Summary of this function goes here
%   Detailed explanation goes here

%GaAs Lattice Constant
ratio = (5.6533/3.89);

%User Input: Ratio of Diamond atom size to actual size

%INSTRUCTIONS FOR INPUT INTO ALLVALUES MATRIX
%-----------------------------------------%
```

```
%1st line: Input dimensions of repeating crystal
%2nd Line: Origin point of cubic crystal
%3rd Line: X-vector of unit crystal
%4th Line: Y-vector of unit crystal
%5th Line: Z-vector of unit crystal
%6th Line to End: Coordinate points of each of the atoms starting with
the origin


if (direction == 100)
    Values = [cell_size, cell_size, cell_size
         0,0,0
         0,-3.89000000000000,0
         0,0,-3.89000000000000
         3.89000000000000,0,0
         0,0,0
         0,-3.89000000000000,0
         1.94500000000000,-1.94500000000000,0
         3.89000000000000,0,0
         3.89000000000000,-3.89000000000000,0
         0,-1.94500000000000,-1.94500000000000
         1.94500000000000,0,-1.94500000000000
         1.94500000000000,-3.89000000000000,-1.94500000000000
         3.89000000000000,-1.94500000000000,-1.94500000000000
         0,0,-3.89000000000000
         0,-3.89000000000000,-3.89000000000000
         1.94500000000000,-1.94500000000000,-3.89000000000000
         3.89000000000000,0,-3.89000000000000
         3.89000000000000,-3.89000000000000,-3.89000000000000
         0.972500000000000,-0.972500000000000,-0.972500000000000
         0.972500000000000,-2.91750000000000,-2.91750000000000
         2.91750000000000,-2.91750000000000,-0.972500000000000
         2.91750000000000,-0.972500000000000,-2.91750000000000
         2.91750000000000,-0.972500000000000,-0.972500000000000
         2.91750000000000,-2.91750000000000,-2.91750000000000
         0.972500000000000,-0.972500000000000,-2.91750000000000
         0.972500000000000,-2.91750000000000,-0.972500000000000
            ];
end

if (direction == 110)
    Values = [cell_size, cell_size, cell_size
           0,0,0
           0,-3.89000000000000,0
           2.75064537881567,0,2.75064537881567
           -2.75064537881567,0,2.75064537881567
           0,0,0
           0,-3.89000000000000,0
           -1.37532268940783,-1.94500000000000,1.37532268940783
           -2.75064537881567,0,2.75064537881567
           -2.75064537881567,-3.89000000000000,2.75064537881567
           1.37532268940783,-1.94500000000000,1.37532268940783
           0,0,2.75064537881567
           0,-3.89000000000000,2.75064537881567
           -1.37532268940783,-1.94500000000000,4.12596806822350
           2.75064537881567,0,2.75064537881567
```

```
            2.75064537881567,-3.89000000000000,2.75064537881567
            1.37532268940783,-1.94500000000000,4.12596806822350
            0,0,5.50129075763134
            0,-3.89000000000000,5.50129075763134
            0,-0.972500000000000,1.37532268940783
            1.37532268940784,-2.91750000000000,2.75064537881567
            -1.37532268940784,-2.91750000000000,2.75064537881567
            0,-0.972500000000000,4.12596806822350
            -1.37532268940784,-0.972500000000000,2.75064537881567
            0,-2.91750000000000,4.12596806822350
            1.37532268940784,-0.972500000000000,2.75064537881567
            0,-2.91750000000000,1.37532268940783
    ];
end

if (direction == 111)
     Values = [cell_size, cell_size, cell_size
              0,0,0
           0,-3.17634375823555,-2.24564920001278
           2.75064537881567,-1.58791377749518,2.24601421082792
           -2.75064537881567,-1.58791377749518,2.24601421082792
           0,0,0
           0,-3.17634375823555,-2.24564920001278
           -1.37532268940783,-2.38212876786537,0.000182505407570810
           -2.75064537881567,-1.58791377749518,2.24601421082792
           -2.75064537881567,-4.76425753573074,0.000365010815141620
           1.37532268940783,-2.38212876786537,0.000182505407570810
           0,-1.58791377749518,2.24601421082792
           0,-4.76425753573074,0.000365010815141620
           -1.37532268940783,-3.97004254536055,2.24619671623549
           2.75064537881567,-1.58791377749518,2.24601421082792
           2.75064537881567,-4.76425753573074,0.000365010815141620
           1.37532268940783,-3.97004254536055,2.24619671623549
           0,-3.17582755499037,4.49202842165585
           0,-6.35217131322592,2.24637922164306
           0,-1.58804282830648,0.561594805410766
           1.37532268940784,-3.97017159617185,0.561777310818337
           -1.37532268940784,-3.97017159617185,0.561777310818337
           0,-3.17595660580166,2.80760901623869
           -1.37532268940784,-2.38199971705407,1.68460191082473
           0,-4.76412848491944,1.68478441623230
           1.37532268940784,-2.38199971705407,1.68460191082473
           0,-3.17621470742426,-0.561229794595624
    ];
end

%INSTRUCTIONS FOR THE INFORMATION MATRIX (INFO)
%-----------------------------------------------------------------%

%Asks for information about each atom listed above
%Input Atomic No, Mass No, and Mass for each atom IN THAT ORDER
%Input the information in the same order as you input the coordinates
for
%the atom.
%Example: 1 2 3 correlates with Atomic No: 1, Mass No: 2, and Mass: 3
```

```
    info = [

        31 70 69.723
        31 70 69.723
        31 70 69.723
        31 70 69.723
        31 70 69.723
        31 70 69.723
        31 70 69.723
        31 70 69.723
        31 70 69.723
        31 70 69.723
        31 70 69.723
        31 70 69.723
        31 70 69.723
        33 75 74.9216
        33 75 74.9216
        33 75 74.9216
        33 75 74.9216
        33 75 74.9216
        33 75 74.9216
        33 75 74.9216
        33 75 74.9216
            ];


dimensions = Values(1,:);
cube = dimensions(1);
v = dimensions(1); h = dimensions(2); d = dimensions(3);
cellsize = 8*(v)^3 + 6*(v)^2 + 3*(v) + 1;

error = Values(2,:);
mat = Values(3:5,:);
Values(1:5,:) = [];
data = Values;
[y,x] = size(data);


%Organizes the AllValues matrix into seperate matrices
%These matrices are:

%dimensions: number of translations of unit cell in each direction
%cube: for cubic translation, 'cube' = all values of dimensions
%v: separates dimensions into separate components (useful for non-cubic
%   translations, and initializing counter-variables)
%error: origin based on structural model.  error is subracted from
points
%       to make origin at (0,0,0).
%mat: create matrix occupied by basis vectors of the unit cell
%data: points occupied by atoms in specified structure
%y,x: rows (number of sites), and columns (number of coordinates) in
'data'
%     matrix
```

```
%-------------------------------------------------------------------------
---%

info_1D = info;
i = 1;

while i < cube
    info_1D = [info_1D; info];
    i = i+1;
end

info_2D = info_1D;
j = 1;

while j < cube
    info_2D = [info_2D info_1D];
    j = j+1;
end

info_3D = info_2D;
k = 1;

while k < cube
    info_3D = cat(3, info_3D, info_2D);
    k = k+1;
end

info = info_3D;

%'info' matrix consists of information about each atom in unit
structure.
%Each loop adds atomic information for added unit cells.  'i loop' adds
as
%many rows of 'info' set as specified by 'cube' (number of unit cells
in
%each direction). 'j loop' adds columns, and 'k loop' adds depth to
%information matrix.  This loop sequence essentially creates a data
%structure with atomic information for each unit cell in the total
%simulated structur.

%-------------------------------------------------------------------------
---%
mat = mat-[error;error;error];
mat = mat*ratio;
%Set coordinate origin to (0,0,0), and scale unit lengths to size of
real
%material.

a = mat(1,:);
b = mat(2,:);
c = mat(3,:);


a_vect = a;
```

```
b_vect = b;
c_vect = c;
% fprintf(outfile,'// Unit cell definition\n');
% fprintf(outfile,'Unit_nAtoms:%f\n',cellsize);
%fprintf(outfile,'Unit_aX:%1.4f\nUnit_aY:%1.4f\nUnit_aZ:%1.4f\n\nUnit_b
X:%1.4f\nUnit_bY:%1.4f\nUnit_bZ:%1.4f\n\nUnit_cX:%1.4f\nUnit_cY:%1.4f\n
Unit_cZ:%1.4f\n\n', a, b, c);
%Separates 'mat' into individual lattice vectors.  Print vector
components
%to file.

mag_A = norm(a);
mag_B = norm(b);
mag_C = norm(c);
%Finds the magnitude of each vector (a,b,c)

if round(mag_A*100)/100 ~= round(mag_B*100)/100 || round(mag_B*100)/100
~= round(mag_C*100)/100
    fprintf('\nError: Matrix dimensions are not equal, check
inputs.\n');
end
%Prints an error message if the magnitude of a, b, and c vectors are
not
%equal. If you are not running a cubic structure, ignore this message.

data = data*ratio;
A = a;
B = b;
C = c;
Error = error;
i = 1;
%Scale 'data' matrix (atom coordinates based on structural model).
%Initialize A, B, C, and Error to corresponding vectors above.

while i<y
    A = [A;a];
    B = [B;b];
    C = [C;c];
    Error = [Error; error];
    i = i+1;
end

B_2D = B;
C_2D = C;
Error = Error*ratio;

%Creates vectors with the nuber of rows equal to the number of atoms in
%unit cell, and separates into vector components.
%-------------------------------------------------------------------------
---&

data = data - Error;
data_2D = data;
%Set atom positions relative to origin at (0,0,0).
```

```
All_Data = data;
i = 1;
%Initialize variables.

while i < cube
    ACopy = i*A;
    All_Data = [All_Data; data + ACopy];
    B_2D = [B_2D; B];
    C_2D = [C_2D; C];
    i = i+1;
end

C_3D = C_2D;
data_2D = All_Data;
j = 1;

while j < cube
    BCopy = j*B_2D;
    All_Data = [All_Data data_2D+BCopy];
    C_3D = [C_3D C_2D];
    j = j+1;
end

data_3D = All_Data;
k = 1;

while k < cube
    CCopy = k*C_3D;
    All_Data = cat(3, All_Data, data_3D+CCopy);
    k = k+1;
end


%Each iteration adds coordinates of translated atoms to 'All_Data'
matrix.
%'XCopy' multiplies iteration number by lattice vector, this value is
added
%to original atom position to give position of new atom in translated
unit
%cell.  All atom positions are entered into 3D data structure
'All_Data'.

%-------------------------------------------------------------------------
---%

count = 0;
[row, col, dep] = size(All_Data);
l = 1;
m = 1;
e = 0;
List = [];
List_Final = [];
%intializes variables to undergo iteration
mat = mat';
%'mat' consists of basis vectors.  Vectors are transposed into proper
```

```
%format for linsolve function.

for k = 1:dep;

    for i = 1:3:col;

        for j = 1:row;

            vals = [All_Data(j,i,k); All_Data(j,i+1,k);
All_Data(j,i+2,k)];
            information = [info(j,i,k); info(j,i+1,k); info(j,i+2,k)];
            varargout = linsolve(mat, vals);
            varargout = round(varargout*100)/100;

            %Uses linsolve to find relative location of each atom. We
divide
            %each atom by the dimensions multiplied by the magnitude of
the
            %vector to ensure the maximum value of any given point can
be
            %1, 1, 1 --- UPDATE: Removed the scaling factor. If you
want to
            %reapply, divide vals by v, h, and d respectively.

            [t,u] = size(List);
            g = 1;
            e = 0;

            while g < t+1
                if List(g, :) == varargout'
                    e = 1000;
                end

                g = g+1;
            end

            List = [List;varargout'];
            %Checks for any repeats in the crystal. If any points are
            %repeated, then the repeat is deleted and the iteration
moves
            %on.

            if e ~= 1000

               List_Final(m,1) = information(1);
               List_Final(m,2) = information(2);
               List_Final(m,3) = information(3);
               List_Final(m,4) = varargout(1);
               List_Final(m,5) = varargout(2);
               List_Final(m,6) = varargout(3);

            m = m+1;
           %Generates 2D data structure of all unique atoms in total
           %structure. Rows corresponding to each atom, and columns
```

```
            %containing information and position for each atom.
             end
        end
    end
end

%-------------------------------------------------------------------------
---%
%Initialize Variables, Input Defect Information

sites = List_Final; %List_Final is total list of all atoms in
translated structure.
[x,y] = size(List_Final);
interstitials = zeros(x,y); %Initializes matrix to be filled with
positions of interstitial values.
check = sites(:,4)*4; %multiply by 4 to get whole numbers, use mod(4)
to find values corresponding to 0.25, and 0.75 locations.
defect_number = zeros(x,1);
%Initialize variables used for finding tetrahedral interstitial
positions
%in List_Final matrix.

for i = 1:x
    if mod(check(i),4) == 1 || mod(check(i),4) == 3
        interstitials(i,:) = sites(i,:);
        defect_number(i) = i;
    end
end
%Tetrahedral interstital sites occur at positions offset by 1/4 and 3/4
%lattice sites.  This loop uses modular arithmetic to identify sites at
%these positions, and add them to a list of total interstitial sites.

interstitials(all(interstitials==0,2),:)=[];
defect_number(all(defect_number==0,2),:)=[];

sub_empty = zeros(size(interstitials));
for i = 1:size(interstitials,1)
    if mod(i,8) >= 5 || mod(i,8) == 0
        sub_empty(i,:) = interstitials(i,:);
        interstitials(i,:) = [0 0 0 0 0 0];
    end
end
%Since sub_empty sites are initially listed after normal tetrahedral
sites,
%these will always be the 5-8 sites in the list of tetrahedral sites
for
%each unit cell.

interstitials(all(interstitials==0,2),:)=[];
sub_empty(all(sub_empty==0,2),:)=[];
[x1,y1] = size(interstitials);
[x2,y2] = size(sub_empty);
%Creates matrix including only sites of interstitials, no rows of [0 0
0]
```

```
nNNAs = defects(1);
nNAsAs = defects(2);
nNAs = defects(3);
nAsi = defects(4);
nN_int = defects(5);
nAsanti = defects(6);
nDi_int = defects(7);
nAsGa_NAs = defects(8);
nBi_sub = defects(9);
nBi_pairs = defects(10);
nBi_tet = defects(11);
nBianti = defects(12);
displac = defects(13);
%User inputs number of each type of defect to be present in the final
%simulated structure.  The number is based of the users calculations of
N
%fraction.

sites_new = sites;
for n = 1:size(defect_number,1)
    sites_new((defect_number(n)-(n-1)),:) = [];
end

%defect_site = randperm(x1);
interstitial_site = randperm(x2);
Gaantisites = randperm(size(sites_new,1));
Asantisites = randperm(size(interstitials,1));
%Initialize vector consisting of random distribution of 'interstitial'
row
%numbers.  This will be used to randomly assign positions to defects.

NNAs_location = zeros(nNNAs,y);
NAsAs_location = zeros(nNAsAs,y);
NAs_location = zeros(nNAs,y);
Asi_location = zeros(nAsi,y);
N_int_location = zeros(nN_int,y);
Asanti_location = zeros(nAsanti,y);
Bianti_location = zeros(nBianti,y);
Bisub_location = zeros(nBi_sub,y);
%-------------------------------------------------------------------------
---%
%Anti-site displacement

for i = 1:nAsanti
    Asanti_location(i,:) = [33 75 74.9216
sites_new(Gaantisites(i),4:6)];
    sites_new(Gaantisites(i),:) = Asanti_location(i,:);
end
Gaantisites(1:nAsanti) = [];

if displac ~= 0
    Asanti_sites = zeros(14*nAsanti,3);
for i = 1:nAsanti
    origin = Asanti_location(i,:);
    Asanti_sites(((i-1)*14)+1,:) = origin(:,4:6) + [0 0.5 0.5];
    Asanti_sites(((i-1)*14)+2,:) = origin(:,4:6) + [0 -0.5 0.5];
```

```
    Asanti_sites(((i-1)*14)+3,:) = origin(:,4:6) + [0.5 0.5 0];
    Asanti_sites(((i-1)*14)+4,:) = origin(:,4:6) + [0 -0.5 -0.5];
    Asanti_sites(((i-1)*14)+5,:) = origin(:,4:6) + [0 0.5 -0.5];
    Asanti_sites(((i-1)*14)+6,:) = origin(:,4:6) + [-0.5 -0.5 0];
    Asanti_sites(((i-1)*14)+7,:) = origin(:,4:6) + [-0.25 -0.25 0.25];
    Asanti_sites(((i-1)*14)+8,:) = origin(:,4:6) + [0.25 0.25 0.25];
    Asanti_sites(((i-1)*14)+9,:) = origin(:,4:6) + [0.25 -0.25 -0.25];
    Asanti_sites(((i-1)*14)+10,:) = origin(:,4:6) + [-0.25 0.25 -0.25];
    Asanti_sites(((i-1)*14)+11,:) = origin(:,4:6) + [0.25 -0.25 0.25];
    Asanti_sites(((i-1)*14)+12,:) = origin(:,4:6) + [-0.25 -0.25 -
0.25];
    Asanti_sites(((i-1)*14)+13,:) = origin(:,4:6) + [0.25 0.25 -0.25];
    Asanti_sites(((i-1)*14)+14,:) = origin(:,4:6) + [-0.25 0.25 0.25];
end
%Each (As)Ga repells its nearest-neighbor atoms.  There are 14 possible
%occupied neighboring sites: 6 Ga (Octohedral coordination @ antisite),
and
%8 As/Defect (4 tetrahedral sites from lattice, 4 possible occupied
%tetrahedral sites).

Asanti_defect = zeros(10*nAsanti,y);
for i = 1:size(Asanti_sites,1)
    for j = 1:size(sites_new,1)
        for k = 1:nAsanti
            origin = Asanti_location(k,4:6);
            v = Asanti_sites(i,:) - origin;
            if Asanti_sites(i,:) == sites_new(j,4:6)
              sites_new(j,4:6) = 1.019*v + origin;
            else for l = 1:size(interstitials,1)
                    if Asanti_sites(i,:) == interstitials(l,4:6)
                        interstitials(l,4:6) = 1.127*v + origin;
                    end
                    if Asanti_sites(i,:) == sub_empty(l,4:6)
                        sub_empty(l,4:6) = 1.127*v + origin;
                    end
                end
            end
        end
    end
end
end



%Scan through Anti-site locations, determine atoms affected
(Asanti_sites).
% If affected site occurs in crystal, check what type of site it is
using
% mod() to find tetrahedral sites.  To maintain list of tetrahedral
sites
% in the lattice (interstitials), tetrahedral interstitial defects
% (sub_empty), and FCC lattice sites (sites_new): scan each list for
% matching coordinates, then replace list entry with vector scaled to
% atomic displacement (Staab, T. E. M., et al. Physics B: Condensed
Matter
% 340 (2003)). Now, sites_new contains all FCC lattice sites,
interstitials
```

```
% contains tetrahedral sites in Zinc Blende structure, and sub_empty
% contains remaining tetrahedral sites to be occupied by interstitial
% defects.  All dispacements due to (As)Ga sites are accounted for in
these
% matrices.
%-------------------------------------------------------------------
---%
%Bi(Ga) Antisites

for i = 1:nBianti
    Bianti_location(i,:) = [83 209 208.9804
sites_new(Gaantisites(i),4:6)];
    sites_new(Gaantisites(i),:) = Bianti_location(i,:);
end
Gaantisites(1:nBianti) = [];

if displac ~= 0
    Bianti_sites = zeros(8*nBianti,3);
for i = 1:nBianti
    origin = Bianti_location(i,:);
    Bianti_sites(((i-1)*8)+1,:) = origin(:,4:6) + [-0.25 -0.25 0.25];
    Bianti_sites(((i-1)*8)+2,:) = origin(:,4:6) + [-0.25 0.25 -0.25];
    Bianti_sites(((i-1)*8)+3,:) = origin(:,4:6) + [0.25 0.25 0.25];
    Bianti_sites(((i-1)*8)+4,:) = origin(:,4:6) + [0.25 -0.25 -0.25];
    Bianti_sites(((i-1)*8)+5,:) = origin(:,4:6) + [-0.25 0.25 0.25];
    Bianti_sites(((i-1)*8)+6,:) = origin(:,4:6) + [0.25 -0.25 0.25];
    Bianti_sites(((i-1)*8)+7,:) = origin(:,4:6) + [-0.25 -0.25 -0.25];
    Bianti_sites(((i-1)*8)+8,:) = origin(:,4:6) + [0.25 0.25 -0.25];
end
%Each (Bi)Ga repells its nearest-neighbor atoms.  There are 8 possible
%occupied neighboring sites (must include unoccupied interstitials).

Bianti_defect = zeros(10*nBianti,y);
for i = 1:size(Bianti_sites,1)
    for j = 1:size(interstitials,1)
        for k = 1:nBianti
            origin = Bianti_location(k,4:6);
            v = Bianti_sites(i,:) - origin;
            if Bianti_sites(i,:) == interstitials(j,4:6)
              interstitials(j,4:6) = 1.13*v + origin;
            end
            if Bianti_sites(i,:) == sub_empty(j,4:6)
                sub_empty(j,4:6) = 1.13*v + origin;
            end
         end
    end
end
end
%(Bi)Ga antisites section used same code as (As)Ga antisites, modified
to
%include only tetrahedral sites.  Displacement values taken from
Ciatto,
%et al, "How much room for (Bi)Ga heteroantisites in GaAs(1-x)Bi(x)?"
%Appl. Phys. Letters 99, 141912 (2011).

%**Note: (Bi)Ga accounts for less than 5% of Bi incorporated into GaAs.
```

```
%-------------------------------------------------------------------------
---%
%(Bi)As subsititution
% Bi will substitute for As in GaAs structure.  As occupies sites in
% 'interstitials' matrix

for i = 1:nBi_sub
    Bisub_location(i,:) = [83 209 208.9804
interstitials(Asantisites(i),4:6)];
    interstitials(Asantisites(i),:) = Bisub_location(i,:);
end
Asantisites(1:nBi_sub) = [];

if displac ~= 0
    Bisub_sites = zeros(8*nBi_sub,3);
for i = 1:nBi_sub
    origin = Bisub_location(i,:);
    Bisub_sites(((i-1)*8)+1,:) = origin(:,4:6) + [-0.25 -0.25 0.25];
    Bisub_sites(((i-1)*8)+2,:) = origin(:,4:6) + [-0.25 0.25 -0.25];
    Bisub_sites(((i-1)*8)+3,:) = origin(:,4:6) + [0.25 0.25 0.25];
    Bisub_sites(((i-1)*8)+4,:) = origin(:,4:6) + [0.25 -0.25 -0.25];
    Bisub_sites(((i-1)*8)+5,:) = origin(:,4:6) + [-0.25 0.25 0.25];
    Bisub_sites(((i-1)*8)+6,:) = origin(:,4:6) + [0.25 -0.25 0.25];
    Bisub_sites(((i-1)*8)+7,:) = origin(:,4:6) + [-0.25 -0.25 -0.25];
    Bisub_sites(((i-1)*8)+8,:) = origin(:,4:6) + [0.25 0.25 -0.25];
end
%Each (Bi)Ga repells its nearest-neighbor atoms.  There are 8 possible
%occupied neighboring sites (must include unoccupied interstitials).

Bi_sub_defect = zeros(10*nBi_sub,y);
for i = 1:size(Bisub_sites,1)
    for j = 1:size(sites_new,1)
        for k = 1:nBi_sub
            origin = Bisub_location(k,4:6);
            v = Bisub_sites(i,:) - origin;
            if Bisub_sites(i,:) == sites_new(j,4:6)
              sites_new(j,4:6) = 1.07*v + origin;
            end
         end
    end
end
end

%Ciatto, et al. "How much room for (Bi)Ga heteroantisites in
%GaAs(1-x)Bi(x)?" Appl. Phys. Letters 99, 141912 (2011).
%-------------------------------------------------------------------------
---%
%Place Di-interstitial Defects
Di_int_sites = [sites_new; interstitials];
for i = 1:size(Di_int_sites,1)
    if Di_int_sites(i,4:6) == 0
        Di_int_sites(i,4:6) = [20 20 20];
    end
    for j = 1:nAsanti
        if Di_int_sites(i,4:6) == Asanti_location(j,4:6)
            Di_int_sites(i,:) = [0 0 0 0 0 0];
```

```
        end
    end
end
Di_int_sites(all(Di_int_sites==0,2),:)=[];

rand = randperm(size(Di_int_sites,1));
Di_int = zeros(size(Di_int_sites));
for i = 1:nDi_int
    Di_int(i,:) = Di_int_sites(rand(i),:);
    Di_int_sites(rand(i),:) = [0 0 0 0 0 0];
end
Di_int(all(Di_int==0,2),:) = [];
for i = 1:size(Di_int,1)
    if Di_int(i,4:6) == 20
        Di_int(i,4:6) = [0 0 0];
    end
end
t = zeros(1,size(Di_int,1));
for i = 1:size(sites_new,1)
    for j = 1:size(Di_int,1)
        if sites_new(i,4:6) == Di_int(j,4:6)
            t(j) = i;
        end
    end
end
for i = 2:length(t)
    if t(i) > t(i-1)
%         t,i
        t(i) = t(i)-1;
    end
end
for i = 1:length(t)
    if t(i) > 0
        sites_new(t(i),:) = [];
    end
end

t = zeros(1,size(Di_int,1));
for i = 1:size(interstitials,1)
    for j = 1:size(Di_int,1)
        if interstitials(i,4:6) == Di_int(j,4:6)
            t(j) = i;
        end
    end
end
for i = 2:length(t)
    if t(i) > t(i-1)
        t(i) = t(i)-1;
    end
end
for i = 1:length(t)
    if t(i) > 0
        interstitials(t(i),:) = [];
    end
end
```

```
As_Di = zeros(size(Di_int));
Ga_Di = zeros(size(Di_int));
for i = 1:size(Di_int,1)
    if mod(Di_int(i,4)*4,4) == 1 || mod(Di_int(i,4)*4,4) == 3
        As_Di(i,:) = Di_int(i,:);
    else Ga_Di(i,:) = Di_int(i,:);
    end
end
As_Di(all(As_Di==0,2),:)=[];
Ga_Di(all(Ga_Di==0,2),:)=[];

for i = 1:size(sites,1)
    if sites(i,:) == 20
        sites(i,:) = [0 0 0 0 0 0];
    end
end
for i = 1:size(As_Di,1)
    if As_Di(i,:) == 20
        As_Di(i,:) = [0 0 0 0 0 0];
    end
end
for i = 1:size(Ga_Di,1)
    if Ga_Di(i,:) == 20
        Ga_Di(i,:) = [0 0 0 0 0 0];
    end
end
%fprintf('\nThere are %1.0f Di_interstitial defects on Ga
sites\n',size(Ga_Di,1))
%nGa_Di_mix = input('How many mixed Di-interstitials:   ');
nGa_Di_mix = defects(14);
%fprintf('\nThere are %1.0f Di interstitial defects on As
sites\n',size(As_Di,1))
%nAs_Di_mix = input('How many mixed Di-interstitials:   ');
nAs_Di_mix = defects(15);

Ga_Di_mix = zeros(nGa_Di_mix,6);
As_Di_mix = zeros(nAs_Di_mix,6);
for i = 1:nGa_Di_mix
    Ga_Di_mix(i,:) = Ga_Di(i,:);
end
Ga_Di(1:nGa_Di_mix,:) = [];
for i = 1:nAs_Di_mix
    As_Di_mix(i,:) = As_Di(i,:);
end
As_Di(1:nAs_Di_mix,:) = [];

%-------------------------------------------------------------------------
---%
%As Di-interstitial

a = 2.61/5.6533; b = 2.72/5.6533; c = 2.75/5.6533;
A = acosd((b^2 + c^2 - a^2)/(2*b*c));

A1 = A/2; A2 = A/2;
b1 = c*sind(A1); b2 = c*cosd(A1);
c1 = b*sind(A2); c2 = b*cosd(A2);
```

```
x = sind(45);

As_Di_position = zeros(size(As_Di,1)*3,6);
if size(As_Di,1) ~= 0
for i = 1:size(As_Di)
    origin = As_Di(i,:)+ [0 0 0 0 0 0.25];
    As_Di_position((i-1)*3+1,:) = [33 75 74.9216 origin(4:6)];
    As_Di_position((i-1)*3+2,:) = [33 75 74.9216 (origin(4:6) + [-b1*x
-b1*x -b2])];
    As_Di_position((i-1)*3+3,:) = [33 75 74.9216 (origin(4:6) + [c1*x
c1*x -c2])];
end
end

a = 2.57/5.6533; b = 2.55/5.6533; c = 2.55/5.6533;
A = acosd((b^2 + c^2 - a^2)/(2*b*c));

A1 = A/2; A2 = A/2;
b1 = c*sind(A1); b2 = c*cosd(A1);
c1 = b*sind(A2); c2 = b*cosd(A2);
x = sind(45);

As_Di_mix_position = zeros(size(As_Di_mix*3,1)*3,6);
if size(As_Di_mix,1) ~= 0
for i = 1:size(As_Di_mix)
    origin = As_Di_mix(i,:) + [0 0 0 0 0 0.25];
    As_Di_mix_position((i-1)*3+1,:) = [33 75 74.9216 origin(4:6)];
    As_Di_mix_position((i-1)*3+2,:) = [31 70 69.723 (origin(4:6) + [-
b1*x -b1*x -b2])];
    As_Di_mix_position((i-1)*3+3,:) = [31 70 69.723 (origin(4:6) +
[c1*x c1*x -c2])];
end
end

%-------------------------------------------------------------------------
---%
%Ga Di-interstitials
a = 2.70/5.6533; b = 2.71/5.6533; c = 2.72/5.6533;
A = acosd((b^2 + c^2 - a^2)/(2*b*c));
A1 = A/2; A2 = A/2;
b1 = c*sind(A1); b2 = c*cosd(A1);
c1 = b*sind(A2); c2 = b*cosd(A2);
x = sind(45);

Ga_Di_position = zeros(size(Ga_Di,1)*3,6);
for i = 1:size(Ga_Di)
    if size(Ga_Di,1) ~= 0
    origin = Ga_Di(i,:) + [0 0 0 0 0 -0.25];
    Ga_Di_position((i-1)*3+1,:) = [31 70 69.723 origin(4:6)];
    Ga_Di_position((i-1)*3+2,:) = [31 70 69.723 (origin(4:6) + [-b1*x -
b1*x b2])];
    Ga_Di_position((i-1)*3+3,:) = [31 70 69.723 (origin(4:6) + [c1*x
c1*x c2])];
    end
end
```

```
a = 2.57/5.6533; b = 2.55/5.6533; c = 2.55/5.6533;
A = acosd((b^2 + c^2 - a^2)/(2*b*c));
A1 = A/2; A2 = A/2;
b1 = c*sind(A1); b2 = c*cosd(A1);
c1 = b*sind(A2); c2 = b*cosd(A2);
x = sind(45);

Ga_Di_mix_position = zeros(size(Ga_Di_mix,1)*3,6);

if size(Ga_Di_mix,1) ~= 0
    for i = 1:size(Ga_Di_mix)
        origin = Ga_Di_mix(i,:) + [0 0 0 0 0 0.25];
        Ga_Di_mix_position((i-1)*3+1,:) = [31 70 69.723 origin(4:6)];
        Ga_Di_mix_position((i-1)*3+2,:) = [33 75 74.9216 (origin(4:6) +
[-b1*x -b1*x -b2])];
        Ga_Di_mix_position((i-1)*3+3,:) = [33 75 74.9216 (origin(4:6) +
[c1*x c1*x -c2])];
    end
end

sites_total = [sites; As_Di_position; As_Di_mix_position;
Ga_Di_position; Ga_Di_mix_position];
%-------------------------------------------------------------------------
---%
% Add (As)Ga-(N)As Pairs

As_sites = interstitials;
Ga_sites = sites_new;

%Determine defect sites
rand = randperm(size(As_sites,1));
Ga_defect_sites = zeros(nAsGa_NAs,6);
As_defect_sites = zeros(nAsGa_NAs,6);
for i = 1:nAsGa_NAs
    As_defect_sites(i,:) = [7 14 14 As_sites(rand(i),4:6)];
    interstitials(rand(i),:) = [100 100 100 100 100 100];
    Ga_defect_sites(i,:) = [33 75 74.9216 (As_sites(rand(i),4:6) -
[0.25 0.25 0.25])];
end
for i = 1:nAsGa_NAs
    for j = 1:size(sites_new)
        if sites_new(j,4:6) == Ga_defect_sites(i,4:6)
           sites_new(j,:) = [100 100 100 100 100 100];
        end
    end
end
sites_new(all(sites_new==100,2),:)=[];
interstitials(all(interstitials==100,2),:) = [];

%-------------------------------------------------------------------------
---%
% Bi Pairs
% Bi pairs referrs to a paired set of substitutional Bi on As sites
% surrounding a single Ga atom ("GaAs2Bi2").  Start by choosing a Ga
```

```
% ('sites_new') to host the Bi pair, add [0.25 0.25 0.25], etc. to Ga
site
% to find tetrahedral sites surrounding specific Ga atom.  Search for
these
% tet. sites in 'interstitials', randomly choose two to convert from As
to
% Bi.

rand = randperm(size(sites_new,1));
Bi_pair_host = zeros(size(nBi_pairs,1),6);

% Select host
for i = 1:nBi_pairs
    Bi_pair_host(i,:) = sites_new(rand(i),:);
    sites_new(rand(i),:) = 100;
end

% Find tetrhedral sites surrounding host
pair_host_tet = zeros(4*nBi_pairs,6);
for i = 1:nBi_pairs
    pair_host_tet(4*(i-1)+1,4:6) = Bi_pair_host(i,4:6) + [0.25 0.25
0.25];
    pair_host_tet(4*(i-1)+2,4:6) = Bi_pair_host(i,4:6) + [-0.25 -0.25
0.25];
    pair_host_tet(4*(i-1)+3,4:6) = Bi_pair_host(i,4:6) + [-0.25 0.25 -
0.25];
    pair_host_tet(4*(i-1)+4,4:6) = Bi_pair_host(i,4:6) + [0.25 -0.25 -
0.25];
end

% Choose As to replace
% Make rand_pair set of 4 (4 tetrahedral sites per host) to ensure that
2
% atoms from each are replaced.
Bi_pairs = zeros(2*nBi_pairs,6);

for i= 1:nBi_pairs
    rand_pair = randperm(4);
    Bi_pairs(2*(i-1)+1,:) = [83 209 208.9804 pair_host_tet(4*(i-
1)+rand_pair(1),4:6)];
    Bi_pairs(2*(i-1)+2,:) = [83 209 208.9804 pair_host_tet(4*(i-
1)+rand_pair(2),4:6)];
end

% Find host and Bi_pairs in 'sites_new' and 'interstitials',
respectively,
% and remove entries so no more than one defect is place on a lattice
site.
for i = 1:nBi_pairs
    for j = 1:size(sites_new)
        if sites_new(j,4:6) == Bi_pair_host(i,4:6)
            sites_new(j,:) = 100;
        end
    end
end
sites_new(all(sites_new==100,2),:)=[];
```

```
for i = 1:size(Bi_pairs,1)
    for j = 1:size(interstitials,1)
        if interstitials(j,4:6) == Bi_pairs(i,4:6)
            interstitials(j,:) = 100;
        end
    end
end
interstitials(all(interstitials==100,2),:)=[];


% Bi tetramers
% Bi tetramers have a Ga atom surrounded by 4 Bi atoms, replacing all
of
% the As in tetrahedral sites around the host Ga.  The same strategy as
was
% used with Bi pairs will be used to locate a host atom and the
tetrahedral
% sites associated with it.  In this case, all tetrahedral sites are
% occupied by Bi, so there is no need to randomly choose two sites for
each
% defect.

rand = randperm(size(sites_new,1));
Bi_tet_host = zeros(nBi_tet,6);

% Select host
for i = 1:nBi_tet
    Bi_tet_host(i,:) = sites_new(rand(i),:);
    sites_new(rand(i),:) = 100;
end

% Find tetrhedral sites surrounding host
tet_host_tet = zeros(4*nBi_tet,6);
for i = 1:nBi_tet
    tet_host_tet(4*(i-1)+1,4:6) = Bi_tet_host(i,4:6) + [0.25 0.25
0.25];
    tet_host_tet(4*(i-1)+2,4:6) = Bi_tet_host(i,4:6) + [-0.25 -0.25
0.25];
    tet_host_tet(4*(i-1)+3,4:6) = Bi_tet_host(i,4:6) + [-0.25 0.25 -
0.25];
    tet_host_tet(4*(i-1)+4,4:6) = Bi_tet_host(i,4:6) + [0.25 -0.25 -
0.25];
end

%Replace As with Bi
Bi_tet = zeros(4*nBi_tet,6);
for i= 1:nBi_tet
    Bi_tet(4*(i-1)+1,:) = [83 209 208.9804 tet_host_tet(4*(i-
1)+1,4:6)];
    Bi_tet(4*(i-1)+2,:) = [83 209 208.9804 tet_host_tet(4*(i-
1)+2,4:6)];
    Bi_tet(4*(i-1)+3,:) = [83 209 208.9804 tet_host_tet(4*(i-
1)+3,4:6)];
```

```
    Bi_tet(4*(i-1)+4,:) = [83 209 208.9804 tet_host_tet(4*(i-
1)+4,4:6)];
end

% Find host and Bi_tet in 'sites_new' and 'interstitials',
respectively,
% and remove entries so no more than one defect is place on a lattice
site.
for i = 1:nBi_tet
    for j = 1:size(sites_new)
        if sites_new(j,4:6) == Bi_tet_host(i,4:6)
            sites_new(j,:) = 100;
        end
    end
end
sites_new(all(sites_new==100,2),:)=[];

for i = 1:size(Bi_tet,1)
    for j = 1:size(interstitials,1)
        if interstitials(j,4:6) == Bi_tet(i,4:6)
            interstitials(j,:) = 100;
        end
    end
end
interstitials(all(interstitials==100,2),:)=[];

%-------------------------------------------------------------------------
---%
%Place other defects
defect_site = randperm(size(interstitials,1));
for i= 1:size(defect_site,1)
    for j = 1:size(Di_int)
        if interstitials(defect_site(i),:) == Di_int(j,:)
            defect_site(i) = 0;
        end
    end
end
defect_site(all(defect_site==0,2),:)=[];

for i = 1:nNNAs
    NNAs_location(i,:) = interstitials(defect_site(i),:);
    interstitials(defect_site(i),:) = 100;
end
defect_site(1:nNNAs) = [];
defect_site(all(defect_site==0,2),:)=[];
for j = 1:nNAsAs
    NAsAs_location(j,:) = interstitials(defect_site(j),:);
    interstitials(defect_site(j),:) = 100;
end
defect_site(1:nNAsAs) = [];

for k = 1:nNAs
    NAs_location(k,:) = interstitials(defect_site(k),:);
    interstitials(defect_site(k),:) = 100;
end
defect_site(1:nNAs) = [];
```

```
interstitials(all(interstitials==100,2),:) = [];

for i = 1:nAsi
    Asi_location(i,:) = sub_empty(interstitial_site(i),:);
end
interstitial_site(1:nAsi) = [];

for i = 1:nN_int
    N_int_location(i,:) = sub_empty(interstitial_site(i),:);
end
interstitial_site(1:nN_int) = [];

%Each loop assigns a position to different types of defects.  For
example:
% When i = 1, if defect_site(1) = 4, the first row of NNAs_location is
% filled with the 4th row of 'interstitials' (the location of the 4th
%interstitial in the list).  This allows for a random distribution of
%defects throughout the structure.  Afterwards, the 1:nXXX rows of
%'defect_site' are cleared so that when j = 1, NAsAs_location(1,:)
%~= NNAs_location(1,:).
%Note: All defect site assignments are made after placement of As
%anti-sites to ensure that defects are displaced as well.

%-------------------------------------------------------------------------
---%
%Add defects to defined positions
N1disp_NNAs = [-0.0553 -0.0553 -0.0553];
N2disp_NNAs = [0.0924 0.0924 0.0924];

% Ndisp_NAsAs = [0 -0.1109 0];
% Asdisp_NAsAs = [0 0.0742 0];

Ndisp_NAsAs = [0 -0.2016 0];
Asdisp_NAsAs = [0 0.115 0];

NNAs_position = zeros(nNNAs*2,y);
NAsAs_position = zeros(nNAsAs*2,y);
NAs_position = NAs_location;
Asi_position = Asi_location;
N_int_position = N_int_location;
% Since some defects call for two atoms occupying a single lattice
site,
% each defect atom is displaced from the center of the site.  Here, the
user
% will input displacement vectors relative to the lattice site as a row
% vector ([a b c]).  No displacement vector is needed for (As)As, or
(N)As
% substitution.

for m = 1:nNNAs
    NNAs_position((2*m-1),:) = [7 14 14 (NNAs_location(m,4:6) +
N1disp_NNAs)];
    NNAs_position((2*m),:) = [7 14 14 (NNAs_location(m,4:6) +
N2disp_NNAs)];
end
```

```
for m = 1:nNAsAs
    NAsAs_position((2*m-1),:) = [7 14 14 (NAsAs_location(m,4:6) +
Ndisp_NAsAs)];
    NAsAs_position((2*m),:) = [33 75 74.9216 (NAsAs_location(m,4:6) +
Asdisp_NAsAs)];
end

for m = 1:nNAs
    NAs_position(m,:) = [7 14 14 NAs_location(m,4:6)];
end

for i = nAsi
    if i > 0
        for j = 1:nAsi
        Asi_position(j,1:3) = [33 75 74.9216];
        end
    else
        continue
    end
end

for i = nN_int
    if i > 0
        for j = 1:nN_int
        N_int_position(j,1:3) = [7 14 14];
        end
    else
        continue
    end
end

% Loops add defect offset locations for (N-N)As, and (N-As)As defects.
% Using matrix positions 2m and 2m-1 allow for having two defect atoms
per
% lattice site.  Columns 1:3 explicitly state info for atoms involved
in
% the defect.
%-------------------------------------------------------------------------
---%
% %Remaining As sites
%
% nAsAs = size(interstitials,1) - nAsGa_NAs - nNNAs - nNAsAs - nNAs...
%         - nBi_sub - 2*nBi_pairs - 4*nBi_tet;
% AsAs_location = zeros(nAsAs,y);
% for l = 1:nAsAs
%     AsAs_location(l,:) = interstitials(defect_site(l),:);
% end
% defect_site(1:nAsAs) = [];
%
% AsAs_position = AsAs_location;

%-------------------------------------------------------------------------
---%
%Generate List of all atomic positions in system
```

```
Atom_positions = [sites_new; interstitials; Ga_defect_sites; ...
                  As_defect_sites; NNAs_position; NAsAs_position;...
                  NAs_position; Asi_position;...
                  N_int_position; As_Di_position;
As_Di_mix_position;...
                  Ga_Di_position; Ga_Di_mix_position; %Bi_sub_sites;...
                  Bi_pairs; Bi_tet];
% size(sites_new)
% size(interstitials)
% size(Ga_defect_sites)
% size(As_defect_sites)
% size(NNAs_position)
% size(NAsAs_position)
% size(NAs_position)
% size(Asi_position)
% size(N_int_position)
% size(As_Di_position)
% size(As_Di_mix_position)
% size(Ga_Di_position)
% size(Ga_Di_mix_position)
% size(Bi_sub_sites)
% size(Bi_pairs)
% size(Bi_tet)

for i = 1:size(Atom_positions,1)
    for j = 4:6
        if abs(Atom_positions(i,j)) < 0.01
            Atom_positions(i,j) = abs(Atom_positions(i,j));
        end
    end
end
%Since minimum distance from any point (relative to basis vectors) is
%0.2183, any vector location with a value <0.01 can be considered 0
with
%rounding error.  Loop scans for '0-coordinates' and takes their
absolute
%value to ensure there are no '-0.0000' entries in output.

trans = (mat*Atom_positions(:,4:6)')';

file = strcat('sim_', num2str(sim_num), '_', num2str(direction),
'.xyz');
outputfile = fopen(file, 'wt');


fprintf(outputfile,'%1.0f\n\n',size(Atom_positions,1));
for n = 1:size(Atom_positions,1)
    i = Atom_positions(n,1);
    if (13 < i) && (i < 15)
        fprintf(outputfile,'Si ');
    end
    if (30 < i)&&(i < 32)
        fprintf(outputfile,'Ga ');
    end
    if (32 < i)&&(i < 34)
```

```
        fprintf(outputfile,'As ');
    end
    if (6 < i)&&(i < 8)
        fprintf(outputfile,'N ');
    end
    if (82 < i)&&(i < 84)
        fprintf(outputfile,'Bi ');
    end
    fprintf(outputfile,'%1.4f %1.4f
%1.4f\n',trans(n,1),trans(n,2),trans(n,3));
end

fclose(outputfile);
end
```

F.4 Input File Generation

```
function [  ] = param_maker( direction, sim_data, run_number )

[Atom_positions, a, b, c, y] = MCMD_Input_func(sim_data(1),
sim_data(2), direction, sim_data(4:18));

param_file = fopen('params.txt', 'wt');

fprintf(param_file, '// Random generator\n');
fprintf(param_file, ['RndSeed:', num2str(5310*run_number), '\n']);
fprintf(param_file, '\n');

fprintf( param_file,'// File description\n');
fprintf(param_file, ['FileHeader:sim_', num2str(sim_data(1)), ' ',
num2str(direction), ' run ', num2str(run_number), '\n\n']);

fprintf(param_file, '// Scan settings\n');
fprintf(param_file, 'ScnTiltSt:0.0\n');
fprintf(param_file, 'ScnTiltEnd:0.0\n');
fprintf(param_file, 'ScnTiltStep:0.0\n');
fprintf(param_file, 'ScnAzSt:0\n');
fprintf(param_file, 'ScnAzEnd:0\n');
fprintf(param_file, 'ScnAzStep:0\n');
fprintf(param_file, '//\n\n');

fprintf(param_file, '// Simulation settings\n');
fprintf(param_file, 'SimNParticles:100\n');
fprintf(param_file, 'SimTime:20.0\n');
fprintf(param_file, 'SimzVelo:146.66\n');
fprintf(param_file, 'SimPotProx2:16.0\n');
fprintf(param_file, '// end simulation settings\n\n');

fprintf(param_file, '// Unit cell definition\n');
```

```
Number_atoms = size(Atom_positions);
fprintf(param_file, ['Unit_nAtoms:', num2str(Number_atoms(1)),
'\n\n']);
fprintf(param_file,'Unit_aX:%1.4f\nUnit_aY:%1.4f\nUnit_aZ:%1.4f\n\nUnit
_bX:%1.4f\nUnit_bY:%1.4f\nUnit_bZ:%1.4f\n\nUnit_cX:%1.4f\nUnit_cY:%1.4f
\nUnit_cZ:%1.4f\n\n', a, b, c);


for n = 1:size(Atom_positions,1)
    Atom_positions(n,y+1) = n;
      fprintf(param_file,'Atom%1.0f_ANo:%1.4f \nAtom%1.0f_MNo:%1.4f
\nAtom%1.0f_Mass:%1.4f \n',Atom_positions(n,end),Atom_positions(n,1),
Atom_positions(n,end), Atom_positions(n,2), Atom_positions(n,end),
Atom_positions(n,3));
      fprintf(param_file,'Atom%1.0f_a:%1.4f \nAtom%1.0f_b:%1.4f
\nAtom%1.0f_c:%1.4f \n\n', Atom_positions(n,end) ,Atom_positions(n,4),
Atom_positions(n,end), Atom_positions(n,5), Atom_positions(n,end),
Atom_positions(n,6));
      fprintf(param_file, '\n');
end

fprintf(param_file, '\n// end unit cell\n\n');

fprintf(param_file, '// Ion definition\n');
fprintf(param_file, 'Ion_ANo:2\n');
fprintf(param_file, 'Ion_MNo:4\n');
fprintf(param_file, 'Ion_Mass:4.0015\n');
fprintf(param_file, '// end ion\n\n');

%find Nitrogen Atom
%only works for defects with nitrogen
%can change in future
Nitrogen_indices = find(Atom_positions(:,1) < 8);

fprintf(param_file, '// Probablity distribution collection\n');
fprintf(param_file, ['PColl_Atom:' num2str(Nitrogen_indices(1)) '\n']);
fprintf(param_file, '//\n\n');

fprintf(param_file, '// Crystal def\n');
fprintf(param_file, 'Crys_Trans:0\n');
fprintf(param_file, '// end crystal def\n');

fclose(param_file);
end
```

Appendix G

Materials Parameters and Samples

This appendix lists a variety of materials parameters as well as samples used in this thesis. Table. G.1 lists the materials parameters of GaAs, GaN, and GaBi. In addition, Table G.2 lists the GaAsN samples used in Chapter 3 and 4. Finally, Table G.3 lists the GaAsNBi samples used in Chapter 5 and 6.

Table G.1 Materials parameters for GaAs, GaN, and GaBi

Materials	lattice parameter (Å)	thermal vibration amplitude (Å)	C_11 (GPa)	C_12 (GPa)
GaN	4.5 [1]	-	296 [2]	154 [2]
GaBi	6.33 [3, 4]	-	73 [5]	32 [5]
GaAs	5.6533 [6]	0.078 [7]	119 [6]	53.8 [6]

Table G.2 GaAsN Films

RMBE #	x (%)	As4/Ga Ratio	RMS Roughness	GaAs FWHM
96	2.5	38	0.94 nm	32
96 (Annealed)	2.5	38	0.98 nm	36
97	3.2	38	n/a	n/a
112	2.1	38	1.02 nm	35
122 (Annealed)	2.1	38	1.05 nm	34
122	0.6	29	n/a	n/a
158	1.9	25	1.22 nm	38
158 (Annealed)	1.9	25	1.18 nm	40

Table G.3 GaAsNBi Films

RMBE	x (%)	y (%)	As4/Ga Ratio	RMS Roughness	GaAs FWHM
1283	1.8	5.6	20	0.34 nm	14.5 arcsec
1284	1.8	3	20	0.45 nm	13.7 arcsec
1285	1.4	1.6	20	0.46 nm	13.9 arcsec
1286	0	0.9	20	0.39 nm	14.1 arcsec
1293	3.2	0.7	20	0.32 nm	14.3 arcsec
1294	3.2	1.7	20	0.42 nm	14.4 arcsec
1295	3.2	2.3	20	0.40 nm	13.8 arcsec
1296	3.2	0	20	0.37 nm	13.8 arcsec

G.1 References

[1] W. Li, M. Pessa, and J. Likonen. Appl. Phys. Lett 78, 2864 (2001).

[2] K. Kim, W.R. Lambrecht, and B. Segall, Phys. Rev. B 53, 16310 (1996).
[3] A. Janotti, S.-H. Wei, and S. Zhang, Phys. Rev. B 65, 115203 (2002).

[4] M. Yoshimoto, W. Huang, and K. Oe, MRS Proceedings 829, 845 (2004).

[5] S.Q. Wang, and H.W. Ye, Phys. Satt. Sol. B. (240), 45 (2003).

[6] O. Madelung, *Semiconductors-Basic Data, 2nd rev. ed.*, (Springer, Berlin, 1996), p. 105.

[7] J.L. Whitton, G. Carter, J. H. Freeman, and G. A. Gard. J. Mat. Sci 4, 208 (1969).